

**RARE EARTH METAL (SAMARIUM, LANTHANUM) SULFIDE
/GRAPHENE OXIDE COMPOSITE THIN FILMS FOR
SUPERCAPACITOR APPLICATION**

A THESIS SUBMITTED

TO



D.Y.PATIL EDUCATION SOCIETY (DEEMED TO BE UNIVERSITY), KOLHAPUR

FOR THE DEGREE

OF

DOCTOR OF PHILOSOPHY

IN

PHYSICS

UNDER THE FACULTY OF

CENTRE FOR INTERDISCIPLINARY STUDIES

BY

Ms. TRUPTI TANAJI GHOGARE

M. Sc

UNDER THE GUIDANCE

OF

PROF.C.D.LOKHANDE

M.Sc., Ph. D.

CENTRE FOR INTERDISCIPLINARY STUDIES

D.Y.PATIL EDUCATION SOCIETY (DEEMED TO BE UNIVERSITY), KOLHAPUR

(M.S) INDIA. [2020]

DECLARATION

I hereby declare that the thesis entitled “ **Rare earth metal (Samarium, Lanthanum) sulphide/graphene oxide composite thin films for supercapacitor application**” submitted for the award of degree of **Doctor of Philosophy** in the faculty of Centre for Interdisciplinary Studies of D.Y. Patil Education Society (Deemed to be University), Kolhapur is completed and written by me, has not previously formed the basis for the award of any Degree or Diploma or other similar title of this or any other University in India or any other country or examining body to the best of my knowledge. Further, I declare that I have not violated any of the provisions under Copyright and Piracy/Cyber/IPR Act amended from time to time.

Place: Kolhapur

Date: 07/10/2020

(Ms.Trupti T.Ghogare)

CERTIFICATE

This is to certify that the thesis entitled, “ **Rare earth metal (Samarium, Lanthanum) sulphide / graphene oxide composite thin films for supercapacitor application**”, which is being submitted herewith for the award of the degree of **Doctor of Philosophy** in **Physics** under the faculty of Centre for Interdisciplinary Studies of D.Y. Patil Education Society (Deemed to be University), Kolhapur, is the result of the original research work completed by **Ms. Trupti Tanaji Ghogare** under my supervision and guidance and to the best my knowledge and belief, the work embodied in this thesis has not formed earlier the basis for the award of any degree or similar title of this or any other University or examining body.

Place: Kolhapur

Date: 07/10/2020

Research Guide

Prof. C.D. Lokhande

ACKNOWLEDGEMENT

I am Trupti Tanaji Ghogare. At the completion of my Ph.D. thesis, I would like to express my sincere gratitude towards my advisor, Prof. C. D. Lokhande (Research Director and Dean, D.Y. Patil Education Society (Deemed to be University), Kolhapur) for the continuous support of my Ph.D. study and related research, for his motivation, and immense knowledge. I found a very thirsty researcher in him, while approaching regarding any research related query. His guidance helped me in all the time of research and writing of this thesis. Apart from research work, I am really inspired from his many rare human qualities such as, diligent planning of work, management of time, consistency of work, discipline, dedication and hard work.

All faculty members of the department have been very kind enough to extend their help at various phases of research. I do hereby acknowledge all them. I am also thankful non-teaching staff of Centre for Interdisciplinary Studies department and all members for their kind co-operation during my research work.

I wish to express my appreciation my seniors Dr. R.N. Bulakhe, Dr. T. P. Gujar, Dr. R. B. Pujari, Dr. A.M. Patil for co-operation, scientific discussion and the encouragement providing to me during the course of research work. I would also like to express my sincere thanks to, Mr. Abhishek C. Lokhande for providing me very important sample characterization data, during entire research work timely. I also have a thank to my all laboratory colleagues Mr. Pranav Katarak, Mr. Navanath Padalkar, Mr. Shrikant Sadawar, Ms. Shital Kale, Mrs. Supriya Marje, Mr. Shivaji Ubale, Mr. Vikas Mane, Mr. Dhanaji Malvekar, and Ms. Priti Bagwade and all other research scholar of department, who all have enlarged their support in a very exceptional way, and I benefited plenty from them, across their academic and personal interactions, their suggestions at different places of my research work.

I am especially thankful to Prof. H.M. Pathan, Department of Physics, Savitribai Phule Pune University for his good support, encouragement and for making me available the laboratory facility at the stage of before and after Ph.D work.

Some special thanks are reserved to my parents Mom (Sharda T. Ghogare), Papa (Tanaji S. Ghogare), Brother (Tushar T. Ghogare), Dr.Yashwantrao Thorat, Dr.V.V.Bhosale, sir to my best friends and entire relatives. My hard working parents have sacrificed their lives for my education with unconditional love and care and I would not have made it this far without them.

Place: Kolhapur

- Trupti

Date: 07/10/2020

SUMMARY OF RESEARCH WORK LIST OF PUBLICATIONS

Papers Accepted/Submitted at International Journals

- 1) **Trupti T.Ghogare**, R.B. Pujari, A. C.Lokhande, C. D.Lokhande, “ Hydrothermal synthesis of nanostructured β -LaS₂ thin films”, Applied Physics A 124 (2018), 248-250.
- 2) **Trupti T.Ghogare**, A.C.Lokhande, R. B. Pujari, C.D.Lokhande, Lanthanum sulfide/Graphene oxide composite thin film and their's supercapacitor application. SN Applied Sciences 2 (2019), 110-119.
- 3) **Trupti T.Ghogare**, A.C.Lokhande, M.R.Phadatare, C. D. Lokhande, A Graphene oxide /samarium sulfide composite electrode for supercapacitor application. Surfaces and Interfaces, 19 (2020), 100507-100512.
- 4) **Trupti T. Ghogare**, R. N. Bulakhe, S.B.Ubale, I. In and C. D. Lokhande Soft Chemically Deposited Nanocrystallite Samarium Sulfide (Sm₂S₃) Thin Film: Supercapacitive Properties (In process).
- 5) R. B. Pujari, A.C.Lokhande, **Trupti T.Ghogare**, S.B. kale, C.D. Lokhande, Nanocrystalline monoclinic Yb₂S₃ thin films from simple chemical synthesis approach and their characterization, Journal of Materials Science: Materials in Electronics 29 (2018), 14116-14121.
- 6) S. B.Ubale, **Trupti T. Ghogare**, A. C. Lokhande, C. D. Lokhande, Hydrothermal synthesis of Sm₂O₃thin film and their's supercapacitor application. SN Applied Sciences 2 (2020), 1-5.
- 7) V.D. Patake, **Trupti T. Ghogare**, A.D. Gulbake, C.D. Lokhande, The electrochemical performance of electrodeposited chitosan bio-nanopolymer in non-aqueous electrolyte: a new anodic material for supercapacitor, SN Applied Sciences 2 (2020), 1063-1067.
- 8) H.L. Pushpalatha, **Trupti T. Ghogare**, N.H. Vibhu, P.P.Bagawade, R.N. Bulakhe, Insik In, C.D. Lokahnde, Supercapacitive Evaluation of Soft Chemically Deposited Yttrium Sulfide (Y₂S₃) Thin Films (In process).

Papers Presented at National/International Conferences

1. **Trupti T.Ghogare**, R. N.Bulakhe, P.P.Bagawade, V.J.Mane, D. B Malavekar, I. In and C.D.Lokhande, “Graphene Oxide/Molybdenum Oxide (GO/MnO₃) Composite Thin Film as a Supercapacitor Electrode.” International Conference on Smart Material and Nanotechnology (ICSMN-2020) Organised by SKN Sinhgad Collage of Engineering, Pandharpur.
2. **Trupti T. Ghogare**, V. C. Lokhande, T. Ji, U.M.Patil and C. D. Lokhande, “A graphene oxide /samarium sulfide (GO/Sm₂S₃) composite thin film: Preparation and Electrochemical study”. 4th International Conference on Physics of Materials and Materials Based Device Fabrication (4th ICPMM-MDF-2019) Organised by Shivaji University, Kolhapur.

INDEX

Chapter no.	Title	Page No.
I	Introduction of Supercapacitor and Literature Survey of Supercapacitive Rare Earth Chalcogenides	1-25
II	Theoretical Background of Deposition Methods and Thin Film Characterization Techniques	26-49
III	Synthesis, Characterization and Supercapacitive Performance of Samarium Sulfide and Graphene Oxide/Samarium Sulfide Composite Thin Films	50-85
IV	Synthesis, Characterization and Supercapacitive Performance of Lanthanum Sulfide and Graphene Oxide/Lanthanum Sulfide Composite Thin Films	86-121
V	Chemical Synthesis of Manganese Oxide Thin Film: Characterization and Supercapacitive Performance	122-135
VI	Device Fabrication of Symmetric and Asymmetric Supercapacitive Performance Evaluation	136-172
VII	Summary and Conclusions	173-182

Chapter-1

Introduction of Supercapacitor *and Literature Survey of* *Supercapacitive Rare Earth* *Chalcogenides*

Sr. No.	Title		Page no.
1.1	General Introduction		1
	1.1.1	Need of Energy Storage Devices	
	1.1.2	Supercapacitor and their classification	2-3
		(A) Electrochemical Double Layer Capacitor (EDLCs)	4
		(B) Pseudocapacitor	5
		(C) Hybrid Supercapacitor	6
	1.1.3	New Trends in Supercapacitor	7
1.2	Literature Survey of Rare Earth Metal Chalcogenides		9
	(A)	Literature Survey of Rare Earth Metal Chalcogenides Thin Films and Their Properties	9-11
	(B)	Literature Survey of Rare Earth Metal Chalcogenides Thin Films and their Supercapacitor application	12-14
	(C)	Literature Survey of Graphene Oxide and Graphene Oxide composite Thin Films Supercapacitor	15-17
1.3	Purpose of Dissertation		18-20
References			21-25

1.1. General Introduction:

Due to climate change and fast development of the global economy, energy has become a primary spotlight in the scientific and industrial communities. With concerns of the environment pollution, increasing mining cost and the reduction of fossil fuel, there is an urgent need for a capable, clean and renewable energy source, and energy storage procedure [1].

Even though great hard works have been made on the development of high performance Li-ion batteries and fuel cells [2-4], the poor power capability and high maintenance cost have kept them away from many applications. Newly, supercapacitors have drawn great attention because of their high charge discharge rate, long life cycle, outstanding power density and no short circuit concern that are of concern with current batteries or fuel cells. The supercapacitors, also known as ultracapacitors or electrochemical capacitors, store energy with an electric double layer capacitance (EDLC) achieved by ion adsorption or pseudocapacitance dominated by surface redox reaction. Pseudocapacitors with conducting polymers or metal oxides as electrode material, although demonstrate a high capacitive performance, but cannot maintain this performance after prolonged cycling. On the other hand, EDLC can be charged and discharged as many as one million cycles without performance degradation [5].

Moreover, ion transportation is faster than a redox reaction, resulting in a high charge-discharge rate and power density in EDLC. At this time, the energy density of EDLC is generally 3-5 Wh/kg⁻¹, which is one order of magnitude below commercialized lithium-ion batteries (100-275 Wh/kg⁻¹) [6,7]. Therefore, increasing the energy capacity with minimum sacrifice of power density is now a major topic in supercapacitor research.

1.1.1. Need of Energy Storage Devices

There is an increasing requirement for high-quality energy supplies for portable, stationary and mobile applications. Different types of electrochemical energy storage applications such as fuel

cells [8, 9], batteries [10,11] and supercapacitors [12, 13] have received a great attention in the past decade due to mounting concerns about environmental protection and energy saving. In the past, lithium-ion batteries were widely used in various applications such as cell phones, laptops, computers etc. But in general, electrochemical devices have a great aptitude for large-scale applications such as hybrid electric vehicles and smart grids [14, 15] and the requirements differ depending on the applications in terms of scale, energy and power supply.

Currently, modern day electrical and electronic device demand high current, energy and power requirements with extreme safety and precautions. Supercapacitors are one of the solutions to meet these tremendous requirements of high power density, emitting a large amount of energy in a short time period. And at ideal conditions, supercapacitors can replace batteries satisfying power requirements in electric vehicle systems combining both high power density of supercapacitors and high energy density of batteries. When in need of rapid acceleration, supercapacitors can dispense large amounts of power batteries could help in electrically charging the capacitors and to power the vehicle. These supercapacitors require a high recyclability, high energy and power densities higher than the batteries under the same operating potential and reliable discharge characteristics [16].

1.1.2. Supercapacitor and their classification:

Supercapacitors (also known as ultra-capacitors or electric double layer capacitor) are energy storage devices that have low internal resistivity and very high capacitance behavior. The energy storage mechanism involves the separation of charges between the interface of the electrode and the electrolyte [17, 18]. This device, in particular, can store and deliver energy at a relatively high capacity in comparison to batteries [19]. A supercapacitor comprises of a separator, two electrodes and an electrolyte but the electrode material plays the major role in determining its performance [20, 21]. Major benefits of using a supercapacitor are its flexible packaging, high power, long life cycle, wide operational ranges (-40°C to 77°C), lightweight and low maintenance [22].

A supercapacitor can be best used in applications that require short load cycle and high reliability. Some of the examples of these types of devices are electric vehicles, load cranes, and forklifts [23]. In addition, some of the most promising applications of supercapacitors are low emission hybrid vehicles and fuel cell vehicles [24, 25]. Although, the energy density of a supercapacitor is more than conventional capacitors, but still they are not up to the mark of fuel cells and batteries, as be seen in **Fig. 1.1**. So, in such devices, supercapacitors can be used along with fuel cells or batteries serving as a temporary storage energy device with high power capacity to store energy while banking [26].

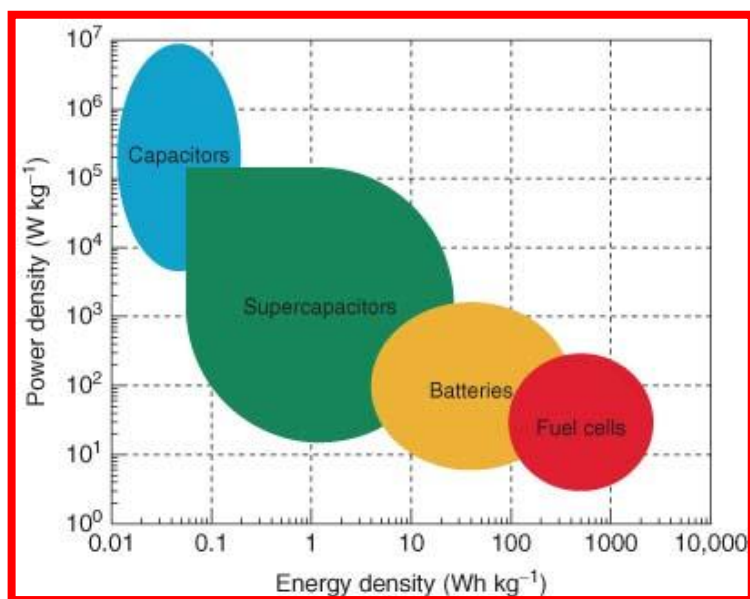


Fig.1.1: Energy vs. Power density Ragone plot of different energy storage devices [115].

Classification of Supercapacitors:

The operation principle of a supercapacitor is based on the amount of energy stored as ions between the electrolyte and the electrode. Based on different types of storage mechanisms, as shown in **Fig.1.2**, supercapacitors are classified into three major types: as electrochemical double layer capacitor (EDLCs), pseudo-capacitor and hybrid supercapacitor.

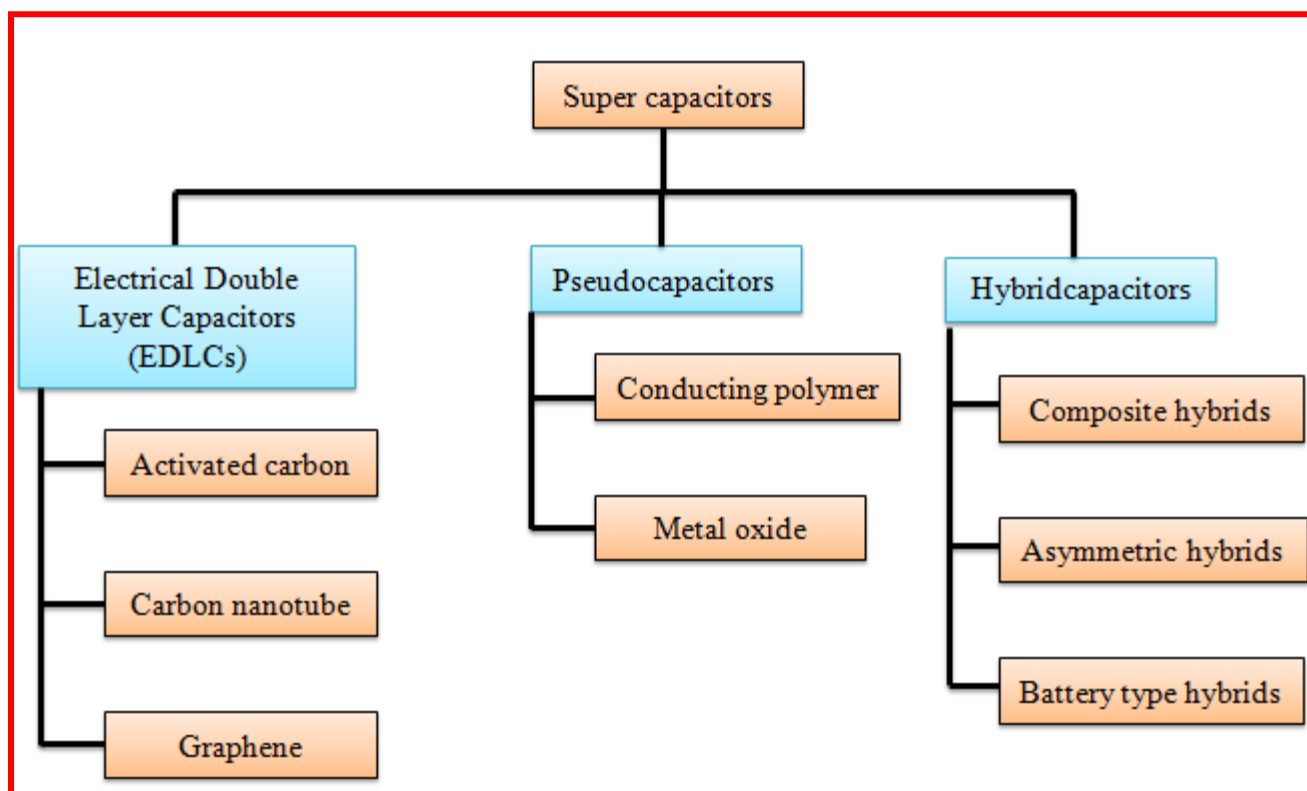


Fig.1.2: Classification of Supercapacitor

A) Electric double layer Capacitor (EDLCs):

EDLCs are constructed using two carbon based materials as electrodes, an electrolyte and a separator. EDLCs can either store charge electrostatically or via non faradic process, which involves no transfer of charge between electrode and the electrolyte [27-29]. The principle of energy storage used by EDLCs is the electrochemical double layer. When voltage is applied, there is an accumulation of charge on electrode surfaces, due to the difference in potential there is an attraction of opposite charges, these results to ions in electrolyte diffusing over the separator and onto pores of the opposite charged electrode. To avoid recombination of ions at electrodes a Helmholtz double layer of charge is formed as shown in **Fig.1.3**. The double layer, combined with the increase in specific surface area and distances between electrodes decreased, allows EDLCs to attain higher energy density [30-31]. Additionally, due to the EDLCs storage mechanism this allows for very fast

energy uptake, delivery and better power performance. Due to non-faradic process, that is no chemical reaction. It eliminates swelling observed in active material which batteries demonstrate during charging and discharging. A few differences between EDLCs and batteries can be noticed as

- (i) EDLCs can withstand millions of cycles unlike batteries that can withstand few thousands at best.
- (ii) Charge storage mechanism does not involve solvent of the electrolyte; in Li-ion batteries it contributes to solid electrolyte inter phase when high-potential cathodes are used or graphite anodes [32-34]. However, due to the electrostatic surface charging mechanism, EDLCs devices experience a limited energy density, which is why today's EDLCs research is mainly focused on increasing energy performance and improving temperature range where batteries cannot operate. Performance of EDLC can be adjusted depending on the type of electrolyte used.

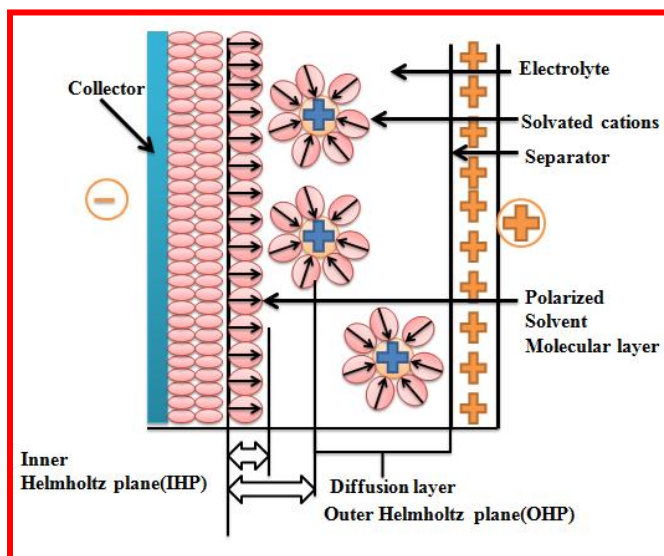


Fig. 1.3: shows Helmholtz double layer formation at the electrode-electrolyte interface [116].

B) Pseudocapacitors:

Compared to EDLCs, that store charge electro-statically. Pseudocapacitors store charge via faradic process which involves the transfer of charge between electrode and electrolyte in **Fig.1.4 [35]**. When a potential is applied to a pseudocapacitor reduction and oxidation takes place on the electrode

material, which involves the passage of charge across the double layer, resulting in faradic current passing through the supercapacitor cell. The faradic process involved in pseudocapacitors allows them to achieve greater specific capacitance and energy densities compared to EDLCs. Examples are metal oxides, conducting polymers. Which leads to interest in these materials but due the faradic nature, it involves reduction-oxidation reaction just like in the case of batteries; hence they also suffer lack of stability during cycling and low power density [36-40].

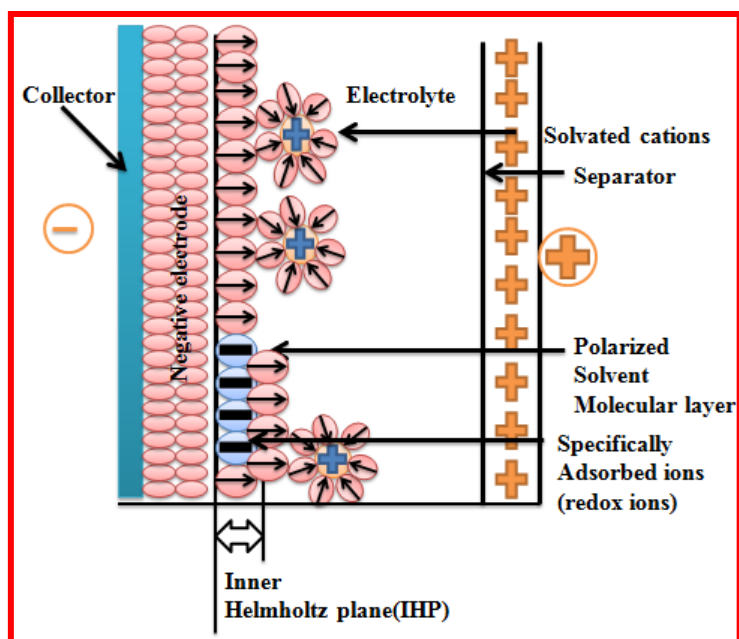


Fig. 1.4: shows electrochemical charge storage involved in the pseudocapacitor [117].

C) Hybrid Supercapacitor:

As mentioned earlier, EDLCs possess good power performance and life cycle whereas pseudocapacitors exhibit comparatively higher capacitance and energy density. But still they lack in cyclic performance and also the material gets deteriorated with time. So in hybrid capacitors a combined performance characteristics is demonstrated which was formerly unattainable. By combining the features of both, that is by combining the power density of supercapacitor electrodes and the energy source of pseudo capacitive materials, they were able to outperform EDLCs and pseudo-capacitors [41-46]. But technically, an increase in energy density occurs still at the expense

of good cyclic stability which poses as a drawback of hybrid supercapacitors [47]. So recently, a lot of research works have been reported testing hybrid supercapacitor with several combinations of different electrode materials along with inorganic and organic electrolytes with the interest of improving the energy and power density and still having a good life cycle [49, 50].

1.1.3. New Trend in Supercapacitor

The supercapacitors are the new emerging energy storage technology that will take a key role in the future of energy systems. The higher energy storage capacity of supercapacitors is the main feature which makes them a required option among different manufacturers [51]. With steady progress in research, supercapacitors are attaining more attention in markets all over the world. For instance, automotive and rail sections are opening new possibilities in emerging sections such as grid energy storage. Increase in demand of hybrid/electric vehicles because of severe government rules regarding emissions is proposed to promote the development of supercapacitor market [52-54]. Indeed, the new consumer's electronic devices like cell phones and sensors require different power demand because of their multiple functionalities. Batteries respond very slowly at room temperature due to their chemical reactions. Therefore, in many cases, batteries will not provide complete power needs of all these electronic appliances in next generation energy storage systems. The growing demand for supercapacitors from industries is due to its advantages over lithium-ion batteries in terms of power density and number of cycles. Supercapacitors can convey large amount of energy at high power and fast charge-discharge rates, which make them appropriate for supplying high power in multifunctional electronic devices. Even these good features of supercapacitors, the commercial applicability of supercapacitors is restricted due to its low energy density. Currently, researchers are trying to enhance the energy density of supercapacitors by applying various approaches without hindering their other features.

In past few decades, carbon-based materials are most frequently used in commercial supercapacitors [57-60]. Nevertheless, the low specific capacitance of carbon-based materials restricts its commercial use. Current research suggests that, pseudocapacitive transition metal oxides are more promising electrode materials for supercapacitors due to their low cost, lower resistance value and environmental compatibility [61]. Also, the fast and reversible surface redox reactions of pseudocapacitive materials significantly improve the specific capacitance and energy storage capacity of the supercapacitors. The cyclic stability of pseudocapacitive materials is inadequate due to the dissolution of active electrode material in liquid electrolyte during cycling.

Therefore, the study of solid-state supercapacitors is more important in which solid polymer electrolyte is used as an alternative to liquid electrolyte. The solid-state supercapacitors have advantages over aqueous capacitors as it overcomes the problem of electrolyte leakage, flexibility and ease of handling [62-64]. Also, the current research is focused on the development of supercapacitors using different ionic liquid electrolytes. These electrolytes are more advantageous, as they are non-flammable, nontoxic and thermally stable at temperature up to 300 °C [65-70]. Further, the potential window of supercapacitors with this ionic liquid electrolyte is increased up to 4-6 V [71]. The overall electrochemical performance of supercapacitor depends not only on the electrode material used but also on the electrolyte, separator and supporting substrate [72]. The choice of superior electrode material along with appropriate electrolyte effectively increases the specific capacitance and energy density of supercapacitor [73-76]. The utilization of high performance, nontoxic and low-cost electrode materials with proper electrolyte helps to achieve peak values of specific capacitance and energy density of supercapacitor [77-79].

1.2. Literature Survey of Rare Earth Metal Chalcogenides:

[A] Literature Survey of Rare Earth Metal Chalcogenides Thin Films and Their Properties-

Rare earth metal chalcogenides (S, Te, and Se) has been studied for different applications such as magnetic, optical, nuclear and superconducting etc. Many intermetallic compound systems between rare earths have been reported. In last few years, rare earth based films have exhibited outstanding superconducting properties. Kanna et al [80] et al synthesized copper and rare earth-doped (lanthanum, neodymium and gadolinium) thin films and studied their magnetic properties. The optical band gap energy of copper nano ferrites was 1.72 eV; it shifted to 5.01 to 5.14 eV on doping the rare-earth (La, Nd and Gd) element into the copper nanoferrites. The X-ray diffraction confirmed with tetragonal crystal structure and grains-like surface morphology. Kumbhar and Lokhande [81] prepared dysprosium compound from aqueous acidic bath onto stainless steel, copper, brass, titanium and indium-tin oxide (ITO) substrates by electrodeposition method. The films deposited between temperature range of 25 to 55° C were-gray, uniform and adherent and thickness up to 0.25 microns. Kumbhar and Lokhande [82] prepared dysprosium compound from non-aqueous ethanol bath onto different substrates by electrodeposition method and obtained film thickness up to 0.20 microns. Ramay et al [83] deposited uniform and homogeneous thin films of Dy_2O_3 , $\text{Cr/Dy}_2\text{O}_3$ and $\text{Cu/Dy}_2\text{O}_3$ on Si substrate in thickness range of 100 ± 5 nm using reactive magnetron sputtering process. The structural analysis exhibited the crystalline nature with cubic structure and uniform distribution of nano-sized grains like surface morphology. Kruk et al [84] studied physicochemical properties of yttrium oxide doped with neodymium and lanthanum. The transparent La, Nd, YO_3 were prepared by use of the ethylene diamine tetraacetic acid (EDTA) gel process. The optical properties were measured in between 500 and 1000 nm. The X-ray pattern shows cubic crystal structure and grains like surface morphology obtained. Jundale and Lokhande [85] synthesized Sm film from a Sm tartarate bath was carried out onto different substrates (stainless steel, brass, copper and titanium) by electrodeposition method. The concentration of tartaric acid, pH, temperature etc here optimized. The effect of pH and

temperature on deposition showed that the good quality films could be deposited at pH = 2 and at room temperature. Jundale and Lokhande [86] electro synthesized Sm-Se thin films. From aqueous bath on different substrates (stainless steel, brass, copper, titanium and FTO coated glass). It was found that different compounds of Sm-Se are formed depending upon the concentration of selenide ions in the bath. All the thin films were polycrystalline in nature and band gap energy of Sm-Se thin film was 2.82 eV. Jundale and Lokhande [87] synthesized Sm_2S_3 thin film by electrodeposition method. A deposited film was found to be polycrystalline cubic crystal structure and optical band gap is 2.08 eV. The photoelectrochemical technique showed that the films are p-type. Jundale and Lokhande [88] prepared Sm-Te from aqueous solution by electrodeposition method onto different substrates. These films show polycrystalline cubic crystal structure and spongy and fibrous surface morphology with band gap energy of 2.52 eV. Jundale and lokhande [89] electro synthesized p- Sm_2S_3 films were from aqueous onto Ti and stainless steel coated substrates. X-ray diffraction showed that films are microcrystalline and free from elemental Sm and S. The optical absorption studies showed that the band gap is 2.08 eV. The photo electrochemical studies of the films were carried out by forming a p- $\text{Sm}_2\text{S}_3/\text{KI-I}_2\text{-KC1/C}$ cell configuration. The current voltage characteristics were studied in the dark and under white light illumination and at different temperatures. The capacitance-voltage characteristics were studied at 1 kHz frequency. Jeong and Bae [90] prepared Y_2O_3 by a modified solvothermal method and used in transparent ceramics and luminescent devices. An X-ray diffraction analysis of the synthesized powders indicated the formation of the Y_2O_3 cubic structure. The surface morphology of synthesized powder spherical grains like and hexagonal in shape. Mohite and Lokhande [91] prepared yttrium chalcogenides thin films by electrodeposition method. The cracked surface morphology was found and the x-ray diffraction patterns of yttrium chalcogenides show the polycrystalline nature. From optical absorption studies the band gap energies of films were found

to be 1.85, 1.6 and 1.7 eV for YS, YSe, and YTe films, respectively. Mohite and Lokhande [92] prepared yttrium selenide (YSe) thin film on different substrates from non-aqueous bath by electrodeposition method. The nature of contact between Y-Se and stainless steel was ohmic and the band gap was 1.6 eV. Mohite and Lokhande [93] prepared Y-Te thin film by electrodeposition method from non-aqueous bath. The deposited films were amorphous or consisted of fine grains like surface morphology with band gap energy of 1.84 eV. Jodgudri et al [94] prepared SnS and YS thin films by room temperature electrodeposition method. The composition of films corresponds SnS and YS having band gap of 1.41 eV and 1.85 eV, respectively.

1.2.1 Literature Survey of Rare Earth Metal Chalcogenides Thin Films and Their Properties-

Sr. No.	Material	Deposition Method	Crystal Structure	Band gap	Ref
1.	Cu doped La,Ne and Ga film	Sonochemical method	Tetragonal	1.72 eV	80
2.	Dy Films	Electrodeposition	-	-	81
3.	Dy Films	Electrodeposition	-	-	82
4.	Dy ₂ O ₃ film	Magnetron sputtering system	Cubic		83
5.	La _{0.1} , Nd _{0.1} , Y _{1.8} O ₃ powder	EDTA gel technique process	Cubic	-	84
6.	Sm thin film	Electrodeposition	-	-	85
7.	Sm-Se Thin film	Electrodeposition	Orthorohmbic	-	86
8.	Sm ₂ S ₃ Films	Electrodeposition	Cubic	2.08 eV	87
9.	SmTe films	Electrodeposition	Cubic	2.52 eV	88
10.	Sm ₂ S ₃	Electrodeposition	-	2.08 eV	89
11.	Y ₂ O ₃ nanopowder	Solvothermal method	Cubic	-	90
12.	Yttrium (Y-S, Te,Se)	Electrodeposition	-	1.85,1.6 , 1.7 eV	91
13.	Y-Se film	Electrodeposition	-	1.6 eV	92
14.	Y-Te film	Electrodeposition	-	1.84 eV	93
15	Y-S film	Electrodeposition	-	1.85 eV	94

From the literature survey, it is revealed that the rare earth metal chalcogenides based thin films showed good electronic, magnetic, optical and structural properties as seen in **Table. 1.2.1**. In particular, these rare earth materials can be used for energy storage devices because of good electrical conductivity.

[B] Literature Survey of Rare Earth Metal Chalcogenides Thin Films and Their Supercapacitor application:

According on literature survey, rare earth metal chalcogenides materials showed good chemical and physical properties for different applications. The physical and chemical methods of electrode preparation strongly affect the electrical conductivity and hence the electrochemical performance [95]. The rare earth materials are a special class of materials which exhibits the dielectric and magnetic properties due to the electron transition and morphological variation. Now a days, rare earth based chalcogenides thin films have been used in energy storage device such as supercapacitor, **Yadav [96]** prepared La_2O_3 thin film by CBD method and reported specific capacitance of 147 Fg^{-1} in 1 M KOH electrolyte within -0.1 to 0.8 V/SCE potential window and cycling stability measured for 2,000 CV cycles of 96 % with ED and PD of 35 Whkg^{-1} and 23 kWkg^{-1} . **Patil et al [97]** prepared $\alpha\text{-La}_2\text{S}_3$ thin film using successive ionic layer adsorption and reaction (SILAR) method and obtained maximum capacitance of 256 Fg^{-1} in 1 M LiClO_4 electrolyte within -1.2 to 0 V/SCE potential window with cycling stability of 85 % over 1000 cycles for nano-grains like surface morphology. **Patil et al [98]** prepared lanthanum telluride (La_2Te_3) thin film by CBD method and obtained specific capacitance 469 Fg^{-1} with ED and PD of 126 Wh kg^{-1} and 2.5 kW kg^{-1} , respectively in 1 M KOH electrolyte. **Patil et al [99]** prepared lanthanum sulfide (La_2S_3) thin film prepared by CBD method and obtained specific capacitance 294 Fg^{-1} with ED and PD 43 Wh kg^{-1} and 25 kW kg^{-1} , respectively with cycling stability of 89 % over 1000 CV cycles. **Patil et al [100]** synthesized lanthanum selenide (La_2Se_3) nanoflakes from an aqueous medium by means of a

CBD method and obtained specific capacitance of 331 F g^{-1} with ED of 31.62 Whkg^{-1} at a PD of 7 kWkg^{-1} and electrochemical stability for 1000 CV of 81%. **Patil et al [101]** synthesized lanthanum selenide (La_2Se_3) nanocubes thin film via successive ionic layer adsorption and reaction (SILAR) method and utilized for energy storage application with specific capacitance 363 Fg^{-1} , ED 80 Wh kg^{-1} and PD 2.5 kW kg^{-1} in $0.8 \text{ M LiClO}_4/\text{PC}$ electrolyte and cyclic stability for 1000 CV of 83%. **Kumbhar et al [102]** synthesized $\alpha\text{-Sm}_2\text{S}_3$ thin film by SILAR method and reported specific capacitance of 294 Fg^{-1} in 1 M LiClO_4 electrolyte. An electrode stability of 89% retained after 1000 cycles. The honeycomb like surface morphology of $\alpha\text{-Sm}_2\text{S}_3$ thin film plays an important role in supercapacitive behavior of material, since better surface morphology provides high surface area. **Kumbhar et al [103]** synthesized samarium sulfide (Sm_2S_3) by successive ionic layered adsorption and reaction (SILAR) method and reported specific capacitance of 248 Fg^{-1} in 1.5 M LiClO_4 electrolyte. The highest PD and ED of 15.6 kWhkg^{-1} and 54.6 Whkg^{-1} are obtained. An electrochemical stability of 94% is retained after 1500 cycles. **Kumbhar et al [104]** synthesized of samarium selenide (Sm_2Se_3) thin films through one step chemical route method and used for supercapacitor application with specific capacitance 316 Fg^{-1} in 1 M LiClO_4 electrolyte. The nanorods like porous network of the electrode resulted from this assembly exhibited excellent cycling stability 87% for 1000 charge-discharge cycles. **Kumbhar et al [105]** synthesized of samarium telluride (Sm_2Te_3) by SILAR method and reported specific capacitance and ED of 144 Fg^{-1} and 10 Whkg^{-1} in $1 \text{ M LiClO}_4\text{-PC}$ electrolyte. The film surface consists of cloud-like morphology. The electrochemical stability of 69.3% for 1000 CV cycles was reported. **Kumbhar et al [106]** synthesized samarium sulfide (Sm_2S_3) thin films with diffused nanoflakes morphology by facial chemical synthesis method and used for supercapacitor application with specific capacitance of 213 Fg^{-1} , ED and PD of 39.39 Whkg^{-1} and 4.33 kWkg^{-1} , respectively in $1 \text{ M LiClO}_4\text{-PC}$ electrolyte. The highest PD and ED of 15.6 kWhkg^{-1} and 54.6 Whkg^{-1} , respectively are obtained.

1.2.2. Literature Survey of Rare Earth Metal Chalcogenides Thin Films Supercapacitor-

Sr. No.	Material	Deposition method	Surface morphology	Electrolyte	ED and PD	Specific capacitance (Fg^{-1})	Electrochemical stability	Ref .
1.	La_2O_3 thin film	CBD	Rod shaped	1 M KOH	ED-35 Whkg^{-1} PD-23 kWkg^{-1}	147	2,000 CV 96%	96
2.	$\alpha\text{-La}_2\text{S}_3$ thin film	SILAR	Nano-grains	1M LiClO_4		256	1000 CV 85%	97
3.	La_2Te_3 thin film	CBD	Cinnamon	1M KOH	ED-126 Wh kg^{-1} PD- 2.5 kW kg^{-1}	469	1000 CV 74 %	98
4.	La_2S_3 thin film	CBD	Grains	1M LiClO_4	ED-43 Wh kg^{-1} PD- 25 kW kg^{-1}	294	1000 CV 89 %	99
5.	La_2Se_3 thin film	CBD	Nano falkes	2M KOH	E.D-31.62 Whkg^{-1} P.D- 7 kWkg^{-1}	331	1000 CV 81%	100
6.	La_2Se_3 thin film	SILAR	Nanocubes	0.8 M LiClO_4/PC	ED-80 Wh kg^{-1} , PD-2.5 kW kg^{-1}	363	1000 CV 83%	101
7.	$\alpha\text{-Sm}_2\text{S}_3$ thin film	SILAR	Honeycomb	1 M LiClO_4/PC		294	1000 CV 89%	102
8.	Sm_2S_3 thin film	SILAR	Porous network	1.5 M LiClO_4/PC	ED-15.6 kWhkg^{-1} PD- 54.6 Whkg^{-1}	248	1500 CV 94%	103
9.	Sm_2Se_3 thin film	Chemical route	Nanorods	1 M LiClO_4/PC		316	1000 CV 87%	104
10.	Sm_2Te_3 thin film	SILAR	Cloud-like	1 M LiClO_4/PC	ED-144 Fg^{-1} PD- 10 Whkg^{-1}	144	1000 CV 69.3%	105
11.	Sm_2S_3 thin film	Chemical synthesis method	Flakes	1 M LiClO_4/PC	ED-39.39 Whkg^{-1} PD-4.33 kWkg^{-1}	248	1500 CV 94%	106

Literature survey reveals that the rare earth metal chalcogenides based pseudocapacitor is still in initial stage as seen in **Table. 1.2.2**. In particular, high capacitance, high redox activity of rare earth metal chalcogenides should be extensively investigated.

[C] Literature Survey of Graphene oxide Based Composite Thin Films and Their Supercapacitor application:

Zhang et al [107] prepared layered graphene oxide nanostructures with sandwiched conducting polymers composite film by exfoliated method and used as electrode for supercapacitor application. The sandwich like surface morphology exhibited an excellent electrocapacitive performance with a high specific capacitance over 500 Fg^{-1} . An electrochemical stability of 70 % is retained after 1000 cycles. **Gund et al [108]** prepared GO/MoO₃ composite electrode by SILAR method and used for supercapacitor application. The X-ray diffraction pattern of composite electrode shows tetragonal crystal structure and SEM images demonstrate that the surface structure of GO and Mn₃O₄ thin films can be easily tuned by forming the composite of GO and Mn₃O₄ materials leading to excellent processability of a system. This composite electrode demonstrates good specific capacitance (344 Fg^{-1}) and ED (93 Wh/kg^{-1}), and long cycling life time (3000), since the GO sheets significantly alters surface structure and provides strong support to limit the dissolution of Mn₃O₄ particles in electrolyte solution during the fast charging–discharging. **Zhang et al [109]** synthesized nanocomposites of reduced graphene oxide/lanthanum oxide by a simple reflux process. The rod-like surface morphology is obtained for reduced graphene oxide/lanthanum oxide composites. The supercapacitor device displayed a specific capacitance of 156.25 Fg^{-1} at a current density of 0.1 A/g and excellent cycle stability of 78% of after 500 cycles.

Rajagopal et al [110] synthesized of lanthanum oxide/hydroxide nanoparticle (LaNPs)-doped rGO composite nanosheets. The uniform deposited LaNPs on the rGO composite nanosheets showed a areal capacitance of 889.29 Fcm^{-2} than LaG (428.58 Fcm^{-2}) and LaG (260.72 Fcm^{-2}). **Dezfuli et al [111]**

synthesized Sm_2O_3 nanoparticles (SmNs) and anchored them onto the surface of reduced graphene oxide (RGO) through a self-assembly thereof by utilizing a facile sonochemical procedure. The SmNs decorated RGO (SmNRGO) nanocomposites were found to possess a specific capacitance (SC) of 321 Fg^{-1} in a $0.5 \text{ M Na}_2\text{SO}_4$ solution. The nanocomposite revealed a unique cycling durability (maintaining 99 % of its SC even after 4000 cycles). **Majumder et al [112]** synthesized polypyrrole/copper oxide/europium oxide (PPY/CuO/ Eu_2O_3); via a facile in situ chemical oxidative polymerization method, which exhibited the maximum specific capacitance of 320 Fg^{-1} at the current density of 1 Ag^{-1} in $1 \text{ M H}_2\text{SO}_4$ electrolyte. The maximum ED for pure PPY was found to be 4.2 Wh/kg^{-1} with the PD 249.26 W/kg^{-1} at the current density of 1 Ag^{-1} . The PPY/CuO/ Eu_2O_3 ternary nanocomposite incorporated with inorganic fillers (CuO and Eu_2O_3) has endured 3000 charge/ discharge cycles with 92.89% capacitance retention.

Huang et al [113] synthesized graphene oxide/carbon nanotube (GO/CNT) hybrid films self-assembled on a Ti substrate via simple casting of aqueous dispersion by chemical vapor deposition method. The electrochemical performance with specific capacitances of 428 and 145 Fg^{-1} at current densities of 0.5 and 100 A g^{-1} in $1 \text{ mL}^{-1} \text{ H}_2\text{SO}_4$ electrolyte, respectively as well as a remarkable retention rate of 98% of the initial value after 10,000 charge/discharge cycles was obtained. **Huang et al [114]** studied a novel composite of CuS-rGO is successfully synthesized through a facile solvothermal method assisted by ethylene glycol. The CuS hollow spheres are wrapped by flexible rGO to overcome the issues of structural change and aggregation of rGO nanosheets during charge and discharge process and greatly improved the conductivity. The CuS/rGO electrode displayed a significantly enhanced specific capacitance of 2317.8 Fg^{-1} and an excellent cycling stability of 96.2% retention after 1200 cycles at a current density of 1.0 Ag^{-1} .

1.2.3. Literature Survey of Graphene Oxide and Graphene Oxide composite Thin Films Based Supercapacitor-

Sr. No.	Material	Deposition method	Surface morphology	Electrolyte	ED and PD	Specific capacitance (Fg^{-1})	Electrochemical stability	Ref.
1.	GO/Conducting polymer	Exfoliated Method	Sandwich like	1 M KOH	-	500	1,000 CV 70 %	107
2.	GO/Mn ₃ O ₄	SILAR	Nanograins	1M Na ₂ SO ₄	ED- 93 Wh/kg ⁻¹	344	3000 CV 87%	108
3.	RGO/La ₂ O ₃	CBD	Rod-like	2M KOH	ED- 13.02 Wh/kg, PD- 15.62 kW/kg ⁻¹	156.2	500 CV 78 %	109
4.	La ₂ O ₃ /hydroxide rGO	Hydrothermal Method	Layered and crumbled sheet	1M Na ₂ SO ₄	-	889.29 F cm ⁻²	1000 CV 84 %	110
5.	Sm ₂ O ₃ /RGO	Facile sonochemical Method	Grains like	0.5M Na ₂ SO ₄	ED- 38.1 Wh/kg, PD- 500 kW/kg ⁻¹	321	4000 CV 99%	111
6.	PPY/CuO/Eu ₂ O ₃	Facile in situ chemical oxidative polymerization method	Grains like	1M H ₂ SO ₄	ED- 11.1 Wh/kg, PD- 271.52 kW/kg ⁻¹	320	3000 CV 92.89%	112
7.	GO/CNT composite	Chemical vapor deposition method	Graphite-like	1 mol L ⁻¹ H ₂ SO ₄	-	428	10 000 GCD 98%	113
8.	CuS/rGO composite	Solvothermal method	Hollow spheres	6 M KOH	-	2317.8	1200 CV 96.2%	114

From the graphene oxide based composite literature survey, it is found that the Go/rare earth metal chalcogenides composite thin films pseudocapacitor show good electrochemical behavior. In particular, graphene based material showed improvement of specific capacitance and long life cycle with stability.

1.3. Purpose of Dissertation:

The supercapacitor plays a significant part in new technology with higher specific capacitance, energy-power density, long life cycle, and quick charge/discharge. The increasing supercapacitor energy and power densities will make them more helpful for portable electronic power applications. Rare earth materials possess unique and better characteristic of a wide potential application suitable for the high technological devices. These rare earth chalcogenides showed a good contribution in electrochemical behavior as seen from **Table-1.2.2 and 1.2.3**. Graphene oxide, conducting polymers (polyaniline, polypyrrole, polythiophene) show better (>5000) values of specific capacitance compared to rare earth metal oxide but provide poor electrochemical stability. These carbonic electrode materials are typically used for electrochemical energy storage because of their high conductivity and fast redox electroactivity. Though, in order to make development towards the application of supercapacitor, an effort has been undertaken to improve electrochemical properties along with good electrical conductivity and the interface between electrode-electrolyte.

The literature study illustrates that extensive variety of materials have been investigated as an electrode material in fabricating supercapacitors, including carbonaceous materials, conducting polymers, metal oxides, rare earth metal oxide or their composites. The new trends of research are focused on the preparation of mixed rare earth metal (La, Sm) sulfide/ graphene oxide-based composite materials to gain the better electrochemical performance with peak value of energy density and power density. The raise in both operating potential window and energy density of rare earth metal (La, Sm) sulfide/ graphene oxide-based composite result in the considerable increase in overall electrochemical performance of the supercapacitors. The composite supercapacitors are the important awaiting class of electrochemical capacitors with the prospect to deliver high energy density at high charging-discharging rates. In addition to this, drawbacks of one material can be fulfilled by another

in composite and synergistic result of the two or more materials enhances the resulting electrochemical performance.

The lanthanum sulfide (La_2S_3) and samarium sulfide (Sm_2S_3) are the most studied materials which have promising potential characteristics in the supercapacitor field. However, there are not many reports on their composite based rare earth supercapacitors. To increase the high performance capable supercapacitors, it is necessary to fabricate superior electrode material which is capable of achieving peak values of specific capacitance and energy density without compromising its power density. The major reason behind making rare earth metal (La, Sm) sulfide/GO composite thin film is to accomplish improved electrochemical performance to fabricate high performance supercapacitor. The selection of (La, Sm) sulfide/GO composite is based on the following considerations: i) La_2S_3 and Sm_2S_3 are two widely investigated pseudocapacitive materials because of their physical and chemical properties, specific capacitance, redox activity and multiple oxidation states, ii) these materials own good capacitive retention and long term cycling stability and iii) the operating different potential window, specific capacitance and energy density of the supercapacitor.

The present work is focused on the synthesis of rare earth metal (La, Sm) sulfide/ graphene oxide-based composite thin film using hydrothermal method or SILAR method on stainless steel (SS) substrate. Both methods offer several advantages for the deposition of pinhole free and well stoichiometric thin films. The various preparative parameters such as precursor, concentration, pH of solution, deposition temperature, and no. of cycles, time will be optimized to get uniform, high quality and well adherent thin films. The best composition of (La, Sm) sulfide/GO composite thin film will be determined for obtaining high performance composite electrodes.

The physical and chemical properties of thin films of rare earth material consist of phase and structural study, micro-structural study and morphological study, which have strong bearing on the properties of materials. The X-ray diffraction (XRD) technique will be used for the phase

identification. Fourier Transform Raman spectroscopy (FT-Raman) will be used to study the chemical bonding in the present material. Surface morphology of the films will be studied using field emission scanning electron microscopy (FE-SEM) and surface wettability study will be carried out using Rame Hart's Goniometer for contact angle measurement.

The electrochemical supercapacitive properties of the rare earth metal (La, Sm) sulfide/graphene oxide-based composite thin films deposited by hydrothermal and SILAR methods will be studied by cyclic voltammetry (CV), galvanostatic charge-discharge (GCD) and electrochemical impedance spectroscopy (EIS) techniques. All these measurements will be carried out in three electrode cell using platinum as a counter, saturated calomel electrode (SCE) as a reference electrode and prepared thin film as a working electrode in a aqueous electrolyte. The supercapacitor performance of (Sm,La) sulfide/GO composite thin film electrodes will be evaluated with respect to various parameters such as scan rate, charge/discharge current density, specific capacitance, energy density, power density and cyclic stability cycles.

The most important objective of present work is to improve the specific capacitance, specific energy density and power density of supercapacitor by using GO based rare earth material. First aim is to synthesis the (La, Sm) sulfide/ GO composite thin films using simple and cost effective chemical methods (Hydrothermal and SILAR). In addition, symmetric and asymmetric supercapacitor devices based on best supercapacitive properties of the (La, Sm) sulfide/ graphene oxide-based composite thin film electrodes will be fabricated and their performance evaluation will be carried out.

References:

1. R. Kotz and M. Carlen, *Electrochim. Acta.*, **45** (2000), 2483–2498.
2. P. Simon, Y. Gogotsi, B. Dunn, *Sci.*, **343** (2014), 1210-1211.
3. Y.S.Su, A.Manthiram, *Nat. Commun.*, **3** (2012), 1166-1171.
4. C. Xiang, M.Li, M.Zhi, A. Manivannan, N. Wu, *J. Power source*, **226** (2013), 65-70.
5. G.A. Snook, P.Kao, A.S.Best, *J. Power Source*, **196** (2011), 1-12.
6. A.K. Singh, D. Sarkar, K. Karmakar, K. Mandal, G.G. Khan, *ACS Appl. Mater. Interfaces*. **8** (2016), 20786–20792.
7. V.N Vasile and Obreja, *Physica E Low Dimens. Syst. Nanostruct.***40** (2008), 2596-2605.
8. A.Hajizadeh and M. A.Golkar, *Int J. Elec. Power*, **32** (2010), 488-497.
9. E.L.Eriksson and E.M. Gra, *Appl. Energy*, **202** (2017), 348-364.
10. S.Bourderau, T.Brousse, D.M.Schleich, *J. Power Source*, **81**(1998), 233-236.
11. G.Pognon, T.Brousse, L.Demarconnay, D. Belanger, *J.Power Source*, **196** (2011), 4117-4122.
12. K. Naoi, W. Naoi, S.Aoyagi, *Acc Chem Res.*, **46** (2013), 1075-1083.
13. M.D. Stoller, S. Park, Y. Zhu, J. An, R.S. Ruoff, *Nano. lett.* **8** (2008), 3498-3502.
14. H. Wan, X. Ji, J. Jiang, J. Yu, L. Zhang, S. Bie, H. Chen, Y. Ruan, *J. Power Source*, **243** (2013), 396-402.
15. D.P. Dubal, D.S. Dhawale, R.R. Salunkhe, C.D. Lokhande, *J. Electroanal. Chem.*, **647** (2010), 60–65.
16. G.Wang, L.Zhang, J.Zhang, *Chem. Soc. Rev.* **41** (2012), 797-828.
17. X. Chen, R. Paul, L. Dai, *Natl. Sci. Rev.* **4** (2017), 453–489.
18. J.Xu, L.Gao, J. Cao, W.Wang, Z. Chen, *Electrochim. Acta.* **56** (2010), 732-736.
19. C.Martin, M.Alias, F.Christien, O.Crosnier, D.Belanger, T.Brousse, *Adv. Mater.* **21** (2009), 4735-4741.
20. S.Ghosh, O. Inganas, *Adv.Mater.***11** (1999), 14-17.
21. R.R. Salunkhe, J. Tang, Y. Kamachi, T. Nakato, J. H. Kim, Y. Yamauchi, *ACS Nano*, **9** (2015), 6288–6296.
22. R.R. Salunkhe, Y.V. Kaneti, J. Kim, J.H. Kim, Y.Yamauchi, *Acc. Chem. Res.* **49** (2016), 2796-2806.
23. U.M.Patil, R.R.Salunkhe, K.V.Gurav, C.D.Lokhande, *Appl. Surf. Sci.* **255** (2008), 2603-2607.
24. M.Zhi, C.Xiang, J.Li, M.Li, N.Wu, *Nanoscale*, **5** (2013), 72-88.
25. S. Parveen, S.S. Raut, M.K. Tiwari, B.R. Sankapal, S.N. Pandey, *J. Alloys Compd.* **781**(2019), 831-841.
26. B.M.Sanchez, T.Brousse, C.R.Castro, V.Nicolosi, P.S.Grant, *Electrochim. Acta.* **91** (2013), 253-260.
27. I.Shakir, M.Nadeem, M.Shahid, D.J.Kang, *Electrochim. Acta.***118** (2014), 138-142.
28. S.S. Karade, A. Agarwal, B. Pandit, R.V. Motghare, S.A. Pande, B.R. Sankapal, *J. Colloid Interface Sci.* **535**(2019), 169-175.

29. S.A.Pande, B.Pandit, B.R. Sankapal, J. Colloid Interface Sci. 514(2018), 740-749.
30. S.S.Raut, B.R.Sankapal, M.D.Shahriar, A.Hossain, S.Pradhan, R.R.Salunkhe, Y. Yamauchi, Eur. J. Inorg. Chem. **2018** (2018), 137-142.
31. W.Sugimoto, T.Ohnuma, Y.Murakami, Y.Takasu, Electrochem. Solid-State Lett. **4** (2001), A145-A147.
32. S.Dutta, J.Akther, S.De, AIP Conf. Proc. **1832** (2016), 532-535.
33. E. Frackowiak, Phys. Chem. Chem. Phys. **9** (2007), 1774-1785.
34. L.F.Aval, M.Ghoranneviss, G. B. Pour, Mater. Renew. Sustain. Energy Rev. **7** (2018), 29-34.
35. G.Wang, L.Zhang, J.Zhang, Chem. Soc. Rev. **41** (2012), 797-828.
36. S. Zhang, Y. Li, N. Pan, J. Power Source, **206** (2012), 476-482.
37. H. Wang, B. Feng, Y. Ye, J. Guo, H. T. Fang, Electrochim. Acta **240** (2017), 122-128.
38. J. H. Lee, J. Y. Lim, C. S. Lee, J. T. Park, J. H. Kim, Appl. Surf. Sci. **420** (2017), 849-857.
39. T.Huang, X.Song, X.Chen, F.Sun, Q.Su, L.Li, Z.Tan, New J. Chem., **42** (2018) 5128-5134.
39. M. A. Bavio, G. G. Acosta, T. Kessler, A. Visintin, Energy **130** (2017) 22-28.
40. J. Ma, X. Guo, Y. Yan, H. Xue, H.Pang, Adv. Sci. **6** (2018),1700986-1700989.
41. L.Liang, X.Sun, J. Zhang, J.Sun, L. Hou, Y. Liu, C. Yuan, Mater. Horiz., **6** (2019), 871-910.
42. Y. H. Peng, M. X. Guo, F. Shao, S. Liu, Q. Zhu, S. W. Bian, RSC Adv. **6** (2016), 74874-74878.
43. Y. Li, Y. Zhang, H. Zhang, T.Xing, G.Chen, RSC Adv., **9** (2019), 4180-4185.
44. J.Zhang, P.Liu, L.Jin, C.Jin, S.Bian, Chemistry Select, **2** (2017), 8618 – 8624.
45. Z.S.Iro, C.Subramani, S.S.Dash, Int. J. Electrochem. Sci. **11** (2016) 10628.
46. A.Kashale,M. Madagonda, S. Kolekar, B.Sathe, J. Chang, H. Dhakal, A. Ghule, RSC Adv., **7** (2017), 36886-36889.
47. L.Wang, M.Huang, S.Chen, L.Kang, X.He, Z.Lei, F.Shi, H.Xu, Z.Liu, J.Mater.Chem.A, **5** (2015), 19107-19115.
48. L.Xu, Y.Li, M.Jia, Q.Zhao, X.Jin, C.Yao, RSC Adv., **7** (2017), 45066-45074.
49. N. R. Chodankar, G. S. Gund, D. P. Dubal, C. D. Lokhande, RSC Adv. **4** (2014), 61503-61509.
50. K.Jeyasubramanian, T.S.Raja, S.Purushothaman, M.V.Kumar, I.Sushmitha, Electrochim. Acta., **227** (2017), 401-405.
51. P.Kulkarni, S.K.Nataraj, R.G.Balakrishna, D.H. Nagaraju, M.V. Reddy, J. Mater. Chem. A, **5** (2015), 22040-22094.
52. W.Yan, K.Zhuo, J.Ji, Q.Zhang, S.Sang, Int. J. Electrochem. Sci., **14** (2019), 4496 – 4507.
53. G.Yang, S.Park, Materials **12** (2019), 1177-1180.
54. M.A.Bavio, G.G.Acosta, T.Kessler, A.Visintin, Energy **130** (2017), 22-28.
55. Y.Wang, Y. Ding, X. Guo, G. Yu, Nano Res. **2** (2019), 1-10.
56. C. Di, Q. Wang, R. Wang, G. Shen, J. Mater. Chem. A. **3** (2015), 10158-10162.

57. A.Burke, J. Power Source. **91** (2000), 37-40.
58. V.C.Lokhande, A.C.Lokhande, C.D. Lokhande, J.H. Kim, T.S. Ji, J. Alloy Compd., **682** (2016), 381-403.
59. C.Sanrato,M.Odziemkowski, M.Ulmann, J.Augustynski, J.Am.Chem.Soc. **123** (2001), 10639-10649.
60. S.H.Baeck, K.S.Choi, T.F.Jaramillo, G.D.Stucky, E.W.Mcfarland, Adv. Mater. **15** (2003), 1269-1271.
61. A.Srinivasan, M.Miyauchi, J. Phys. Chem. C, **116** (2012) 15421-15426.
62. V.Subramanian, H.Zhu, R.Vajtai, P.M.Ajayan, B.Wei, J. Phys. Chem. B **109** (2005), 20207-20214.
63. J.Wang, J.Polleux, J.Lim, B.Dunn J.Phys.Chem. C, **111** (2007), 14925-14930.
64. L.N.Jin, P.Liu, C.Jin, J.N.Zhang, S.W.Bian, J. Colloid Interface Sci. **510**(2018), 1-11.
65. T. Hao, W. Wang, D. Yu, J. Electron. Mater., **47** (2018), 4108–4115.
66. J. Cui, L.Cao, D.Zeng, X.Wang, W.Li, Z. Lin, P.Zhang, Hindwi **2018** (2018), 2464981-2464986.
67. X.Duan, J.Yang, H.Gao, J.Ma, L.Jiao, W.Zheng, Cryst. Eng. Comm. **14** (2012), 4196-4200.
68. Y.X.Zhang, S.Zhu, M.Dong, C.P.Liu, Z.Q.Wen, Int. J. Electrochem. Sci., **8** (2013), 2407 – 2416.
69. D. Guo, X. Yu, W. Shi, Y. Luo, Q. Li, T. Wang, J. Mater. Chem. A **2**(2014), 8833-8838.
70. M.Huang, X.L.Zhao, F.Li, W.Li, B.Zhang, Y.X.Zhang, J. Mater. Chem. A, **3** (2015), 12852-12857.
71. Y. Shen, X.Miao, D. Song , Y. Li , Y.Qu , J. Yu , J. Tang, H. Qin , L.wang, J. Ren, B.Wang, Int. J. Electrochem. Sci., **14** (2019), 2767 – 2779.
72. S. C. Sekhar, G. Nagaraju, S.M. Cha, J.S.Yu, Dalton Trans., **45** (2016), 19322-19328.
73. M. Zhang, Y. Jia, H. Li, Int. J. Electrochem. Sci., **13** (2018), 9749 – 9758.
74. H.Fang, L.Zhang, Y.Xing, S.Zhang, S.Wu, Int. J. Electrochem. Sci., **13** (2018), 8736 – 8744.
75. X. J. Wang, X. A. Xia, W. J. Meng, C. X. Yang, M. Q. Guo, Y. Zhao, F. Q. Yang, J. Electron. Mater. **47**(2018), 6774–6780.
76. S. Ramesh , K. Karuppasamy, H.S. Kim, H.S. Kim, J.H. Kim, Sci.Rep., **8** (2018), 16543-16549.
77. J.F. Gao, W.B. Zhang, Z.Y. Zhao, L.B. Kong, Sustainable Energy Fuels, **2** (2018), 1178-1188.
78. M.Chen, J.Wang, H.Tang, Y.Yang, B.Wang, H.Zha, D.Wang, Inorg. Chem. Front.,**3** (2016), 1065-1070.
79. A.M.Patil, V.C. Lokhande, T.Ji, C.D. Lokhande, Electrochimi. Acta **307**(2019), 30-42.
80. R.R. Kanna ,K.Sakthipandi, S.M. Maraikkayar, N.Lenin, J. Rare Earths, **36** (2018), 1299-1309.
81. P.P.Kumbhar and C.D.Lokhande, Indian J. Chem. Technol., **1** (1994), 311-313.
82. P.P.Kumbhar and C.D.Lokhande, Indian J. Chem. Technol., **1** (1994), 194-196.

83. S.M.Ramay, A.Mahmood, H.M.Ghaithan, N.S.Zayed, A.Aslam, A.Murtaza, N.Ahmad, S.A.Saleem, J. Rare Earths, **37** (2019), 989-994.
84. A. Kruk, M. Mrozek, J. Domagała, T. Brylewski, W. Gawlik, J. Energetic Mater., **43** (2014), 3611–3617.
85. S.B.Jundale, and C.D.Lokhande, Mater. Chem. Phys., **27**(1991), 265-278.
86. S.B.Jundale, and C.D.Lokhande, Mater.Chem.Phy., **38** (1994), 325-331.
87. S.B.Jundale and C.D.Lokhande, Indian J. Pure Appl. Phys., **30**(1992), 215-220.
88. S.B.Jundale and C.D.Lokhande, Mater. Chem. Phys., **37** (1994), 333-338.
89. S.B.Jundale and C.D.Lokhande, Sol. Energy Mater Sol., **28** (1992), 151–157.
90. K.Jeong, D.Bae, Korean J. Mater. Res.**22** (2012), 22-29.
91. U.K.Mohite and C.D.Lokhande, Appl. Surf. Sci.**92** (1996), 151-154.
92. U.K.Mohite, S.A.Jodgudri, C.D.Lokhande, J.Physics **19** (1995), 1152-1157.
93. U.K.Mohite and C.D.Lokhande, Bull. Electrochem.**13** (1997), 71-74.
94. S.A.Jodgudri, U.K.Mohite, K.M.Gadave, C.D.Lokhande, Indian J. Pure Appl. Phys., **32** (1994), 772-777.
95. M. Majumder, R. B. Choudhary, A.K. Thakur, C.S. Rout, G. Gupta, New J. Chem.,**42** (2018), 5295-5308.
96. A.A.Yadav, V.S.Kumbhar, S.J.Patil, N.R.Chodankar, C.D.Lokhande, Ceram.Int.**42** (2016) 2079-2084
97. S.J. Patil, V.S. Kumbhar, B.H. Patil, R.N Bulakhe, C.D. Lokhande, J. Alloys Compd. **611** (2014), 191-196.
98. S.J. Patil, B.H. Patil, R.N. Bulakhe, C.D.Lokhande, RSC Advance. **4** (2014), 56332-56341.
99. S.J. Patil, C.D. Lokhande, Mater. Des. **87** (2015), 939-948.
100. S.J.Patil, R.N.Bulakhe, C.D. Lokhande, ChemPlusChem **80** (2015), 1478-1487.
101. S.J. Patil, V.C. Lokhande, N.R. Chodankar, C.D. Lokhande, J. Colloid Interface Sci. **469**(2016), 318-324.
102. V.S.Kumbhar, A.D. Jagadale, C.D. Lokhande, J. Power Source, **234** (2013), 107-110.
103. V.S.Kumbhar, A.C.Lokhande, N.S.Gaikwad, C.D.Lokhande, Mater. Sci. Semicond. Process. **33** (2015), 136-139.
104. V.S. Kumbhar, A.C. Lokhande, N.R. Chodankar, N.S. Gaikwad, C.D. Lokhande, Mater. Lett. **223** (2018), 45-48.
105. V.S.Kumbhar, A.C.Lokhande, N.S.Gaikwad, C.D. Lokhande, Mater. Sci. Semicond. Process. **46** (2016), 29-34.
106. V.S. Kumbhar, A.C. Lokhande, N.S. Gaikwad, C.D. Lokhande, Ceram. Int. **41** (2015), 5758-5764.
107. L.Zhang, S, Zhao, X. N.Tian, X. S. Zhao, Langmuir, **26** (2010), 17624–17628.

- 108.** G.S.Gund, D.P.Dubal, B.H.Patil, S.S.Shinde, C.D. Lokhande, *Electrochim. Acta.* **92** (2013), 205-215.
- 109.** Ji.Zhang, Z.Zhang, Y.Jiao, H.Yang, Y.Li, J.Zhang, P.Gao, *J.Power Source*, **419** (2019), 99–105.
- 110.** R. Rajagopal, K.S. Ryu, *J. Ind. Eng. Chem.* **60** (2018), 441–450.
- 111.** A. S.Dezfuli, M. R. Ganjali, H.R.Naderi, *Appl. Surf. Sci.* **402** (2017), 245-253.
- 112.** M. Majumder, R.B. Choudhary, A. K. Thakur , I. Karbhal, *RSC Adv.*,**7** (2017), 20037-20048.
- 113.** Z.D. Huang, B. Zhang, S.W.Oh, Q.B. Zheng, X.Y.Lin, N. Yousefi, J.K. Kim, *Chem.*, **22** (2012), 3591- 3599.
- 114.** K.J.Huang, J.Z.Zhang, Y.Liu, Y.M.Liu, *Int. J. Hydrogen Energy*, **40** (2015), 10158-10167.
- 115.** B. K. Kim, S. Sy, A.Yu, J. Zhang, *Handbook of Clean Energy Systems*,(2015)1-25.
- 116.** https://en.wikipedia.org/wiki/Double-layer_capacitance
- 117.** <https://en.wikipedia.org/wiki/Pseudocapacitance>

Chapter-2
Theoretical Background
of Deposition Methods
and Thin Film
Characterization
Techniques

Sr. No.	Title	Page. No.
2	<i>Introduction</i>	26
2.1	<i>Theoretical Background</i>	27
2.1.1	<i>Successive Ionic Layer Adsorption and Reaction (SILAR) Method.</i>	28-32
2.1.2	<i>Hydrothermal Method.</i>	32-34
2.1.3	<i>Thin Film Characterization Techniques</i>	35
2.1.3.1	<i>X-ray Diffraction (XRD)</i>	35-37
2.1.3.2	<i>Fourier Transforms Infrared Spectroscopy (FT-IR)</i>	37-38
2.1.3.3	<i>Field Emission Scanning Electron Microscopy (FE-SEM)</i>	39
2.1.3.4	<i>Contact Angle Measurement</i>	40
2.1.3.5	<i>Brunauer-Emmett-Teller (BET)</i>	41-42
2.1.3.6	<i>X-ray Photoelectron Spectroscopy (XPS)</i>	43-44
2.1.4	<i>Electrochemical techniques to study supercapacitive properties</i>	45
2.1.4.1	<i>Cyclic Voltammetry (CV)</i>	45
2.1.4.2	<i>Galvanostatic Charge/Discharge (GCD)</i>	46
2.1.4.3	<i>Electrochemical Impedance Spectroscopy (EIS)</i>	47
References		49

2. Introduction:

Thin film technologies are progressively evolving for the fabrication of technologically advanced devices, which cover a wide scope of applications such as: DSSCs, supercapacitors and sensors etc. [1-3]. Depositing thin film materials ranges from pure elements, metals to more complex compounds, such as nitrides [4], oxides [5], polymers [6] etc. Nowadays, the distinction between thick and thin film not only is determined by thickness of layer but also by technologies used. Thin film methods, which are currently available can deposit a material to a from few nanometers to the angstrom level. In fact, a peculiar characteristic of thin film technology is that, thin film can be formed at the atomic or molecular level, a layer at a time. Depositions occur from vapor or solution state and based on physical processes or chemical reactions [7].

Thin films are evaluated from various physicochemical techniques for the material identifications and surface textural assessment. Thin films of various materials can be identified using X-ray diffraction (XRD) [8], Fourier transforms infrared spectroscopy (FT-IR) [9] while its surface textural behavior can be tested from Field-emission scanning electron microscopy (FE-SEM) [10], and contact angle (CA) [11]. Present chapter deals with theoretical background of successive ionic layer adsorption and reaction (SILAR) and hydrothermal methods of thin film preparation [12, 13].

The present chapter includes theoretical background of hydrothermal and SILAR methods with different characterization techniques, such as X-ray diffraction (XRD), X-ray photoelectron spectroscopy (XPS), fourier transforms infrared spectroscopy (FT-IR), field emission scanning electron microscopy (FE-SEM), Brunauer Emmett teller (BET) and contact angle measurement (CA). The electrochemical performance evaluation techniques like cyclic

voltammetry (CV), galvanostatic charge-discharge (GCD) and electrochemical impedance spectroscopy (EIS) were employed to study the supercapacitive properties of prepared thin films. All electrochemical performances were evaluated in standard three electrode system with prepared thin film as a working electrode, platinum as a counter electrode and saturated calomel electrode (SCE) as a reference electrode.

2.1. Theoretical Background:

2.1.1. Successive Ionic Layer Adsorption and Reaction (SILAR) Method-

The best feature of film formation such as, uniform, adherent and thin is possible using SILAR method. Like CBD method, the thin film formation takes place when ionic product exceeds the solubility product. But, the formed precipitate in the bulk of solution cannot be eliminated. In order to avoid such unnecessary precipitation or loss of material. The CBD is modified as SILAR method. For the deposition of metal chalcogenide thin films SILAR method was used in mid 1980 [14]. Ristov et al [15] originally reported a SILAR method as multiple chemical dipping techniques and Nicolau et al [16] preferred name as SILAR method. SILAR means successive ionic layer adsorption and reaction method. Generally, SILAR method involves adsorption, rinsing and reaction. Photograph of SILAR is shown in (Fig.2.1).



Fig. 2.1. Photograph of SILAR Unit.

Reaction Mechanism of Four Beaker System-

(a) **Adsorption:** It is a first step of deposition process, where cations are adsorbed on the surface of the substrate and form the Helmholtz electric double layer. This layer is formed due to the Vander Waals force and it composed of two layers. The positively charged cations form inner electric layers. The second layer is of counter layer of cation having negative charged anions.

(b) **Rinsing I:** The purpose of rinsing is to remove the loosely adsorbed cations on the substrate surface. Generally, double distilled water (DDW) is used as rinsing solution.

(c) **Reaction:** The anions from anion precursor solution react to pre adsorbed cations and form a compound.

(d) **Rinsing II:** The purpose of rinsing II is to remove the excess and unreacted species and the reaction by product from the diffusion layer.

Generally, Thin film deposition mainly depends upon thicknesses of film and it is controlled by using different preparative parameters like concentration of cation and anions, temperature of bath, adsorption and reaction time, rinsing time, complexing agent etc in

(Fig.2.2).

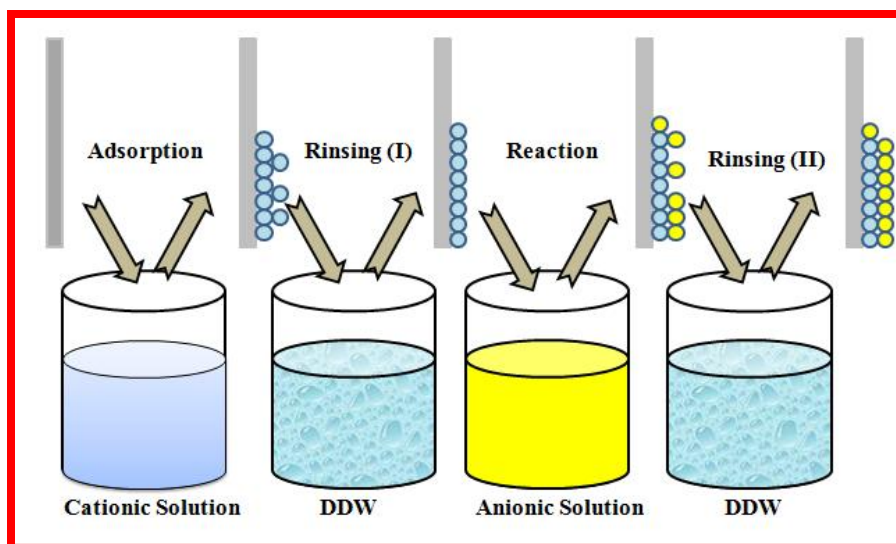


Fig. 2.2: Schematic Diagram of Four Beaker System Reaction Mechanism.

Advantages of SILAR method [17]:

- a) It is simple, economical method used for large area deposition.
- b) It is a low temperature process.
- c) The deposition rate can be easily controllable.
- d) Any type of substrate can be used.
- e) It does not require high quality targets or vacuum at any stage.
- f) The thickness of the film can be easily controlled over an adsorption and reaction time and wide range by changing the deposition cycles.

Effect of preparative parameters:

The growth kinetics depends on the concentration of ion, nucleation and growth process on immersed substrates. Effect of various deposition conditions on these parameter are given below:

- (i) **Concentration-** In chemical deposition methods, the film growth is affected by changing the concentration of precursor solution. If concentration of metal ion is above the certain ion concentration, the rate of reaction becomes high and lower film thickness obtained. If metal ion concentration increases, this leads to an increase in chalcogenides ion concentration and formation of maximum film thickness.
- (ii) **pH-** The concentration of H^+ ions is controlled by using complexing agent. The pH of solution increased by increasing concentration of H^+ ion and resulted metal ion concentration decreases. For higher pH, the rate of reaction is faster and at a certain pH value, the concentration of metal ion decreases to a level such that the ionic product of metal and chalcogenide becomes less than the solubility product of metal chalcogenide and a film will not be formed.

(iii) Temperature- The variation of film thickness can possible using varying the temperature of solution bath. The dissociation of complex and the anion of the compound depend on the temperature. At the higher temperature, dissociation is greater and resulted higher rate of deposition. At room or lower temperature the film formation rate is slow. The thickness is increased with increase in temperature linearly.

(iv) Complexing agent- The metal ion concentration can be controlled with adding the of complexing agent. The concentration of complexing agent decreases the concentration of metal ions. Therefore, the rate of reaction and precipitate formation is reduced leading to larger terminal thickness of the film. The deposition of thin film on surface substrate is an only adsorption phenomenon. The thin film formation occurs by combination of released metal ion form complex metal ion source and chalcogenide source. The use of complexing agent is to complexed metal ion.

In the following, in view of a better understanding but without limiting the generality of the process, we shall discuss the growth mechanism taking as an example the growth of CdS thin films. The solution of CdSO_4 and Na_2S are used as immersion baths. **Fig.2.3** shows experimental set-up of manually operated SILAR deposition system. It mainly consists of beakers of cationic precursor (CdSO_4), anionic precursor (Na_2S) and double distilled water. For the deposition of CdS thin film, at least four beakers are needed. The beakers of precursor and beaker of rinsing are alternately placed, each rinsing beaker being placed between a beaker containing a solution of a salt of the cation and another containing a solution of salt of the anion. For the deposition of CdS thin films, a well cleaned glass substrate is immersed in cationic precursor solution of CdSO_4 (**Fig.2.3 (a)**) in which Cd^{2+} and SO_4^{2-} ions are adsorbed on the surface of the substrate (CdOH^+ adsorption is neglected). The substrate is rinsed in ion exchange water (**Fig.2.3 (b)**) to

remove unabsorbed Cd^{2+} and SO_4^{2-} ions. In order to avoid the homogeneous precipitation in the diffusion layer at the next immersion in the Na_2S solution, the rinsing time must be experimentally determined or calculated so that the residual activity of the Cd^{2+} in the diffusion layer $[\text{Cd}^{2+}]$ should be $[\text{Cd}^{2+}] < K_{\text{so}}[\text{H}^+]/K[\text{HS}^-]$. Here $K_{\text{so}} \approx 10^{-28}$ is the solubility product of CdS. The substrate is then immersed in an anionic precursor (**Fig. 2.3 (c)**) solution. During the next immersion in the Na_2S solution, the HS^- , S^{2-} , OH^- and Na^+ ions diffuse from the solution in the diffusion layer towards solid solution interface until their concentration in the diffusion equals those in bath. The immersion time is experimentally calculated. The HS^- and S^{2-} enter the outer Helmholtz layer, react with the adsorbed Cd^{2+} and form CdS monolayer. This is followed by rinsing again in ion exchange water (**Fig. 2.3 (d)**) to remove Cd^{2+} and S^{2-} ions, unreacted and loosely bounded CdS material and other byproducts. This completes one deposition cycle for the deposition of CdS film. By repeating such deposition cycles, continuous CdS films on the substrate surface is possible [17]. The overall reaction can be written as,

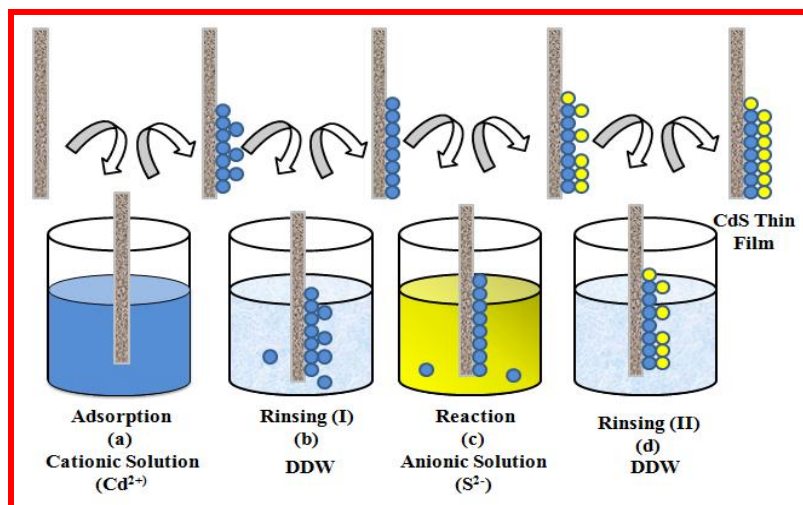
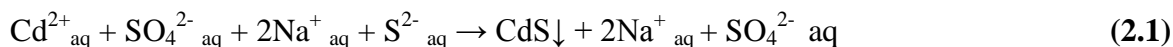


Fig.2.3. The scheme of SILAR method for the deposition of CdS thin film: (a) cationic precursor (Cd^{2+}), (b) ion exchange water (DDW), (c) anionic precursor (S^{2-}) and (d) ion exchange water (DDW).

2.1.2. Hydrothermal Method-

Hydrothermal method is a simple method for the production of nanomaterials. It is nothing but the special case of solvothermal process, which is generally defined as a chemical reaction taking place in a solvent at temperatures above the solvent boiling point and at pressure above 1 bar [18]. The medium used for the solvent preparation can be water (hydrothermal), ammonia (ammonothermal), alcohol (alcothermal, glycothermal), or any organic or inorganic solvent. The hydrothermal method accomplishes that on increasing deposition temperature and pressure, the fundamental properties of water and its ability as a solvent changes. The important characteristics like ionic product, density, thermal conductivity, heat capacity, viscosity and dielectric constant are highly temperature and pressure dependant. Therefore, by regulating the synthesis parameters, specific solvent properties can be easily obtained. The hydrothermal method has been most popular, gathering interest from scientists and technologists of different discipline particularly in the last 15 years.

The majority of minerals formed in the post-magmatic and metasomatic stages in presence of water at elevated pressure and temperature conditions are said to be of hydrothermal origin. This covers a vast number of minor species including or deposits. It is well known that the largest single crystal formed in nature (beryl crystal of >100 gm) and some of the largest quantities of single crystals created by man in one experimental run (quartz crystal of several hundreds of gram) are both of hydrothermal origin. In spite of the fact the hydrothermal technique has made tremendous progress, there is no unanimity about its definition. The term hydrothermal usually refers to any heterogeneous reaction in presence of aqueous solvent or mineralizers under high pressure & temperature condition to dissolve and recrystalline materials that are relatively insoluble at ordinary condition [19, 20].

A batch reactor is used for the conventional hydrothermal synthesis process. In this, the precursors are simply dissolved or suspended in water in an autoclave which can endure high temperature and pressure [21, 22]. The autoclave is sealed and heated to the required temperature, while the pressure is most often autogenously generated. The pressure of more than several hundred bars can be easily obtained even at low temperature depending on the degree of autoclave filling [23]. The volume of the autoclave varies from few milliliters for laboratory synthesis to thousands of liters for industrial material production. The maximum temperature and pressure can be as high as 1000 °C and 500 bars. However, for commercial applications temperatures below 500 °C are usually preferred [24]. The schematic of hydrothermal autoclave is shown in **Fig. 2.4**. It consists of teflon liner inserted in a stainless steel shell, which is sealed with the stainless steel lid. Besides, hydrothermal method has many advantages; some of them are listed below:

- The process is eco-friendly since it is carried out in a closed system and the contents can be easily recovered and reused after cooling down to room temperature.
- The equipment and processing required are simpler and the reaction is low energy consumption.
- By controlling hydrothermal temperature and duration of the treatment, various crystalline products with different composition, structure and morphology can be obtained.
- Hydrothermal method is unique for the synthesis of thermodynamically metastable phases.
- The crystalline size and morphology can be altered to nanoscale simply by adjusting the synthesis parameters e.g. temperature, pH, precursor concentration, deposition time etc.

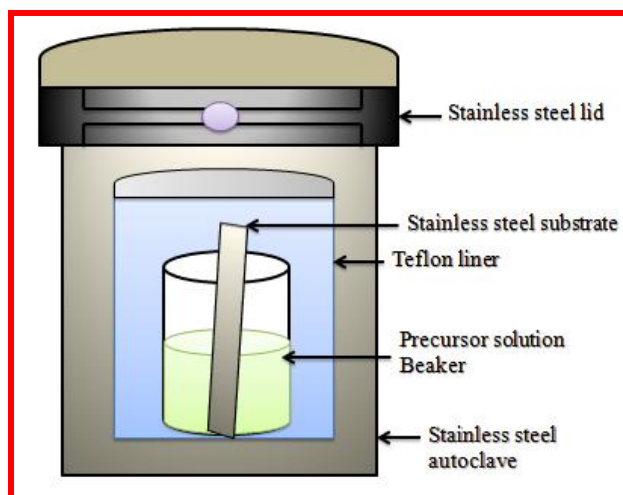


Fig.2.4 Schematic of hydrothermal autoclave.

2.1.3. Thin Film Characterization Techniques:

This chapter gives a brief description of the various characterization techniques used during the research work.

2.1.3.1 X-ray Diffraction (XRD):

The X-ray diffraction is a powerful tool to analyze the crystal structure of crystalline materials by means of X-rays, directed towards a crystal of known wavelength (λ). The interaction of the beam with solid material produce diffraction pattern, which is dependent on the crystal structure of the material. The X-ray diffraction is used to demonstrate the periodic arrangements of atoms in the materials by knowing the lattice parameters and the interplanar spacing which is of the order of X-ray wavelength. The diffraction pattern follows the condition of Bragg's law [25] i.e.

$$2d\sin\theta = n\lambda, \quad (2.2)$$

Where, n is the diffraction order, λ is the wavelength, d is the spacing between consecutive parallel planes and θ is the glancing angle. The structural identification made from the diffraction pattern is further correlated with the international recognized database Joint Committee on Powder Diffraction Standards (JCPDS). X-ray diffractometer (XRD) from Phillips (PW3050/60) as well as Bruker D-8 advance are used in this research and typical working schematic with model as shown in **Fig. 2.5**. The measurement was performed by using 40 kV, 30 mA Cu K α incident beam ($\lambda=1.54$ Å). The measurements were conducted at scan rate of 0.05 °/s and 2θ range from 10° to 80°. The three methods are available to determine the crystal structure of sample,

I] Laue method

II] Rotating crystal method and,

III] Powder method

In order to simply analyze the crystal structure of sample, powder method is commonly used. The oldest method as a Laue method is used for the determination of crystal structure, where wavelength of X-ray is variable and angle of incidence is fixed. If the angle of incidence is fixed and wavelength is variable then that method is called rotating crystal method. In case of powder method, the wavelength is taken as a fixed and angle of incidence is variable. **Fig. 2.5 (A)** displays the schematic of X-ray diagram and **Fig. 2.5 (B)** shows the photograph of Bruker D-8 advanced X-ray diffractometer.

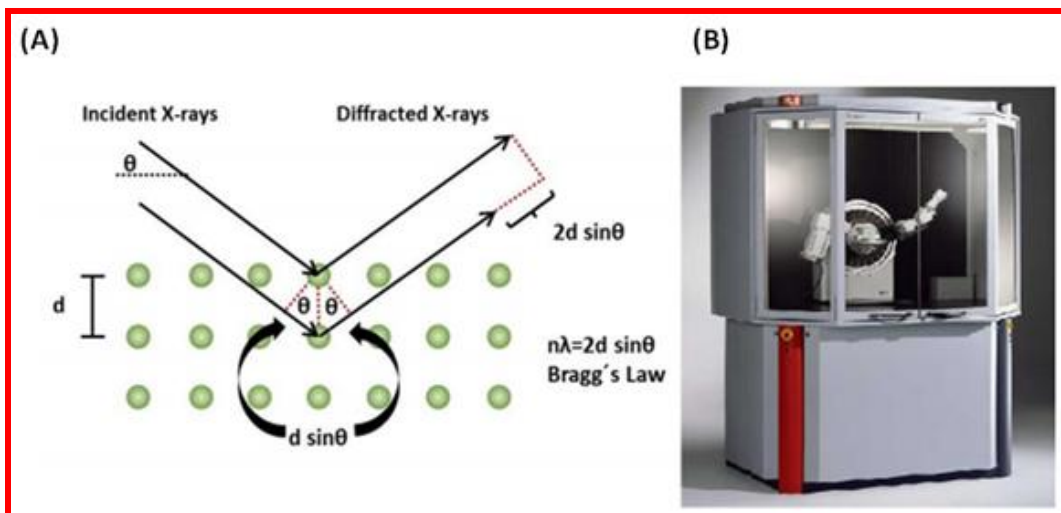


Fig. 2.5: [A] Schematic diagram of X-ray diffraction and [B] Photograph of Bruker D-8 Advance X-ray Diffraction Instruments [24].

The particle size ‘D’ of deposited material is calculated from full width at half maximum (FWHM) by Scherer’s relation [25],

$$D = \frac{K \cdot \lambda}{B \cos \theta} \quad (2.3)$$

Where, β is full width of half maxima of the peak (FWHM), θ is Bragg’s angle and K is constant (0.9).

2.1.3.2. Fourier Transforms Infrared Spectroscopy (FT-IR):

Fourier transform infrared spectroscopy (FT-IR) is the most widely used analytical vibrational spectroscopic technique, to investigate sample interactions when irradiated with IR light. This technique utilizes Fourier transform method to convert complex interferogram spectrum to infrared spectrum of frequency domain (intensity versus wavenumber). FT-IR technique replaced the dispersive method, where the spectrum is a collection of signals individually. The IR spectrum obtained by FT-IR can be measured simultaneously in an entire range of wave numbers. The main part of FT-IR system is Michelson interferometer which

consists of beam splitter and two mirrors. The schematic representation of FT-IR spectroscopy is shown in **Fig.2.6**.

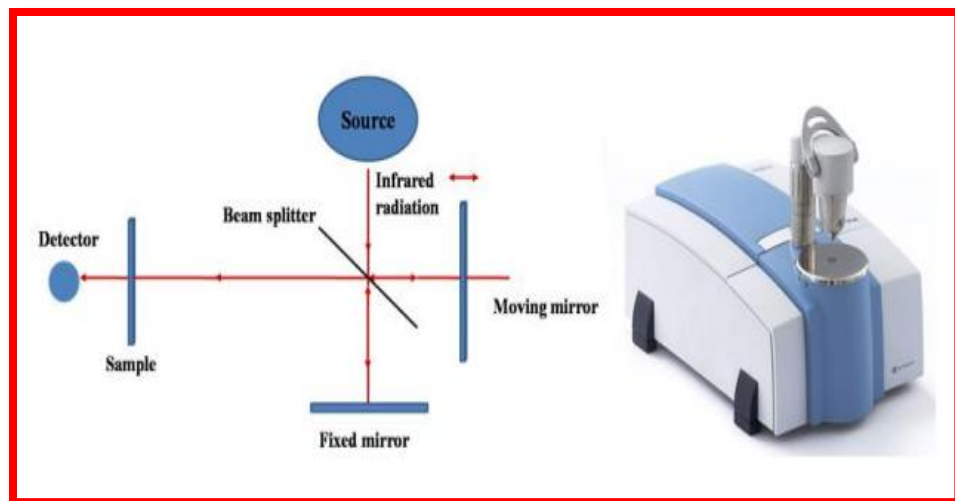


Fig.2.6: Michelson-Interferometer FT-IR System and Fourier Transform Infrared Spectrometer Model [26].

The incident beam from the source is projected towards beam splitter and splits into two halves. One part of the beam is transmitted to moving mirror and reflected to splitter. The other part of the beam strikes a fixed mirror and reflected towards splitter. Thereafter, constructive or destructive interference is obtained by the recombination of two beams. The sample is placed between interferometer and detector. The spectrum difference between the source and sample is detected by detector, which is referred as interferogram and is a complex spectrum. The interferogram is then converted by using Fourier transformation. FT-IR study gives the qualitative information of material such as molecular structure and vibration characteristics of atom in functional groups. In this study, infrared spectra of the developed materials are characterized by using a Fourier Transform Infrared Spectrometer (Bruker, Germany model: 3000 Hyperion Microscope with Vertex 80 FTIR System) over the frequency range 4000 to 400 cm^{-1} [27].

2.1.3.3. Field-emission scanning electron microscopy (FE-SEM):

Field emission scanning electron (FE-SEM) microscopy is a powerful tool used for the microstructure analysis at high resolution surface [28]. As compared to other optical and scanning electron microscopies, it uses electrons to illuminate a surface of the sample. The technique is capable of imaging at much higher magnification than light microscopes, due to much smaller wavelength of electrons compared to visible light [29]. The common materials used for filaments are tungsten and lanthanum hexaboride. The FE-SEM uses field emission gun producing a clear image, less electrostatic distortions and spatial resolution < 2 nm better than SEM.

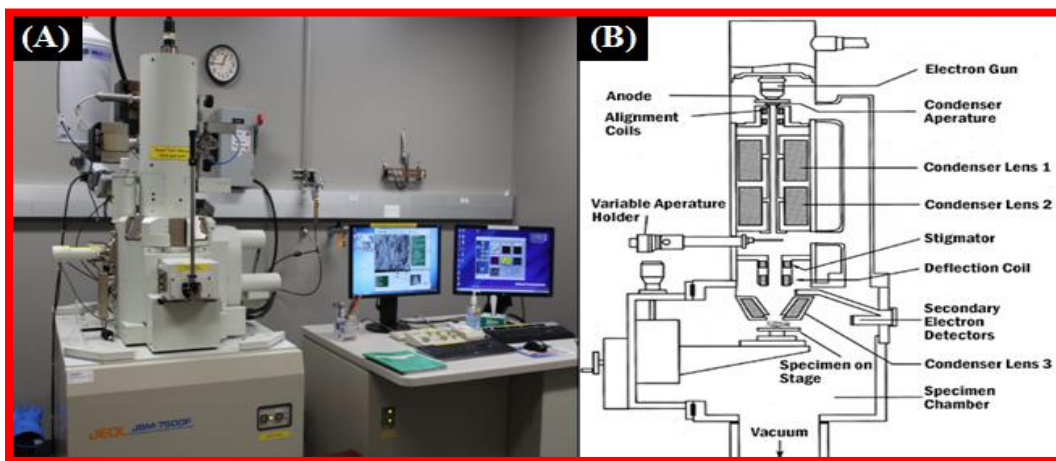


Fig. 2.7: (A) Photograph and (B) diagram of field-emission scanning electron microscopy (FE-SEM) [30].

There are two classes of emission sources, thermionic emitter and field emitter. The electrons are released from the source of field emission and accelerated at a very high electric field gradient. In the high vacuum column (less than 10^{-7} pa) released primary electrons are allowed to focus and deflect through electronic lenses which produce a narrow beam that bombards the object. The secondary electron is lands on the lens detector and collected to produce an electronic signal. The recorded electrical signals are amplified and translated into

scan image. The scanned images are seen on the display. **Fig. 2.7 (A)** shows the photograph and **Fig. 2.7 (B)** schematic is the diagram of FE-SEM.

2.1.3.4. Contact Angle Measurement:

The angle formed between the liquid–solid interface and the liquid–vapor interface is the contact angle. The static sessile drop contact angle is measured by a contact angle goniometer using an optical subsystem to capture the profile of a pure liquid on a solid substrate. The present system includes high resolution camera and software to capture and analyze the contact angle. The drop of the liquid applied on the solid substrate is 1 and 10 microliters (μl). For controlling or modifying of electrode surface wettability is an important aspect of the application of supercapacitor [31]. The wettability measure the ability of material to interact with liquid. The contact angle (θ) of a liquid sample on a solid thin film surface is shown in **Fig. 2.8 (A, B)**.

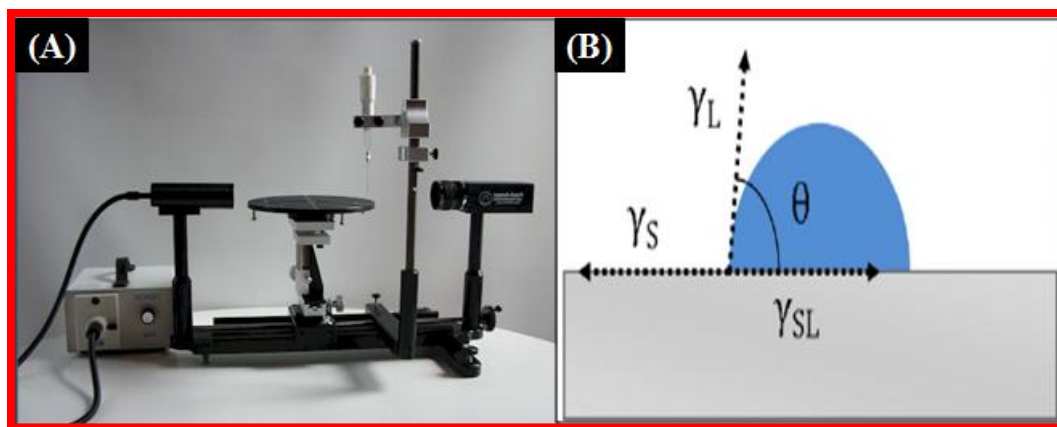


Fig.2.8: (A) Photograph of Rame-Hart NRL CA Meter and (B) Contact angle of a liquid and solid sample [31].

The contact angle is the angle between surface of a solid and tangent drawn to the liquid surface, measures inside the liquid. If the contact angle is greater than 90° then it is hydrophobic in nature and surface is less wettable [32]. Super hydrophobic surface means contact angle is

above 170° . If the contact angle is less than 90° , the surface is hydrophilic and wettable. In case of super hydrophilic condition, the contact angle is less than 5° and surface is more wettable. The different methods are used to measure contact angle. If the three phases are in equilibrium condition, then net force is zero. The contact angle (θ) is calculated by the Young's relation [13],

$$\gamma_{s,v} = \gamma_{s,l} + \gamma_{l,v} \cos \theta \quad (2.4)$$

Where, $\gamma_{s,v}$ is the solid-vapour, $\gamma_{s,l}$ is the solid-liquid and $\gamma_{l,v}$ is the liquid-vapour interfacial energies.

2.1.3.5. Brunauer-Emmett-Teller [BET]:

The Brunauer-Emmett-Teller (BET) is very commonly used technique for the determination of specific surface areas and porosity of the materials. The specific surface area of the material is determined by the adsorption of gas molecules on the surface of solid and by calculating the amount of adsorbate gas corresponding to a monomolecular layer on the surface. The quantity of gas adsorbed or condense on the surface of solid at a constant temperature depends on the pressure of gas. The gas is adsorbed on the surface as well as in the pores of the specimen. The amount of gas adsorbed or condensed at a given pressure gives the information about pore structure. Normally, the non-corrosive gases like nitrogen are used for BET measurement [33]. The schematic illustration of the dynamic flow method apparatus used for the measuring specific surface area is predicted in [Fig. 2.9].

The BET theory is an extension of the Langmuir theory, which is a theory for monolayer molecular adsorption to multilayer adsorption with the following hypotheses: (a) gas molecules physically adsorb on the solid, (b) there is no interaction between each adsorption layer; and (c) the Langmuir theory can be applied to each layer. The BET technique is widely used in surface

science for the estimation of surface areas of solids by the physical adsorption of gas molecules. The total surface area (S_{total}) and a specific surface area (S_{BET}) are estimated from the following expression;

$$S_{\text{total}} = \frac{VmNs}{V} \quad (2.5) \text{ and,}$$

$$S_{\text{BET}} = \frac{S_{\text{total}}}{a} \quad (2.6)$$

Where, S is the adsorption cross section of the adsorbing species, N is the Avogadro's number, V_m is the molar volume of the adsorbate gas and a is the mass of the adsorbent [34].

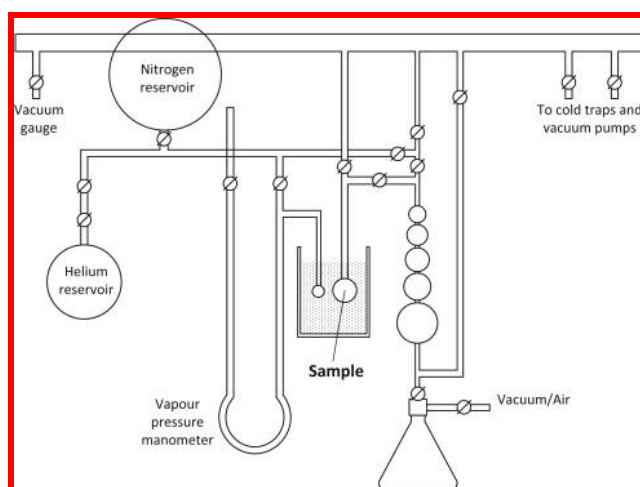


Fig. 2.9: Schematic illustration of the dynamic flow method apparatus [33].

2.1.3.6. X-ray Photoelectron Spectroscopy (XPS):

X-ray photoelectron spectroscopy (XPS) is also known as electron spectroscopy for chemical analysis (ESCA) which has the fundamental ability to know the surface properties of materials or thin films. It works on the principle of photoelectric effect in which soft X-rays are used as a source of photons. When X-ray beam is allowed to incident on the material, it causes electrons to be escape from the surface layer of material. The ejected electrons are called as

photoelectrons. The identification of elements in the sample is made directly from the kinetic energies of these photoelectrons. The relative concentration of elements is determined from the intensities of photoelectrons. The kinetic energy of ejected electrons is given by the relation [35],

$$K.E. = h\nu - B.E. - \Phi_s \quad (2.7)$$

Where, K.E. = kinetic energy of ejected photoelectron, $h\nu$ = characteristic energy of X-ray photon

B.E. = binding energy of the atomic orbital from which the electrons originated, Φ_s = spectrometer work function.

In XPS, the photon is absorbed by the atom in a molecule, this leads to ionization and emission of inner shell (core) electrons. Every element has characteristic binding energy related to each core level atomic orbital, which means each element give rise to characteristic peaks in the photoelectron spectrum. The kinetic energies are determined by the photon energies and their respective binding energies. The commonly used X-ray source are Mg K α radiation $h\nu = 1253.6$ eV and Al K α radiation $h\nu = 1486.6$ eV. Therefore, the emitted photoelectrons have kinetic energies in between 0 to 1250 eV for Mg source and 0 to 1480 for Al source. In XPS, firstly the measurements are carried out over total accessible energies known as survey scan. This ensures the presence of all the elements in the sample. Though the XPS measures kinetic energy of emitted electrons, it is actually the binding energy of electron plotted to construct the energy spectrum. Thus, the XPS spectrum consists of number of electrons detected with respect to their binding energy. The number of electrons gives the amount of that element present in the sample. The presence of peaks at particular binding energies represents the presence of particular element in the sample. These characteristic energy peaks are related to the electronic configuration of that electron within the atoms, such as 1s, 2p, 3d, 3p etc. This leads to the

identification of oxidation state of the element. The ray diagram of XPS technique is shown in **Fig. 2.10**. This technique is surface sensitive as the electrons have very short inelastic mean free path in solids. For an electron emitted towards the surface, there is less possibility of inelastic scattering before it escaped from the solid. The XPS is not fully surface phenomenon; some signals originate from few atomic layers of the surface, while the small amount of signals comes out from much deeper part of the element.

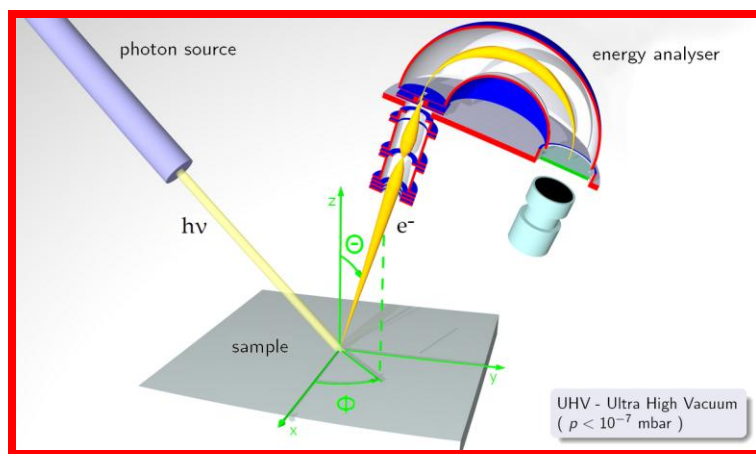


Fig.2.10: Ray diagram of XPS [36].

2.1.4. Electrochemical Techniques to Study Supercapacitive Properties:

2.1.4.1. Cyclic voltammetry (CV)-

The cyclic voltammetry is nothing but the current density against fixed potential range. **Fig. 2.11** shows the CV plot. The measured faradic current in the cyclic voltammetry depends on the kinetics of electron transfer and the scanning rate in which the actual redox species diffuses to the electrode surface. From **Fig. 2.11**, it is seen that in the initial point reduction process occurs [35, 36]. The corresponding peak potential at point E_{pa} , the faradic current is maximum, called cathodic current and that potential is referred as cathodic or reduction potential. If we reverse the potential, a peak current at negative side at a point E_{pc} is maximum and after that current will decrease in the magnitude. The negative peak current is observed due to the

oxidation and corresponding potential is called oxidation potential and surface of electrode is fully oxidized [37].

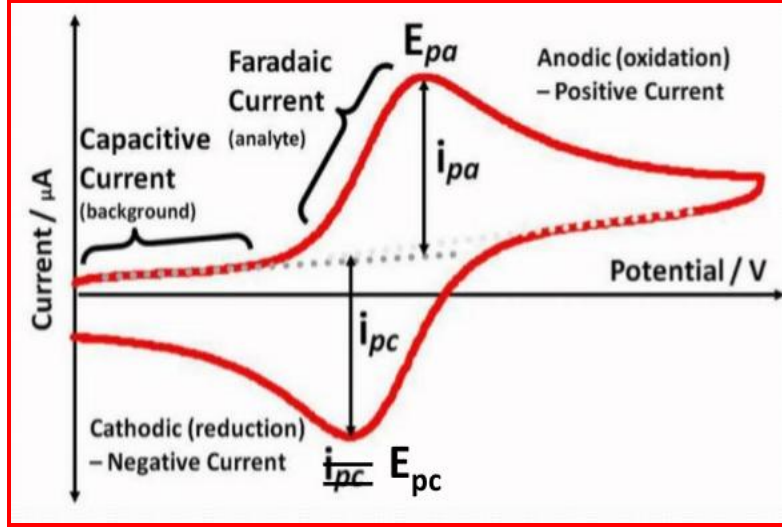


Fig. 2.11: The typical CV curve of cyclic voltammeter [42].

The interfacial capacitance of electrode material is evaluated by changing the scan rate (time response) or potential ranges (V). The capacitance of electrode calculated from CV curve using equation,

$$C = \frac{\int Idt}{dV/dt} \quad (2.9)$$

Where, C is the capacitance, $\int Idt$ is the average current density and dV/dt is the scan rate. As increase the scan rate, corresponding charging and discharging are at higher power levels [27]. In case of pure EDLC's electrode material, the shape of CV curve is rectangular [43]. If the electrode material behaves pseudocapacitive nature then the prominent peaks occurs in the CV curve.

2.1.4.2. Galvanostatic Charge/Discharge (GCD):

This technique elaborates charge storage capability of material as well as energy storage and power delivery. Constant current is supplied to working electrode and it is fully charged up to some higher potential V_2 and then discharged with opposite direction current but with same magnitude up to lower potential V_1 . The GCD curve is plotted between potential applied to electrode versus time required for charging and discharging in **Fig.2.12**. Specific capacitance (C_s), power density (PD) and energy density (ED) parameters of material, which decides supercapacitor nature of material, can be calculated using following equations [44].

$$C_s = \frac{I \times \Delta t}{\Delta V \times m} \quad (2.10),$$

$$ED = \frac{0.5 \times C_s \times (V^2_{max} - V^2_{min})}{3.6} \quad (2.11)$$

And,

$$PD = \frac{E.D \times 3600}{T_d} \quad (2.12)$$

Where, I is the constant current, δt is time interval for the voltage change δv , m is the mass of deposited thin film, T_d is the discharge time of supercapacitor. The operating potential window and capacitance of supercapacitor must be large to attain the maximum value of specific energy and specific power. The capacitance and operating potential window of supercapacitor depend upon the active electrode material and the electrolyte used.

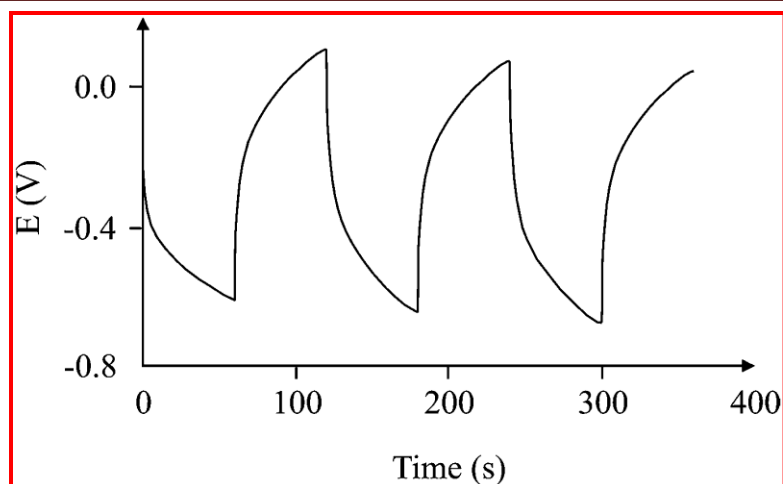


Fig. 2.12: The typical GCD curve of galvanostatic charge-discharge [45].

2.1.4.3. Electrochemical impedance spectroscopy (EIS):

Impedance is nothing but sum of complex resistance come across when an electric current flows through a circuit made of resistors, capacitors, or inductors, or any combination of these. **Fig. 2.13 (A)** shows the different layers present in between the electrode-electrolyte interface and is represented by the electronic components. Electrochemical impedance spectroscopy (EIS) used to study the variation of the impedance of an electrochemical system with the frequency. Impedance spectroscopy is mostly referred with interfacial charge transfer resistance (R_{ct}), electrolyte resistance (R_s) and diffusion of reactants. Also, using EIS measurement it is possible to readily separate the interfacial capacitance and charge-transfer resistance, as well as to identify diffusion components in the electrolyte [46]. The complex impedance of real part (Z') against imaginary part (Z'') is commonly known “Nyquist plot” **Fig. 2.13 (B)**. Nyquist plots provide a sense of the type of processes that govern at the low, mid-high and high frequency behavior of the system [47]. Bode plot represents the modulus of complex impedance ($|Z|$) and phase angle (Φ) of an AC as a function of frequency (f). The values of

complex impedance (z) and phase angle (Φ) are determined using assembled basic electronic components.

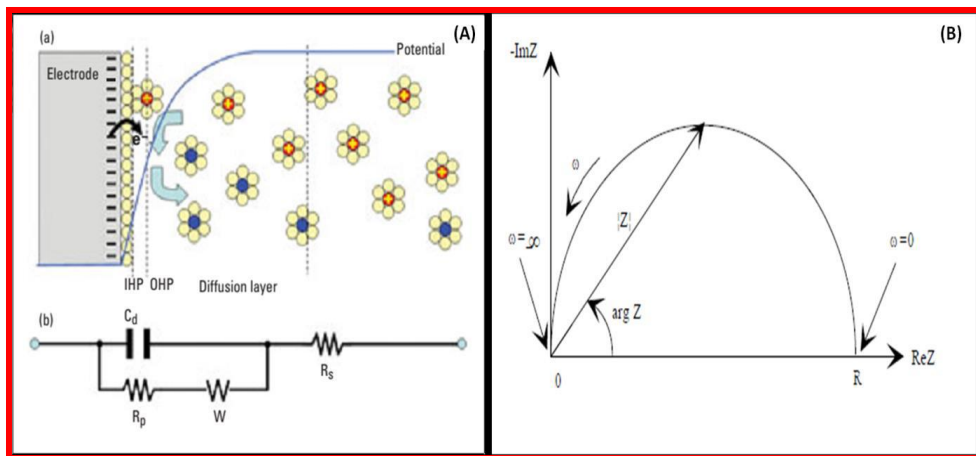


Fig.2.13 (A) Electrode-electrolyte interface separated by layers with dotted line represents electronic components and (B) Nyquist plot with impedance vector.

References:

1. M. Gratzel, J. Photochem. Photobiol., C, **4** (2003), 145-153.
2. M. K. L. Tenorio, C. S. Ferreira, Q. H. Rebelo, R. F. Souza, R. R. Passos, E. A. Pineda, L. A. Pocriška, Mater. Res. **21** (2018), e20170521-e20170528.
3. K. Wetchakun, T. Samerjai, N. Tamaekong, C. Liewhiran, C. Siri Wong, V. Kruefu, A. Wisitsoraat, A. Tuantranont, S. Phanichphant, Sens. Actuators, B **160** (2011), 580–591.
4. J. S. Becker, S. Suh, S. Wang, R. G. Gordon, Chem. Mater. **15** (2003), 2969-2976.
5. J. Yang, H. Liu, W. N. Martens, R. L. Frost, J. Phys. Chem. C **114** (2010), 111–119.
6. J. Zhao, J. Wu, B. Li, W. Du, Q. Huang, M. Zheng, H. Xue, H. Pang, Prog. Nat. Sci., **26** (2016) 237-242.
7. D. Barreca and C. Massignan, Chem. Mater. **13** (2001), 588-593.
8. https://serc.carleton.edu/research_education/geochemsheets/techniques/XRD.html
9. Y. Liu, W. Wei, K. Hsu, and W. Ho, Thermochim. Acta, **412** (2004), 139–147.
10. I. V. Simiti, U. T. Napoca, I. Chicinas, G. Batin, Rom. Journ. Phys., **49** (2004), 955–965.
11. https://en.wikipedia.org/wiki/Contact_angle
12. B. R. Sankapal, R. S. Mane, C. D. Lokhande, Mater. Res. Bull. **35** (2000) 177–184.
13. P. K. Katkar, S. J. Marje, S. S. Pujari, S. A. Khalate, A. C. Lokhande, U. M. Patil, ACS Sustainable Chem. Eng. **7** (2019), 11205–11218.
14. P. P. Chandra, A. Mukherjee, P. Mitra, J. Mater., **2014** (2014), 56-62.
15. M. Ristov, G. J. Sinadinovski, I. Grozdanov, M. Mitreski, Thin Solid Films **149** (1987) 65-94.
16. Y. F. Nicolau, J. C. Menard, J. Cryst. Growth **92** (1988) 128-142.
17. H. M. Pathan and C. D. Lokhande, Bull. Mater. Sci., **27** (2004), 85–111.
18. <https://www.elsevier.com/books/handbook-of-hydrothermal-technology/byrappa/978-0-12-375090-7>
19. K. Byrappa and T. Adschiri, Prog. Cryst. Growth Charact. Mater. **53** (2007) 117-166.
20. M. Yoshimura and K. Byrappa, J. Mater. Sci. **43** (2008) 2085–2103.
21. R. I. Walton, Chem. Soc. Rev., **31** (2002), 230–238.
22. A. Rabenau, Angew. Chem. Int. Ed. Engl. **24** (1985), 1026–1040.
23. P. Shanbogh, D. Swain, C. Narayana, A. Rao, N. G. Sundaram, Cryst. Growth Des. **18** (2018), 1935-1939.
24. C. Giannini, M. Ladisa, D. Altamura, D. Siliqi, T. Sibillano, L. D. Caro, Cryst. **6** (2016), 87-110.
25. D. M. Moore, R. C. Reynolds, Oxford University Press: Oxford, Clay Miner., **25** (1989) 543-545.
26. C. Berthomieu, R. Hienerwadel, Photosynth. Res. **101** (2009), 157–170.
27. S. Konwer, R. Boruah, S. K. Dolui, J. Electron. Mater., **40** (2011), 2248-2255.
28. http://www.c.in/meesa/SEM/tutorial/SEM_MS.pdf
29. <http://www.psgtech.edu/coeindutech/3.%20Testing%20Capabilities/FESEM.pdf>
30. https://www.google.com/search?q=FESEM+instrument&tbm=isch&ved=2ahUKEwjvhpGjkszpAhXhG7cAHZjDDKoQ2-cCegQIABAA#imgsrc=r9fObOM3_mZ96M
31. A. Marmur, C. D. Volpe, S. Siboni, A. Amirfazli, J. W. Drelich, Surf. Innovations, **5** (2017) 1-24.
32. M. M. Vadiyar, S. C. Bhise, S. K. Patil, S. S. Kolekar, A. R. Shelke, N. G. Deshpande, J. Y.

- Chang, K.S. Ghule, A.V. Ghule, J. Chem. Comm. **52** (2016), 2557-2560.
33. K.S.W. Sing, Adv. Colloid Interface Sci., **3** (1998), 76-77.
34. M.Naderi, Progress in Filtration and Separation., (2015), 585-608.
35. https://en.wikipedia.org/wiki/X-ray_photoelectron_spectroscopy
36. <https://www.phl.com/surface-analysis-techniques/xps-esca.html>
37. S. Ramesh, K. Karuppasamy, H. S. Kim, H. S.Kim, J.H. Kim, Sci. Rep. **8** (2018) 16543-16553.
38. J. Zhu, W. Zhou, Y. Zhou, X. Cheng, J. Yang, J. Electron. Mater., **48** (2019) 1531–1539.
39. P.T.Kissinger, W.R. Heineman, J. Chem. Educ., **60** (1983), 702-706.
40. A.Gabino and Carriedo, J. Chem. Educ. **65** (1988), 1020-1022.
41. N. Elgrishi, K. J. Rountree, B. D. McCarthy, E. S. Rountree, T. T. Eisenhart, J. L. Dempsey, J. Chem. Educ. **95** (2018) 197–206.
42. [https://chem.libretexts.org/Bookshelves/Analytical_Chemistry/Supplemental_Modules_\(Analytical_Chemistry\)/Instrumental_Analysis/Cyclic_Voltammetry](https://chem.libretexts.org/Bookshelves/Analytical_Chemistry/Supplemental_Modules_(Analytical_Chemistry)/Instrumental_Analysis/Cyclic_Voltammetry)
43. Y.Wang, Y. Song, Y. Xia, Chemical Society Reviews, **45** (2016), 5925–5950.
44. <https://pubs.rsc.org/en/content/articlehtml/2015/ra/c4ra17132b>
45. B. E. Conway, Springer, Electrochemical Supercapacitors, (1999) 221-257.
46. <https://www.gamry.com/application-notes/EIS/basics-of-electrochemical-impedance-spectroscopy/>
47. A.J. Bard, L.R. Faulkner, Electrochemical Methods: Fundamentals and Applications, 2nd Edition, Wiley Interscience Publications (2000), 864.

Chapter-3
Synthesis, Characterization and
Supercapacitive Performance
Evaluation of Graphene
Oxide/Samarium Sulfide
Composite Thin Film

Sr.no.	Title		Page no.
3.A	SECTION – A.1 <i>Synthesis of Samarium Sulfide (Sm₂S₃) Thin Film Using Hydrothermal Method</i>		50
	3.A.1	<i>Introduction</i>	51
	3.A.1.1	<i>Substrate Cleaning</i>	51
	3.A.1.2	<i>Experimental Setup For Deposition of Samarium Sulfide (Sm₂S₃) Thin Films</i>	52
	3.A.1.3	<i>Material Characterization</i>	52
	3.A.1.4	<i>Results and Discussion</i>	53
		(A) <i>Samarium Sulfide (Sm₂S₃)Thin Film Formation and Reaction Mechanism</i>	53
		(B) <i>XRD Study</i>	54
		(C) <i>FE-SEM Study</i>	55
		(D) <i>Surface Wettability Study</i>	56-57
		(E) <i>UV-Visible Spectroscopy Study</i>	58
		(F) <i>BET Study</i>	59
		(G) <i>XPS Study</i>	60
	SECTION-A.2 <i>Supercapacitive Performance Evaluation of Samarium Sulfide thin films</i>		
3.A.2	<i>Introduction</i>		61
	3.A.2.1	<i>Experimental setup for supercapacitive studies</i>	62
	3.A.2.2	<i>Result and Discussion</i>	63
		(A) <i>Cyclic voltammetry (CV) study</i>	64
		(B) <i>GCD studies</i>	64
		(C) <i>Stability studies</i>	65
		(D) <i>EIS studies</i>	65-66
	SECTION-B.1 <i>Synthesis of Graphene Oxide/Samarium Sulfide (GO/Sm₂S₃) Composite Thin Film Using SILAR Method</i>		
3.B.1	<i>Introduction</i>		67
	3.B.1.1	<i>Experimental Setup of Graphene Oxide/Samarium Sulfide (GO/Sm₂S₃)</i>	68
	(a)	<i>Synthesis of Graphene Oxide by Modified Hummers method</i>	68
	(b)	<i>Synthesis of Graphene Oxide Thin Film</i>	69
	(c)	<i>Synthesis of Samarium Sulfide (Sm₂S₃) Thin</i>	69
	(d)	<i>Synthesis of Graphene Oxide/Samarium Sulfide (GO/Sm₂S₃) Composite Thin Film</i>	70
	3.B.1.2	<i>Result and Discussion</i>	71
		(A) <i>Graphene Oxide/Samarium Sulfide (GO/Sm₂S₃) Composite Thin Film Formation and Reaction</i>	71

			<i>Mechanism</i>	
		(B)	<i>XRD Study</i>	72
		(C)	<i>FT-IR Study</i>	72
		(D)	<i>FE-SEM Study</i>	73-74
		(E)	<i>Surface Wettability Study</i>	75
		(F)	<i>BET Study</i>	76
	<p style="text-align: center;">SECTION-B.2 <i>Supercapacitive Performance Evaluation of Graphene Oxide/Samarium Sulfide (GO/Sm₂S₃) Composite Thin Films</i></p>			
3.B.2	<i>Introduction</i>			77
	3.B.2.1	<i>Experimental set up for Supercapacitive Studies</i>		78
	3.B.2.2	<i>Result and Discussion</i>		78
		(A)	<i>Cyclic voltammetry (CV) study</i>	78
		(B)	<i>GCD studies</i>	79
		(C)	<i>Stability studies</i>	80
		(D)	<i>EIS studies</i>	81-82
3.5	<i>Conclusions</i>			83
	<i>References</i>			84-85

Section-A.1

3. A. Synthesis of Samarium Sulfide (Sm_2S_3) Thin Films Using Hydrothermal Method-

The present section A.1 deals with the synthesis and characterization of samarium sulfide (Sm_2S_3) by hydrothermal method and samarium sulfide/graphene oxide ($\text{Sm}_2\text{S}_3/\text{GO}$) composite thin films using successive ionic layer adsorption and reaction (SILAR) method and their supercapacitive evaluation in aqueous electrolytes. In the Sections 3.A.1 and 3.B.1, synthesis of Sm_2S_3 and $\text{Sm}_2\text{S}_3/\text{GO}$ composite thin films by hydrothermal and SILAR methods respectively have been carried out and films are characterized using different characterization techniques. Sections '3.A.2' and '3.B.2' deal with the supercapacitive evaluation of films deposited by hydrothermal and SILAR methods, respectively.

3. A.1 Introduction:

The current section deals with synthesis and characterization of Sm_2S_3 thin film by hydrothermal method. The rare earth metal chalcogenides show attractive physical and chemical properties with respect to their potential applications [1]. The existence of samarium sulfide (Sm-S) system in different phases such as SmS, $\alpha\text{-Sm}_2\text{S}_3$, Sm_3S_4 , Sm_2S_5 etc. depends upon the synthesis parameters such as concentration, temperature and methodology [2]. Recently, in the literature surveys, rare earth based chalcogenides synthesized by different chemical methods are used in energy storage device such as supercapacitor. Kumbhar et al [3] synthesized $\alpha\text{-Sm}_2\text{S}_3$ thin film by SILAR method and used as an electrode in supercapacitor study. Also, Kumbhar et al [4] synthesized Sm_2S_3 thin film by chemical bath deposition (CBD) method and tested supercapacitor properties in 1 M $\text{LiClO}_4\text{-PC}$ electrolyte. However, there is no report on Sm_2S_3 synthesis by hydrothermal method and its supercapacitor application.

In present work, inexpensive hydrothermal method for used to synthesis of porous nano-grains like Sm_2S_3 thin film on stainless steel substrate. The XRD, SEM, FT-IR, contact angle, BET and XPS analyses of Sm_2S_3 thin film are carried out. The Sm_2S_3 film is used for supercapacitor performance testing in aqueous 1 M Na_2SO_4 electrolyte.

3. A.1.1 Substrate Cleaning

Substrate cleaning is very significant for obtaining good quality thin films as the stainless steel substrate surface provides nucleation centers which results in growth of thin films. The conducting substrate is a primary requirement for supercapacitors. The stainless steel (SS) used because of many good features (a) it has highly conducting and (b) it is easily available, low cost and eco friendly.

The SS substrates were cleaned using following procedure:

- The SS substrates were first cleaned with double distilled water (DDW), followed by ultrasonication in DDW, acetone and ethanol for 20 min and,
- Finally, the SS substrates were dried in an oven and used for the film deposition.

3. A.1.2 Experimental Setup for Deposition of Samarium Sulphide (Sm_2S_3) Thin Films by Hydrothermal Method-

In order to synthesize Sm_2S_3 thin film, the cationic precursor for samarium (**A**) 0.1 M ($\text{SmCl}_3 \cdot 6\text{H}_2\text{O}$) solution was prepared in 20 ml DDW under stirring. To this solution, 0.1 M tartaric acid ($\text{C}_4\text{H}_6\text{O}_6$) solution prepared in DDW was added under continuous stirring to get the pH value of 2 ± 0.1 . The anionic precursor for sulphide ion (S^{2-}) source was (**B**) 0.2 M sodium thiosulfate ($\text{Na}_2\text{S}_2\text{O}_3 \cdot x\text{H}_2\text{O}$) 20 ml solution in DDW. Both solutions were mixed in equal ratio in a glass beaker. Well cleaned SS substrates were dipped in the solution (**C**) and the beaker was kept at

393 K for 1 h under pressure 17×10^{-5} Psi in a teflon lined sealed stainless steel autoclave (D) as shown in **Fig.3.1**. The precipitation started in the bath and Sm_2S_3 thin film was formed on the SS substrate [E]. The thickness of Sm_2S_3 film was measured by weight difference method using sensitive microbalance. The loading Sm_2S_3 on SS was $0.4 \mu\text{g cm}^{-2}$.

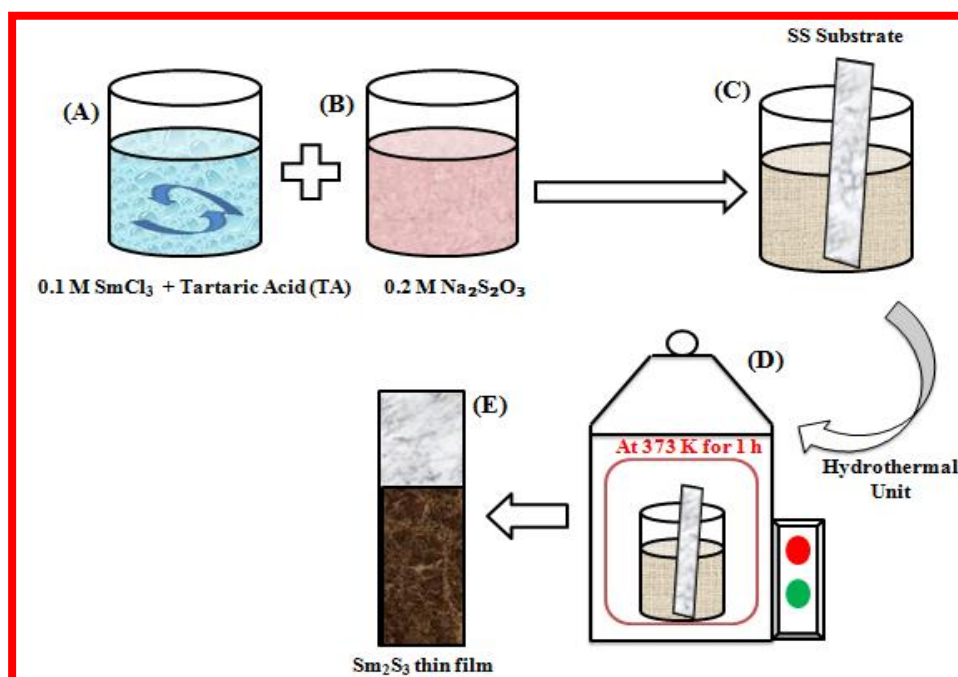


Fig. 3.1 Schematic diagram of Sm_2S_3 thin film deposition by hydrothermal method.

3. A.1.3 Material Characterization:

The crystal structure of Sm_2S_3 film was examined using a Bruker AXS D8 advance model X-ray diffractometer with primary monochromatic radiation from Cu K α line ($\lambda = 1.54 \text{ \AA}$) in the 2θ range of 20 – 80° . The X-ray photoelectron spectroscopy (XPS) data was analyzed for identifying chemical composition and oxidation states of Sm_2S_3 thin film using ESCALAB 250Xi X-ray photoelectron spectrometer microprobe. The surface morphology was observed using field emission scanning electron microscope (FE-SEM, JEOL-6360, Japan). The wettability test was conducted by contact angle measurement (water as a solvent) using Rame-Hart NRL CA Goniometer. The

specific surface area and porosity were measured by the Brunauer-Emmett-Teller (BET) and the pore size distribution was measured from the adsorption curve by the Barrette-Joyner- Halenda (BJH) method. The optical band gap of the material was determined from UV-vis spectrophotometer of Agilent Technologies Cary 60 model in the wavelength range of 200 to 800 nm. Electrochemical measurements of Sm_2S_3 thin film were carried out using Zive MP1 model of Wonatech Company using three electrode cell, which consists Sm_2S_3 thin film as a working electrode, platinum strip as a counter electrode and the saturated calomel electrode (SCE) as reference electrode.

3. A.1.4 Results and Discussion-

A) Samarium Sulfide Thin Film Formation and Reaction Mechanism-

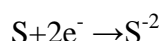
The Sm_2S_3 thin films were prepared by hydrothermal method by immersing SS substrate into beaker containing Sm^{+3} and S^{-2} precursor solutions. The growth mechanism of Sm_2S_3 thin film during deposition at the nucleation sites on the substrate results into formation of uniform and adherent thin film. The film formation process contributes two important steps, as initial nucleation followed by the crystal growth process. In film formation process, nucleation on substrate surface takes place and further growth of nucleation sites create clusters due to the decomposition of metal complex molecules. The Sm_2S_3 thin film formation by the hydrothermal method can be explained as follows. In aqueous acidic pH region SmCl_3 provides Sm^{+3} ions and $\text{Na}_2\text{S}_2\text{O}_3$ provides S^{-2} ions. The SS substrate is dipped in this solution and kept at 393 K for 1 h in a hydrothermal autoclave. At this temperature, Sm^{+3} and S^{-2} ions react onto the SS surface due to an attractive force between ions in the solution and substrate surface. Further, the chemical reaction between Sm^{+3} and S^{-2} ions leads to the formation of adherent Sm_2S_3 thin film. The SmCl_3 precursor was complexed with tartaric acid (TA) to give Sm^{+3} tartaric acid complexed ions as [5],



$\text{Na}_2\text{S}_2\text{O}_3$ dissociate in water as,



The electrons released from (3.4) react with sulphur from (3.3), as



When cations ($\text{Sm}(\text{C}_4\text{H}_6\text{O}_6)^{+3}$) and anions (S^{2-}) are formed the reaction between $\text{Sm}(\text{C}_4\text{H}_6\text{O}_6)^{+3}$ ions and S^{2-} ions takes place on SS substrate and Sm_2S_3 thin film is formed as,

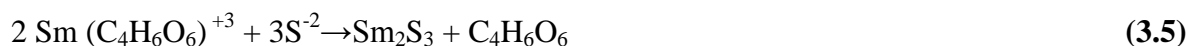


Table no.1: Optimized parameters are given below.

Sr.no.	Parameters	Values
1.	Concentration	0.1 M samarium trichloride ($\text{SmCl}_3 \cdot 6\text{H}_2\text{O}$), 0.1 M tartaric acid ($\text{C}_4\text{H}_6\text{O}_6$) 0.2 M sodium thiosulfate ($\text{Na}_2\text{S}_2\text{O}_3 \cdot x\text{H}_2\text{O}$).
2.	Temperature	393 K
3.	Time	1 hr
4.	Pressure	17×10^{-5} Psi
5.	pH	2 ± 0.1

B) XRD Study-

Fig.3.2 shows X-ray diffraction pattern of samarium sulfide thin film. The characteristic diffraction peaks are indexable to orthorhombic samarium sulfide crystal structure. The peaks at $2\theta = 20.03, 23.81, 29.72, 31.14, 47.68$ and 50.75° are attributed to the basal planes of (103), (011), (220), (150), (141), (008) and (332), respectively to Sm_2S_3 (JCPDS Card no.44-1259, 81-1436, 86-0659, 21-1069). Kumbhar et al [3, 4] synthesized samarium sulfide thin film by SILAR and CBD methods and obtained $\alpha\text{-Sm}_2\text{S}_3$ phase with orthorhombic crystal structure. The broader and intense

peaks shown by an asterisk (*) in XRD pattern (**Fig.3.2**) are due to SS substrate. Using Scherrer formula the crystallite size of 54 nm is calculated for (220) plane.

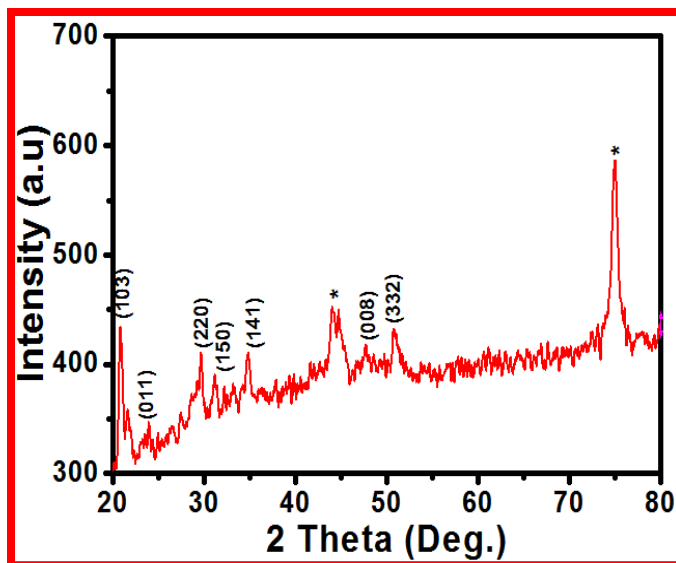


Fig. 3.2: The X-ray diffraction pattern of Sm_2S_3 thin film.

C) FTIR Study-

Fig.3.3 shows the FTIR spectrum of Sm_2S_3 thin film in the range of $600\text{--}4000\text{ cm}^{-1}$. It reveals the chemical information and major functional groups existing in Sm_2S_3 material. The presence of different types of oxygen functionalities in Sm_2S_3 thin film is confirmed. Broad and wide peak at 3448.37 cm^{-1} is attributed to the OH^- symmetric stretching vibrations [6]. The narrow and strong absorption band at 674.69 cm^{-1} is assigned to the pairing mode between Sm-S stretching of tetrahedral sites. The absorption peaks at 873.88 , 1016.24 , 1201.41 , 1407.59 and 1584.98 cm^{-1} are associated with vibrations mode of C-C aromatics and C-O carboxyl groups [7]. The band at 2317.23 cm^{-1} is attributed to vibration of the surface adsorbed OH^- molecules and carbonate ions present in atmosphere on Sm_2S_3 . These characteristic bands confirm the formation of Sm_2S_3 material.

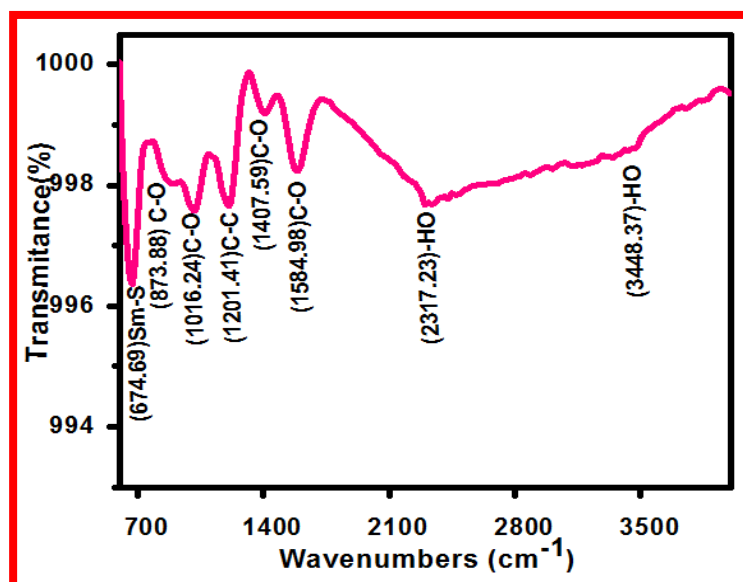


Fig. 3.3: FT-IR spectrum of Sm_2S_3 thin film.

D) FE-SEM Study-

The surface morphology of Sm_2S_3 thin film at three different magnifications (5 kX, 15 kX and 50 kX) taken with scanning electron microscope (SEM) is shown in **Fig.3.4 (a-c)**. It clearly shows formation of non uniform spherical grains consisting of nanocrystallites distributed all over the substrate. At 5 kX magnification, agglomerations of different sized nanocrystallites forming spherical micro-grains of typical diameters around 1.24 μm are seen. At 15 kX magnification, spherical grains of different diameters are observed. **Fig.3.4 (c)** shows micrograph at 50 kX magnification with typical micro grains of 1.16 μm diameters. The agglomerated porous morphology is due to the formation of irregular spherical micro grains. Such porous surface morphology provides easy path for ions during redox reaction, thereby increasing the charge ability of an electron [8, 9].

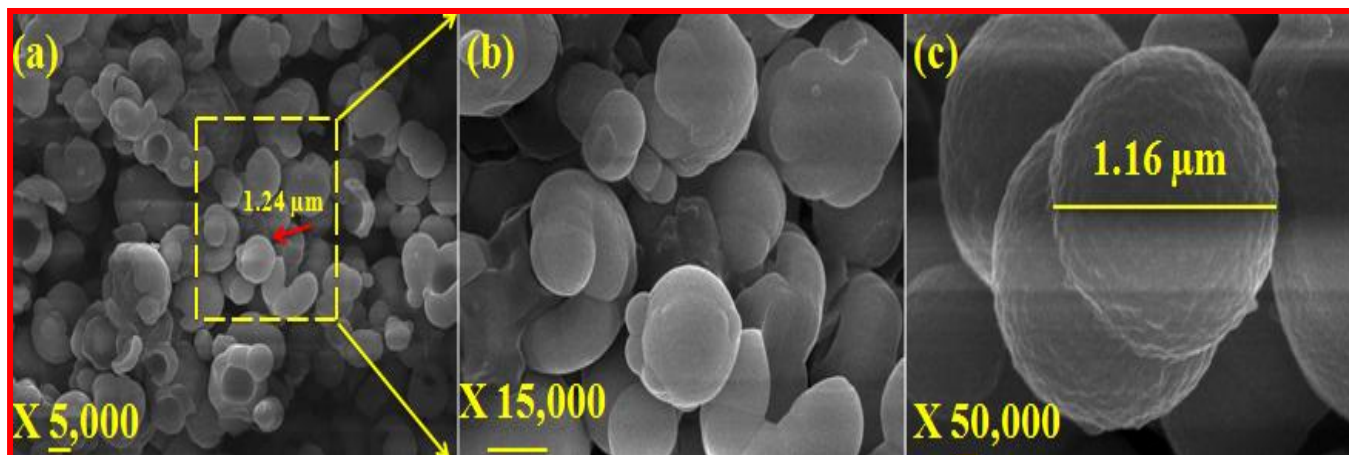


Fig. 3.4: FE-SEM images of Sm₂S₃ thin film at (A) 5 kX, (B) 15 kX, and (C) 50 kX magnifications.

E) Surface Wettability Study -

The wettability of Sm₂S₃ thin film was measured from contact angle study as shown in **Fig.3.5**. The contact angle of 81.3° represents the hydrophilic characteristic. For energy storage application, with contact angle less than 90°, the film surface is said to be hydrophilic [10]. The hydrophilic nature of film surface allows more interaction of electroactive sites of Sm₂S₃ thin film with electrolyte ions which is desirable for supercapacitor application [11]. Kumbhar et al [3] prepared α-Sm₂S₃ thin film by SILAR method and reported contact angle of 45° for the porous surface.

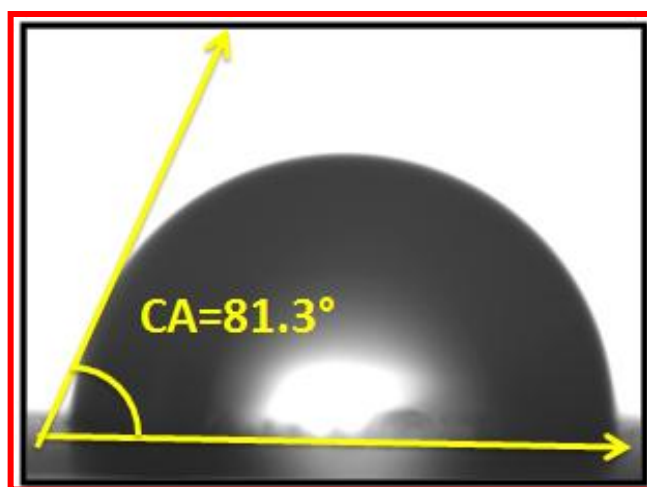


Fig. 3.5: Contact angle of Sm₂S₃ thin film.

F) Uv-Visible Spectroscopy-

Optical absorbance of Sm_2S_3 powder is recorded in the wavelength range 200 to 800 nm by Uv-visible spectroscopy technique in order to determine band gap (E_g) [12]. **Fig.3.6** shows plot of the $(\alpha h\nu)^2$ vs. $h\nu$ and inset shows absorbance (α) with wavelength (λ). The sharp increase in absorption at low wavelength side is attributed to its wide band gap. The estimated direct band gap is 2.90 eV for Sm_2S_3 thin film. Kumbhar et al [3] obtained band gap is 2.50 eV for $\alpha\text{-Sm}_2\text{S}_3$ thin film prepared by SILAR method.

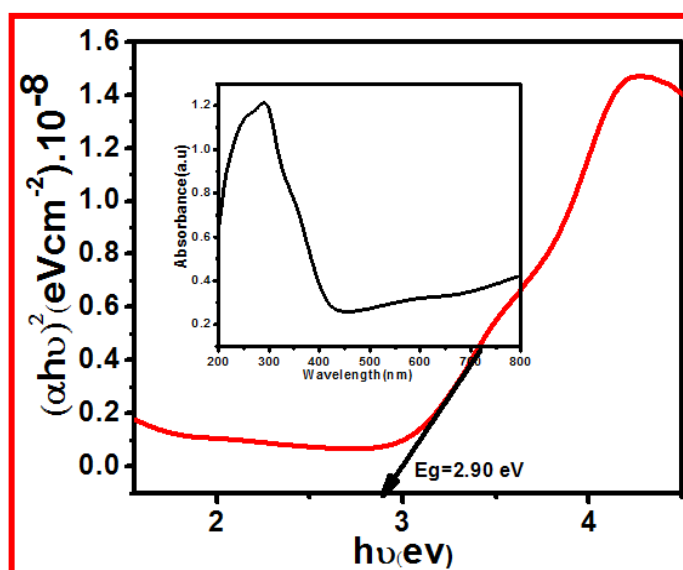


Fig. 3.6: Plot of the $(\alpha h\nu)^2$ vs. $h\nu$ and inset shows absorbance vs. wavelength graph of Sm_2S_3 thin film.

G) Brunauer–Emmett–Teller (BET) Study-

Brunauer–Emmett–Teller (BET) measurement was used to determine the surface area of Sm_2S_3 powder scratched from thin film sample. **Fig.3.7** shows the N_2 adsorption–desorption isotherm of Sm_2S_3 powder [13]. The narrow hysteresis loop at low and higher relative pressures indicate that the porous structure is quite open and there is no considerable delay in the capillary evaporation with respect to the capillary condensation of nitrogen. A distinct hysteresis loop observed in the range of ca. 0.1–1.0 P/P₀ might be attributed to the existence of a micro porous

structure. The curve in inset **Fig. 3.7** shows Barrett-Joyner-Halenda (BJH) pore size distribution of Sm_2S_3 powder which is a feature of micro grains porous materials. The presence of a pore size structure comprises of 12.2 nm. The surface area is calculated by Brunauer, Emmett and Teller (BET) equation using software [14],

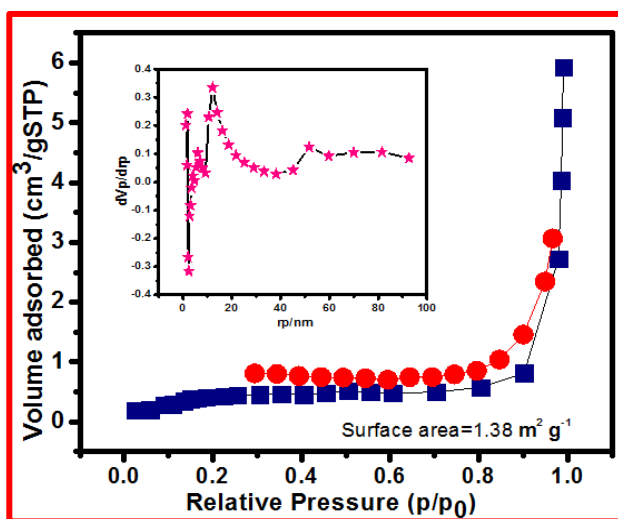


Fig. 3.7: Nitrogen adsorption-desorption isotherms and inset shows pore size distribution curve for Sm_2S_3 film powder.

$$\frac{1}{[V_a(\frac{P_0}{P}-1)]} = \frac{c-1}{Vmc} \times \frac{P}{P_0} \times \frac{1}{Vmc} \quad (3.7)$$

Where, P is partial vapour pressure of adsorbate gas in equilibrium with the surface at 77.4 K (b.p. of liquid nitrogen), in Pascal, P_o is saturated pressure of adsorbate gas, in Pascal, V_a is volume of gas adsorbed at standard temperature and pressure (STP) [273.15 K and atmospheric pressure ($1.013 \times 10^5 \text{ Pa}$) in milliliters], V_m is volume of gas adsorbed at STP to produce an apparent monolayer on the sample surface in milliliters and C is dimensionless constant related to the enthalpy of adsorption of the adsorbate gas on the powder sample. The calculated surface area is $1.38 \text{ m}^2 \text{ g}^{-1}$.

H) XPS Study-

The XPS is one of the fundamental techniques to detect the chemical composition of surface species and surface electronic states of deposited film powder. **Fig.3.8** shows the XPS spectra of Sm_2S_3 thin film powder. The atomic composition of the sample contained samarium (Sm) and sulfur (S), as expected. The chemical state of Sm_2S_3 undergoes a semiconductor-metal transition under influence of pressure, but can also be metallic as such as a function of preparation condition. In the semiconducting state of Sm is in a 3^+ state and S is in a metallic state 2^+ state. The chemical states of Sm in Sm_2S_3 shown in **Fig. 3.8 (a)** indicate two peaks at the binding energies of 1083.17 and 1110.12 eV. The peak observed at 1083.17 eV corresponds to Sm^{+3} states. The state of S2p present in Sm_2S_3 is shown in **Fig.3.8 (b)**. The binding energy peak at 162.2 eV corresponds to S^{2-} sulfide state of Sm_2S_3 . The peak at 168.5 eV belongs to the existence of sulfur (S) layer on the film surface which is quite comparable with the results reported by kumbhar et al [3]. During deposition, few of Na^+ and S^{2-} ions recombine to form Na_2S which is further oxidized resulting into Na_2SO_4 . This phase is small enough to affect supercapacitive properties of Sm_2S_3 thin film.

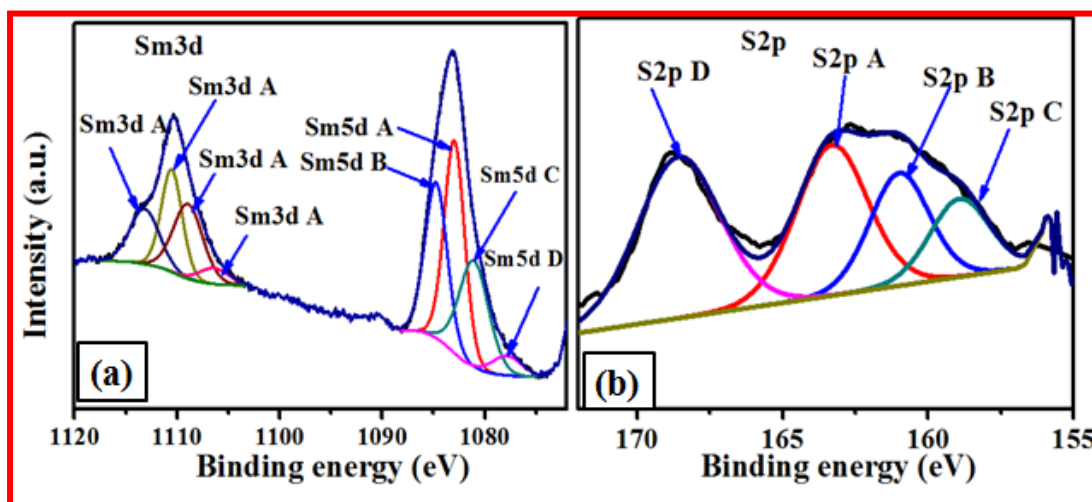


Fig.3.8: XPS spectra Sm_2S_3 thin film (a) Sm region, and (b) S region.

Section: A.2

Supercapacitive Performance Evaluation of Sm_2S_3 Thin Films

3. A.2 Introduction:

The current section-A.2 deals with the electrochemical measurements of hydrothermally prepared Sm_2S_3 thin film in 1 M Na_2SO_4 electrolyte by means of CV, GCD and EIS techniques. Further, the effect of scan rate, current density and electrochemical cycling on the electrochemical performance of Sm_2S_3 thin films is studied. In order to correlate the electrochemical properties of Sm_2S_3 thin film in 1 M Na_2SO_4 electrolyte is chosen. In present part, three-electrode cell configuration namely platinum as a counter electrode, saturated calomel electrode (SCE) as a reference and Sm_2S_3 thin film as a working electrode is used. The electrochemical properties of Sm_2S_3 thin films are examined with respect to various parameters like scan rate, specific capacitance, and cycling stability and EIS using CV, GCD and EIS technique.

3. A.2.1 Experimental Set Up for Supercapacitive Studies:

The electrochemical measurements of Sm_2S_3 thin film are carried out in a conventional three-electrode system with 1 M Na_2SO_4 as an aqueous electrolyte. The aqueous electrolytes are cheaper, easier to purify, and have a lower resistance, but they limit the cell voltage to typically 1 V, thereby limiting the maximum achievable power [15]. To build the working electrode for the electrochemical measurements, apart from 1 cm^2 area of thin film, remaining part is sealed with insulating tape. **Fig.3.9** shows photographs of (A) schematic diagram of experimental three electrode system and (B) automatic battery cycler with CV cycles graphs on the computer screen.

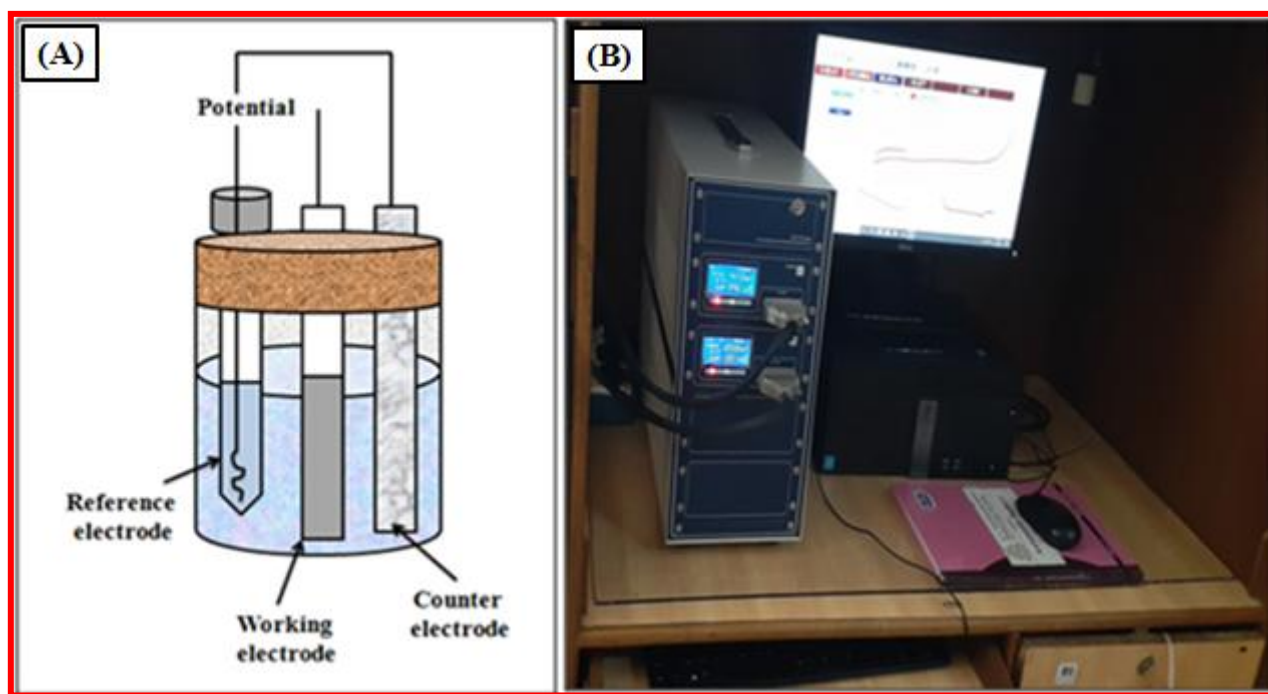


Fig.3.9: (A) Schematic diagram of three electrode system, and (B) experimental set up consisting of automatic battery cycler with CV cycles graphs on the computer screen.

3. A.2.2 Results and Discussion-

(A) Cyclic Voltammetry (CV) Study:

The CV is an important parameter for the determination of redox potentials and electron-transfer redox reactions involved [16]. The CV study was carried out within the potential window of 0 to -1 V/SCE in 1 M Na₂SO₄ at different scan rates of 5-100 mVs⁻¹, as shown in **Fig.3.10**. An electrode reaction of Sm₂S₃ in Na₂SO₄ electrolyte solution is considered as a reversible. Slightly observed redox peaks with intercalation/deintercalation of Na⁺ ion can be represented as follows,



The specific capacitance (Cs) of material is obtained from CV curves using eq.(2.9) [17]. The maximum specific capacitance of 153 Fg⁻¹ is observed at 5 mVs⁻¹.

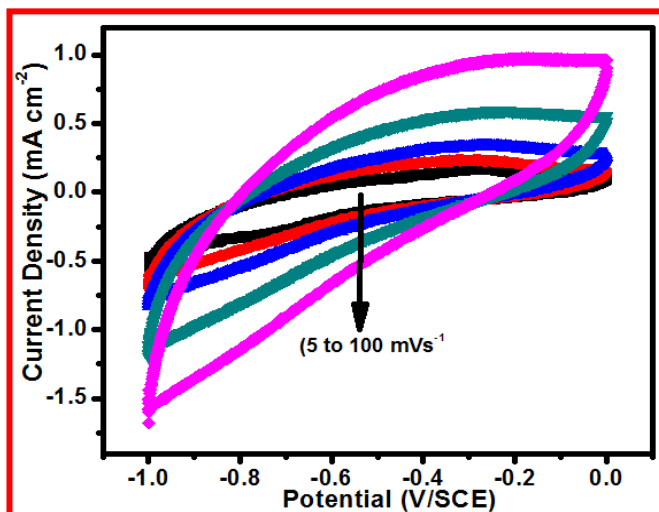


Fig.3.10: Cyclic voltammetry of Sm_2S_3 electrode at 5 to 100 mVs^{-1} scan rates.

Fig.3.11 shows the variation of specific capacitance (C_s) with scan rate. It indicates that with an increase in scan rate, specific capacitance decreases (153 to 33 Fg^{-1}). Simply, the capacitance decreased with increasing the scan rate, as at lower scan rates the electrolyte ions have sufficient time to penetrate the pores of the material, while at higher scan rates ions accumulate only on the outer surface [18, 19].

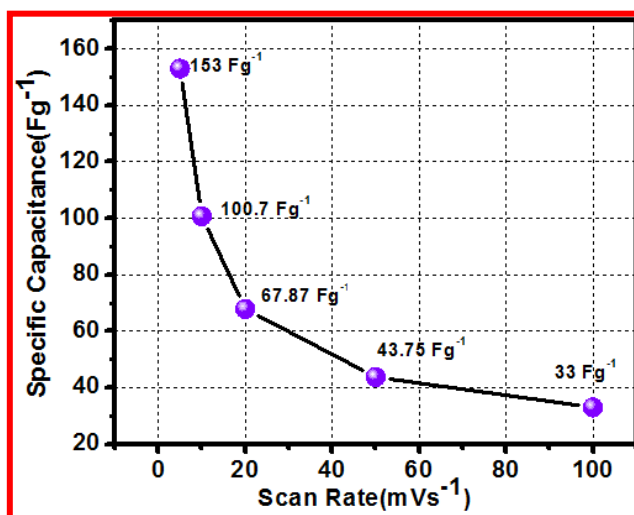


Fig.3.11: variation of specific capacitance (C_s) with scan rate of Sm_2S_3 electrode.

(B) GCD Study:

The galvanostatic charge-discharge behavior of Sm_2S_3 electrode at current densities of 0.1, 0.2 and 0.5 mA cm^{-2} is shown in **Fig.3.12**. Both the charge-discharge curves are non-symmetrical and non-linear due to the result of the combined effect of faradaic and non-faradaic reactions [20-22]. The small voltage IR-drop is related to the ohmic loss of the electrode.

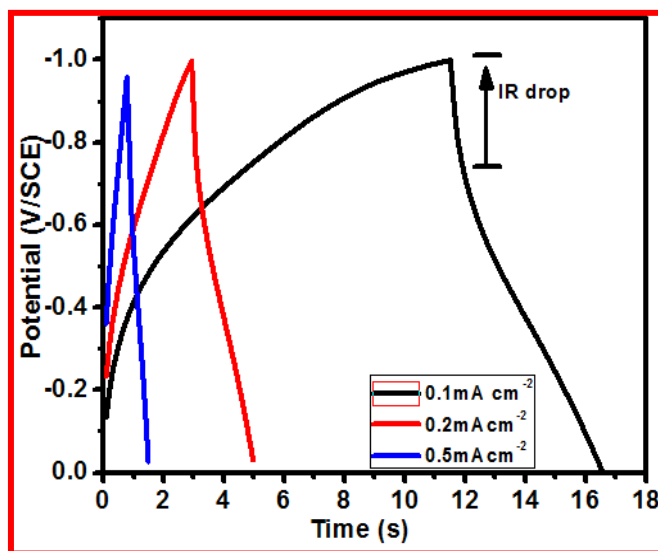


Fig.3.12: Galvanostatic charge/discharge plots of Sm_2S_3 electrode at 0.1, 0.2 and 0.5 mA cm^{-2} current densities.

(C) Stability Studies:

The better electrochemical cycling stability of electrode is a prime requirement for supercapacitor application along with superior C_s value. The cycling stabilities of Sm_2S_3 thin films studied in 1 M Na_2SO_4 at a 100 Mvs^{-2} for 1000 CV cycles, is illustrated in **Fig. 3.13**. The plots of capacity retention with respect to CV cycle number and inset of CV are shown in **Fig. 3.13**. The capacity retention for Sm_2S_3 thin films after 1000 CV cycles is 81.5 %. Inset of **Fig. 3.13** shows shape of CV curves at 2nd and 1,000th cycles. The loss in capacitance accredited to degradation of material in electrolyte solution due to porous nature of electrode surface [23].

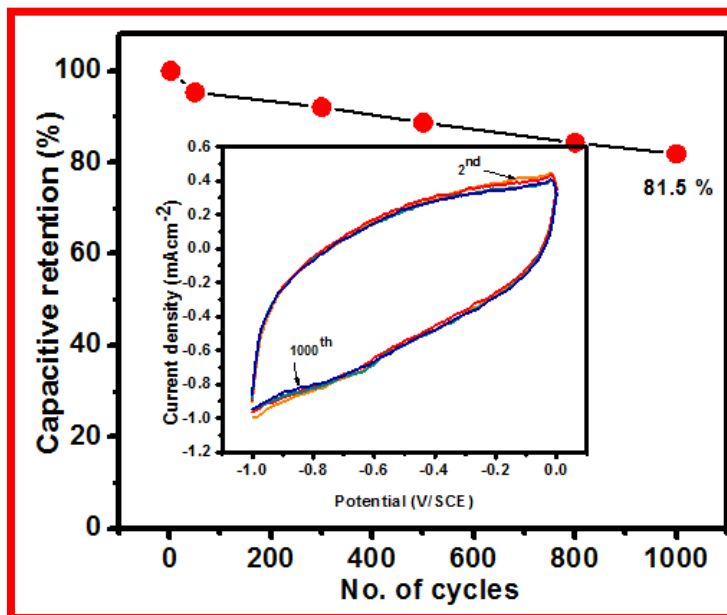


Fig. 3.13: Capacitive retention for 1,000 CV cycles at 100 mVs^{-1} scan rate and inset displays no. of CV cycles of Sm_2S_3 electrode.

(E) EIS Study:

Fig.3.14 shows the Nyquist plot of Sm_2S_3 electrode investigated using EIS technique within the frequency range of 0.1 to 10,000 Hz at 10 mV amplitude. The series resistance (R_s : $78.9 \Omega \text{ cm}^{-2}$) and charge transfer resistance (R_{ct} : $33.43 \Omega \text{ cm}^{-2}$) in the high frequency region, low Cs value [24]. In the present study, small quantity of material deposited ($0.4 \mu\text{m} \cdot \text{cm}^{-2}$) leads to high resistance of electrode and hence low Cs. Inset of figure of shows the equivalent circuit fitted for Nyquist plot in parallel combination with R_s , R_{ct} , Q and W parameters. The corresponding equivalent circuit. The solution resistance (R_s) of $78.9 \Omega \text{ cm}^{-2}$ is observed from the initial part of impedance plot in high frequency and charge transfer resistance (R_{ct}) of $33.43 \Omega \text{ cm}^{-2}$ and Warburg resistance (W) of $79.5 \Omega \text{ cm}^{-2}$ and double layer of capacitance (Q) of $0.729 \Omega \text{ cm}^{-2}$ are obtained in the low-frequency region in impedance plot. The electrochemical impedance parameters of Sm_2S_3 thin film are given in **Table 3.2**.

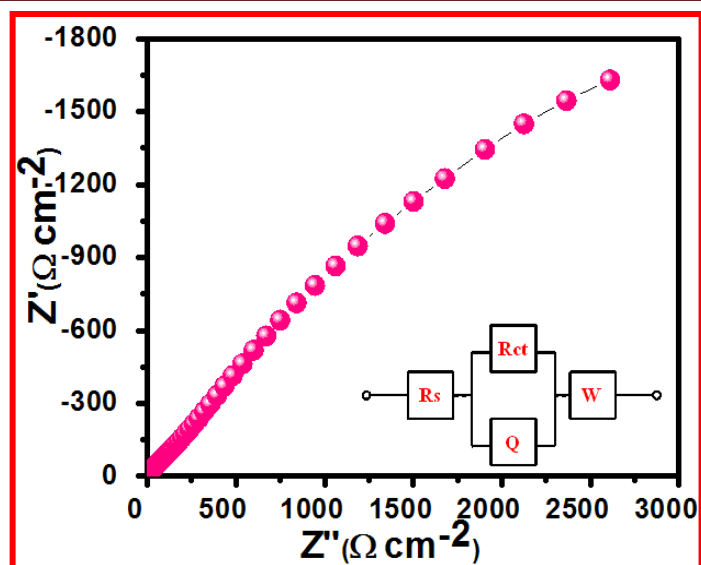


Fig.3.14: Electrochemical impedance spectroscopy (EIS) of Sm_2S_3 electrode and inset shows equivalent circuit.

Table 3.2: Obtained electrochemical parameters values of Sm_2S_3 thin film based supercapacitor.

Parameter	Value of Parameter
C_s (Fg^{-1})	153
Capacitive retention (%)	81.5
R_s ($\Omega \text{ cm}^{-2}$)	78.9
R_{ct} ($\Omega \text{ cm}^{-2}$)	33.43
Q (F)	0.729
W ($\Omega \text{ cm}^{-2}$)	79.5

SECTION: B.1

Synthesis of Samarium Sulfide and Graphene Oxide/Samarium Sulfide (GO/Sm₂S₃) Composite Thin Films Using SILAR Method-

3. B.1 Introduction:

During last three decades, successive ionic layer adsorption and reaction (SILAR) method, has emerged as one of the solution methods to deposit a variety of compound materials in thin film form. The SILAR method is inexpensive, simple and convenient for large area deposition. A variety of substrates such as insulators, semiconductors, metals and temperature sensitive substrates (like polyester) can be used since the deposition is carried out at or near to room temperature. As a low temperature process, it also avoids oxidation and corrosion of the substrate. The prime requisite for obtaining good quality thin film is the optimization of preparative provisos viz. concentration of the precursors, nature of complexing agent, pH of the precursor solutions and adsorption, reaction, rinsing time and temperature. The present section-B.1 deals with the synthesis and characterization of Sm₂S₃ and GO/Sm₂S₃ composite thin film by SILAR method. Further, the films are characterized with structural, morphological and electrochemical studies.

3. B.1.1 Experimental Setup of Graphene Oxide/Samarium Sulfide (GO/Sm₂S₃) Using SILAR Method –

(a) Synthesis of Graphene Oxide Synthesized by Modified Hummers method-

The GO was synthesized from graphite flakes using a modified Hummer's method [25]. Typically, graphite (5 g) and NaNO₃ (2.5 g) were mixed with 120 ml of H₂SO₄ (95%) in a 500 ml flask **Fig.3.15 (A)**. The mixture was stirred for 30 min in an ice bath. While vigorous stirring, KMnO₄ (15 g) was slowly added to the suspension in **Fig.3.15 (B)**. Upon addition, the ice bath was removed and the mixture was kept stirred over night at room temperature with time, the mixture gradually turned into light brownish color. The solution was stirred for 15 min and 50 ml 30% H₂O₂

was added to the mixture in **Fig3.15 (C)**. For purification, the mixture was washed with DDW for several times until pH is reached to 7.00 in **Fig.315 (D)**[26].

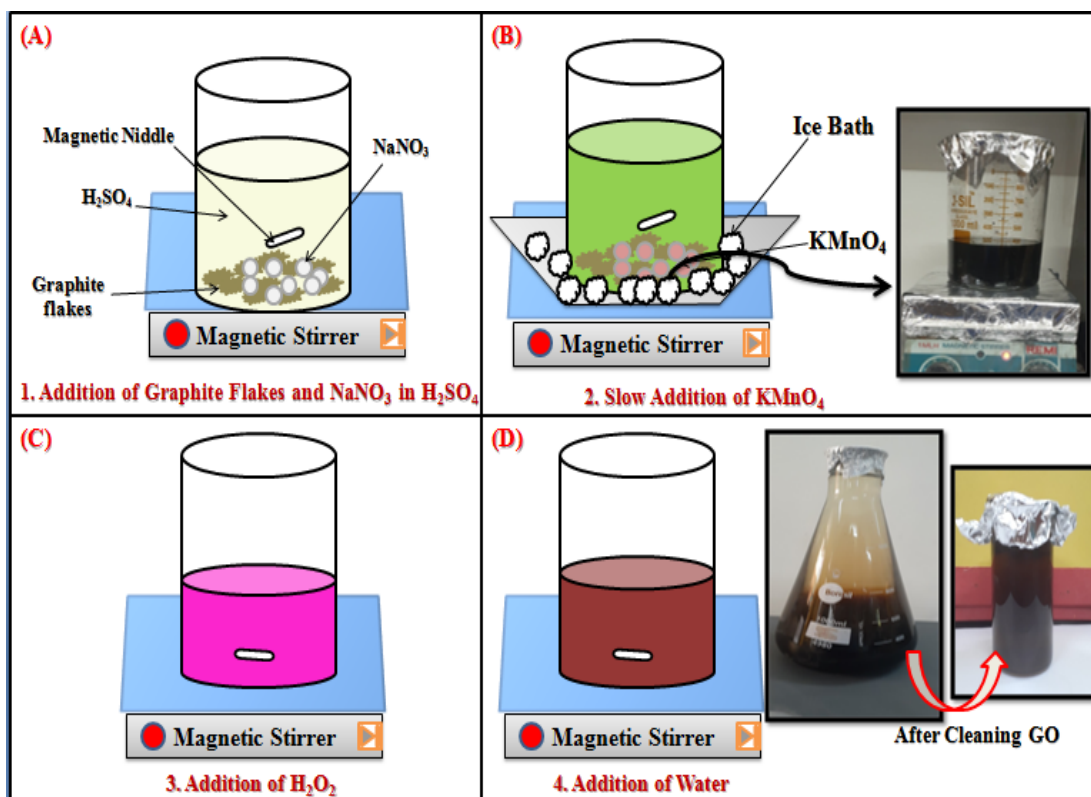


Fig. 3.15 Synthesis of graphene oxide (GO) by modified Hummers method.

(b) Synthesis of Graphene Oxide Thin Film Synthesized by Layer by Layer (LBL) Method-

For the preparation of GO thin films, layer by layer (LBL) method (**Fig.3.16**) was used. The prepared GO of 1 mg ml^{-1} was exfoliated in 120 ml DDW using ultrasonic treatment for 1 h. This process provided a well-dispersed brown colored solution of GO sheets. A 40 ml GO from this solution was taken and the cleaned glass and SS substrates were dipped for 40 s, withdrawn gradually and dried with air drier for 20 s to improve the adherence of GO sheets to the substrate. Such 100 cycles were repeated to achieve the optimum thickness of GO films.

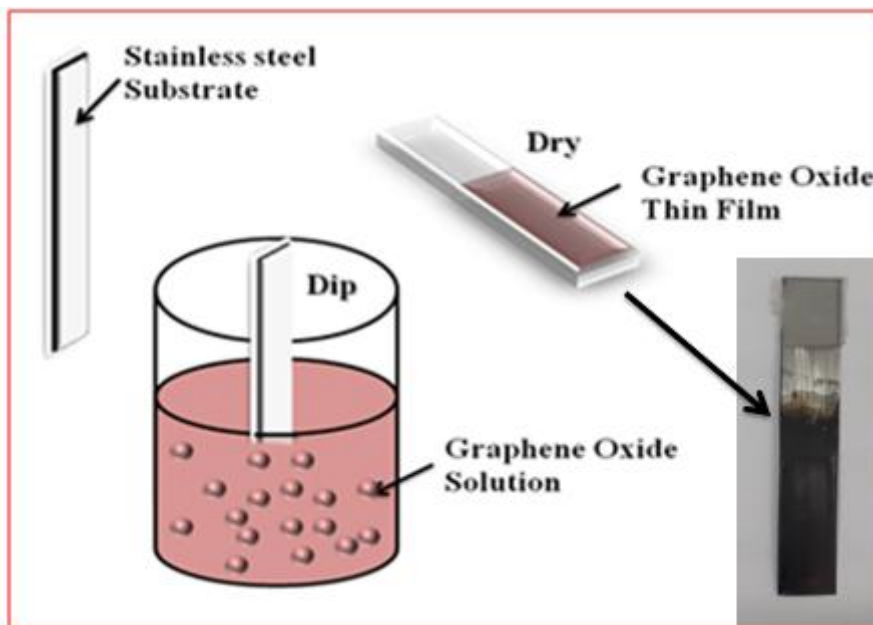


Fig.3.16: Schematic diagram deposition of GO on SS substrate by LBL method.

(c) Synthesis of Samarium Sulfide Thin Film -

The deposition of Sm_2S_3 thin film was carried out using a SILAR method. For Sm_2S_3 thin film deposition, substrate was dipped in 0.1 M samarium trichloride (SmCl_3) solution for 20 s, where cationic Sm^{+3} ions are adsorbed on substrate, followed by 10 s rinsing in DDW to remove the loosely bound species of Sm^{+3} . Then, substrate is dipped in 0.5 M sodium sulfide (Na_2S) anionic S^{-2} precursor for 20 s to form a film of Sm_2S_3 . Again, the substrate is rinsed for 10 s in DDW to take out the overloaded S^{-2} ions. In this way, one SILAR cycle of Sm_2S_3 formation is completed and 100 such deposition cycles are repeated to get the terminal thickness of Sm_2S_3 film. The SILAR deposition of Sm_2S_3 thin film is shown in **Fig.3.17**.

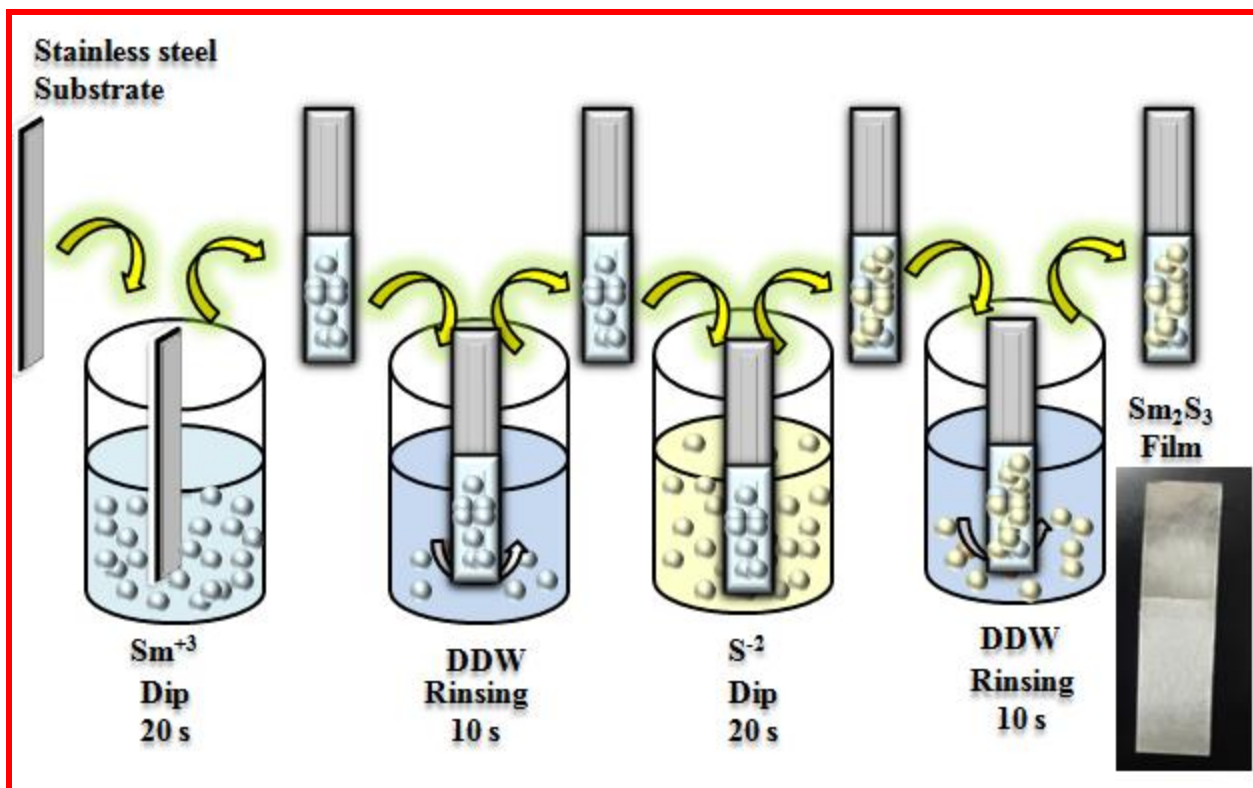


Fig.3.17: Schematic diagram for preparation of Sm_2S_3 thin film by SILAR method.

(d) Synthesis of Graphene Oxide/Samarium Sulfide ($\text{GO}/\text{Sm}_2\text{S}_3$) Thin Film-

For $\text{GO}/\text{Sm}_2\text{S}_3$ composite thin film deposition, initially substrate is dipped in solution of GO for 40 s and then air dried for 20 s for GO to deposit on substrate by LBL method. The deposition of Sm_2S_3 over GO is carried out as per above procedure to complete one cycle of $\text{GO}/\text{Sm}_2\text{S}_3$ composite and 100 such deposition cycles are repeated to obtain darkish brown colored film as shown in **Fig.3.18**. The loading of GO on stainless steel substrate is 0.069 gm.cm^{-2} and 0.083 gm.cm^{-2} in $\text{GO}/\text{Sm}_2\text{S}_3$ composite film.

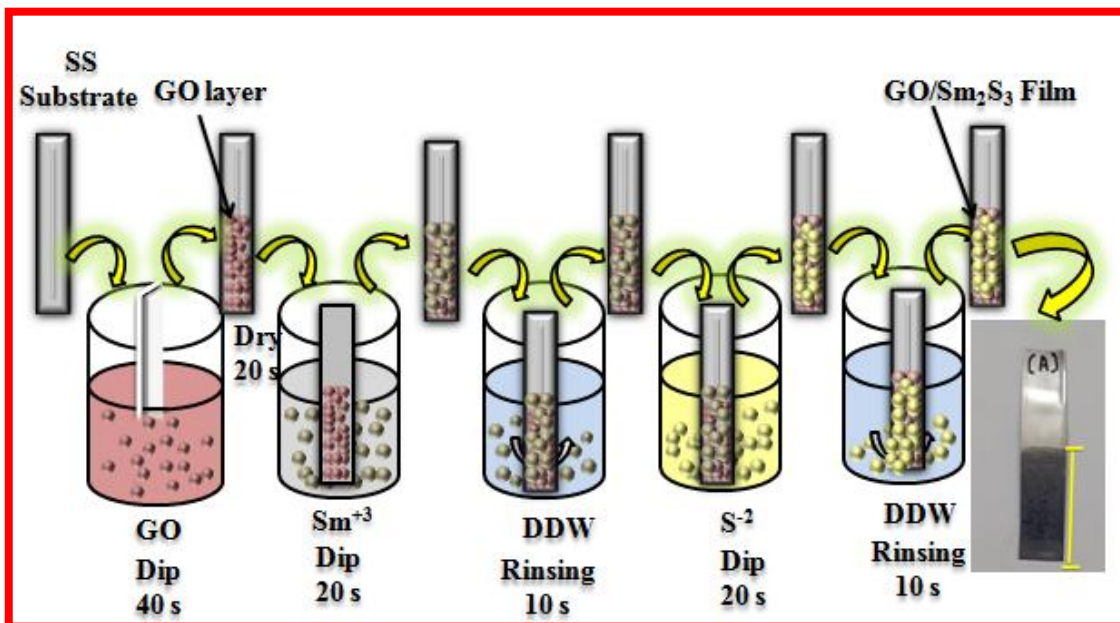


Fig.3.18: Schematic diagram for preparation of GO/Sm₂S₃ composite thin film by SILAR method.

3. B.1.2 Results and Discussion-

(A) Reaction Mechanism of GO/Sm₂S₃ Composite Thin Film-

The GO/Sm₂S₃ composite thin films were prepared by dipping the substrates in GO solution and air dried, so the GO sheets are deposited on the substrate. Subsequently, immersing the substrate in separately placed cationic and anionic precursors with rinsing between every immersion, so the ion-by-ion deposition process of Sm₂S₃ on GO sheets takes place and the layer of GO/Sm₂S₃ composite is formed on the substrate surface. The growth of Sm₂S₃ on GO sheets is on the basis of ion-by-ion mechanism, which involves the growth of nucleation sites on the GO sheets [27]. The same procedure was repeated number of times to obtain adherent and optimum film of GO/Sm₂S₃ composite. Finally, uniform and well adherent GO/Sm₂S₃ composite thin film was formed on the SS surface. Schematic diagram of the film formation of GO/Sm₂S₃ composite is shown in **Fig. 3.18**.

(B) XRD Study-

Fig.3.19 displays the X-ray diffraction (XRD) patterns of GO, Sm_2S_3 and $\text{GO}/\text{Sm}_2\text{S}_3$ composite thin films on SS substrate. The intense peak observed at $2\theta=10.0^\circ$ with (001) plane due to GO material is shown as inset **Fig.3.19 (a)** [28]. The pattern shows the strong intense peak of graphene oxide for both GO and $\text{GO}/\text{Sm}_2\text{S}_3$ composite materials. **Fig. 3.19 (b)** shows XRD pattern of Sm_2S_3 and $\text{GO}/\text{Sm}_2\text{S}_3$ material. The peaks match with (101), (103), (013), and (212) planes of orthorhombic Sm_2S_3 crystal structure (JCPDS card no. 44-1259). The peaks in XRD patterns shown by asterisk (*) are due to SS substrate.

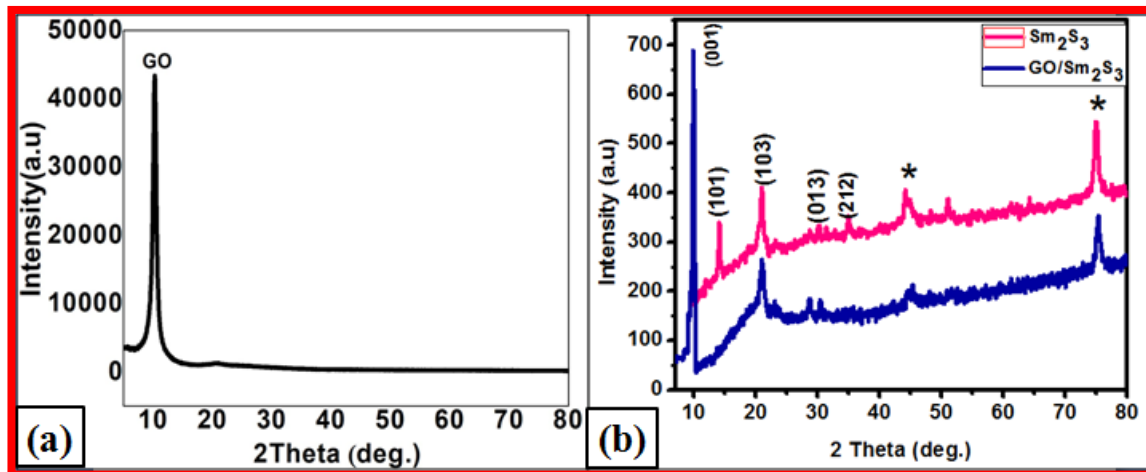


Fig. 3.19: The X-ray diffraction patterns of (a) GO and (b) Sm_2S_3 and $\text{GO}/\text{Sm}_2\text{S}_3$ composite thin films on stainless steel substrate

C) FTIR Study-

Fig. 3.20 (a-c) shows the FTIR spectra of GO, Sm_2S_3 and $\text{GO}/\text{Sm}_2\text{S}_3$ composite thin films in the range of $600\text{--}4000\text{ cm}^{-1}$. The FTIR spectra reveal the chemical information and major functional groups existing in Sm_2S_3 and $\text{GO}/\text{Sm}_2\text{S}_3$ materials. In Sm_2S_3 and $\text{GO}/\text{Sm}_2\text{S}_3$ composite thin films peaks at 3303.66 and 3291.99 cm^{-1} are attributed to the OH^- symmetric stretching vibrations. The two narrow and strong absorption bands at 636.56 and 845.85 cm^{-1} are assigned to

the pairing mode between Sm-S stretching of tetrahedral and octahedral sites in Sm_2S_3 and $\text{GO}/\text{Sm}_2\text{S}_3$, respectively. For $\text{GO}/\text{Sm}_2\text{S}_3$ composite, band intensity increases and becomes narrow. The absorption peaks at 1025.58 , 1087.04 and 1385.03 cm^{-1} are associated with vibrations mode of C-C aromatics and C-O carboxyl groups, respectively in GO in **Fig.3.20 (a)** [29]. For Sm_2S_3 , the band at 1656.56 cm^{-1} is attributed to vibrations of the surface adsorbed O-H molecules and carbonate ions present in atmosphere with Sm-S atoms. While, for $\text{GO}/\text{Sm}_2\text{S}_3$ composite spectrum, the vibrational band at 1501.73 and 1493.95 cm^{-1} of C-O carboxyl groups of GO overlaps with the vibration mode of the O-H group and carbonate ions from Sm_2S_3 in **Fig.3.20 (b, c)**. These characteristic bands confirm the formation of GO, Sm_2S_3 and $\text{GO}/\text{Sm}_2\text{S}_3$ composite thin films.

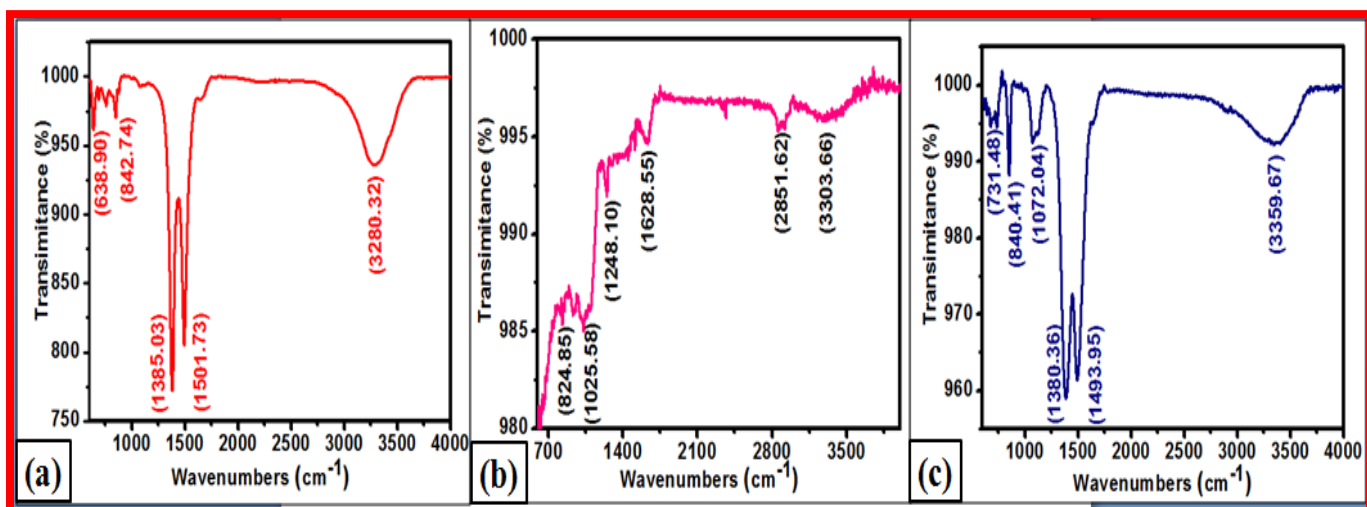


Fig. 3.20: FT-IR spectra of (a) GO, (b) Sm_2S_3 and (c) $\text{GO}/\text{Sm}_2\text{S}_3$ composite thin films.

D) FE-SEM Study-

The FE-SEM is used to study the surface morphologies of the films. The images of GO (5 and 40 kX), Sm_2S_3 (1 and 5 kX) and $\text{GO}/\text{Sm}_2\text{S}_3$ (5 and 40 kX) composite films are shown in **Fig. 3.21 (a-f)**. From micrograph image in **Fig. 3.21 (a, b)**, GO shows homogeneous layered structure. The surface morphology of Sm_2S_3 film looks like a cracked-mud (**Fig. 3.21 (c, d)**), while $\text{GO}/$

Sm₂S₃ composite film in **Fig. 3.21 (e)** shows at 5 kX magnification GO/Sm₂S₃ composite material deposited over the substrate at 40 kX magnification in (**Fig. 3.21 (f)**) clearly seen that the surface morphology is porous nano-strips like which helps to electrolyte to reach easily at a surface and is efficiently utilized for the improvement of electrode-electrolyte interaction.

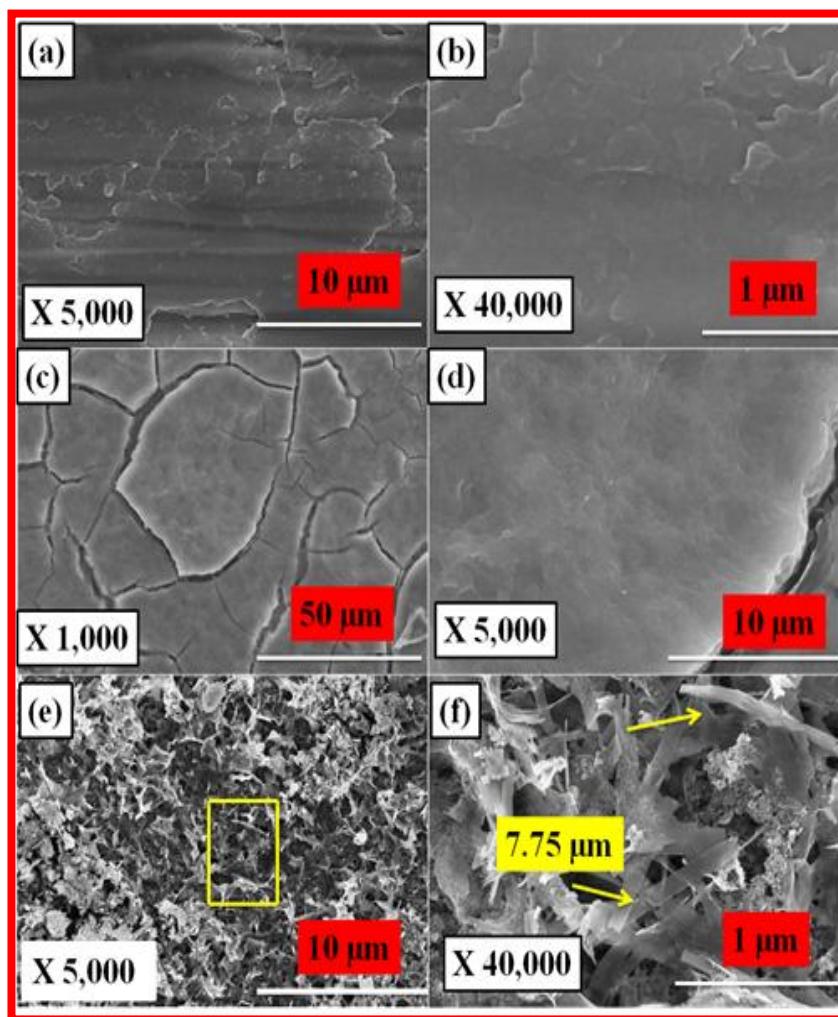


Fig. 3.21: FE-SEM images of (a, b) GO (5 and 40 kX), (c, d) Sm₂S₃ (1 and 40 kX) and (e, f) GO/Sm₂S₃ composite (5 and 40 kX) thin films, respectively.

E) Surface Wettability Study -

The surface wettability measurement gives an idea about the wettability of material in electrochemical devices. Generally, the wettability of surface depends on local in homogeneity, chemical composition and microstructure of the surface. **Fig. 3.22 (a, b)** shows hydrophilic nature of GO and Sm_2S_3 with contact angles of 80° and 78.1° , respectively [30]. The adsorption of liquid drop on GO/ Sm_2S_3 composite thin film shows superhydrophilicity with contact angle of 5° as shown in **Fig. 3.22 (c)**. **Kumbhar et al [6]** reported contact angle of 21° for Sm_2S_3 thin film prepared by SILAR method.

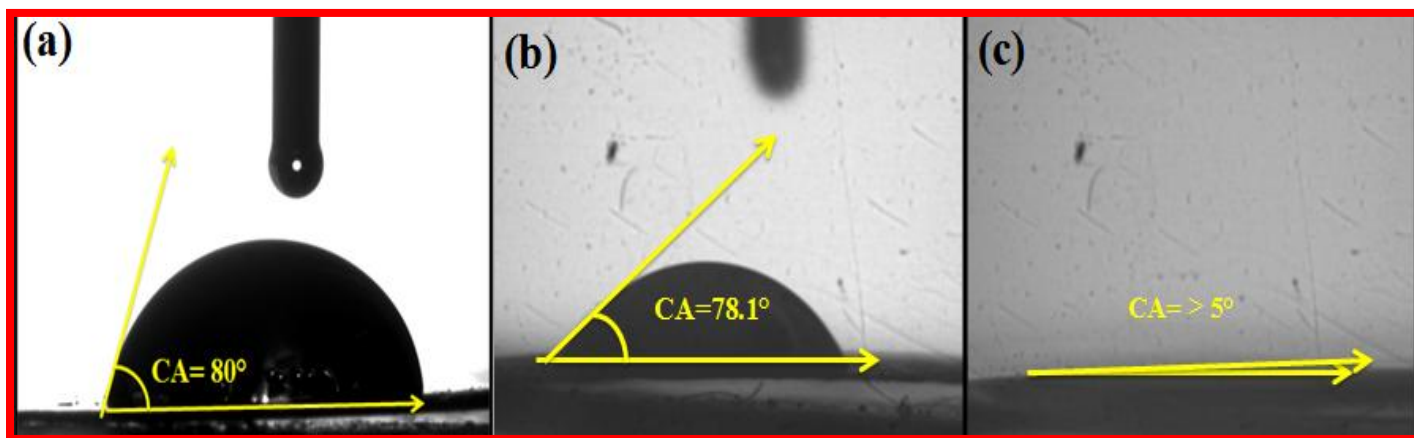


Fig.3.22: Contact angles of (a) GO (b) Sm_2S_3 and (c) GO/ Sm_2S_3 composite thin films.

F) BET Study:

The nitrogen adsorption-desorption isotherm curve of GO/ Sm_2S_3 composite thin film and the corresponding pore size distribution (inset) are provided in **Fig.3.23**. The nitrogen isotherm is classified as a type IV isotherm with a small hysteresis loop. A small step of nitrogen adsorption and desorption branching occurs at a relative pressure (P/P_0) between 0.4 and 0.6, as a representative of existence of mesopores. On the basis of the nitrogen adsorption-desorption isotherm, the BET surface area of GO/ Sm_2S_3 composite thin film is calculated to be $31.43 \text{ m}^2\text{g}^{-1}$. The pore size distribution data calculated from the adsorption branches of the nitrogen isotherms

using the BJH (Barrett-Joyner-Halender) technique suggest formation of mesopores structure with a narrow pore size distribution, centered at 21.79 nm. These mesoporous networks of nano-strips-like morphology provide low resistant way through the porous structure which helps to improve charge transport and power capacity [31].

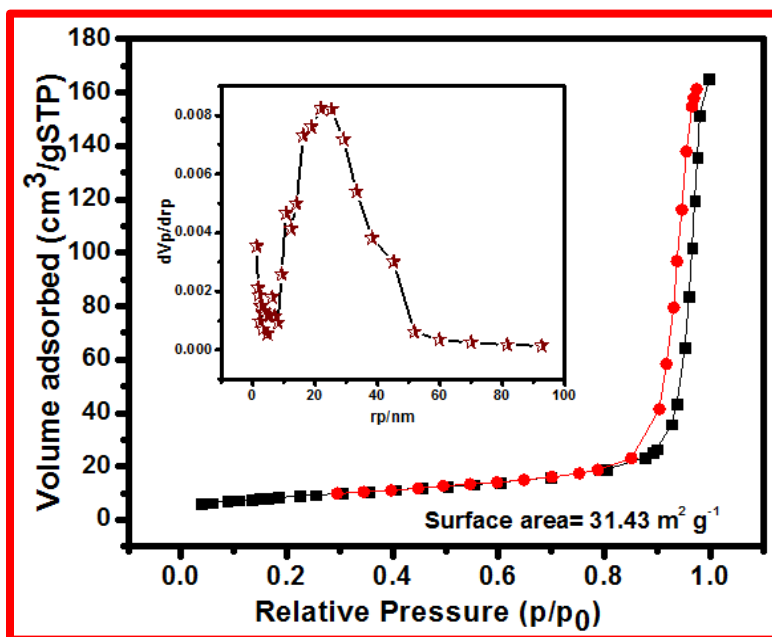


Fig.3.23: Nitrogen adsorption-desorption isotherms and inset shows pore size distribution curve of GO/Sm₂S₃ composite thin film.

Section: B.2

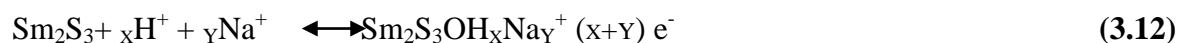
Supercapacitive Performance Evaluation of Sm₂S₃ and GO/Sm₂S₃ Composite Thin Film by SILAR Method

3. B.2 Introduction:

Recently, rare earth metal chalcogenides based electrode materials are gaining attention in the field of supercapacitors. Various materials like Yb₂S₃ [32], Sm₂S₃ [8], La₂S₃ [33], La₂O₃ [34], etc. are tested as electrodes in supercapacitor devices. The advantage of rare earth metal sulfides over their oxide counterparts is their relatively higher conductivity charge storage, which helps to improve supercapacitive performance of rare earth metal sulfide. Samarium has various oxidation states (-3, -1, +1, +2, +3, +4, +5) which is prime prerequisite for a material to be pseudocapacitive. This section comprises evaluation of supercapacitive properties of chemically deposited Sm₂S₃ and GO/Sm₂S₃ composite thin films. The electrochemical measurements of Sm₂S₃ and GO/Sm₂S₃ composite thin films were carried out using conventional three electrode system, which includes Sm₂S₃ and GO/Sm₂S₃ composite thin films as a working electrode, platinum as a counter electrode and saturated calomel electrode (SCE) as a reference electrode in 1 M Na₂SO₄ electrolyte. The working electrode for electrochemical measurement was built by sealing the thin film by insulating tape except 1 cm⁻² area.

3. B.2.1 Experimental set up for Supercapacitive Studies:

The supercapacitive performance of Sm₂S₃ and GO/Sm₂S₃ composite was tested in 1 M Na₂SO₄ electrolyte with -1.0 to 0 V/SCE potential window in three electrode system. The mass of active GO/Sm₂S₃ composite electrode material was 0.83 mg cm⁻². The electrochemical redox reaction occurred in an electrolyte solution is given as,



3. B.2.2. Results and Discussion-

(A) Cyclic Voltammetry (CV) Study:

The cyclic voltammetry (CV) study is key technique to test best electrode for the SC applications, it is necessary to perform electrochemical evaluations. First, the CV measurements for GO thin film was performed in a 1 M Na₂SO₄ electrolyte over the operating potential range of -1.0 to 0 V/SCE at a scan rate of 5-100 mVs⁻¹, as seen in **Fig.3.24 (a)**. In previous research, **Gund et al [26]** also reported negative operating potentials with the uses of GO/Mo₃O₄ based electrode and 1 M Na₂SO₄ electrolyte, while their SC showed superior supercapacitive performance. From **Fig.3.24 (a)**, it was seen that all the CV curves for the GO thin film show nearly rectangular shape even at a high scan rate of 100 mVs⁻¹. The specific capacitance is obtained of 87.7 Fg⁻¹ at 5 scan rate.

Fig.3.24 (b, c) shows the specific capacitance as a function of the scan rate for Sm₂S₃ and GO/Sm₂S₃ composite electrodes. The specific capacitance decreases as the scan rate is increased from 5 to 100 mVs⁻¹ for Sm₂S₃ and GO/Sm₂S₃ composite electrodes. The Sm₂S₃ and GO/Sm₂S₃ composite electrodes show maximum specific capacitance of (Sm₂S₃ of 173.5 Fg⁻¹) and (GO/Sm₂S₃ 360 Fg⁻¹), at a scan rate of 5 mVs⁻¹. It is observed that the improvement of capacitance for the composite electrode is credited due to the porous arrangement nano-sheets GO with nano-strips of Sm₂S₃ microstructure. During the charge/discharge process, Na⁺ ions from an electrolyte are involved in the charge storage process of both Sm₂S₃ and GO/Sm₂S₃ composite electrodes. The reversible redox reactions are by means intercalation/deintercalation of ions facilitated by high surface area and high electrical conductivity of GO/Sm₂S₃ composite electrode [35].

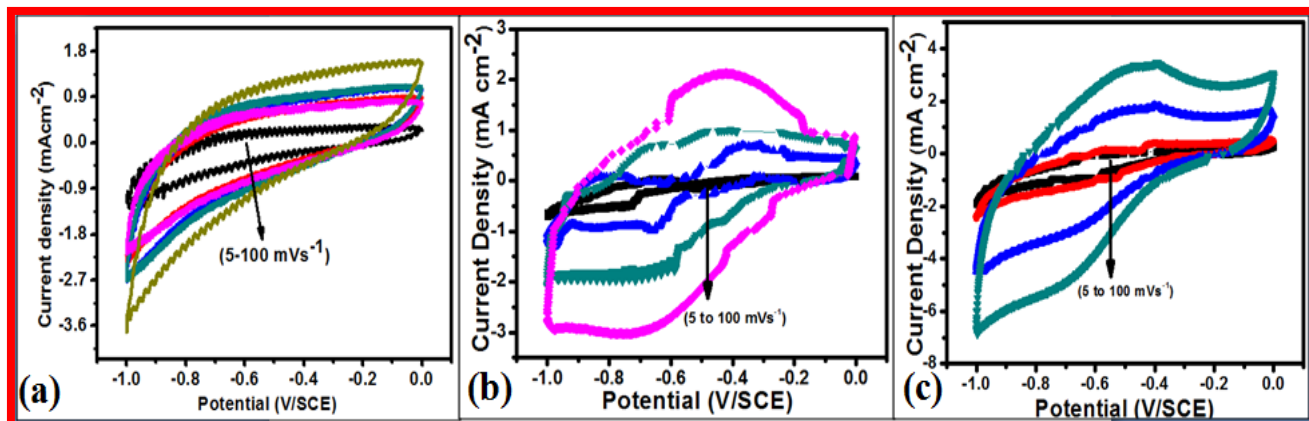


Fig.3.24: The CV curves of (a) GO, (b) Sm_2S_3 and (c) $\text{GO}/\text{Sm}_2\text{S}_3$ composite thin films at 5 mVs^{-1} scan rate in $1 \text{ M Na}_2\text{SO}_4$ electrolyte.

(B) GCD Study:

The galvanostatic charge/discharge measurements of GO, Sm_2S_3 and $\text{GO}/\text{Sm}_2\text{S}_3$ composite electrodes are performed at different current densities. **Fig.3.25 (a-c)** displays the charge/discharge curves at 0.2 , 0.5 and 0.8 mA cm^{-2} current densities in the potential range 0 to -1.0 V/SCE . The discharge curves of all the electrodes show IR-drop in the current at the starting of discharging due to internal resistance. The high surface area of GO allows for a high capacitive contribution from the pseudocapacitive, whereas Sm_2S_3 provides a significant increase to the overall energy density of the electrode. The shape of the discharge curves shows the characteristic of pseudo-capacitor, in agreement with the result of the CV curves [36].

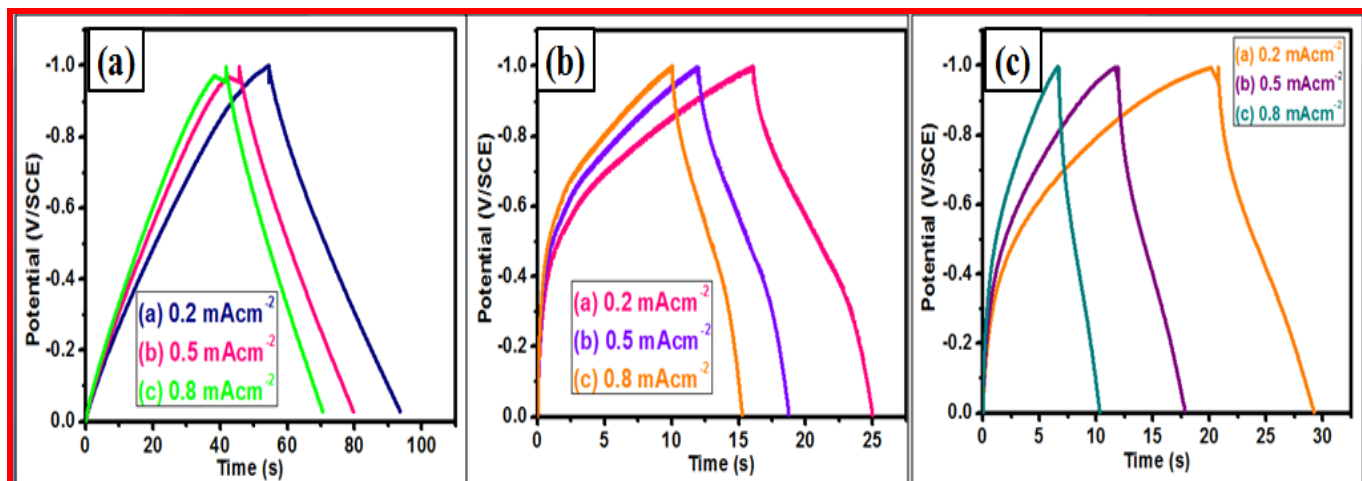


Fig.3.25: Galvanostatic charge-discharge curves of (a) GO, (b) Sm_2S_3 and (c) GO/ Sm_2S_3 composite electrodes at 0.2, 0.5 and 0.8 mAcm^{-2} current densities.

(C) Stability Study:

The stability is one of the most important parameters in an electrochemical study. **Fig.3.26 (a-c)** shows the cyclic stability with capacitive retention of GO, Sm_2S_3 and GO/ Sm_2S_3 composite electrode at a scan rate of 100 mVs^{-1} for the 2nd and 1000th cycles. The capacitive retention of 81.6 % for GO electrode (**Fig.3.26 (a)**), 84.8 % for Sm_2S_3 electrode (**Fig.3.26 (b)**) and 89.4 % for GO/ Sm_2S_3 composite electrode (**Fig.3.26 (c)**) over the 1000 cycles. Inset of **Fig.3.26 (a-b)** shows the no. of CV cycles of every electrode. The composite electrode showed best cyclic stability than GO and Sm_2S_3 electrode. The decrease in cyclic stability from 100% to 89.4 % may be due to the loss of active material caused by the dissolution or detachment during the charging/discharging cycles in the electrolyte.

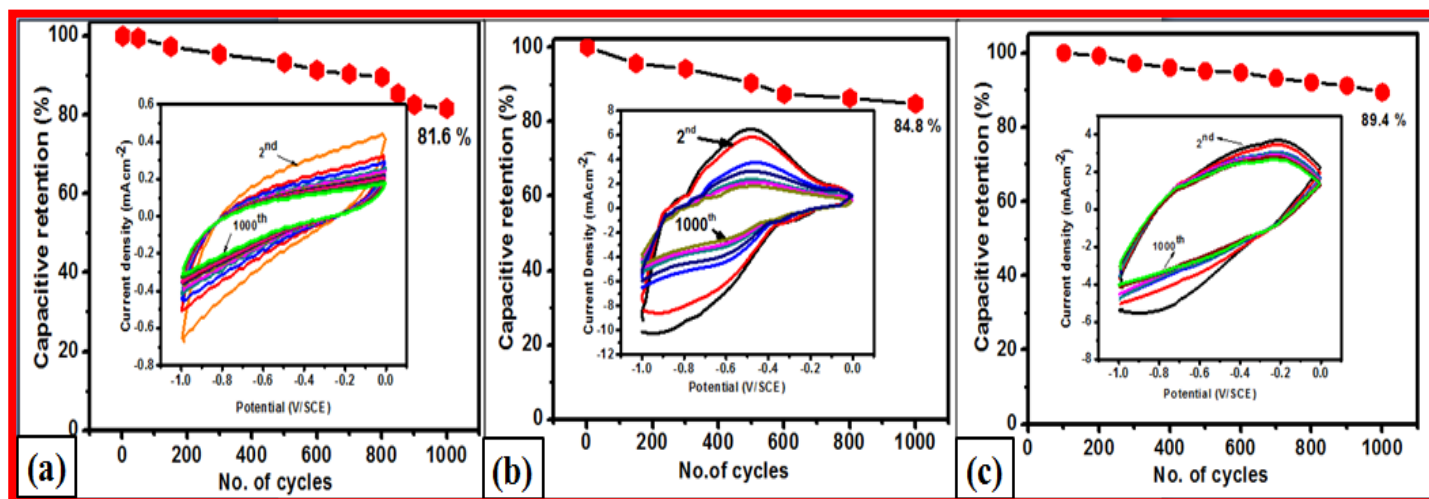


Fig. 3.26: Capacitive retention of (a) GO, (b) Sm_2S_3 and (c) GO/ Sm_2S_3 composite electrode for 2,000 CV cycles at 100 mVs^{-1} scan rate. Inset shows no. of CV cycles of electrodes.

(D) EIS Study:

The electrochemical impedance spectroscopy (EIS) measurement was performed to obtain information of the electrode material surface and charge-transfer resistance and phase angle. The impedance analyzed using Nyquist plots of GO, Sm_2S_3 and GO/ Sm_2S_3 composite electrodes is shown in **Fig.3.27 (a, b)**. The Nyquist plots show a small semicircle at higher frequency regions, which can be attributed to the charge transfer process. The equivalent series resistance (ESR) is obtained at the mid frequency region from the X-intercept of the Nyquist plots. The series resistance (R_s) $0.07 \Omega \text{ cm}^{-2}$, capacitance (Q) is 0.003 F , Warburg resistance (W) is $0.0084 \Omega \text{ cm}^{-2}$ are obtained for GO and inset of **Fig.3.27 (a)** shows magnified and equivalent circuit image of GO electrode. Similarly, **Fig.3.27 (b)** shows series resistance (R_s) is $2.95 \Omega \text{ cm}^{-2}$ and (R_{ct}) as $4.60 \Omega \text{ cm}^{-2}$, capacitance (Q) is 3.83 F and Warburg resistance (W) is $0.00037 \Omega \text{ cm}^{-2}$, while inset shows magnified Nyquist plot and circuit image for Sm_2S_3 . The GO/ Sm_2S_3 composite electrode provides less series resistance (R_s) is $0.56 \Omega \text{ cm}^{-2}$ as shown in **Fig.3.27 (c)**. The low resistance provides easy

path for intercalation and deintercalation of charges as compared to GO and Sm_2S_3 electrodes. The comparison of obtained parameters valued are given in the **Table 3.3**.

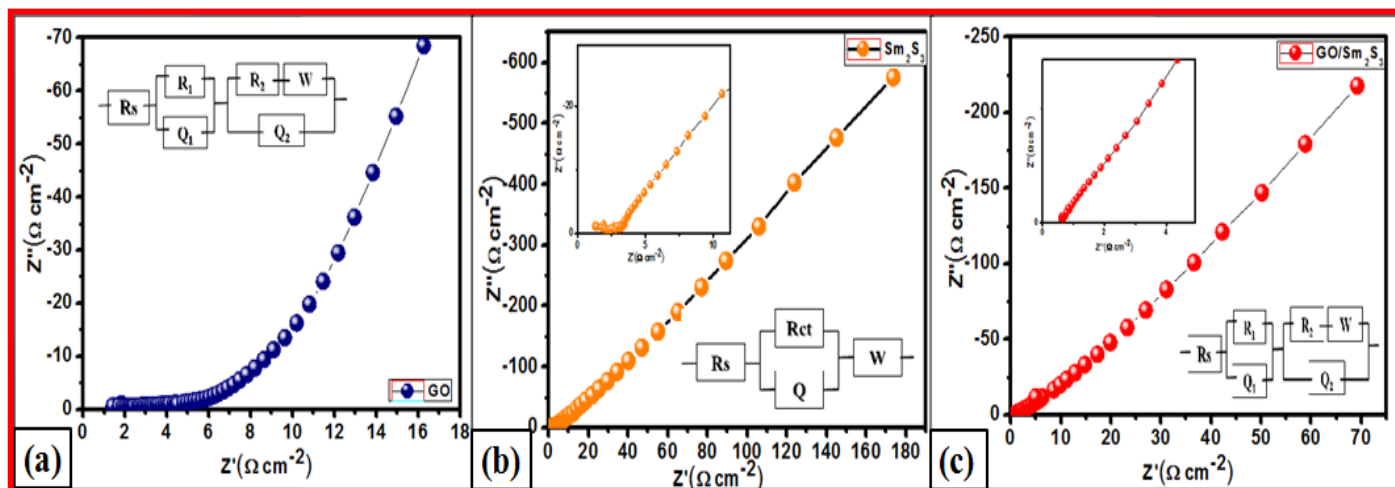


Fig.3.27: Nyquist plots of (a) GO (inset of magnified image) and (b) Sm_2S_3 (inset of magnified image) and (c) GO/ Sm_2S_3 (inset of magnified image) composite electrode.

Table 3.3. Nyquist plot parameters values fitted with equivalent circuit.

GO		Sm_2S_3		GO/ Sm_2S_3	
R_s ($\Omega \text{ cm}^{-2}$)	0.07	R_s ($\Omega \text{ cm}^{-2}$)	2.95	R_s ($\Omega \text{ cm}^{-2}$)	0.56
Q1 (F)	0.003	R_{ct} ($\Omega \text{ cm}^{-2}$)	4.60	Q1(F)	1.58
R_1 ($\Omega \text{ cm}^{-2}$)	6.12	Q (F)	3.83	R_1 ($\Omega \text{ cm}^{-2}$)	3.83
Q2 (F)	0.041	W ($\Omega \text{ cm}^{-2}$)	0.00037	Q2 (F)	0.0003
R_2 ($\Omega \text{ cm}^{-2}$)	0.368			R_2 ($\Omega \text{ cm}^{-2}$)	6.76
W ($\Omega \text{ cm}^{-2}$)	0.0084			W ($\Omega \text{ cm}^{-2}$)	0.00037

3.5 Conclusions:

In summary, simple and cost effective hydrothermal and SILAR methods are employed to synthesis of Sm_2S_3 and $\text{GO}/\text{Sm}_2\text{S}_3$ composite thin films directly on stainless steel substrate. The superhydrophilic and porous surface morphology of Sm_2S_3 and $\text{GO}/\text{Sm}_2\text{S}_3$ composite film showed good contribution in electrochemical reaction. A maximum specific capacitance of 360 Fg^{-1} is observed for composite film by SILAR method and 153 Fg^{-1} for Sm_2S_3 film by hydrothermal method in aqueous electrolyte as well as the good cyclic rate capability (81.5% retention after 1000 CV cycles) and 89.4 % retention after 1000 cycles for composite. The R_s and R_{ct} of composite electrode are $R_s: 0.56 \Omega\text{cm}^{-2}$ as compared to hydrothermally synthesized Sm_2S_3 , $R_s: 78.9 \Omega\text{cm}^{-2}$ is low. These results indicate that $\text{GO}/\text{Sm}_2\text{S}_3$ composite material of has long-term electrochemical stability and having good electrochemical reversibility in aqueous electrolyte. Therefore, it is seen that the porous and more hydrophilic surface of SILAR deposited $\text{GO}/\text{Sm}_2\text{S}_3$ composite thin films are helpful for supercapacitor application.

References:

1. C.M. Forster, W.B. White, Mater. Res. Bull. **41** (2006) 448–454.
2. C. F. Hickey and U. J. Gibson, Phase Transit., **14** (1989) 187-199.
3. V.S. Kumbhar, A.D. Jagadale, N.S. Gaikwad, C.D. Lokhande, Mater. Res. Bull. **56** (2014) 39–44.
4. V.S. Kumbhar, A.C. Lokhande, N.S. Gaikwad, C.D. Lokhande, Ceram. Int., **41** (2015), 5758-5764.
5. V.S. Kumbhar, A.D. Jagadale, N.M. Shinde, C.D. Lokhande, Appl. Surf. Sci. **259** (2012) 39–43.
6. V.S. Kumbhar, A.C. Lokhande, N.S. Gaikwad, C.D. Lokhande, Mat. Sci. Semicon. Proc., **33** (2015), 136-139.
7. D. P. Dubal, G. S. Gund, R. Holze, H. S. Jadhav, C. D. Lokhande, C. J. Park, Dalton Trans., **42** (2013) 6459-6467.
8. V.S.Kumbhar, A.D.Jagadale, C.D.Lokhande, J. Power Source, **234** (2013)107-110.
9. K.J.Huang, J.Z.Zhang, Y.Liu, Y.M.Liu, Int. J. Hydrog. Energy, **40**(2015) 10158–10167.
10. S. Park, K. S. Lee, G. Bozoklu, W. Cai, S.T. Nguyen, R. S. Ruoff, ACS Nano., **2** (2008), 572-578.
11. A. B. Bourlinos, D. Gournis, D. Petridis, T. Szabo, A. Szeri, I. Dekany, Langmuir. **19** (2003), 6050- 6055.
12. https://www.rp-photonics.com/band_gap.html
13. X.Li, Q. Li, Y.Wu, M. Rui, H. Zeng, ACS Appl. Mater. Interfaces., **7** (2015) 19316-19323.
14. <https://particle.dk/methods-analytical-laboratory/surface-area-bet-2/>
15. V. Subramanian, H. Zhu, B. Wei, J. Power Source, **159** (2006) 361-370.
16. T. P. Gujar, W.Y. Kim, I. Puspitasari, K.D. Jung, Oh-Shim Joo, Int. J. Electrochem. Sci., **2** (2007) 666 – 673.
17. X. Guan, Z. Zhang, L. Yang, G. Wang, ChemPluseChem., **82** (2017) 1174-1181.
18. A.M.Goma, L.L.Tan, R. Jose, M.M.Yusoff, K.F.Chong, Mater. Res.Bull., **60** (2014) 5–9.
19. A.M.Gomaa, A.G. Osama, A.M.Hassan, A.Osama, K.F.Chong, Ceram. Int., **41**(2015) 8230–8234.
20. S.B.Ubale, T.T. Ghogare, V.C. Lokhande, T. Ji, C.D. Lokhande, SN Appl. Sci. **2** (2020), 1-5.
21. A.D. Jagadale, V.S. Kumbhar, R.N. Bulakhe, C.D. Lokhande, Energy **64** (2014), 234-241.
22. A.L. Brisse, P. Stevens, G. Toussaint, O. Crosnier, T. Brousse, Electrochim. Acta **279** (2018), 161-167.

23. J. Zhao, J.Wu, B. Li, W.Du, Q. Huang, M. Zheng, H. Xue, H. Pang, *Pro. Nat. Sci: Mat. Int.*, **26** (2016) 237-242.
24. H. Lee, V.S. Kumbhar, J. Lee, Y. Choi, K. Lee, *Electrochim. Acta*, **334** (2020) 135618-135622.
25. J.Song, X.Wang, C.T.Chang, *J. Nanomater.*, **2014** (2014), 1-6.
26. G.S. Gund, D.P. Dubal, B.H. Patil, S.S. Shinde, C.D. Lokhande, *Electrochim. Acta* **92** (2013), 205-215.
27. N. A.Kumar, H.J.Choi, Y. R. Shin, D. W.Chang, L. Dai, J.B. Baek, *ACS Nano.*, **6** (2012) 1715–1723.
28. F. T.Johra, J.W. Lee, W.G. Jung, *J. Ind. Eng. Chem.* **20** (2014) 2883–2887.
29. S. Park, K.S. Lee, G. Bozoklu, W. Cai, S.T. Nguyen, R.S. Ruoff, *ACS Nano.* **2** (2008), 572-578.
30. G.Wang, L.Zhang, J.Zhang, *Chem. Soc. Rev.* **41** (2012), 797-828.
31. A.B. Bourlinos, D. Gournis, D. Petridis, T. Szabo, A. Szeri, I. Dekany, *Languir.* **19** (2003), 6050- 6055.
32. S.B.Ubale, R.N.Bulakhe, V. J. Mane, D.B. Malavekar, I.In, C.D.Lokhande, *Appl. Nanosci.***10** (2020), 1-13.
33. S.J. Patil and C.D. Lokhande, *Mater. Des.* **87** (2015), 939-948.
34. A.A. Yadav, A.C. Lokhande, J.H. Kim, C.D. Lokhande, *J. Ind. Eng. Chem.* **56** (2017), 90–98.
35. C. Xiang, M. Li, M. Zhi, A. Manivannan, N. WuJ. *Power Sources* **226** (2013), 65-70.
36. J. Zhu, W. Zhou, Y. Zhou, X. Cheng, J.Yang, *J. Electron. Mater.* **48** (2019), 1531-1539.

Chapter-4

Synthesis, Characterization and Supercapacitive Performance

Evaluation of Lanthanum Sulfide and Graphene Oxide/Lanthanum Sulfide Composite Thin Film

Sr.no.	Title		Page no.
	SECTION –A.1		
4.A.1	Introduction		86
	4.A.1.1	<i>Synthesis of Lanthanum Sulfide (β-LaS₂) Thin Film Using Hydrothermal Method</i>	87
	4.A.1.2	<i>Experimental Setup For Deposition of Lanthanum Sulfide (β-LaS₂) Thin Films by Hydrothermal Method</i>	87
	4.A.1.3	<i>Material Characterization</i>	88
	4.A.1.4	<i>Results and Discussion</i>	89
		(A) <i>Lanthanum Sulfide (β-LaS₂)Thin Film Formation and Reaction Mechanism</i>	90
		(B) <i>XRD Study</i>	90
		(C) <i>FE-SEM Study</i>	91
		(D) <i>Surface Wettability Study</i>	92
		(E) <i>UV-Visible Spectroscopy Study</i>	92-93
	SECTION-A.2		
	<i>Supercapacitive Performance Evaluation of Lanthanum Sulfide (β-LaS₂)thin films</i>		
4.A.2	<i>Introduction</i>		94
	4.A.2.1	<i>Results and Discussion</i>	95
		(A) <i>Cyclic voltammetry (CV) study</i>	96
		(B) <i>GCD study</i>	96
		(C) <i>Stability studies</i>	97
		(D) <i>EIS studies</i>	98
	SECTION-B.1		
	<i>Synthesis of Lanthanum Sulfide and Graphene Oxide/ Lanthanum Sulfide (GO/La₂S₃) Composite Thin Film Using SILAR Method</i>		
4.B.1	<i>Introduction</i>		99
	4.B. 1.1	<i>Experimental Setup of Graphene Oxide/Lanthanum Sulfide (GO/La₂S₃) Using SILAR Method</i>	100
	(A)	<i>Lanthanum Sulfide (La₂S₃) Thin Film Synthesized by SILAR Method</i>	100
	(B)	<i>Graphene Oxide/ Lanthanum Sulfide (GO/La₂S₃) Composite Thin Film Synthesized by SILAR Method</i>	100
	4.B.1.2	<i>Results and Discussion</i>	101
		(A) <i>Graphene Oxide/Lanthanum Sulfide (GO/La₂S₃) Composite Thin Film Formation and Reaction Mechanism</i>	101
		(B) <i>XRD Study</i>	102
		(C) <i>FT-IR Study</i>	103
		(D) <i>FE-SEM Study</i>	104-105
		(E) <i>Surface Wettability Study</i>	106
		(F) <i>BET Study</i>	107
		(G) <i>XPS Study</i>	108-109
	SECTION-B.2		
	<i>Supercapacitive Perormance Evaluation of Lanthanum Sulfide and Graphene Oxide/Lanthanum Sulfide (GO/La₂S₃) Composite Thin Films</i>		
4.B.2	<i>Introduction</i>		110

	4.B.2.1	<i>Results and Discussion</i>		111
		(A)	<i>Cyclic voltammetry (CV) study</i>	112
		(B)	<i>GCD study</i>	113-114
		(C)	<i>Stability study</i>	115
		(D)	<i>EIS study</i>	116
4.3	<i>Conclusions</i>			117-118
	<i>References</i>			119-121

Section-A.1

4. A.1 Introduction:

Energy is very important for human progress. Energy use and invention, which depend on combustion of fossil fuels, are going to affect the world economy and ecology severely. So, there has been an increasing demand for environment-friendly and high-performance renewable energy storage devices [1]. Electrochemical energy is an inevitable part of the clean energy portfolio. Batteries, supercapacitors (SCs) and fuel cells are unconventional energy devices working on the principle of electrochemical energy conversion [2]. SCs have gained much attention on account of high specific capacitance (Cs), long life cycle, high power density (Pd), being almost maintenance free, experiencing no memory effect, safe and function as a bridge for power-energy difference that exists between capacitor and fuel cells/batteries [3, 4]. These present viable solutions for providing energy in rural areas, where no public grids are available or where a heavy cost of wiring and providing electricity are involved. SCs can also be utilized as power supplies for portable devices like mobile phones, notebook computers, digital cameras etc; being small, lightweight and flexible [5].

In recent years, rare earth chalcogenides are used as an active material for different applications because of their multiple oxidation states, high chemical stability, high reversibility and natural abundance [6, 7]. The literature survey indicates that various chemical methods such as CBD [8], SILAR [9], electrodeposition [10], spray pyrolysis [11], and hydrothermal [12] are used for the synthesis of rare earth metal chalcogenides thin films. Among the different crystal structures of lanthanum chalcogenide are more suitable for supercapacitor application. Hexagonal CeO₂ nanoparticles have been prepared through hydrothermal method which

demonstrated a specific capacitance of 523 Fg^{-1} at a 2 mVs^{-1} scan rate [13]. Patil et al. [14] prepared La_2Se_3 thin film by CBD method which exhibited a specific capacitance of 331 Fg^{-1} at a scan rate of 5 mV^{-1} . Patil et al. [15] prepared La_2S_3 thin film by CBD method which exhibited a specific capacitance of 294 Fg^{-1} . The $\alpha\text{-La}_2\text{S}_3$ thin films have been synthesized for the first time by successive ionic layer adsorption and reaction (SILAR) method and electrode delivers high specific capacitance of 256 Fg^{-1} at scan rate of 5 mVs^{-1} [16].

The surface morphology of synthesized electrode material plays a significant role in electrochemical performances, as the electrochemical reactions occurred through the surface of active material. Hence the synthesis of nanostructured electrode material is being crucial one to achieve the better supercapacitor performance. In the present chapter, section 'A', deals with successfully deposited of $\beta\text{-LaS}_2$ thin films by simple, inexpensive, surfactant free and convenient hydrothermal method. The surface morphology, structural properties and electrochemical supercapacitive performance of the electrode were also studied.

4. A.1.1 Synthesis of Lanthanum Sulfide ($\beta\text{-LaS}_2$) Thin Film Using Hydrothermal Method:

4. A.1.2 Experimental Setup for Deposition of Lanthanum Sulfide ($\beta\text{-LaS}_2$) Thin Films by Hydrothermal Method-

$\beta\text{-LaS}_2$ thin films were deposited on stainless steel substrate from hydrothermal method in an aqueous medium. The 0.1 M lanthanum chloride ($\text{LaCl}_3 \cdot 7\text{H}_2\text{O}$) was dissolved in 20 ml DDW as a source of lanthanum ions (La^{+3}). The pH value of the cationic solution (La^{+3}) was adjusted to 2 ± 0.1 using 0.05 M tartaric acid ($\text{C}_4\text{H}_6\text{O}_6$). For sulfide ion (S^{-2}) source, 0.1 M sodium thiosulphate ($\text{Na}_2\text{S}_2\text{O}_3 \cdot 5\text{H}_2\text{O}$) was dissolved in 20 ml DDW. Then, cationic and anionic solutions were mixed together to get 40 ml of volume in a glass beaker. Well-cleaned stainless steel substrates were dipped in the solution and the beaker was kept at 393 K for 1 h in a

hydrothermal autoclave. After 1 h, uniform white-colored La-S film was obtained on the stainless steel substrate. The schematic diagram of β -LaS₂ deposition is as shown in **Fig. 4.1**.

The films were dried at room temperature.

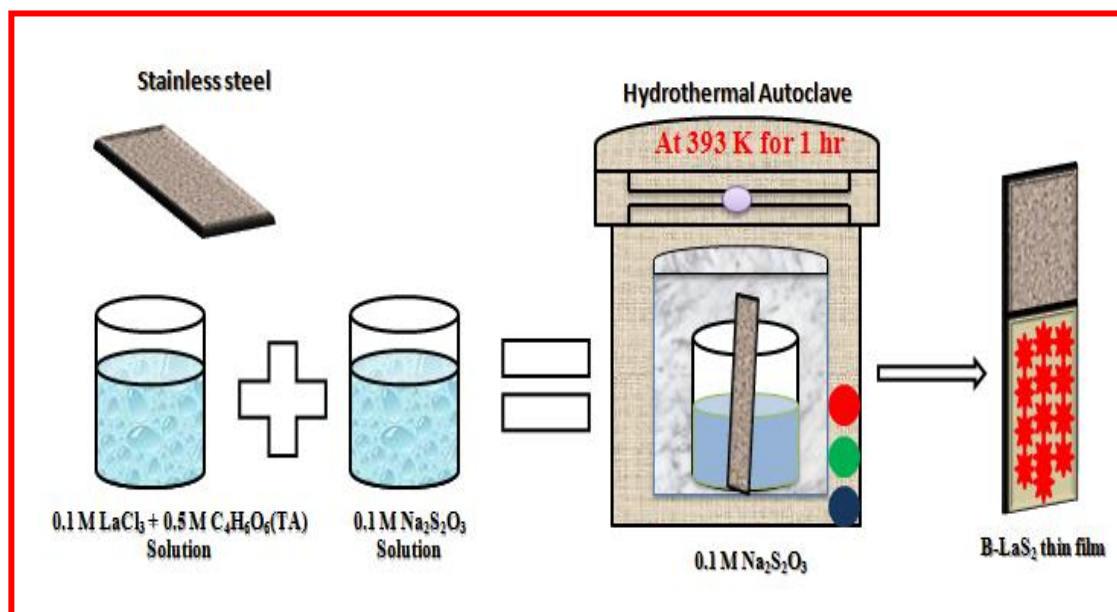


Fig. 4.1 Schematic diagram of β -LaS₂ thin film deposited by hydrothermal method.

4. A.1.3 Material Characterization-

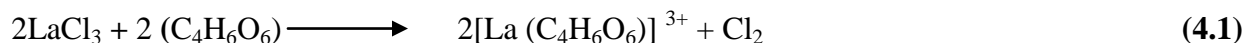
The crystal structure of La-S film was examined using a Bruker AXS D8 advanced model X-ray diffractometer with primary monochromatic radiation from Cu K α line ($\lambda=1.54$ Å) in the 2θ range of 20–80°. The surface morphology was observed using field emission scanning electron microscope (FE-SEM, JEOL-6360, Japan). The wettability test was conducted by contact angle measurement (water as a solvent) using Rame-Hart NRL CA Goniometer. The optical band gap of the material was determined from UV–vis spectrophotometer of Agilent Technologies Cary 60 model in the wavelength range of 200–800 nm. Electrochemical measurements of β -LaS₂ thin film were carried out using Zive MP1 model of Wonatech company using three electrode cell, consisting of β -LaS₂ thin film as a working electrode,

platinum strip as a counter electrode and the saturated calomel electrode (SCE) as a reference electrode.

4. A.1.4 Results and Discussion:

(A) Lanthanum Sulfide (β -LaS₂) Thin Film Formation and Reaction Mechanism

Fig. 4.1 shows the schematic setup for the formation of LaS₂ thin film in aqueous bath. When the ionic product of La³⁺ and S²⁻ exceeds the solubility product of LaS₂ then LaS₂ film is formed on the substrate. The possible reactions which occur in the reaction bath as follows. The LaCl₃ dissolved in DDW acts as a La³⁺ ion source. The La³⁺ ions are complexed with C₄H₆O₆ to form lanthanum complex ions as,



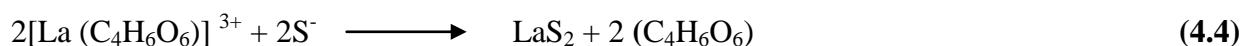
Na₂S₂O₃ acts as a reducing agent which releases S²⁻ ions by the half-cell reaction in solution bath as,



And,



The dissociation of thiosulfate releases S²⁻ ions. The lanthanum ions from complex react with the sulfide ions and LaS₂ is formed on the surface of substrate. The growth of LaS₂ film is based on an ion-by-ion mechanism. By combining eq. (4.1) and (4.3), final reaction become,



Finally, β -LaS₂ thin film is formed on the substrate surface. Further, these films are used for further characterizations.

(B) XRD study

X-ray diffraction technique was used to identify the crystal structure of La-S thin film. Well-resolved diffraction peak in **Fig. 4.2** located at $2\theta=32.8^\circ$ matched well with the (060) plane of the orthorhombic structure of β -LaS₂, (JCPDS no. 42-0788). The crystalline size of β -LaS₂ was estimated by Scherrer's formula. The estimated crystallite size of β -LaS₂ for (060) plane is found to be 8.59 nm. Patil et al [16] prepared α -La₂S₃ thin film by SILAR method and reported orthorhombic crystal structure.

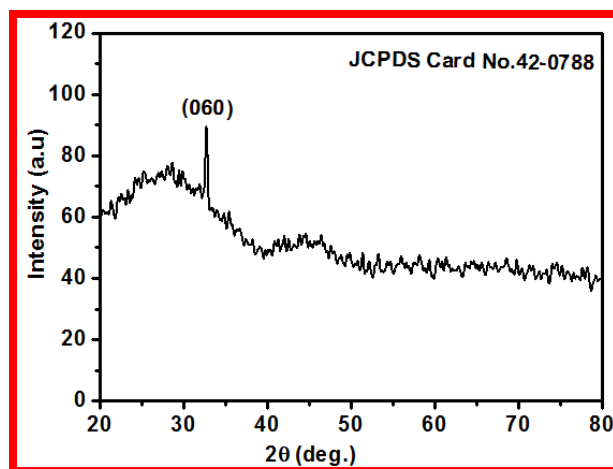


Fig. 4.2: XRD pattern of β -LaS₂ thin film.

(C) FE-SEM Study-

The surface morphology of thin film plays an important role in the supercapacitive behavior of material; mesoporous surface morphology provides high surface area [17]. FE-SEM micrographs at 3kX and 7kX magnifications are shown in (**Fig. 4.3 a, b**). As seen from the FE-SEM micrographs, LaS₂ petals-like surface morphology is non-uniformly distributed over the substrate. The high magnification micrograph (**Fig. 4.3 (b)**) shows interconnected nano-petals

constructed of porous flower-like structure. The size of the petal is around 2–5 μm , while its thickness ranges in nanometer region. **Patil et al.** [14] obtained a nano-flake-like surface morphology of La_2Se_3 by chemical bath deposition method. The porous nanostructure morphology of $\beta\text{-LaS}_2$ thin film is useful in many advanced applications such as supercapacitor [18] and gas sensor [19].

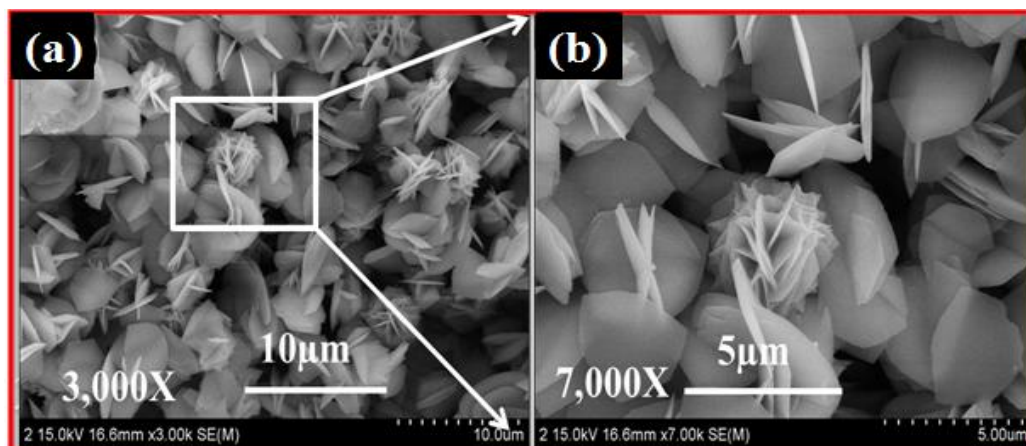


Fig. 4.3: FE-SEM images of $\beta\text{-LaS}_2$ thin film at (a) 3kX and (b) 7kX magnifications.

(D) Surface Wettability Study -

The wettability interaction of $\beta\text{-LaS}_2$ thin film with Na_2SO_4 electrolyte is investigated using the water contact angle. **Fig. 4.4** shows the water contact angle measurement for $\beta\text{-LaS}_2$ film deposited on stainless steel substrates. The film exhibits a contact angle of 46.9° indicating its hydrophilic nature. The film shows hydrophilic nature due to its porosity of the deposited material. Patil et al [9] prepared La_2Se_3 film with contact angle of 13° using a drop of propylene carbonate (PC). Again, Patil et al [16] prepared $\alpha\text{-La}_2\text{S}_3$ thin film by SILAR method and measured contact angle of 11° . Mostly, in supercapacitor application specific capacitance depends upon the porosity of the surface [20].

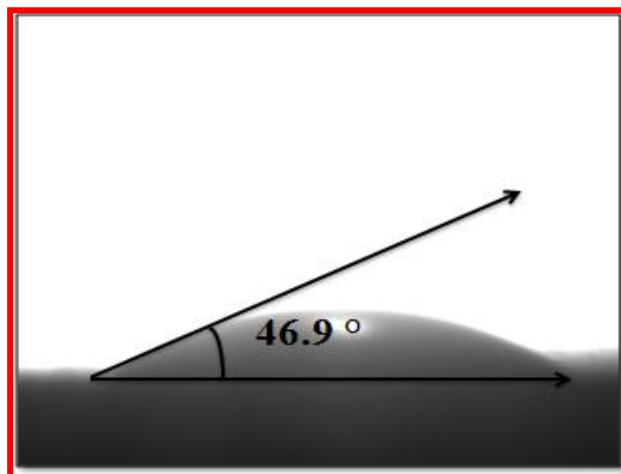


Fig. 4.4: Wettability images of β -LaS₂ thin film deposited by hydrothermal method.

(E) UV-Visible Spectroscopy Study-

The optical absorbance and the corresponding band gap of β -LaS₂ thin film are determined by UV–visible spectroscopy technique. **Fig. 4.5** inset shows variation of β -LaS₂ thin film absorbance (α) with wavelength (λ). This spectrum shows that β -LaS₂ film has low absorption in the visible region. The sharp increase in absorption at wavelength of 300 nm is attributed to its wide band gap. The band gap of β -LaS₂ thin film is determined using the following equation:

$$\alpha = \frac{A(E_g - h\nu)^n}{h\nu} \quad (4.5)$$

Where, α is the absorption coefficient, E_g is band gap, A is constant and n is equal to $\frac{1}{2}$ for direct band gap and 1 for indirect band gap. The plot of variation of $(\alpha h\nu)^2$ vs. $h\nu$ is shown in **Fig. 4.5**. The extrapolated linear portion of the curve on the energy axis ($\alpha = 0$) gives a direct band gap of **3.70 eV** for β -LaS₂ thin film. Li et al [21] prepared γ -La₂S₃ nanoparticles powder by thermal decomposition method and reported energy band gap 2.97 eV.

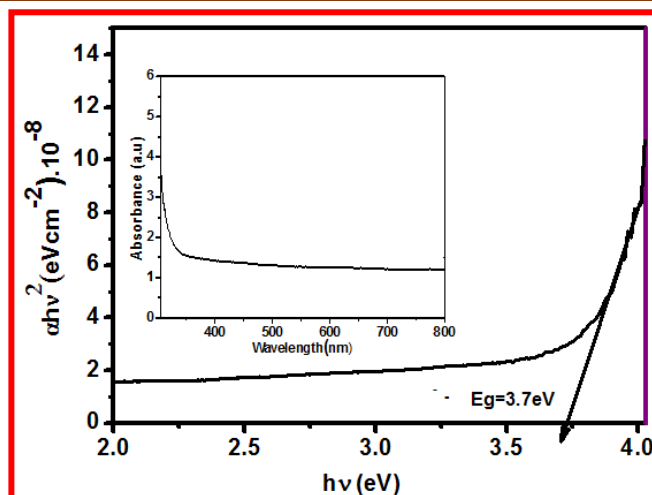


Fig. 4.5: Plot of $(\alpha h\nu)^2$ versus $h\nu$ for $\beta\text{-LaS}_2$ film deposited on glass substrate, (inset shows absorbance curve of $\beta\text{-LaS}_2$ against wavelength of radiation).

Section-A.2

Supercapacitive Performance Evaluation of Lanthanum Sulfide (β -LaS₂) Thin Films

4. A.2 Introduction:

The present section study deals with the electrochemical measurement of hydrothermally deposited β -LaS₂ thin film in 1 M Na₂SO₄ aqueous electrolyte. In this section CV, GCD, cyclic stability and EIS techniques used to find out the best electrode material for fabrication of supercapacitor devices. Also energy density, power density and capacitive retention of the device are studied.

4. A.2.1 Results and discussion:

(A) Cyclic voltammetry (CV) analysis:

Thin film with porous nanostructure and larger surface area is an essential criterion for their application of supercapacitors. The supercapacitive behavior of β -LaS₂ thin film electrodes was studied using cyclic voltammetry (CV) in 1 M Na₂SO₄ electrolyte at the varied scan rates of 5, 10, 20, 50 and 100 mVs⁻¹. **Fig. 4.6 (a)** shows cyclic voltammogram curves of β -LaS₂ at varied scan rates. The β -LaS₂ film exhibits a maximum specific capacitance of 121.42 Fg⁻¹ at 5 mVs⁻¹ scan rate in -1.2 to 0 V/SCE potential window range. The specific capacitance value depends mainly on the nature of electrolyte and its interaction with the electrode surface [22]. The CV shows quasi-rectangular curves without strong reduction and oxidation. The proportional enhancement in current density with the increased scan rate reflects the ideal capacitive nature of the electrode [23]. The intercalation/deintercalation reaction mechanism in β -LaS₂ film electrodes in Na₂SO₄ electrolyte is due to transmission of Na⁺ ions in the β -LaS₂ film electrode. The calculated values of Cs at different scan rates are shown in **Fig. 4.6 (b)**. The Cs

for β -LaS₂ thin film is reduced to 121.42 to 25.5 Fg⁻¹ with an increase in scan rate from 5 to 100 mVs⁻¹, respectively.

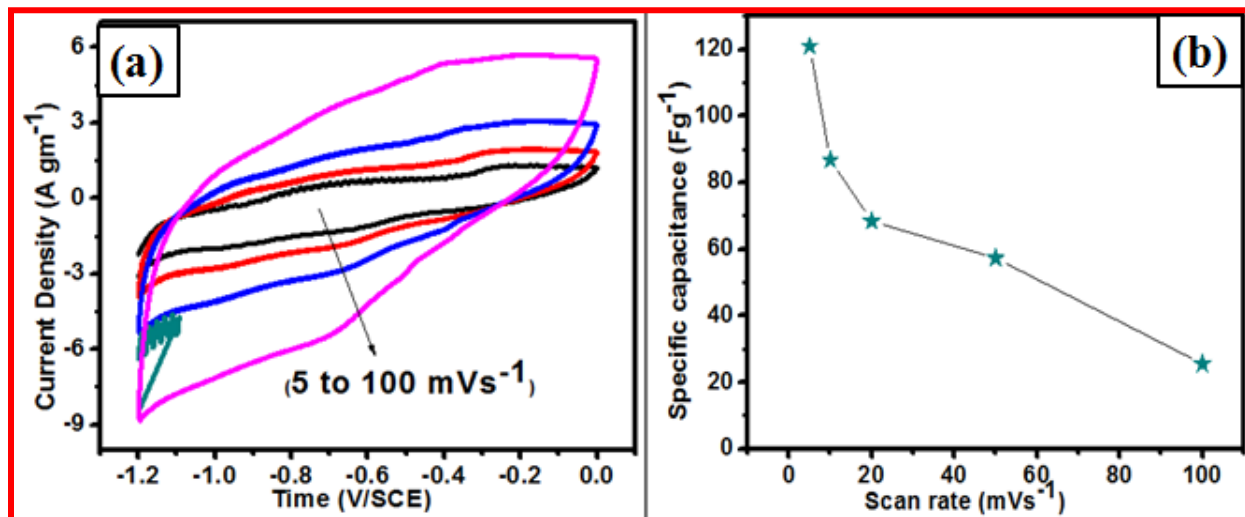


Fig.4.6 (a) CV curves at scan rates of 5 to 100 mV s⁻¹ scan rate, and (b) variation of specific capacitance (Cs) vs scan rate of β -LaS₂ electrode.

(B) GCD Study:

Fig.4.7 shows the charging/discharging curves at current densities 1, 2, 3 and 4 mAcm⁻² in 1 M Na₂SO₄ electrolyte for β -LaS₂ electrode. At current density 1 mAcm⁻², the interaction between β -LaS₂ electrode and electrolyte is higher and takes more time to charge as well as discharge. The curves are non-linear and show faradic interaction at electrode electrolyte interfaces. The nano-flakes like porous morphology and adherence of electrode material can provide fast intercalation reaction at surface of electrode material with electrolyte [24]. The specific capacitance of material mainly depend on the intercalation/deintercalation of ions within the crystalline structure of electrode material accompanied by redox reactions. Intercalation is most likely to take place in layered structures where the bonding between the layers is very weak due to high porosity [25]. In the case of deposited film intercalation also involves charge transfer

to or from the intercalated species, which can donate or accept electrons from the β -LaS₂ thin film.

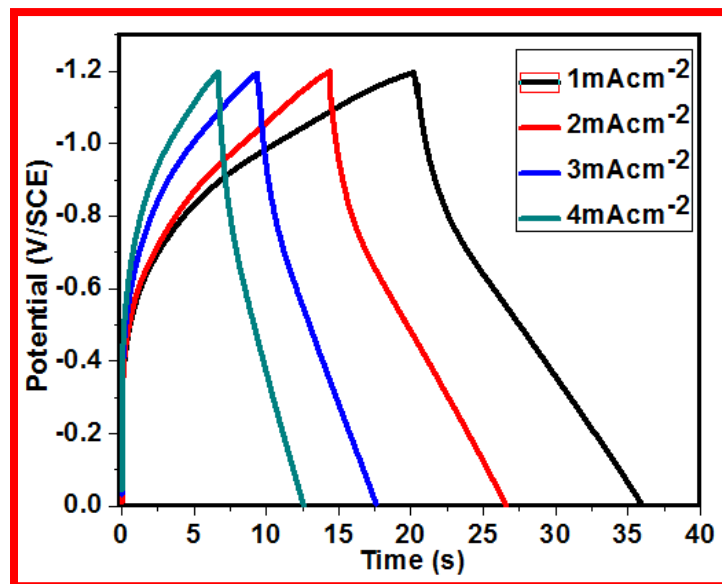


Fig.4.7 GCD curves at different 1, 2, 3 and 4 mA cm⁻² charging current densities.

(C) Stability Studies-

The better electrochemical cycling stability of electrodes is a prime requirement for supercapacitor application along with superior Cs, specific energy and specific power values. The long term electrochemical stability of β -LaS₂ electrodes is measured in 1 M Na₂SO₄ with cycling for 2nd, 50th, 100th and 1000th cycles as shown in **Fig.4.8**. The β -LaS₂ electrode shows good electrochemical stability of 84.2% after 1000 CV cycles. Inset of **Fig.4.8** shows the number of CV cycles of electrode. The slight reduction in specific capacitance after 1000 CV cycles is ascribed to the small degradation and the dissolution of active material into the electrolyte [26, 27].

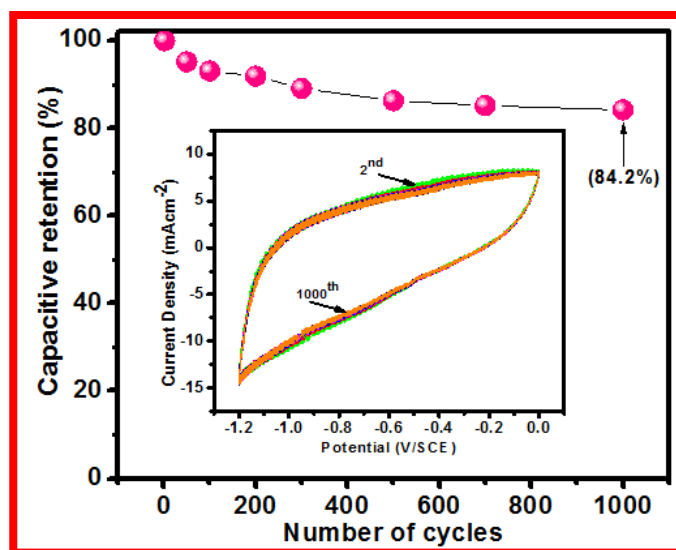


Fig.4.8 The capacitive retention of β -LaS₂ electrode (inset of number of CV curves cycles).

(D) EIS Study-

The EIS measurements are performed with a three-electrode cell configuration in 1 M Na₂SO₄ electrolyte. The Nyquist plot of β -LaS₂ electrode was recorded by applying an AC voltage of 10 mV amplitude in the frequency range from 1 MHz to 0.1 Hz [28]. The electrochemical impedance spectra, in the form of a Nyquist plots for β -LaS₂ electrode are shown in **Fig.4.9 (a)**. **Fig.4.9 (b)** shows an equivalent circuit for best fitted impedance plot. The impedance spectra of the electrodes are studied in three distinct regions. In the lower frequency region, the imaginary part of the impedance spectrum sharply increases indicate the supercapacitive behavior of β -LaS₂ electrode. The semicircle that appears on the real axis at higher frequency region is due to the internal resistance of electrolyte with contact of electrode [29]. From table of parameters in the **Fig.4.9 (b)** the electrolyte resistance R_s value is found to be $1.73 \Omega\text{cm}^{-2}$ and R_{ct} value is $4.93 \Omega\text{cm}^{-2}$ for β -LaS₂ electrode. The smaller values of R_s and R_{ct} ,

suggest that β -LaS₂ electrode allows easy access to electrolyte ions during charge/discharge process.

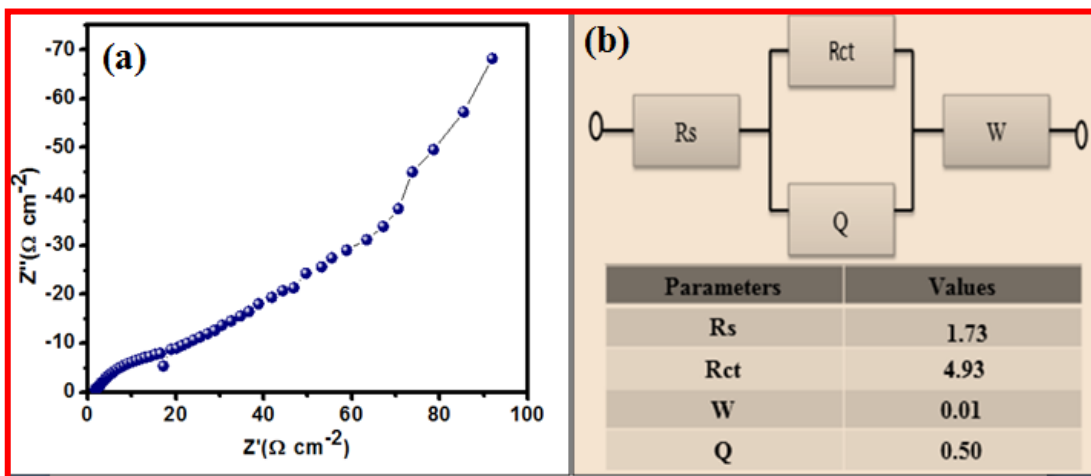


Fig.4.9 (a) Nyquist plot and (b) equivalent circuits fitted to Nyquist plot (inset of table of parameters of β -LaS₂ electrode).

Section-B.1

Synthesis of Lanthanum Sulfide (La_2S_3) and Graphene Oxide/ Lanthanum Sulfide ($\text{GO}/\text{La}_2\text{S}_3$) Composite Thin Film Using SILAR Method

4. B.1 Introduction-

The present section deals with the synthesis and characterization of $\text{GO}/\text{La}_2\text{S}_3$ composite thin film by simple and cost effective SILAR method at room temperature. In this experiment GO was used as base because the GO is a novel unique carbon material, has received tremendous attention because of its physical and chemical properties. It is an ideal matrix for growing and attracting great interest due to its high electrical conductivity, large specific area, structural flexibility, ultrathin thickness, good chemical stability, high surface to volume ratio good mechanical property comparable with or even better than CNT [19].

4. B.1.1 Experimental Setup of Graphene Oxide/Lanthanum Sulfide ($\text{GO}/\text{La}_2\text{S}_3$) Composite Thin Film Using SILAR Method:

In this experiment we have synthesized La_2S_3 and $\text{GO}/\text{La}_2\text{S}_3$ composite thin films by SILAR method and their structural, FT-IR, surface morphological, and wettability properties are studied.

(A) Lanthanum Sulfide (La_2S_3) Thin Film Synthesized by SILAR Method -

The deposition of lanthanum sulfide thin film by SILAR method comprises the successive immersion of the substrate in cationic precursor and anionic precursor solutions at room temperature. Aqueous 0.1 M $\text{LaCl}_3 \cdot 7\text{H}_2\text{O}$ solution was used as the cationic precursor and 0.05 M Na_2S solution was utilized as the anionic precursor. The cleaned stainless steel substrate

was immersed in the cationic precursor for 20 s, where La^{+3} ions were adsorbed on the substrate, followed by 10 s rinsing in DDW to remove the loosely bound species of La^{+3} . Successively, the substrate was dipped in the anionic precursor solution for 20 s to build a layer of lanthanum sulfide. Again, the substrate was rinsed for 10 s in DDW to take out the overloaded or unreacted species. In this way, one SILAR cycle of lanthanum sulfide deposition was completed and 100 such deposition cycles are reiterated to get the terminal thickness of the film. The schematic diagram of La_2S_3 film deposited is shown in **Fig.4.10**.

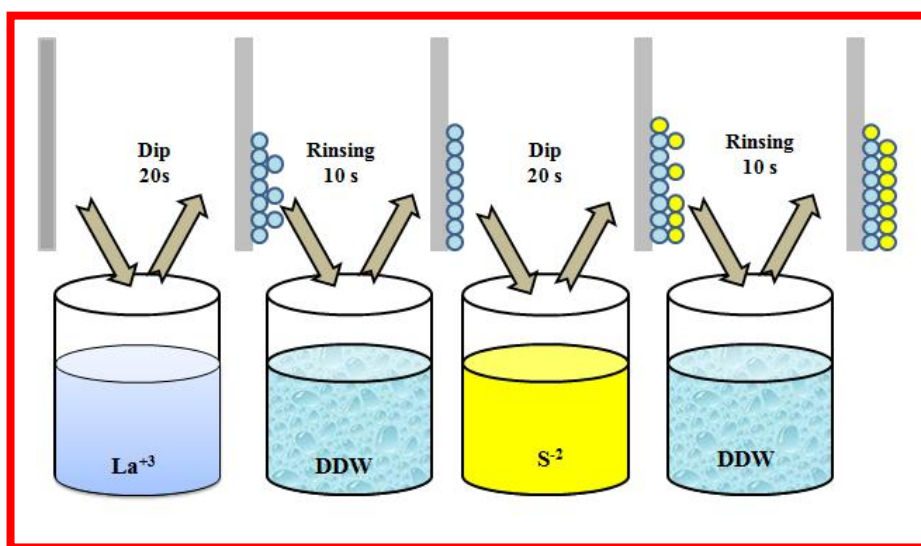


Fig.4.10: Schematic diagram of La_2S_3 thin film by SILAR method.

(B) $\text{GO}/\text{La}_2\text{S}_3$ Composite Thin Film Synthesized by SILAR Method

For the fabrication of composite thin films, the GO solution was used as the source of GO sheets; cationic precursor solution was 0.1 M $\text{LaCl}_3 \cdot 7\text{H}_2\text{O}$ and 0.05 M $\text{Na}_2\text{S} \cdot 9\text{H}_2\text{O}$ was an anionic precursor solution. The single layer of composite film through layer by layer (LBL) and SILAR methods was deposited using the procedure as follows. The well cleaned stainless steel substrate was immersed in a solution of GO for 40 s and then air dried for 20 s for GO sheets deposition on the substrate. Then the substrate was dipped in the cationic precursor solution for

20 s for the adsorption of lanthanum species on the GO sheets. Then, the substrate was rinsed in DDW for 10 s to remove loosely bound La^{+3} species. After, the substrate is immersed in the anionic precursor solution (S^{2-}) for 20 s a layer of lanthanum sulfide material is formed on GO sheets. Again, the substrate was rinsed in DDW for 10 s to separate out the overload or unreacted species. Thus, one cycle of the composite deposition is completed and 100 such deposition cycles were repeated to achieve an optimum thickness of the film. Schematic diagram of $\text{GO}/\text{La}_2\text{S}_3$ composite film deposited is shown in **Fig.4.11**.

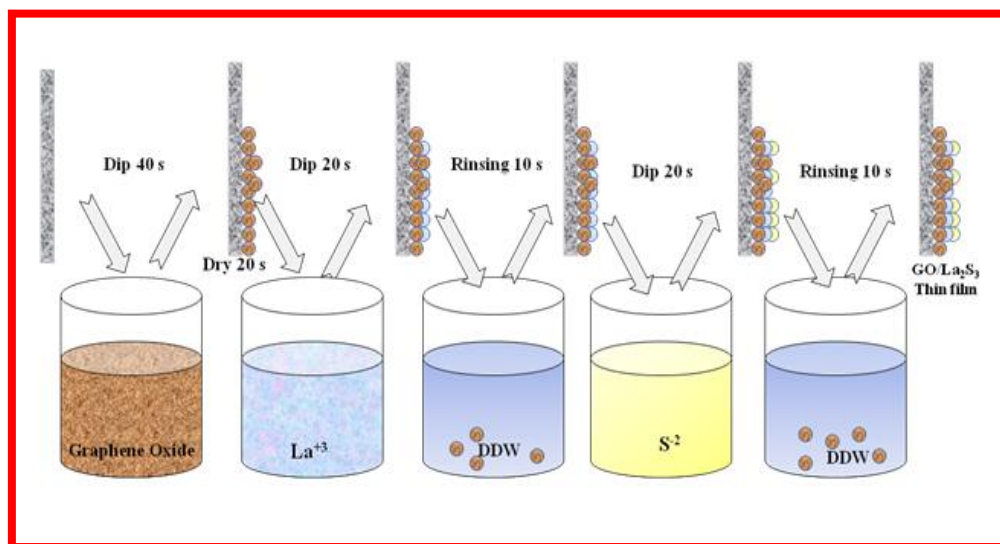


Fig.4.11: Schematic diagram of $\text{GO}/\text{La}_2\text{S}_3$ composite thin film by SILAR method.

4. B.1.2 Results and Discussion

(A) Graphene Oxide/Lanthanum Sulfide ($\text{GO}/\text{La}_2\text{S}_3$) Composite Thin Film Formation and Reaction:

$\text{GO}/\text{La}_2\text{S}_3$ composite thin film was synthesized by dipping a substrate into aqueous solutions of GO, $\text{LaCl}_3 \cdot 7\text{H}_2\text{O}$, and $\text{Na}_2 \text{S} \cdot 9\text{H}_2\text{O}$ separately. The SILAR process is mainly based on ion by ion deposition, which shows the deposition at nucleation places on the immersed surfaces of stainless steel (SS) substrate. The growth mechanism of $\text{GO}/\text{La}_2\text{S}_3$ composite thin

film by SILAR method is represented as follows. When $\text{LaCl}_3 \cdot 7\text{H}_2\text{O}$, and $\text{Na}_2\text{S} \cdot 9\text{H}_2\text{O}$ separately dissolved in DDW water, following two reactions occurred (4.6) and (4.7);



When SS substrate is immersed in the dispersed GO solution for 40 s, the GO nano sheets are adsorbed on the SS substrate and the dark brown color is formed on the substrate. Then GO deposited film immersed into cationic solution of La^{3+} ions then La^{3+} ions are adsorbed on the GO nanosheets due to the attractive forces between the GO nanosheets deposited substrate and the La^{3+} ions [30]. These forces may be cohesive, van der Waals forces or chemical attractive forces and then this substrate immersed into S^{2-} anionic solution. During this process, GO/La^{3+} ions react with S^{2-} ions from the Na_2S anionic solution. Possible reaction is shown below,



In the aqueous solution, Na_2S dissolves to form S^{2-} ions that are at the same time hydrolyzed to generate HS^- and H_2S species. These species serve as the sulfur sources for the ion-exchange reaction that converts 'La' precursors to form La_2S_3 .

(B) XRD Study

The crystal structure of La_2S_3 and $\text{GO/La}_2\text{S}_3$ composite thin films was examined by XRD analysis. **Fig. 4.12** shows the XRD patterns of La_2S_3 and $\text{GO/La}_2\text{S}_3$ composite thin films. All the diffraction peaks are well indexed to the orthorhombic crystal structure of La_2S_3 (JCPDS 21-0459). The sharp and intense peaks located at $2\theta = 10.1^\circ$ indicates GO material. Patil et al [16]

prepared La_2S_3 thin film by CBD method and reported orthorhombic crystal structure. The results confirm that La_2S_3 and $\text{GO/La}_2\text{S}_3$ composites are successfully synthesized. The estimated crystallite size for (130) and (220) planes for La_2S_3 and $\text{GO/La}_2\text{S}_3$ composite thin films is found to be 1.4 and 5.4 nm, respectively.

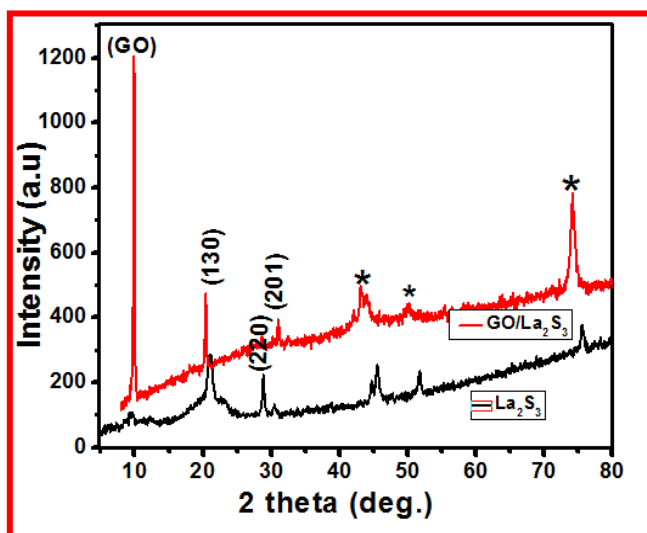


Fig. 4.12 XRD patterns of La_2S_3 and $\text{GO/La}_2\text{S}_3$ composite thin films.

(C) FT-IR Study

Fig. 4.13 demonstrates the FTIR spectra of La_2S_3 and $\text{GO/La}_2\text{S}_3$ composite films in the range of $4000\text{--}450\text{ cm}^{-1}$. The FTIR spectra reveal the chemical information and main functional groups presented in La_2S_3 and $\text{GO/La}_2\text{S}_3$ composite materials. The broad band observed at 3336.01 cm^{-1} is assigned to the symmetric stretching vibrational mode of hydroxyl groups in the La_2S_3 and $\text{GO/La}_2\text{S}_3$ composite film. The two narrow absorption bands at 637.0 and 734.45 cm^{-1} are assigned to the pairing mode between La-S stretching modes of tetrahedral and octahedral sites in La_2S_3 and $\text{GO/La}_2\text{S}_3$ composite films [31].

For GO/La₂S₃ composite thin film, increase in intensity of bands may be related to the quality of material. It suggests an increase in the number of functional groups, which indicates a good quality of GO/La₂S₃ composite film. The absorption peaks at 1639 and 1451.32 cm⁻¹ are related with vibrations mode of C=C aromatics and C=O carboxyl groups in the GO [32]. However, in GO/La₂S₃ spectrum, the bands at 1356.14 and 1130.28 cm⁻¹ are attributed to vibrations of the surface adsorbed O-H molecules and carbonate ions present in the atmosphere with “La” atoms. While for GO/La₂S₃ composite spectrum, the vibrational bands of C=C aromatics and C=O carboxyl groups of GO overlap with the vibration mode of the OH- group and carbonate ions from La₂S₃. The absorption bands around 847.01 cm⁻¹ in the composite material are allocated to the existence of C=O epoxy and C=O alkoxy groups. In addition, the bands at 2875.22 cm⁻¹ possibly attributed to -CH₂ and C-H groups in the La₂S₃ and GO/La₂S₃ composite. These characteristic bands confirm the formation of La₂S₃ and GO/La₂S₃ composite thin films.

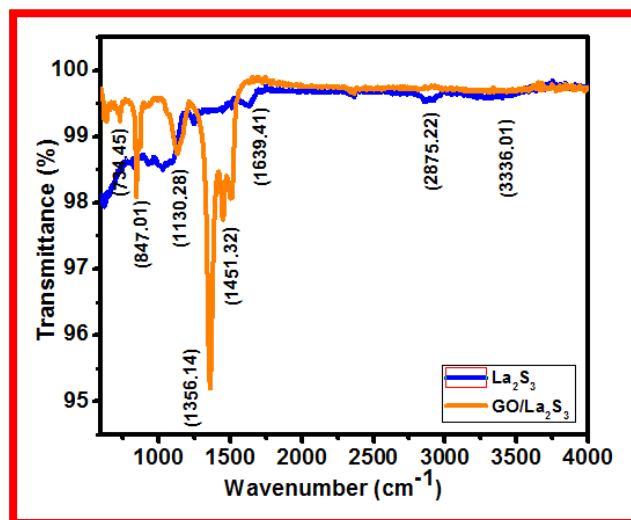


Fig. 4.13 FT-IR spectra of La₂S₃ and GO/La₂S₃ composite thin films.

(D) FE-SEM Study

The surface morphology of thin film plays an important role in the supercapacitive performance of material. The FE-SEM micrographs of La_2S_3 and $\text{GO}/\text{La}_2\text{S}_3$ nanocomposite thin films are shown in **Fig.4.14 (a-f)**. The La_2S_3 images at different magnifications 1 kX, 3 kX and 5 kX magnifications, respectively shown in **Fig.4.14 (a-c)**. The cracks are observed on the surface of La_2S_3 thin film but the particles are strongly interconnected to each other (**Fig.4.14 (a, b)**). At higher magnification (5 kX) pores are observed on the surface of La_2S_3 Thin film (**Fig.4.14(c)**). **Patil et al [20]** synthesized $\alpha\text{-La}_2\text{S}_3$ thin film using SILAR method and obtained porous morphology with small grains distributed over the substrate of the surface. The composition with GO in the La_2S_3 thin film changes surface morphology to grass-lawn like as presented in the (**Fig.4.14 (d-f)**). At magnification of 2 kX it is observed the GO nano-sheets are uniformly distributed on the substrate while at higher magnification (40 kX and 100 kX) grass petals like shape of GO sheets are observed coated with La_2S_3 nano-particles inset of **Fig.4.14 (d)** shows SEM image of GO thin film. The size of petals is typically in 150-250 nm. The change in surface morphology is observed with composition of GO. Similar, observations were reported by Gund et al [30] for $\text{GO}/\text{Mn}_3\text{O}_4$ composite thin film.

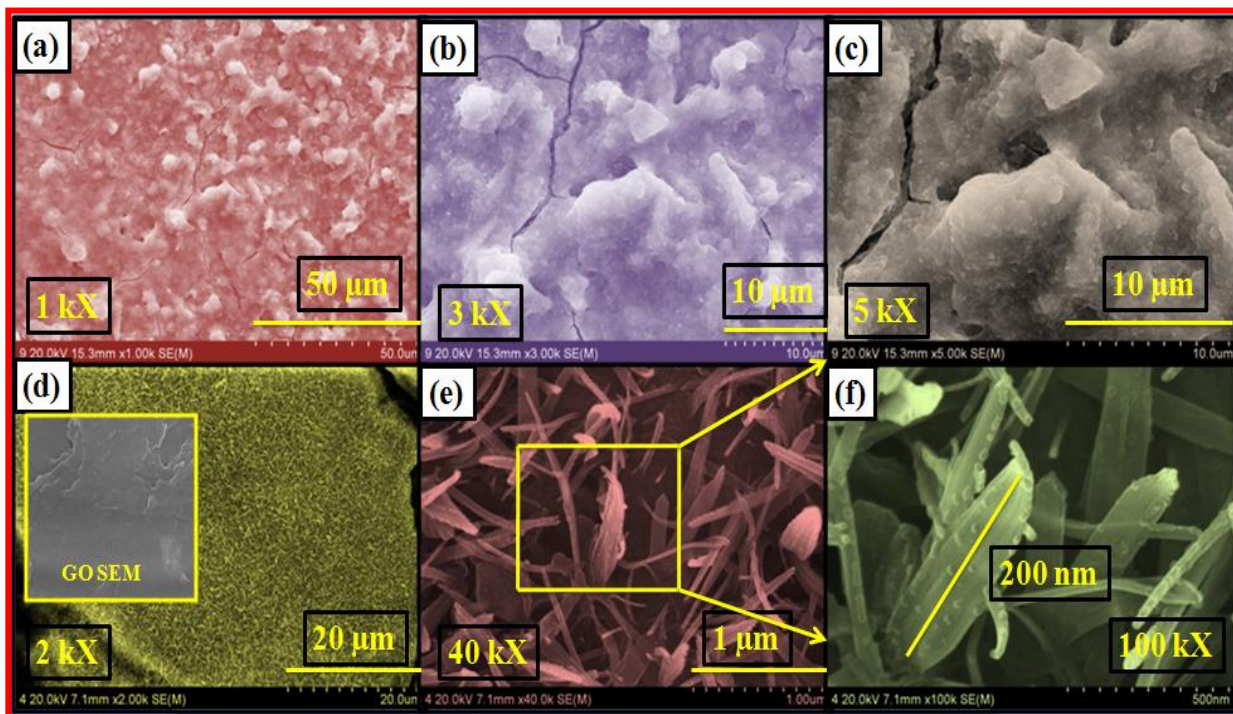


Fig. 4.14 FE-SEM images of La_2S_3 at (a) 1 kX, (b) 3 kX (c) 5 kX and GO/ La_2S_3 composite thin films at 2 kX, (e) 40 kX and (f) 100 kX magnifications.

(E) Surface Wettability Study

The angle formed between the liquid–solid interface and the liquid–vapor interface is the contact angle. The static sessile drop contact angle is measured by a contact angle goniometer using an optical subsystem to capture the profile of a pure liquid on a solid substrate. For the controlling or modifying of electrode surface wettability is an important aspect of the application of supercapacitor [33]. The water contact angle measurement photographs of films are shown in **Fig.4.15 (a, b)**. The La_2S_3 and GO/ La_2S_3 composite films show the contact angles of 47.6° and 37.2° , respectively. This specific property is attributed to nanocrystalline nature that is expected to have high surface energy. Nanocrystalline material with hydrophilic nature is a major

requirement for supercapacitor electrodes. This is useful for making close contact of aqueous electrolyte with the surface of film in supercapacitor application.

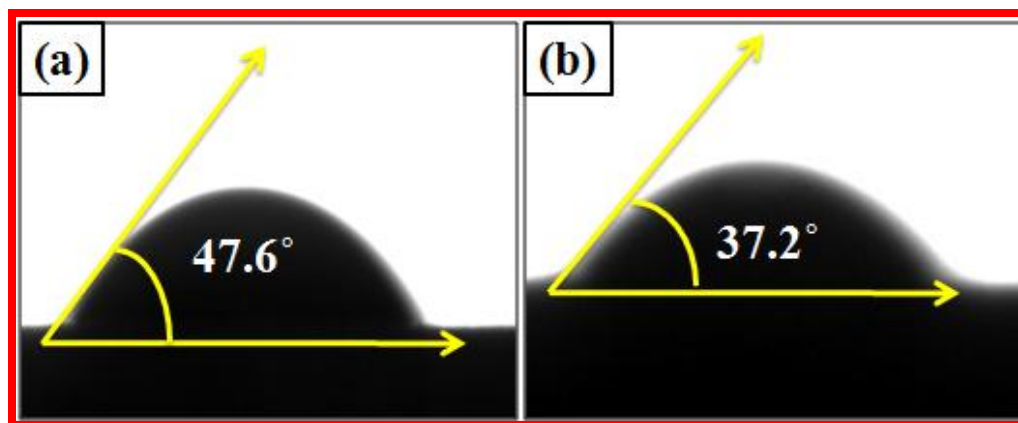


Fig. 4.15 Contact angles of (a) La_2S_3 and (b) $\text{GO/La}_2\text{S}_3$ composite thin films.

(F) BET Study

The specific surface area, pore size distribution and mesoporosity of $\text{GO/La}_2\text{S}_3$ composite material are obtained from N_2 adsorption-desorption isotherms as shown in **Fig. 4.16**. Inset of **Fig. 4.16**, it is seen that the isotherm has typical type II form with a hysteresis loop at high relative pressure. From the adsorption isotherm, the BET specific surface area is calculated to be $32.36 \text{ m}^2\text{g}^{-1}$. The $\text{GO/La}_2\text{S}_3$ composite reveals mesoporous nature with maximum pore size of 19 nm. With such specific surface area and mesoporous nature, $\text{GO/La}_2\text{S}_3$ composite material may enhance the electron and ion transport through ordered mesoporous channels, which subsequently results in higher electrochemical performance.

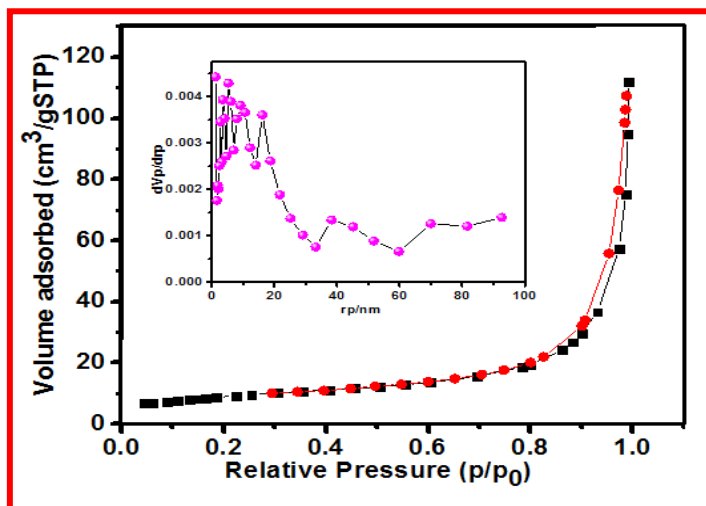


Fig. 4.16: Nitrogen adsorption-desorption isotherms and inset shows pore size distribution curve of GO/La₂S₃ composite material.

(G) XPS Study-

The XPS spectra of GO/La₂S₃ composite thin film are shown in **Fig. 4.17 (a-d)**.

Fig. 4.17(a) reveals the survey scan spectrum of GO/La₂S₃ composite thin film, which shows characteristic peaks for C, La, O and S elements. The La3d core level spectrum of La3d and La3d5A and La3d5B are fitted with four Gaussian peaks as shown in **Fig. 4.17 (b)**. Further, **Fig. 4.17 (c)** shows O1s core level spectrum with four distinct peaks. The peaks situated at binding energies of 531.3, 532, 529.5 and 533.2 eV are indexed to the oxygen atoms in the hydroxyl groups (La–O–H) and adsorbed water (H–O–H). The strong peak appearing at 529.5 eV is assigned to the oxygen atoms in GO (La–O) [31]. **Fig. 4.17 (c)** shows C1s core level spectrum of C1sA, C1sB, C1sC and C1sD are attributed at binding energies of 170.04 and 166.68 eV corresponds to carbon state. **Fig. 4.17 (d)** shows the binding energy peak at 171.0 eV corresponds to S⁻² sulfide state of La₂S₃. The peak at 167.6 eV belongs to the existence of sulfur (S) layer on

the film surface. The results obtained from XPS analysis confirm the formation of GO/La₂S₃ composite thin film, which agrees well with the XRD data.

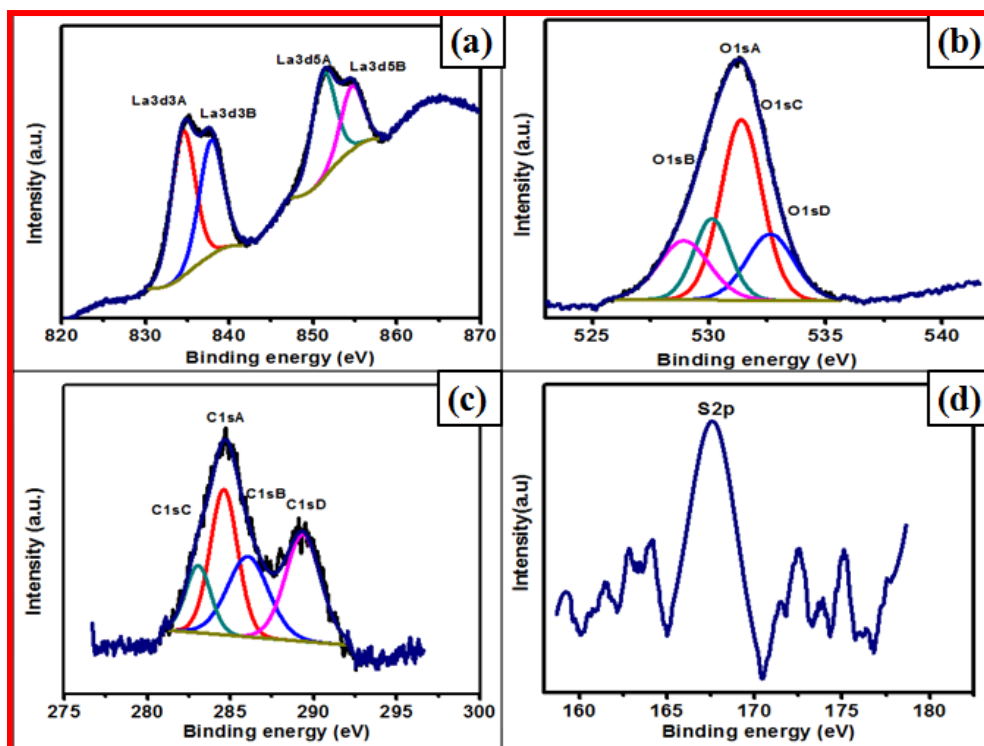


Fig.4.17 : XPS spectra (a) lanthanum region, (b) oxygen region, (c) carbon region, and (d) sulfide region of GO/La₂S₃ composite thin film.

SECTION-B.2

Supercapacitive Performance Evaluation of La_2S_3 and $\text{GO/La}_2\text{S}_3$ Composite Thin Films

4. B.2 Introduction:

The La_2S_3 and $\text{GO/La}_2\text{S}_3$ composite thin films are used as a supercapacitor electrode. The various electrochemical techniques such as CV, GCD, and cyclic stability and EIS studies were used in order to examine the electrochemical performance of $\text{GO/La}_2\text{S}_3$ composite thin films.

4. B.2.1 Results and discussion

(A) CV Study

(I) La_2S_3 Thin Film Electrode

The highly porous microstructure of thin film plays a significant role in supercapacitor application. The composite material formed with Mn_3O_4 [34], NiS [35] or conducting polymer [36] with GO have demonstrated the improved capacitive performance and cycle life through the synergistic effect of both EDLC and pseudocapacitance mechanisms [37]. A cyclic voltammetry (CV) measurement of La_2S_3 thin films was performed at a different scan rate of 5 – 100 mVs^{-1} in the potential window between -1.0 to 0 V/SCE in 1 M Na_2SO_4 electrolyte to check current response of electrode. The CV curves of any material assure the capacitive feature. As increase in scan rate, the electrochemical intercalation/deintercalation reactions happen only on the surface of electrode material, so the contribution of electroactive material is lower as compared with lower scan rate, therefore the specific capacitance value decreases as the scan rate increases as shown in **Fig.4.18 (a)**. The charging/discharging process of La_2S_3 electrode in Na_2SO_4 electrolyte is given as follows,



The increment in current response with the scan rate depicts capacitive behavior. The specific capacitances (C_s) of 181.2, 109, 50, 21.8 and 13.6 Fg^{-1} are decreased with increasing scan rate as seen in **Fig.4.18 (b)**. The decreased capacitance at higher scan rate is attributed to the incomplete utilization of the active electrode sites due to the limited time domain.

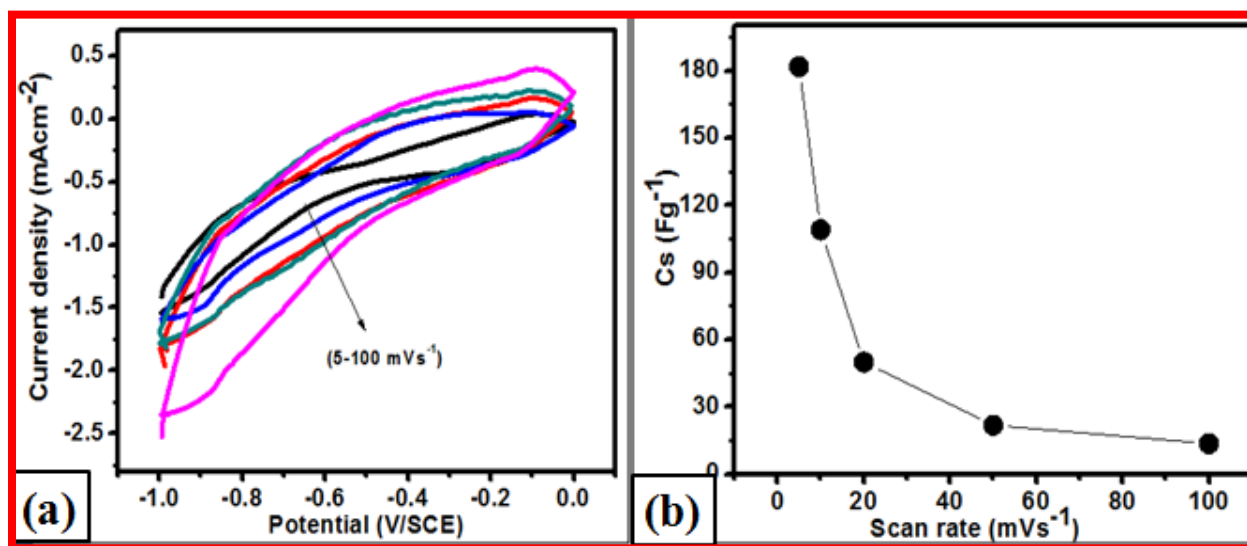


Fig. 4.18: (a) The CV curves at scan rates of (5–100 mVs^{-1}) and (b) Variation of specific capacitance Vs scan rate of La_2S_3 thin film electrode.

(II) GO/ La_2S_3 Thin Film Electrode

Graphene oxide based composite thin film considered as one of the mainly capable materials for the supercapacitors due to its unique structural and property features such as (a) the two-dimensional structure can provide a large surface area, which serves as an wide transport way for electrolytes [38]; (b) the high conductivity of graphene oxide sheets enables a low diffusion resistance, therefore leading to improved power and energy density; and c) the superior mechanical property makes graphene oxide nano-sheets being simply assembled into free-

standing films with strong mechanical stability. The composite thin films have attracted much attention due to the tunable thickness, structural flexibility, lightweight and electrical properties, which are the essential qualities required for supercapacitors [39].

The CV curves of GO/La₂S₃ composite electrodes are obtained at different scan rates of 5-100 mVs⁻¹ in 1 M Na₂SO₄ electrolyte (**Fig.4.19 (a)**). In the GO/La₂S₃ composite, incorporation of small amounts of carbon black nano particles as spacers between graphene oxide nano-sheets, provides an unlock structure for charge storage and ion diffusion channel therefore, resulting in a significant improvement in electrochemical performance. As seen from the **Fig.4.19 (b)**, the CV curves of GO/La₂S₃ composite electrode and specific capacitance decreased from with the increased scan rate in the range of 5-100 mVs⁻¹. The decreased capacitance attributed to the incomplete utilization of the active electrode sites due to the limited time domain.

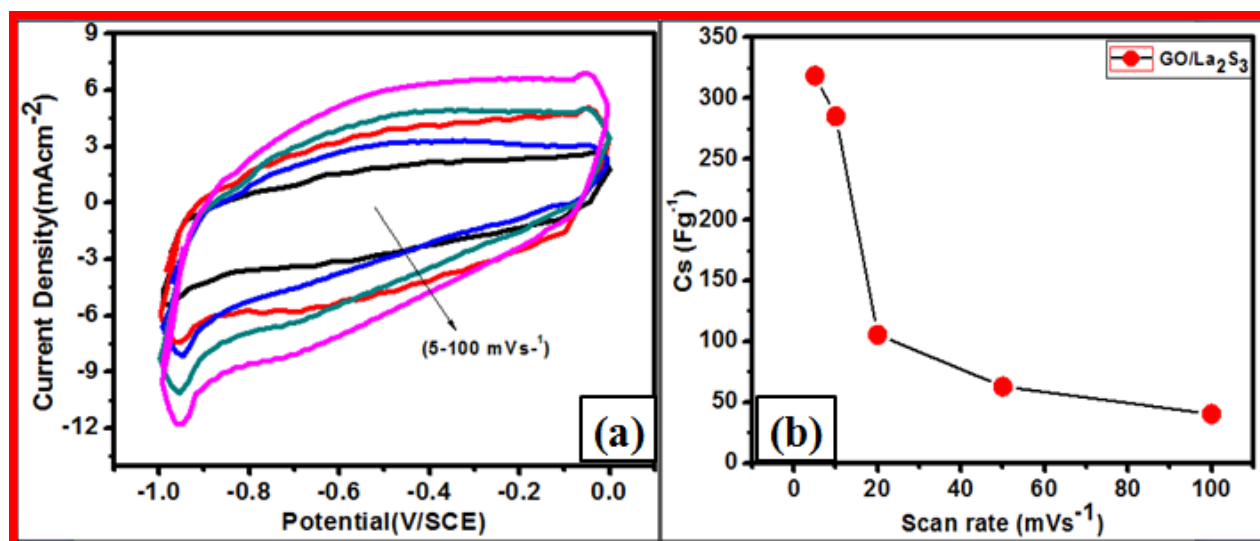


Fig. 4.19: (a) The CV curves at scan rates of 5 – 100 mVs⁻¹ and (b) variation of specific capacitance Vs scan rate of GO/La₂S₃ composite thin film electrode.

(B) GCD Study

(I) La_2S_3 Thin Film

The galvanostatic charge/discharge (GCD) curves of La_2S_3 electrode at different current densities ranging from 0.3, 0.4 to 0.6 mAcm^{-2} within the potential window at 0 to -1.0 V/SCE is displayed in **Fig.4.20 (a)**. All GCD curves are non-triangular shapes, not perfect straight lines, which approves the presence of redox reactions at the electrode and electrolyte interface. The porous surface morphology of La_2S_3 electrode offers more electroactive material interface for easy interaction of electrolyte ions with the electrode material provides fast charge transfer. The more number of electrolyte ions pass inside the electrode pores as time availability is more at lower current density. By using the discharge curve, the specific and areal capacitances were calculated at various current densities of 0.3, 0.4, and 0.6 mAcm^{-2} . The variation C_s with different current densities is shown in **Fig.4.20 (b)**. Patil et al [16] reported C_s of La_2S_3 electrode has a maximum specific capacitance of 202 Fg^{-1} at a current density of 0.7 mAcm^{-2} .

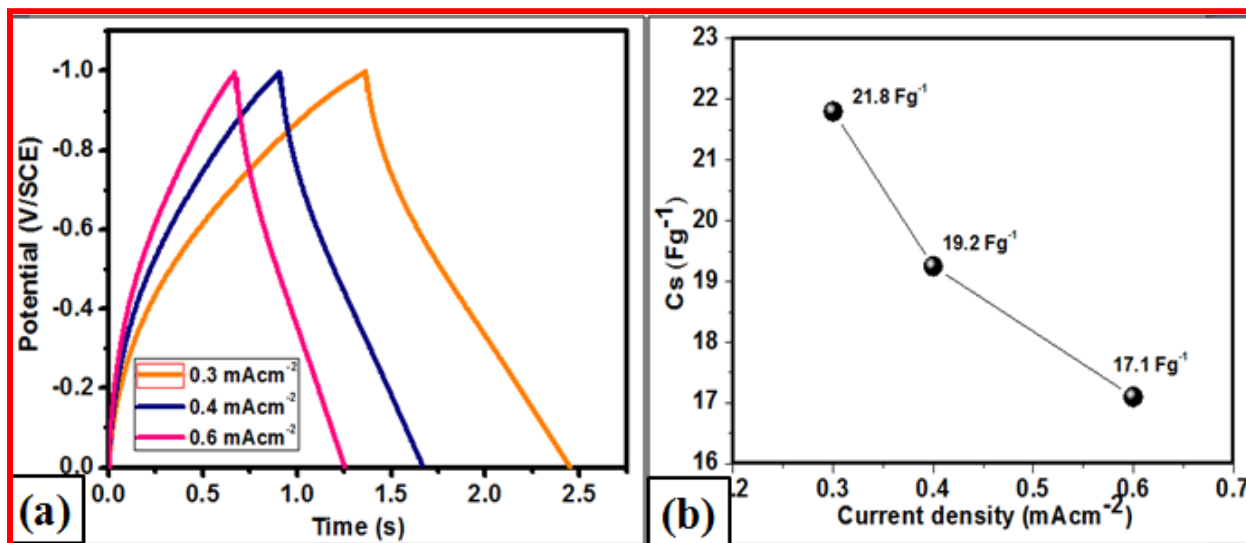


Fig. 4.20: (a) GCD curves of La_2S_3 at 0.3, 0.4 and 0.6 mAcm^{-2} current densities, and (b) C_s with different current densities.

(II) GO/La₂S₃ Composite Thin Film

Furthermore, from GCD study rate capability of GO/La₂S₃ composite thin film electrode is carried out. **Fig.4.21 (a)** illustrates GCD curves at different current densities (0.3, 0.4 to 0.6 mAcm⁻²). The non-linear behavior of charging/discharging curves; suggest the fast and reversible surface redox reactions. The Cs from GCD curves is calculated using **eq. (2.8)**. The calculated Cs of GO/La₂S₃ composite thin film electrodes at different current densities are shown in **Fig.4.21 (b)**. At high current densities, electrode discharges at a faster rate, hence the low Cs is achieved, whereas at low current density electrode discharges and slowly contributes to high Cs [40].

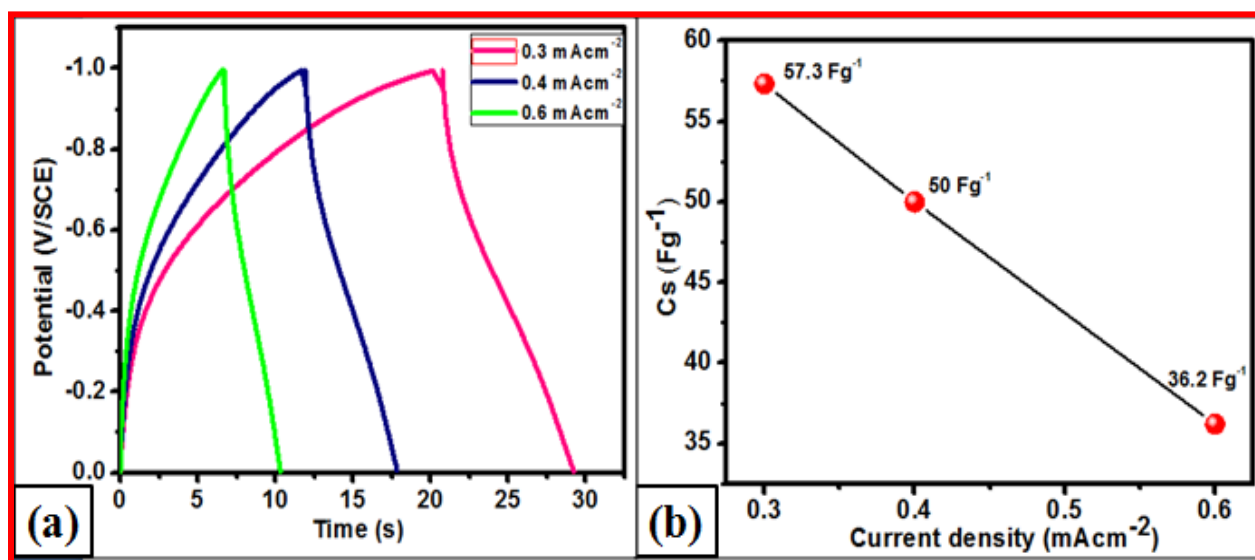


Fig. 4.21: (a) GCD curves of GO/La₂S₃ at 0.5, 0.7, 0.8 and 0.9 mAcm⁻² different current densities, and (b) Cs with different current densities.

(C) Stability Studies-

Cycling stability is one key factor for finding the use of supercapacitor electrodes for many practical applications. The stability test is performed for 1000 CV cycles at a scan rate of 100 mVs^{-1} . **Fig.4.22 (a)** shows plot of capacity retention with respect to number of cycles for La_2S_3 electrode. Inset of **Fig.4.22 (a)** shows the CV curve of 2nd and 1000th cycles. The 85.6 % capacitance retained after 1000th cycles. The loss of capacitance is attributed to slight degradation of active electrode material during cycling. Further, **Fig.4.22 (b)** exhibits capacitive retention of $\text{GO/La}_2\text{S}_3$ composite electrode for increasing cycles and shows upto 88.6 % capacitance retention after 1000 CV cycles. Inset of **Fig.4.22 (b)** shows number CV curves recorded at different CV cycles such as 2nd and 1000th. During the charge/discharge process, Na^+ ions from the electrolyte are involved in the charge storage process of $\text{GO/La}_2\text{S}_3$ electrode [40]. A $\text{GO/La}_2\text{S}_3$ composite electrode exhibits good capacitive retention over 1,000 cycles than La_2S_3 electrode. The ionic pathway of electrolytic ions defuses to approach electroactive sites in the denser electrode, which leads to drop the capacitance values along with varying cycles.

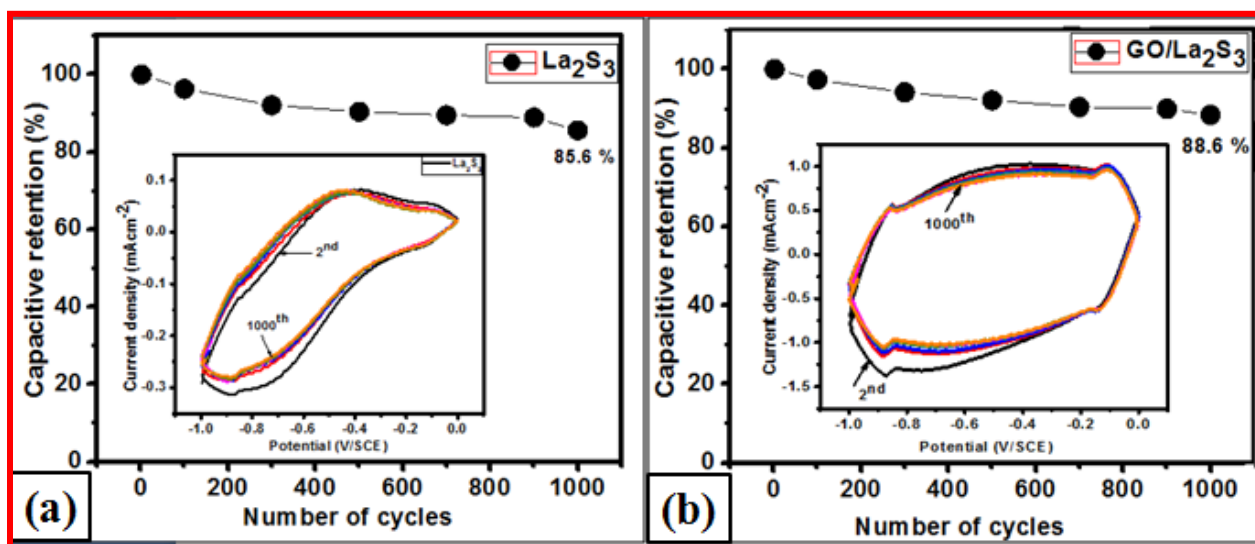


Fig. 4.22: Capacitive retention of (a) La_2S_3 and (b) $\text{GO}/\text{La}_2\text{S}_3$ composite electrodes with inset no. of CV cycles of La_2S_3 electrodes.

(D) EIS Study-

Fig.4.23 (a) shows Nyquist plots of La_2S_3 and $\text{GO}/\text{La}_2\text{S}_3$ composite electrodes in 1 M Na_2SO_4 solution in the frequency region of 100 kHz to 100 mHz at 10 mV AC amplitude. The Nyquist plots consist of semicircle arc in the high frequency reactions and double-layer capacitance at the electrode/electrolyte interface as shown in magnified **Fig. 4.23(b)**. A straight line resulting in the low-frequency region is related to the diffusion of electrolyte ions into the active material. The series resistance (R_s : $0.45 \Omega \text{ cm}^{-2}$) and charge transfer resistance (R_{ct} : $3.64 \Omega \text{ cm}^{-2}$) are estimated for $\text{GO}/\text{La}_2\text{S}_3$ composite electrode. The Nyquist plot clearly demonstrate that the composite electrode provides easier way (less resistance) for intercalation and deintercalation of charges compared to La_2S_3 (R_s : $1.30 \Omega \text{ cm}^{-2}$) and (R_{ct} : $6.59 \Omega \text{ cm}^{-2}$) and also offers compact bonding with stainless steel electrode. Inset of **Fig.4.23 (b)** shows the best fitted equivalent circuit of Nyquist plot.

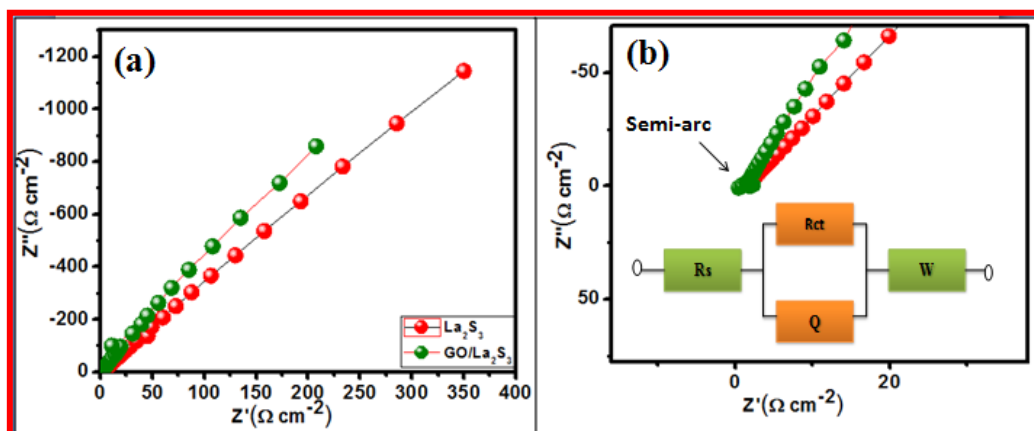


Fig. 4.23: Nyquist plots of (a) La_2S_3 and $\text{GO}/\text{La}_2\text{S}_3$ composite electrodes and (b) magnified Nyquist plots with inset of equivalent circuit.

4.3 Conclusions

In conclusion, the nanostructured β -LaS₂ thin film is synthesized by hydrothermal method and La₂S₃ and GO/La₂S₃ composite thin films are synthesized by SILAR method. According to results, we observed that β -LaS₂ thin film by hydrothermal method shows petals-like surface morphology with specific capacitance of 121.42 Fg⁻¹ at 5 mVs⁻¹ scan rate with cyclic stability is 84.20 % over the 1000th cycles. The La₂S₃ thin film prepared by SILAR method shows compact surface morphology with cracks and value of Cs is 181.2 Fg⁻¹ at 5 mVs⁻¹ scan rate with cyclic stability is 83.6 % after 1000th cycles. So, SILAR prepared La₂S₃ thin film shows higher Cs and superior cyclic stability than hydrothermal prepared β -LaS₂ thin film. The composition of GO in La₂S₃ by SILAR method shows increased surface area with increasing electrical conductivity than La₂S₃. The grass-like surface morphology is important in supercapacitor application. The Cs is 318 Fg⁻¹ at 5 mVs⁻¹ scan rate with higher cyclic stability of 88.6 % over the 1000th cycles. The obtained Rs and Rct values of GO/La₂S₃ composite are lower than β -LaS₂ and La₂S₃ thin film electrodes. The electrochemical analysis indicates that GO based La₂S₃ composite thin film can be used as an electrode for supercapacitor device fabrication. The electrochemical results are given in **Table 4.1**

Table 4.1: Electrochemical parameters of β -LaS₂, La₂S₃ and GO/La₂S₃ composite thin film electrodes.

Thin film	Method	Cs (Fg ⁻¹)	Rs (Ω cm ⁻²)	Rct (Ω cm ⁻²)	Stability (%)	Cycles
β -LaS ₂	Hydrothermal	121.42	1.73	4.93	84.20	1000
La ₂ S ₃	SILAR	181.2	1.30	6.59	85.6	1000
GO/La ₂ S ₃	SILAR	318	0.45	3.64	88.67	1000

References:

1. L.L. Zhang, X.S. Zhao, Chem. Soc. Rev. **38** (2009) 2520–2531.
2. B.E. Conway, J. Electrochem. Soc. **138** (1991) 1539–1548.
3. S. Kondrat, A.A. Kornyshev, Nanoscale Horiz. **1** (2016) 45–52.
4. D.P. Dubal, P.G. Romero, B.R. Sankapal, R. Holze, Nano Energy **11** (2015) 377–399.
5. G.E. Goikolea, J.A. Barrena, R. Mysyk, Sustain. Eng. Rev. **58** (2016) 1189–1206.
6. V. Balaram, Geosci. Front. **10** (2019), 1285–1303.
7. M. Mehmood, J. Ecol. & Nat. Resour. **2** (2018) 000128–000131.
8. I. A. Kariper, Prog. Nat. Sci-Mater., **24** (2014) 663–670.
9. S.J. Patil, V.C. Lokhande, N.R. Chodankar, C.D. Lokhande, J. Colloid Interface Sci., **469** (2016), 318–324.
10. L.K. Wu, L. Liu, J. Li, J.M. Hu, J.Q. Zhang, C.N. Cao, Surf. Coat. Technol. **204** (2010) 3920–3926.
11. K. Paulraj, S. Ramaswamy, Mohd Shkir, I. S. Yahia, Mohamed S. Hamdy, S. Alfaify, J. Mater. Sci. Mater., **31** (2020), 1817–1827.
12. M. Hirano and E. Kato, J. Am. Ceram. Soc., **82** (1999), 786–88.
13. N. Maheswari and G. Muralidharan, Energy Fuels **29** (2015), 8248–8253.
14. S.J. Patil, R. N. Bulakhe, C. D. Lokhande, ChemPlusChem **80** (2015), 1478–1480.
15. S.J. Patil, C.D. Lokhande, Mater. Des., **87** (2015), 939–948.
16. S.J. Patil, V.S. Kumbhar, B.H. Patil, R.N. Bulakhe, C.D. Lokhande, J. Alloys Compd. **611** (2014), 191–196.
17. P.N. Kumata, S.H. Risbud, J. Mater. Sci. Eng. B. **18** (1993), 260–268.
18. H. Wan, X. Ji, J. Jiang, J. Yu, L. Zhang, S. Bie, H. Chen, Y. Ruan, J. Power source, **243** (2013), 396–402.
19. A.A. Yadav, V.C. Lokhande, R.N. Bulakhe, C.D. Lokhande, Microchim. Acta **184** (2017), 3713–3720.
20. N. Tang, W. Wang, H. You, Z. Zhai, J. Hilario, L. Zeng, L. Zhang, Catal. Today. **330** (2018) 286–291.
21. L. Peisen, L. Huanyong, J. Wanqi, J. Rare Earth, **29** (2011) 317–319.

22. D.P. Dubal, D.S. Dhawale, R.R. Salunkhe, S.M. Pawar, C.D. Lokhande, Appl. Surf. Sci. **256** (2010), 4411- 4416.
23. D.P. Dubal, D.S. Dhawale, R.R. Salunkhe, C.D. Lokhande, J. Alloys Compd., **496** (2010), 370-375.
24. B.Guan, Y.Li, B.Yin, K.Liu, D.Wang, H.Zhang, C.Chen, Chem. Eng., **308** (2017), 1165-1173.
25. J. S. Shayeh, A. Ehsani, M.R. Ganjali, P. Norouzi, B. Jaleh, Appl. Surf. Sci. **353** (2015) 594–599
26. P.A.Shinde, V.C.Lokhande, T.Ji, C.D.Lokhande, J. Colloid Interface Sci.**498** (2017) 202-209.
27. T.P. Gujar, V.R. Shinde, C.D. Lokhande, W.Y. Kim, K.D. Jung, O.S.Joo, Electrochem. commun. **9** (2007) 504–510.
28. R.B. Pujari, A.C. Lokhande, A.A. Yadav, J.H. Kim, C.D. Lokhande, Mater.Des., **108** (2016), 510-517.
29. R.Farma, M. Deraman, Awitdrus, I.A. Talib, R.Omar, J.G. Manjunatha, M.M.Ishak, N.H. Basri, B.N.M. Dolah, Int. J. Electrochem. Sci., **8** (2013) 257 – 273.
30. G.S. Gund, D.P. Dubal, B.H. Patil, S.S. Shinde, C.D. Lokhande, Electrochim. Acta., **92** (2013) 205-215.
31. S. Aripnammal and T.Srinivasan, Res. J. Recent Sci. **2** (2013) 102-105.
32. A.B.Nandiyanto, R.Oktiani, R.Ragadhita, Ind. J. Sci. Tech., **4** (2019) 97-118.
33. M.M. Vadiyar, S.C. Bhise, S.K. Patil, S.S. Kolekar, A.R. Shelke, N.G. Deshpande, J.Y. Chang, K.S. Ghule, A.V. Ghule, Chem. Commun., **52** (2016), 2557-2560
34. P. Rosaiah, J. Zhu, O. M. Hussain, Y. Qiu, Appl. Phys. A **124** (2018), 597-600.
35. A.Wang, H. Wang, S. Zhang, C. Mao, J. Song, H. Niu, B. Jin, Y. Tian, Appl. Surf. Sci. **282** (2013), 704–708.
36. K. Zhang, L.L. Zhang, X.S. Zhao, J. Wu, ACS. Chem. Mater., **22** (2010), 3509-3516.
37. T. Brousse, D. Belanger, J.W. Long, J. Electrochem. Soc., **162** (2015), A5185-A5189.
38. Q. Ke and J.Wang, J. Materiomics., **2** (2016), 37-54.
39. S. Z. Hussain, M.Ihrar, S.B. Hussain, W. C.Oh, K. Ullah, SN Appl. Sci., **2** (2020), 764-788.
40. T. Cottineau, M. Toupin, T. Delahaye, T. Brousse, D. Belanger, Appl. Phys. A. Mater. Sci. Process., **82** (2006) 599-606.

Chapter-5
Synthesis, Characterization and
Supercapacitive Performance
Evaluation of Manganese Oxide
Thin Film

Sr.No	Title				Page No.
5	Introduction				122
5.1	Synthesis of Manganese Oxide (MnO ₂) Thin Film by SILAR Method				123
	5.1.1	Experimental Setup For Deposition of Manganese Oxide (MnO ₂) Thin Film			123
	5.1.2	Material Characterization			124
	5.1.2.1	Results and Discussion			124
		(A)	MnO ₂ Thin Film Formation		125
		(B)	XRD Study		126
		(C)	FE-SEM Study		126
		(D)	FTIR Study		127
		(E)	BET Study		128
5.2	Supercapacitive Performance of MnO ₂ Thin Films				128
	5.2.1	Introduction			128
		5.2.1.1	Result and Discussion		129
		(A)	Cyclic Voltammetry (CV)Study		130
		(B)	GCD Study		131
		(C)	Stability Study		132
		(D)	EIS Study		133
5.3	Conclusions				133
References					134-135

5. Introduction:

Manganese dioxide (MnO_2) is one of the most attractive inorganic materials and is a stable compound with excellent chemical and physical properties [1, 2]. Due to its low cost, environmental friendliness, non-toxicity, as well as its structural flexibility and rich polymorphism (α -, β -, γ -, δ -, λ -, and ϵ -type), wide applications have been reported including as a catalyst [3], ion-sieve [4], and ion exchange material [5], and in biosensors [6], lithium ion batteries [7], and supercapacitors [8]. In particular, MnO_2 is a promising material as a replacement for RuO_2 in pseudocapacitors owing to its high theoretical capacitance of $1,233 \text{ Fg}^{-1}$ for a one-electron transfer and complete reduction of Mn IV to Mn III [9]. Moreover, it can be utilized in mild neutral aqueous electrolytes, which ensure environmental compatibility, safety, non-flammability, and convenient assembly in air.

Among various phases, γ - MnO_2 is most widely used in energy storage devices because its electrical activity decreases more slowly than other forms during the electrochemical process [10]. However, capacitances of only $100\text{--}300 \text{ Fg}^{-1}$ have been reported for MnO_2 powders [11], due to their poor electrical conductivity (10^{-5} to 10^{-6} Scm^{-1}) [12] and low available surface areas [13]. Thus, a MnO_2 electrode that provides a short diffusion path for electrolyte ions and a high electrical conductivity of the active materials is needed.

In present work, MnO_2 thin films are prepared at room temperature using SILAR method on cost effective stainless steel (SS) substrate. These films are evaluated from x-ray diffraction (XRD), field emission scanning electron microscopy (FE-SEM) analyses, FTIR and surface area analysis by (BET) studies. Supercapacitive properties of MnO_2 films are tested from cyclic

voltammetry (CV), galvanostatic charge discharge (GCD) and electrochemical impedance spectroscopy (EIS).

5.1. Synthesis of Manganese Oxide (MnO_2) Thin Films Using SILAR Method-

5.1.1 Experimental Setup for Deposition of Manganese Oxide Thin Film by SILAR -

All reagents of analytical grade were used without further purification. In a typical synthesis, 0.1 M solutions of MnSO_4 is used as the cationic precursor and 0.3 M NaOH solution was utilized as the anionic precursor. When cleaned stainless steel (SS) substrate was immersed in the cationic precursor for 20 s, Mn^{+2} ions were adsorbed on the substrate, followed by 10 s rinsing in DDW to remove the loosely bound species of Mn^{+2} . Successively, the substrate was dipped in the anionic precursor solution for 20 s to build a layer of manganese oxide. Again, the substrate was rinsed for 10 s in DDW to take out the overloaded or unreacted species. In this way, one SILAR cycle of dark brownish colored MnO_2 deposition was completed and 100 such deposition cycles were reiterated to get the terminal thickness of the film. **Fig.5.1** shows the schematic diagram of MnO_2 thin film deposition.

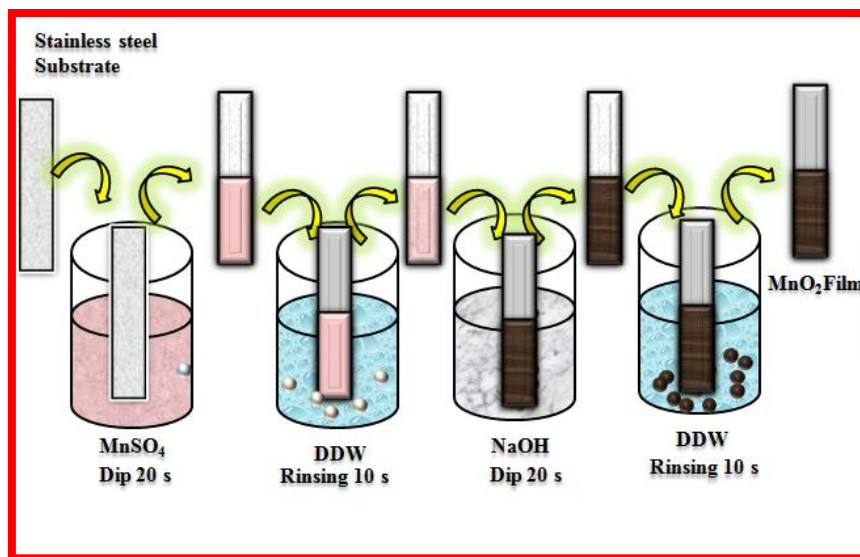


Fig.5.1: Schematic diagram for preparation of MnO_2 thin film by SILAR method.

5.1.2 Material Characterization-

The crystal structure of MnO_2 film was examined using a Bruker AXS D8 advance model X-ray diffractometer with primary monochromatic radiation from Cu $K\alpha$ line ($\lambda = 1.54 \text{ \AA}$) in the 2θ range of $20-80^\circ$. The surface morphology was observed using field emission scanning electron microscope (FE-SEM, JEOL-6360, Japan). The functional group detection was made by Fourier-transform infrared spectroscopy (FT-IR, Broker's, ALPHA-P). N_2 adsorption/desorption was determined by Brunauer-Emmett-Teller (BET) measurements using an ASAP-2010 surface analyzer. Electrochemical measurements of MnO_2 thin film were carried out using Zive MP1 model of Wonatech Company using three electrode cell, that consists of MnO_2 thin film as a working electrode, platinum strip as a counter electrode and the saturated calomel electrode (SCE) as a reference electrode.

5.1.2.1 Results and Discussion-

(A) Manganese Oxide Thin Film Formation -

MnO_2 thin films were fabricated by dipping the substrates into separately placed cationic and anionic precursors with rinsing among every dipping. The growth mechanism of a thin film deposition process is of the ion-by-ion type. The growth of the nucleation sites on the substrate results into formation of thin and adherent film. The MnO_2 thin film formation by SILAR method can be explained as follows. The solution of MnO_4 in water provides Mn^{2+} ions at pH ~ 6 and when substrate is dipped in this solution, Mn^{2+} ions get adsorbed onto the substrate as a result of attractive force between ions in the solution and substrate surface. These forces may be cohesive forces or van der Waals forces or chemical attractive forces. The immersion of substrate in NaOH anionic solution, where the chemical reaction between OH^- and Mn^{2+} ions leads to the formation of adherent MnO_2 layer [14].

(B) XRD Study

The **Fig.5.2** shows the XRD pattern of MnO_2 thin film grown on SS substrate. The characteristic diffraction peaks are indexable to MnO_2 with orthorhombic crystal structure matched with JCPDS card no (98-001-2179). The peaks are matched with (101), (202), (301) and (112) planes. The broader and intense peaks shown by an asterisk (*) in XRD pattern are due to SS substrate. The crystallite size calculated using Scherer's formula is 2.1 nm for (101) plane. The nanocrystalline nature may be helpful for supercapacitor application; as it ease rapid ion diffusion in the active electrode material, which increaseing the charge storing capacity of SCs [15].

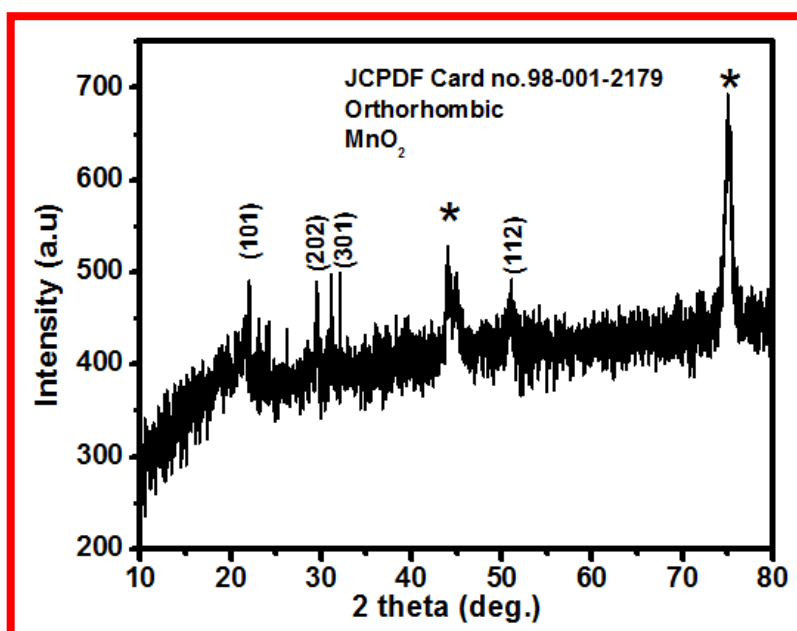


Fig. 5.2: The X-ray diffraction pattern of MnO_2 thin film.

(C) FE-SEM Study

The FE-SEM is a suitable technique to examine the surface morphological properties of thin film surface. **Fig. 5.3 (a, b)** shows the surface micrographs for MnO_2 thin film at two different magnifications (10 kX and 50 kX). **Fig.5.3 (a)** shows that the substrate is well covered with MnO_2 nanoparticles at 10 kX magnification. From the **Fig.5.3 (b)** the spherical nano-grain like surface

morphology of MnO_2 spread over whole surface with porous structure is observed. These nanoparticles are interconnected, forming porous structure. Gund et al [16] prepared MnO_2 thin film by SILAR method and obtained three-dimensional (3D) porous spherical nanoparticles surface morphology. The surface morphology of thin film plays an important role in SCs, because ion intercalation and deintercalation occur at the surface of the thin films. The most beneficial route to improve the rate of intercalation and deintercalation is to form a nanostructure thin film [17].

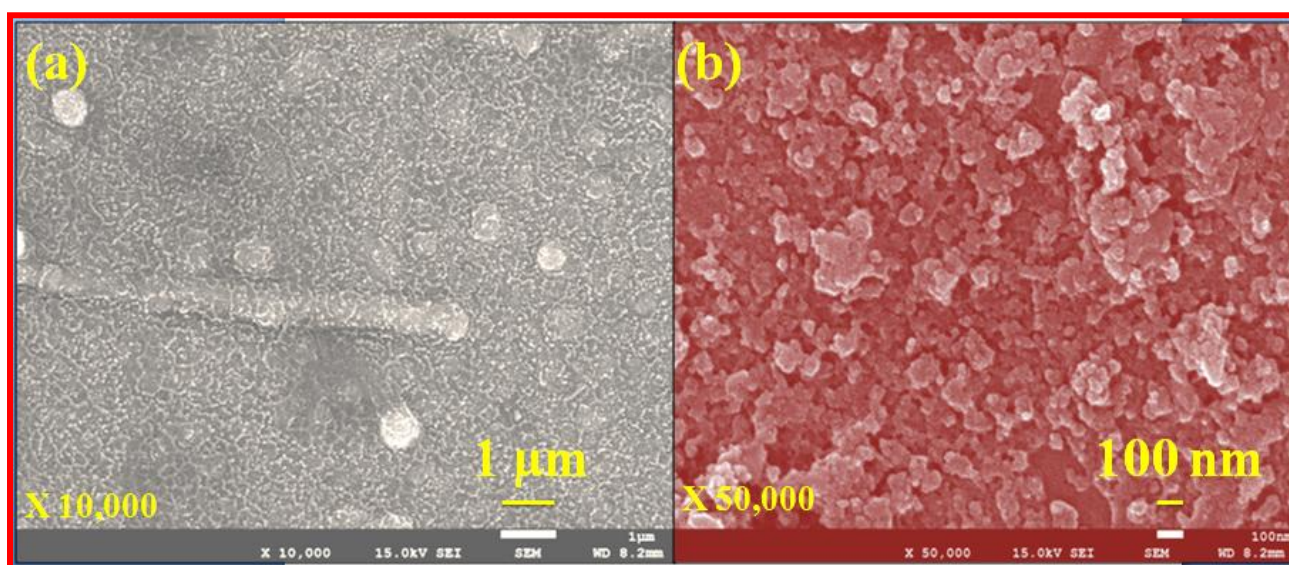


Fig.5.3: FE-SEM images of MnO_2 thin film at (a) 10 kX and (b) 50 kX magnifications.

D) FTIR Study

The FTIR absorption spectra of MnO_2 thin film in the range $4000\text{--}400\text{ cm}^{-1}$ are shown in **Fig.5.4**. The strong bands around at 539.22 cm^{-1} and 764.11 cm^{-1} are related with the characteristic vibrational mode of Mn–O lattice. The absorption peaks at around 1598.62 and 1060.6 cm^{-1} are assigned to –OH bending vibrations combined with Mn atoms [18]. The sharp absorption bands at 2212.3 and 3380.5 cm^{-1} are attributed to the –OH stretching vibrations. Thus results show that MnO_2 film contained hydroxide and Mn–O bonds, which indicate the structure of hydrous MnO_2 [19].

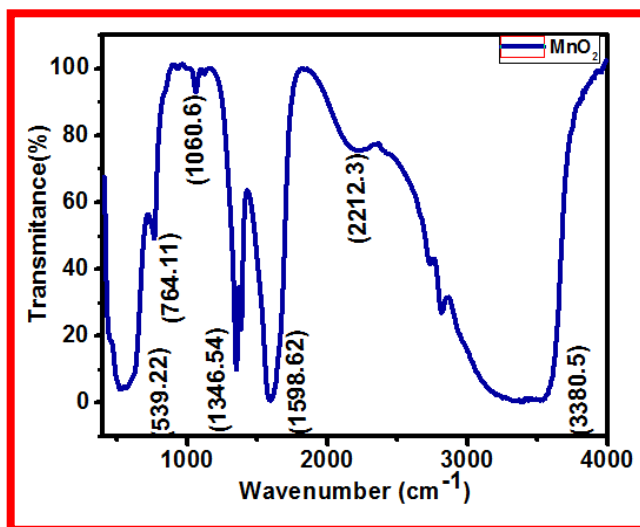


Fig.5.4: FTIR spectrum of MnO₂ thin film.

E) BET Study-

The specific surface area, average pore size, and mesoporous nature of active electrode material play significant role in enhancing the electrochemical performance. Thus, it is very important to determine the specific surface area and average pore volume by Brunauer–Emmett–Teller (BET) methods [20]. **Fig. 5.5 (a)** and **(b)** demonstrate the N₂ adsorption–desorption isotherm and corresponding BJH pore size distribution curve of MnO₂ thin films. A typical type IV form with a clear hysteresis loop at high relative pressure indicate the possession of a lot of mesopores on the 3D-structure matrix. This indicates the mesoporous nature of MnO₂ thin film. According to this result, it is clear that the prepared MnO₂ thin film possess relatively high BET specific surface areas of 23.91 m²g⁻¹. The corresponding pore size distribution calculated by using the Barrett–Joyner–Halenda (BJH) method from the desorption curve, confirms the mesoporous nature of MnO₂ thin film as shown in **Fig.5.5 (b)**. The average pore size distribution range of 10.65 nm, which is the best pore size for the diffusion of ions and electrons within an active electrode material is obtained. The porous nanostructured surface morphology with maximum specific surface area

and suitable pore volume have potential applications in supercapacitors, as it provides a large interface of active electrode material with an electrolyte solution and provides the maximum possible number of active sites for electrochemical reactions [21, 22].

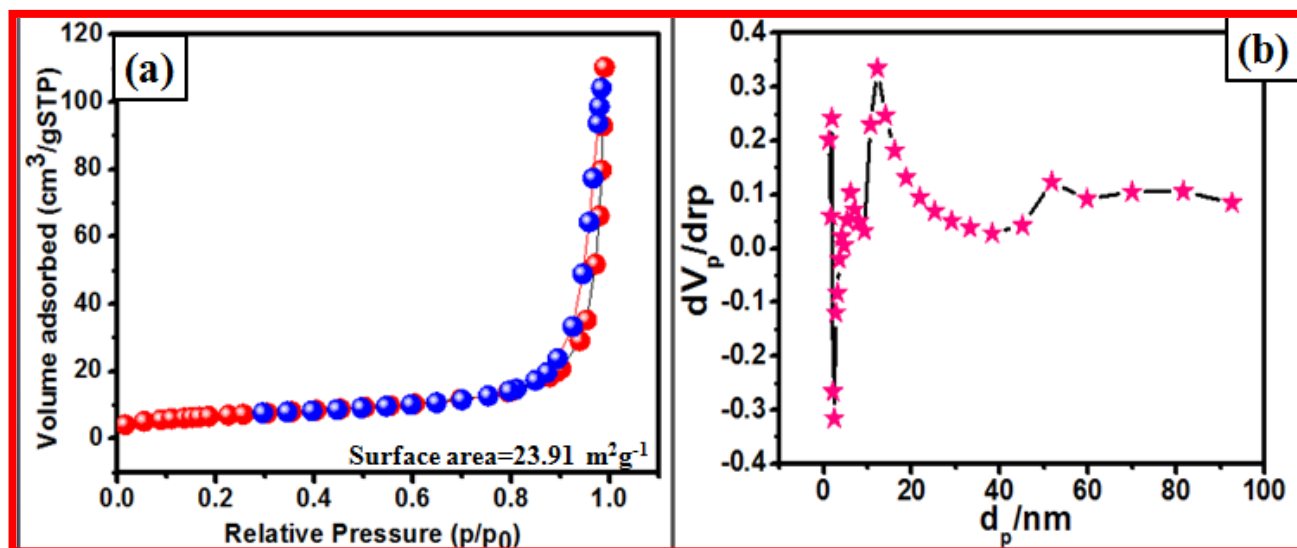


Fig.5.5: (a) Nitrogen adsorption-desorption isotherms and (b) pore size distribution curve of MnO₂ thin film.

5.2 Supercapacitive Performance of Manganese Oxide Thin Films-

5.2.1. Introduction-

Recently, transition metal oxides/sulfides are used as supercapacitor electrode materials due to their high pseudocapacitance [23]. Among them, MnO₂ has showed attention owing to its predominance of high theoretical specific capacitance, low cost, eco friendly and higher electrical conductivity (10^{-5} to 10^{-6} Scm⁻¹) than its oxide/hydroxide counterparts. Specifically, MnO₂ facilitates electrolyte ion diffusion and ion intercalation, which support its intrinsic electrochemical reactivity useful for supercapacitive application [24]. Jadhav et al [25] prepared MnO₂ thin film by SILAR method and obtained specific capacitance of 243 Fg⁻¹. Park et [26] prepared γ -MnO₂ thin film by CBD method and reported specific capacitance of 162 Fg⁻¹. Hu et al [27] prepared δ -MnO₂ thin film by CBD method and obtained specific capacitance of 447 Fg⁻¹ at 2 mVs⁻¹ scan rate. Dubal

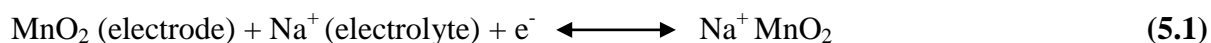
et al [28] prepared MnO₂ thin film using electrodeposition method and reported specific capacitance of 345 Fg⁻¹ for supercapacitor application.

In present work, electrochemical supercapacitive properties of nanostructured MnO₂ films are studied by cyclic voltammetry (CV), galvanostatic charge discharge (GCD) and electrochemical impedance spectroscopy (EIS) techniques in 1 M Na₂SO₄ electrolyte.

5.2.1.1 Results and Discussion-

(A) Cyclic Voltammetry (CV) Study-

Electrochemical supercapacitive performance of MnO₂ films is performed in 1 M Na₂SO₄ electrolyte using three electrode cells. Cyclic voltammetry (CV) technique is applied to obtain specific capacitance of MnO₂ films within active potential window of 0 to +0.5 V/SCE. Fig.5.6 shows the cyclic voltammeter curves measured of MnO₂ electrode tested at 5 to 100 mVs⁻¹ scan rate. The MnO₂ stores charge during formation of an electrical double layer, combined with pseudo-capacitance, which involves the accompanying reduction of Mn⁴⁺ ion at the electrode surface to form Mn³⁺, with the insertion of a cation from the electrolyte (Na⁺), into the structure to satisfy charge neutrality. The electrochemical redox reactions occurring at the electrode surface between MnO₂ film and Na₂SO₄ electrolyte is proposed by following reaction [29].



The rectangular-like CV curves at all scan rates suggest EDLC behavior of MnO₂ electrode without redox (reduction and oxidation) peaks as shown in **(Fig.5. 6 (a))**. Further, scan rate improvement from 5 to 100 mVs⁻¹ does not affect overall shape of CV curve and proportional relation is maintained between voltammetric currents and scan rates. These properties of CV curves

correspond to outstanding capacitive nature and rate abilities of MnO_2 electrode. Specific capacitance (C_s) of material is calculated from CV curves using **equation 2.3**. It is an inverse function of a scan rate, as shown in (**Fig. 5.6 (b)**), which indicates that, specific capacitance of MnO_2 electrode slowly reduces while increasing the scanning rate [30]. The highest capacitances of 672 Fg^{-1} at 5 mVs^{-1} scan rate and of 67.2 Fg^{-1} are obtained at 100 mVs^{-1} scan rate.

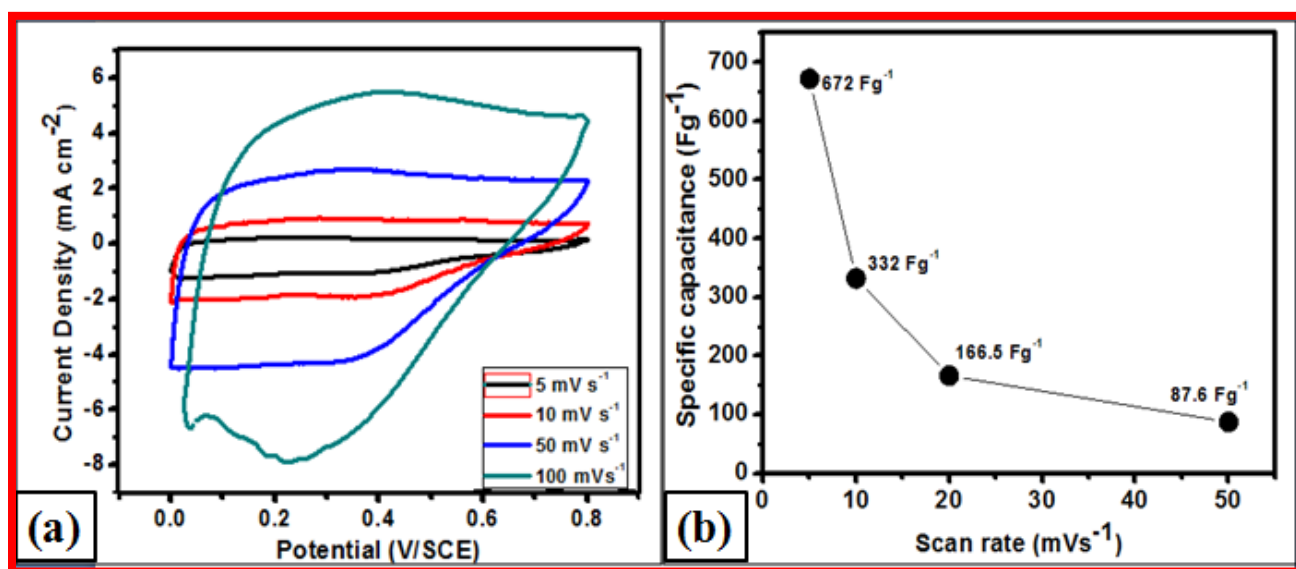


Fig. 5.6: (a) The CV curves at different scan rates of (5- 100 mVs^{-1}) and (b) specific capacitance vs. scan rate for MnO_2 electrode.

(B) Galvanostatic Charge-Discharge (GCD) Study-

Furthermore, electrochemical performance of MnO_2 electrode was also tested from galvanostatic charge/discharge (GCD) measurement at in 1 M Na_2SO_4 electrolyte solution. The electrode was employed for charging and discharging at different current density 2, 4 and 6 mA cm^{-2} , respectively as shown in **Fig.5.7**. The long discharging time is observed at 0.5 mAcm^{-2} current density. The charging/discharging curves have a good triangular and symmetric curves, attributing to their excellent reversibility in faradic reactions with small initial IR drop indicates easy ion

transportation channel provided by interlocked nano-granules for electrolyte ions to reach at the electro-active sites [31, 32]. The specific capacitance (C_s) of 61 Fg^{-1} is calculated from GCD measurement using equation 2.4.

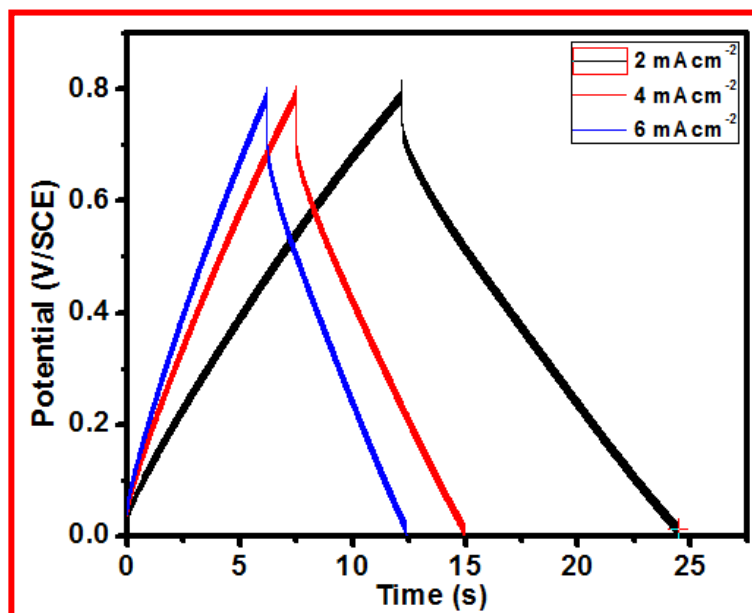


Fig. 5.7: Galvanostatic charge/discharge plots of MnO_2 electrode at 0.5, 0.6 and 0.7 mA cm^{-2} charging current densities.

(C) Stability Study-

The cyclic stability of MnO_2 electrode is also studied by repetitive CV test for 1000 cycles at scan rate of 100 mVs^{-1} . As displayed in (Fig. 5.8), 90% of the primary capacitance was retained even after 1000 cycles, showing a good electrochemical stability. The excellent electrochemical stability is attributed to the exclusive hierarchical structure which helps first-rate electron transfer and extract or inset electrolyte ions throughout the complete electrochemical cycling process. Hu et al [33] prepared MnO_2 thin film and obtained capacitance retention of 83 % after 1000 cycles. Chodankar et al [34] achieved capacitive retention of 95 % after 2500 cycles.

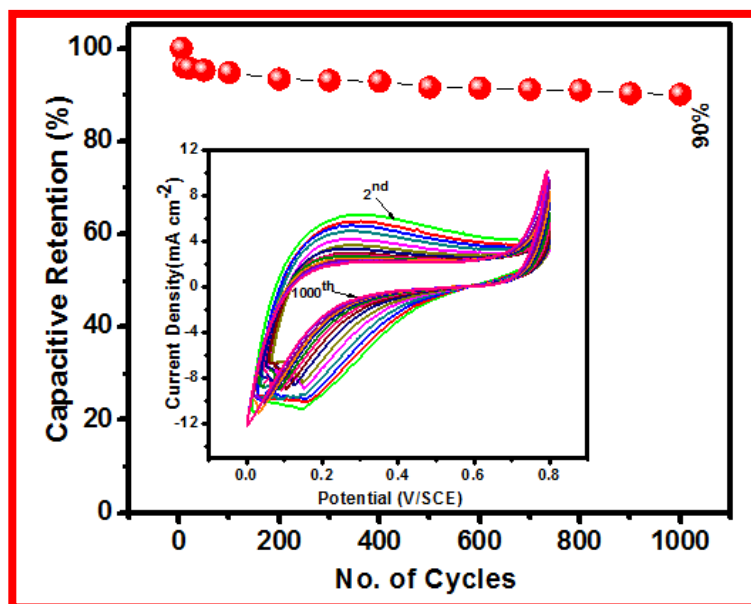


Fig. 5.8: Capacitive retention of MnO₂ thin film for 1000 cycles inset shows no. of CV cycles.

(D) EIS Study

The EIS is one of the fundamental techniques to find usefulness of electrode material for supercapacitor application. MnS film is evaluated for its electrochemical impedance behavior in 1 M Na₂SO₄ electrolyte within frequency range of 100 kHz to 100 mHz at 10 mV ac amplitude. **Fig. 5.9** represents Nyquist plot (impedance spectrum) of MnO₂ film. Intercept of curve to real axis in higher frequency region is known as the equivalent series resistance (R_s) is $1.5 \Omega\text{cm}^{-2}$ and charge transfer resistance (R_{ct}) is $3.6 \Omega\text{cm}^{-2}$. Inset of figure shows magnified Nyquist plot image (lower frequency region), the semi-circle along with the x-axis of material. The values R_s and R_{ct} of MnO₂ demonstrate the better electronic conductivity and electrochemical activity of material. Low R_s value is due to easier ion transportation at the electrolyte-electrode interface.

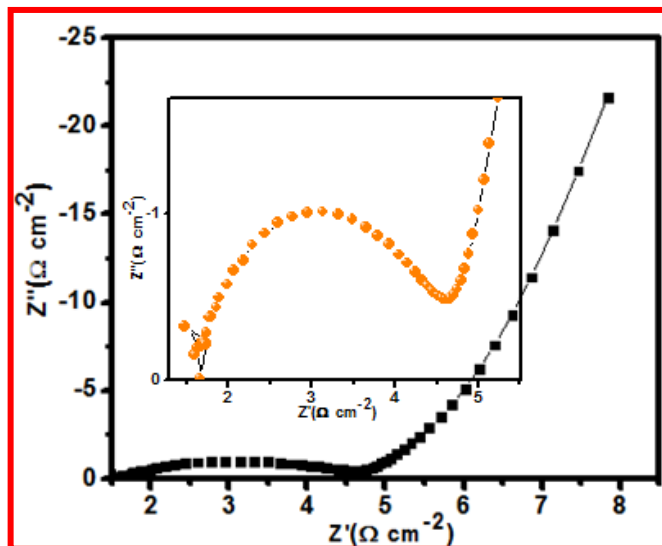


Fig.5.9: Electrochemical impedance spectroscopy (EIS) of MnO_2 electrode inset shows magnified image of Nyquist plot.

5.3 Conclusions

The MnO_2 film is directly deposited on cost effective stainless steel substrates by SILAR method at room temperature. The nanogranules thin film shows highest specific capacitance of 672 Fg^{-1} at 5 mVs^{-1} scan rate in $1 \text{ M Na}_2\text{SO}_4$ electrolyte. The capacitive retention of 90 % is achieved for 1000 CV cycles. Moreover, EIS study of MnO_2 film revealed low equivalent series resistance (R_s) of $1.5 \Omega \text{ cm}^{-2}$ and charge transfer resistance (R_{ct}) $3.6 \Omega \text{ cm}^{-2}$. The outstanding supercapacitive properties coupled with low cost method of film preparation makes MnO_2 as a promising positive electrode material for supercapacitive application.

References:

1. M. Huang, F. Li, F. Dong, Y. X. Zhang, L. L. Zhang, J. Mater. Chem. A **3** (2015), 21380- 21423.
2. D.P.Dubal, D.S.Dhawale, R.R.Salunkhe, C.D.Lokhande, J. Alloys Compd. **509** (2011) 10050–10054.
3. Z.S.Wu, W. Ren, D.W. Wang, F.Li, B.Liu, H.M. Cheng, ACS Nano **4** (2010) 5835–5842.
4. W.Li, J.Yuan, X. Shen, S. Gomez-Mower, L. Xu, S. Sithambaram, M. Aindow, S.L Suib, Adv. Funct. Mater.**16** (2006), 1247–1253.
5. J.W.Long, C.P. Rhodes, A.L Young, D.R Rolison, Nano Lett. **3** (2003) 1155–1161.
6. J.Chen, H.Meng, Y.Tian, R.Yang, D. Du, Z.Li, L.Qu, Y. Lin, Nanoscale Horiz., **4** (2019) 321-33.
7. J.Chen, Y.Wang, X.He, S.Xu, M.Fang,X.Zhao,Y.Shang, Electrochim. Acta, **142** (2014), 152-156.
8. X. Zhao, B.M. Sanchez, P.J. Dobson, P.S. Grant, Nanoscale, **3** (2011) 839-855.
9. T. Brousse, M. Toupin, R. Dugas, L. Athouel, O. Crosnier, D. Belanger, J. Electrochem. Soc. **153** (2006), A2171–A2180.
10. P.A.Shinde,V.C.Lokhande,T.Ji,C.D.Lokhande, J. Colloid Interface Sci. **498** (2017) 202-209.
11. D.Jones, E. Wortham, J. Rozière, F.Favier, J. Pascal, L.Monconduit, J. Phys.Chem. Solids **65** (2004), 235–239.
12. W.F. Wei, X.W. Cui, W.X. Chen, D.G. Ivey, Chem. Soc. Rev., **40** (2011) 1697-1721.
13. Z.M. Hu, X. Xiao, C. Chen, T.Q. Li, L. Huang, C.F. Zhang, J. Su, L. Miao, J.J. Jiang, Y.R. Zhang, J. Zhou, Nano Energy, **11** (2015) 226-234.
14. G.S. Gund, D.P. Dubal, B.H. Patil, S.S. Shinde, C.D. Lokhande, Electrochim. Acta **92** (2013), 205-215.
15. O. Sadak, W. Wang, J. Guan, A. K. Sundramoorthy, S. Gunasekara, ACS Appl. Nano Mater. **2** (2019) 4386–4394.
16. G.S Gund, D.P Dubal, N.R. Chodankar, J.Y. Cho, P.Gomez-Romero, C.Park, C.D. Lokhande, Sci. Rep. **5** (2015), 12454-12460.
17. P.M.Shafi, R. Dhanabal, A.Chithambararaj, S. Velmathi, A. C.Bose, ACS Sustainable Chem. Eng. **5** (2017), 4757–4770.
18. Y. Kumar, S. Chopra, A. Gupta, Y. Kumar, S.J. Uke, S.P. Mardikar, Mater. Sci. Energy Technol. **3** (2020), 566-574.
19. A.B.Nandiyanto, R.Oktiani, R.Ragadhita, Ind. J. Sci. Tech., **4** (2019) 97-118.
20. D. P. Dubal, R. Holze, P. M. Kulal, J. Mater. Sci. **48** (2013)714–719.
21. N.R. Chodankar , D.P.Dubal , G. S. Gund ,C. D. Lokhande, J. Energy Chem. **25** (2016), 463-471.
22. H.Y.Chen, S. Zeng, M.H. Chen, Y.Y. Zhang, L.X. Zheng, Q.W. Li, Small **12** (2016), 2035–2045.
23. M. Jana, S. Saha, P. Samanta, N. C. Murmu, N. H. Kim, T. Kuila, J. H. Lee, J. Power Source **340** (2017), 380-392.
24. D.P. Dubal, D.S. Dhawale, R.R. Salunkhe, V.J. Fulari, C.D. Lokhande,

- J. Alloys Compd. **497** (2010), 166–170.
25. P. R. Jadhav, V. V. Shinde, G. J. Navathe, M. M. Karanjkar, P. S. Patil, AIP Conf. Proc. **1536** (2013), 679-680.
 26. S.Park, H.W.Shim, C. W.Lee, H.J. Song, I. J. Park, J.C. Kim, K.S. Hong, D.W.Kim, Nano Research., **8** (2014) 990-1004.
 27. Y.Hu, J.Wang, X.Jiang, Y. Zheng, Z.Chen, Appl. Surf. Sci. **271** (2013) 193– 201.
 28. D.P.Dubal, W.B.Kim, C.D.Lokhande, J. Alloys Compd. **509** (2011), 10050-10054.
 29. N.R.Chodankar,G.S.Gund,D.P.Dubal,C.D.Lokhande, RSC Adv., **4** (2014), 61503-61513.
 30. X. Y. Yu, L. Yu, X.W.Lou, Adv. Energy Mater. **6** (2016), 1501333-1501340.
 31. H. Zhang, Y.Wang, C. Liu, H. Jiang, J. Alloys Compd. **517** (2012) 1– 8.
 32. D. P. Dubal, D. Aradilla, G. Bidan, P. Gentile, T. J.S. Schubert, J.Wimberg, S. Sadki, P. Gomez-Romero,Sci. Rep. **5** (2015), 1-10
 33. Y.Hu, H.Zhu, J.Wang, J. Alloys Compd. **509** (2011) 10234– 10240.
 34. N. R. Chodankar, D. P. Dubal, G.S.Gund, C.D. Lokhande, Energy Technol. **3** (2015), 625-631.

Chapter-6
Device Fabrication of Flexible
Symmetric and Asymmetric
Super capacitor: Performance
Evaluation

<i>Sr.No</i> <i>Sr.No</i>	<i>Title</i>		<i>Pag</i> <i>e.</i> <i>No.</i>
6	<i>Introduction</i>		136 - 137
	Section-A		
6.1	<i>Supercapacitor Device Fabrication</i>		138
	6.1.A	<i>Experimental Details</i>	138
		6.1.A.1 <i>Preparation of electrodes GO/Sm₂S₃,GO/La₂S₃ and MnO₂</i>	138
		6.1.A.2 <i>Preparation of PVA-Na₂SO₄ gel electrolyte</i>	138
		6.1.A.3 <i>Fabrication of Flexible Asymmetric Supercapacitor Device</i>	138
		(a) <i>GO/Sm₂S₃//PVA-Na₂SO₄//GO/Sm₂S₃ Symmetric Device</i>	138 - 139
		(b) <i>GO/La₂S₃//PVA-Na₂SO₄//GO/La₂S₃ Symmetric Device</i>	140
		(c) <i>GO/Sm₂S₃//PVA-Na₂SO₄//GO/Sm₂S₃Asymmetric Device</i>	141
		(d) <i>GO/La₂S₃//PVA-Na₂SO₄//GO/La₂S₃Asymmetric Device</i>	142
	Section-B		
6.2.B	<i>Introduction</i>		
	6.2.B.1	<i>Electrochemical Performance of GO/Sm₂S₃//PVA-Na₂SO₄//GO/Sm₂S₃ Symmetric Supercapacitor Device</i>	143
		(a) <i>CV Study</i>	144
		(b) <i>GCD Study</i>	145
		(c) <i>Regone Plot With Symmetric Device Demonstration</i>	146
		(d) <i>Cyclic Stability Study</i>	147
		(e) <i>EIS Study</i>	148 - 149
	6.2.B.2	<i>Electrochemical Performance of GO/La₂S₃//PVA-Na₂SO₄//GO//La₂S₃ SymmetricSupercapacitor Device</i>	150
		(a) <i>CV Study</i>	150
		(b) <i>GCD Study</i>	151
		(c) <i>Regone Plot With Symmetric Device Demonstration</i>	152
		(d) <i>Cyclic Stability Study</i>	153
		(e) <i>EIS Study</i>	154
	6.2.B.3	<i>Electrochemical Performance of GO/Sm₂S₃//PVA-Na₂SO₄//MnO₂ Asymmetric Supercapacitor Device</i>	155
		(a) <i>CV Study</i>	156
		(b) <i>GCD Study</i>	157
		(c) <i>Regone Plot</i>	158

		(d)	<i>Cyclic Stability Study</i>	159
		(e)	<i>EIS Study</i>	160
		(f)	<i>GO/ Sm₂S₃//PVA-Na₂SO₄//MnO₂ Asymmetric Device Demonstration</i>	161
	6.2.B.4		<i>Electrochemical Performance of GO/ La₂S₃//PVA-Na₂SO₄//MnO₂ Asymmetric Supercapacitor Device</i>	162
		(a)	<i>CV Study</i>	162
		(b)	<i>GCD Study</i>	163
		(c)	<i>Regone Plot</i>	164
		(d)	<i>Cyclic Stability Study</i>	165
		(e)	<i>EIS Study</i>	166
		(f)	<i>GO/ La₂S₃//PVA-Na₂SO₄//MnO₂ Asymmetric Device Demonstration</i>	167 - 168
6.2	<i>Conclusions</i>			169 - 170
	<i>References</i>			171 - 172

6. Introduction-

The energy storage devices are the key part of the advanced electronic gadgets (like mobile phones, laptops, hybrid electrical vehicles, memory backup system, etc.) that define the dimensions, safety and functioning time of the electronic gadgets [1]. Therefore, researchers and engineers are trying to develop energy storage devices having high energy and power capability along with longer working life. They are also worried about the cost and dimensions of the energy storage devices [2]. Presently, the supercapacitors have attracted significant attention as promising and complementary energy storage devices owing to their best capabilities like excellent power densities, rapid charge discharge ability and long lifetimes as compared to the batteries technology [3]. To commercialize the supercapacitors for practical applications, it is crucial to lift the specific energy and the potential limit of supercapacitors without surrendering its other features [4].

Flexible supercapacitors are one of the emerging classes of energy storage devices which offer many advantageous features including light weight, ease of handling, wide range of operating potential windows and excellent reliability [5]. The fabrication of flexible solid state supercapacitors (FSSSC) becomes an attractive topic in the field of research for electrochemical energy storage/conversion systems. The main difference between conventional supercapacitors and FSSSC is that the FSSSC consist of electrode and electrolyte with certain flexibility and electrolyte is in solid state. The electrochemical performance of FSSSC devices depends on the electrode material used, electrolyte and supporting substrate. Therefore, the selection of proper electrode material, electrolyte and supporting substrate is important to achieve a better electrochemical performance of FSSSC [6].

Device Fabrication of Flexible Symmetric and Asymmetric Supercapacitors: Performance Evaluation

In earlier studies, different flexible substrates similar to carbon cloth, stainless steel, nickel foam, sponge, textiles, etc. are used for the fabrication of high performance flexible electrodes because of their significant mechanical properties, large surface area and excellent electrical conductivity [7]. Among all these, flexible carbon cloth is more suitable supporting substrate because of its excellent conductivity, high flexibility and good strength. Further, many efforts have been committed to develop the active electrode materials, because the fundamental limit of energy storage is determined by the active electrode material. In past, the carbon based materials such as activated carbon (AC) [8], graphene [9], carbon nanotubes [10], etc. are explored as a negative electrode materials to fabricate the asymmetric SCs device because of their unique features like good electrical conductivity, high power density, excellent mechanical property and superior cycling stability [11]. However, the carbon based materials always suffer from certain limitations such as small operating potential window and low specific capacitance, which decreases the resultant specific capacitance and energy density of the SCs device.

In the present chapter, discussion is made on performance of symmetric and asymmetric FSSSC devices using $\text{GO}/\text{Sm}_2\text{S}_3//\text{GO}/\text{Sm}_2\text{S}_3$, $\text{GO}/\text{La}_2\text{S}_3//\text{GO}/\text{La}_2\text{S}_3$, $\text{GO}/\text{Sm}_2\text{S}_3//\text{MnO}_2$ and $\text{GO}/\text{La}_2\text{S}_3//\text{MnO}_2$ electrode materials. This chapter is divided into two sections (A and B). Section ‘A’ deals with the fabrication of symmetric and asymmetric supercapacitor devices, whereas section ‘B’ is related to the electrochemical performance evaluation of symmetric and asymmetric FSSSC devices with demonstration.

SECTION: A

6.1 Supercapacitor Devices Fabrication-

6.1. A Experimental Details:

6.1. A.1 Preparation of Electrodes -

The SILAR method is employed for the preparation of supercapacitor electrodes on flexible stainless steel (SS) substrates. The preparative parameters of GO/Sm₂S₃, GO/Sm₂S₃ and MnO₂ thin films are used from chapter III, IV and V, respectively.

6.1. A.2 Preparation of PVA-Na₂SO₄ Gel Electrolyte-

The polyvinyl alcohol- sodium sulphate (PVA-Na₂SO₄) gel electrolyte was used for symmetric and asymmetric FSSSC devices in order to correlate with the electrochemical performance of GO/Sm₂S₃, GO/La₂S₃, GO/Sm₂S₃, and GO/La₂S₃ composite thin films. The PVA-Na₂SO₄ gel electrolyte was prepared in the following manner: 2 g of PVA and 2 g of Na₂SO₄ were added into 20 ml of DDW. Then the prepared solution was stirred magnetically at room temperature until the formation of clear, viscous and homogeneous appearance [12]. This transparent and viscous solution was employed as a gel electrolyte and separator for the fabrication of FSSSC devices.

6.1. A.3 Fabrication of Flexible Symmetric and Asymmetric Supercapacitor Devices

(a) GO/Sm₂S₃//PVA-Na₂SO₄//GO/Sm₂S₃ Symmetric Supercapacitor Device-

Fig. 6.1 (a-d) shows the steps in the fabrication process involved in symmetric GO/Sm₂S₃//PVA-Na₂SO₄//GO/Sm₂S₃ flexible solid-state supercapacitor device. The GO/Sm₂S₃ films are deposited on a flexible stainless steel substrate using SILAR method, in which each

Device Fabrication of Flexible Symmetric and Asymmetric Supercapacitors: Performance Evaluation

GO/Sm₂S₃ film electrode has an area $5.5 \times 5.5 \text{ cm}^2$. These electrodes are used in the fabrication of symmetric solid-state supercapacitor devices. The edges of GO/Sm₂S₃ electrodes are sealed with insulating tape to avoid any electrical short circuit as shown in **Fig. 6.1 (a)**. For designing symmetric supercapacitor devices or making electrode-electrolyte interfaces, an ion conducting layer is necessary as a separator between the electrodes, hence PVA- Na₂SO₄ electrolyte gel is prepared as discussed in **6.1.A.2**. The thin layer of PVA- Na₂SO₄ electrolyte gel is pasted on Sm₂S₃ film electrode and soaked for 2 h (**Fig. 6.1 (b, c)**). The electrolyte is sandwiched between two symmetric flexible GO/Sm₂S₃ electrodes and the supercapacitor cell assembly is sealed with the help of insulating tape as shown in **Fig. 6.1 (d)**. The PVA-Na₂SO₄ gel electrolyte also acts as a separator between the GO/Sm₂S₃ electrodes for making supercapacitor devices [13].

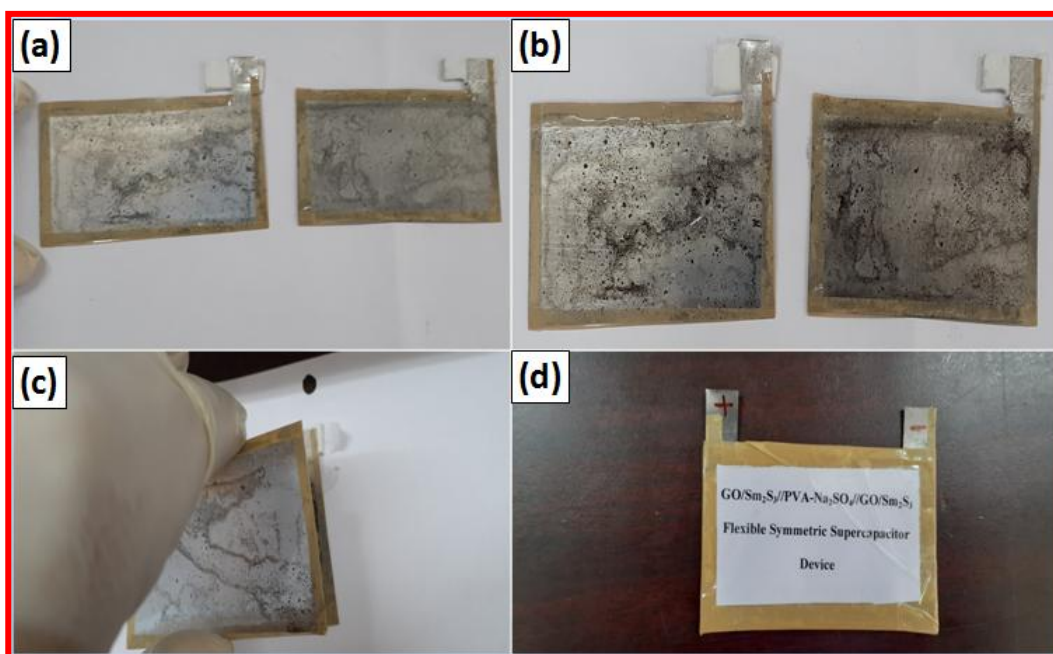


Fig.6.1: Photographs of flexible film electrodes (a) flexible GO/Sm₂S₃ electrode, (b) PVA- Na₂SO₄ electrolyte gel is pasted on two GO/Sm₂S₃ film electrodes soaked for 2 h, (c) the electrolyte gel is sandwiched between two GO/Sm₂S₃ film electrodes, and (d, e) assembly is

Device Fabrication of Flexible Symmetric and Asymmetric Supercapacitors: Performance Evaluation

packed to form flexible symmetric (GO/Sm₂S₃//PVA-Na₂SO₄//GO/Sm₂S₃) supercapacitor device.

(b) GO/La₂S₃//PVA-Na₂SO₄//GO/La₂S₃ Symmetric Supercapacitor Device-

The fabricated GO/La₂S₃ symmetric supercapacitor device uses two identical GO/La₂S₃ thin films with PVA-Na₂SO₄ gel-electrolyte. Initially, the corners and sides of both GO/La₂S₃ films were sealed with the insulating tape in order to avoid direct contacts. Further, these two electrodes were painted with PVA-Na₂SO₄ gel electrolyte in order to form a thin layer of electrolyte and then dried for 3 h at room temperature to remove the water content from the gel electrolyte in **Fig.6.2 (a)**. In the next step, both the electrodes with gel electrolyte were sandwiched on one another in order to form the solid state SCs (**Fig.6.2 (b-d)**). Furthermore, the fabricated device was pressed under definite pressure for 10 min to enhance the interfacial contact of gel electrolyte with GO/La₂S₃ electrodes.

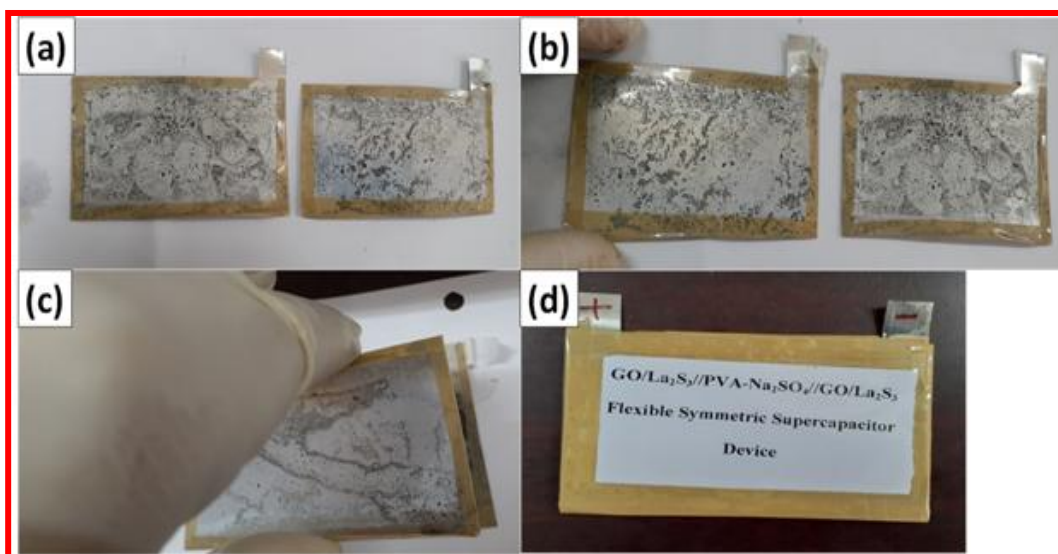


Fig.6.2: Photographs of GO/La₂S₃//PVA-Na₂SO₄//GO/La₂S₃ flexible symmetric supercapacitor device (a) flexible GO/La₂S₃ electrode, (b) PVA-Na₂SO₄ electrolyte gel is

Device Fabrication of Flexible Symmetric and Asymmetric Supercapacitors: Performance Evaluation

pasted on two $\text{GO/La}_2\text{S}_3$ film electrodes soaked for 2 h, (c) the electrolyte gel is sandwiched between two La_2S_3 film electrodes and (d) assembly is packed to form flexible symmetric ($\text{GO/La}_2\text{S}_3/\text{PVA-Na}_2\text{SO}_4/\text{GO/La}_2\text{S}_3$) solid-state supercapacitor device.

(c) $\text{GO/Sm}_2\text{S}_3/\text{PVA-Na}_2\text{SO}_4/\text{MnO}_2$ Asymmetric Supercapacitor Device-

The asymmetric $\text{GO/Sm}_2\text{S}_3/\text{PVA-Na}_2\text{SO}_4/\text{MnO}_2$ and $\text{GO/La}_2\text{S}_3/\text{PVA-Na}_2\text{SO}_4/\text{MnO}_2$ FSSSCs devices were fabricated employing $\text{PVA-Na}_2\text{SO}_4$ gel as an electrolyte and separator. The asymmetric FSSSC electrodes based on $\text{GO/Sm}_2\text{S}_3/\text{PVA-Na}_2\text{SO}_4/\text{MnO}_2$ and $\text{GO/La}_2\text{S}_3/\text{PVA-Na}_2\text{SO}_4/\text{MnO}_2$ thin films with $5.5 \times 5.5 \text{ cm}^2$ area are illustrated in **Fig. 6.3**. The steps involved in the device fabrication process are illustrated in **Fig. 6.3(a-d)**. The large area stainless steel asymmetric electrodes deposited on the substrate (**Fig.6.3 (a, b)**) The schematic of FSSSC $\text{GO/Sm}_2\text{S}_3/\text{PVA-Na}_2\text{SO}_4/\text{MnO}_2$ device incorporated with gel electrolyte is shown in **Fig. 6.3(c, d)**.

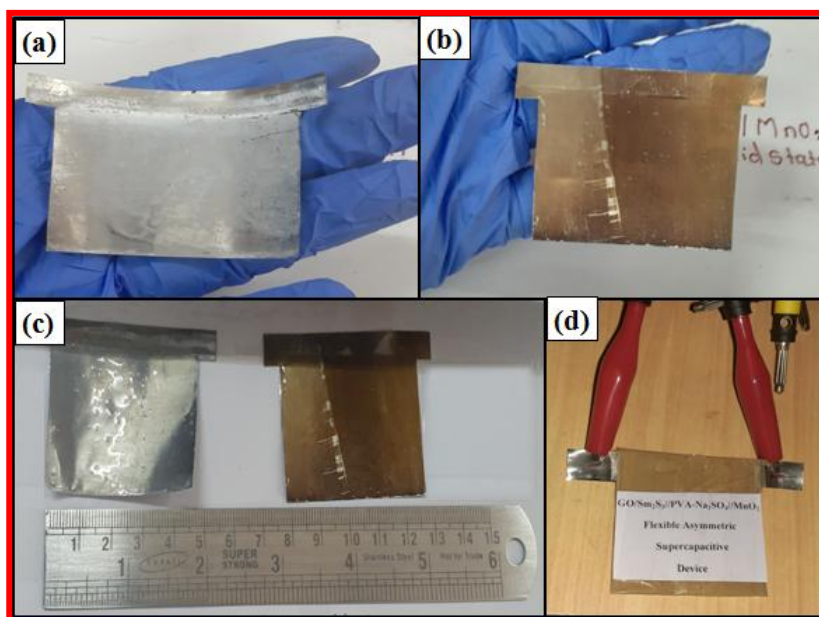


Fig.6.3: Photographs of (a) $\text{GO/Sm}_2\text{S}_3$ film, (b) MnO_2 film, (c) $\text{PVA-Na}_2\text{SO}_4$ electrolyte gel is pasted on GO/Sm_2 and MnO_2 film electrodes and soaked for 2 h, and (d) assembly is

Device Fabrication of Flexible Symmetric and Asymmetric Supercapacitors: Performance Evaluation

packed to form flexible a symmetric (GO/Sm₂S₃//PVA-Na₂SO₄//MnO₂) solid-state supercapacitor device.

(c) **GO/La₂S₃//PVA-Na₂SO₄//MnO₂ Asymmetric Supercapacitor Device-** Same process has been adopted to fabricate GO/La₂S₃//PVA-Na₂SO₄//MnO₂ asymmetric device. **Fig.6.4 (a-e)** shows the fabrication process in asymmetric GO/La₂S₃//PVA-Na₂SO₄//MnO₂ flexible solid-state supercapacitor device [14]. The GO/La₂S₃ composite films are deposited on a stainless steel substrate using SILAR method, in which each GO/La₂S₃ composite film electrode is having area 5.5×5.5 cm². These electrodes are used in the fabrication of a symmetric solid-state supercapacitor devices. The edges of the GO/La₂S₃ composite electrodes are sealed with insulating tape to avoid any electrical short circuit as shown in **Fig. 6.4**.

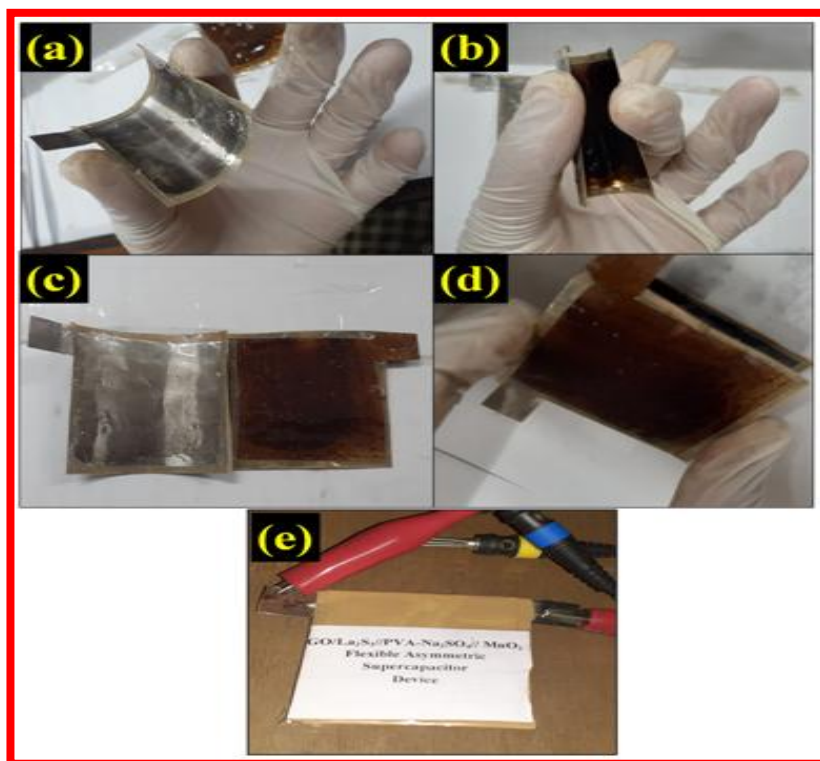


Fig. 6.4: (a) GO/La₂S₃ composite thin film prepared on 5.5 × 5.5 cm² flexible SS substrate, (b) MnO₂ electrodes of (5.5 x 5.5) cm² painted with PVA-Na₂SO₄ gel electrolyte, (c) flexible

asymmetric GO/La₂S₃/PVA-Na₂SO₄/MnO₂ supercapacitor ready for stacking, (d) stacking both electrode and (e) GO/La₂S₃/PVA-Na₂SO₄/MnO₂ asymmetric device ready for supercapacitive study.

SECTION: B

Electrochemical Performance Evaluation

6.2. B Introduction

The present section deals with the electrochemical performance evaluation of symmetric and asymmetric FSSSC devices. The electrochemical properties of FSSSC devices are studied using the CV, GCD, Regone plot, cycling stability and EIS techniques. The two electrode system was used for the evaluation of electrochemical performance of symmetric and asymmetric FSSSC devices. In a symmetric configuration, GO/Sm₂S₃, and GO/La₂S₃ composite thin films act as a cathode as well as an anode. In asymmetric configuration, GO/Sm₂S₃ and GO/La₂S₃ composite thin films are used as an anode and MnO₂ thin film as an cathode.

6.2. B.1 Electrochemical Performance of GO/Sm₂S₃/PVA-Na₂SO₄/GO/Sm₂S₃ FSSSC Supercapacitor Device

(a) CV Study-

The performance of GO/Sm₂S₃/PVA-Na₂SO₄/GO/Sm₂S₃ FSSSC devices is investigated in different potential windows from 1.2 to 1.8 V at scan rate of 100 mVs⁻¹ as shown in **Fig. 6.5 (a)**. The GO/Sm₂S₃/PVA-Na₂SO₄/GO/Sm₂S₃ FSSSC device shows ideal pseudocapacitive performance at potential window up to 1.8 V. Therefore, the electrochemical performance of GO/Sm₂S₃/PVA-Na₂SO₄/GO/Sm₂S₃ FSSSC device is measured in potential windows of 0 to 1.8

Device Fabrication of Flexible Symmetric and Asymmetric Supercapacitors: Performance Evaluation

V. The CV curves measurements of GO/Sm₂S₃//PVA-Na₂SO₄/GO/Sm₂S₃ FSSSC devices are carried out in above potential windows of 0 to 1.8 V at various scan rates of 5 to 100 mVs⁻¹ as shown in **Fig. 6.5(b)**. The specific and aerial capacitances of GO/Sm₂S₃//PVA-Na₂SO₄/GO/Sm₂S₃ FSSSC devices evaluated in accordance with CV curves at different scan rates is plotted in **Fig. 6.5(c)**. The maximum specific capacitance of 12 Fg⁻¹ is obtained at scan rate of 5 mVs⁻¹. As expected, the specific capacitance reduces slowly with increasing scan rate [15].

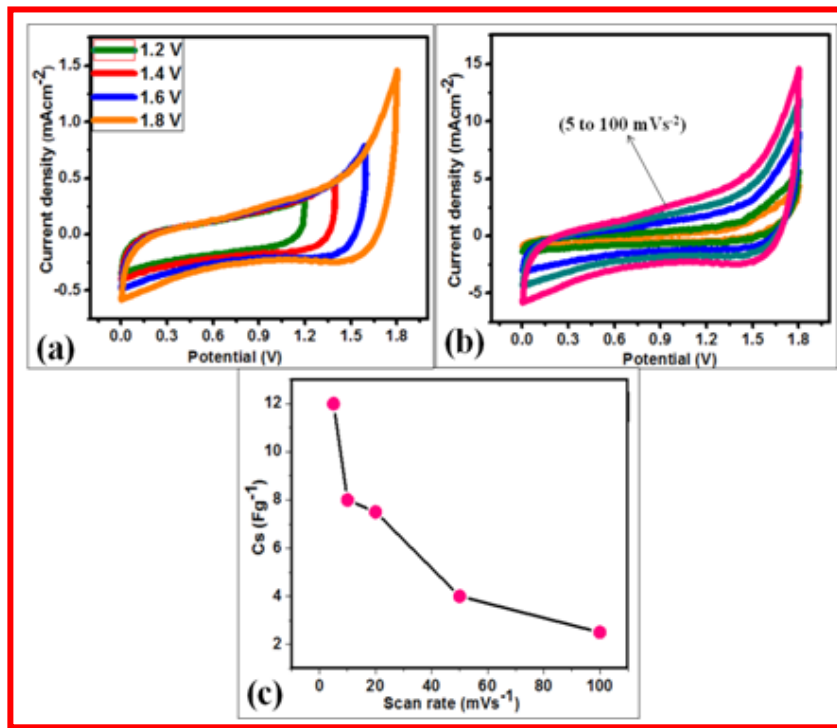


Fig.6.5: (a) The CV curves at different voltage windows, (b) the CV curves at different scan rates, and (c) plot of specific capacitance versus different scan rate for GO/Sm₂S₃//PVA-Na₂SO₄/GO/Sm₂S₃ FSSSC devices.

(b) GCD Study-

Device Fabrication of Flexible Symmetric and Asymmetric Supercapacitors: Performance Evaluation

The galvanostatic charge-discharge (GCD) study is used to examine the applicability of GO/Sm₂S₃/PVA-Na₂SO₄/GO/Sm₂S₃ FSSSC device, since this can easily evaluate the rate capability of device by judging the rate of change of voltage with time during charging and discharging at various current densities within a stable potential window of 0 to 1.8 V. The GCD curves of GO/Sm₂S₃/PVA-Na₂SO₄/GO/Sm₂S₃ FSSSC device at different current densities are shown in **Fig. 6.6 (a)**. The estimated values of specific capacitance at different current densities are plotted in **Fig. 6.6 (b)** and shows a maximum capacitance of 1.44 Fg⁻¹ at 4 mAcm⁻². The difference in specific capacitances evaluated through GCD and CV curves measurement is easily explained [16]. The estimated specific capacitance through CV curve measurements is at a particular voltage, whereas GCD measurement furnishes an average capacitance over the voltage range of 0 to 1.8 V.

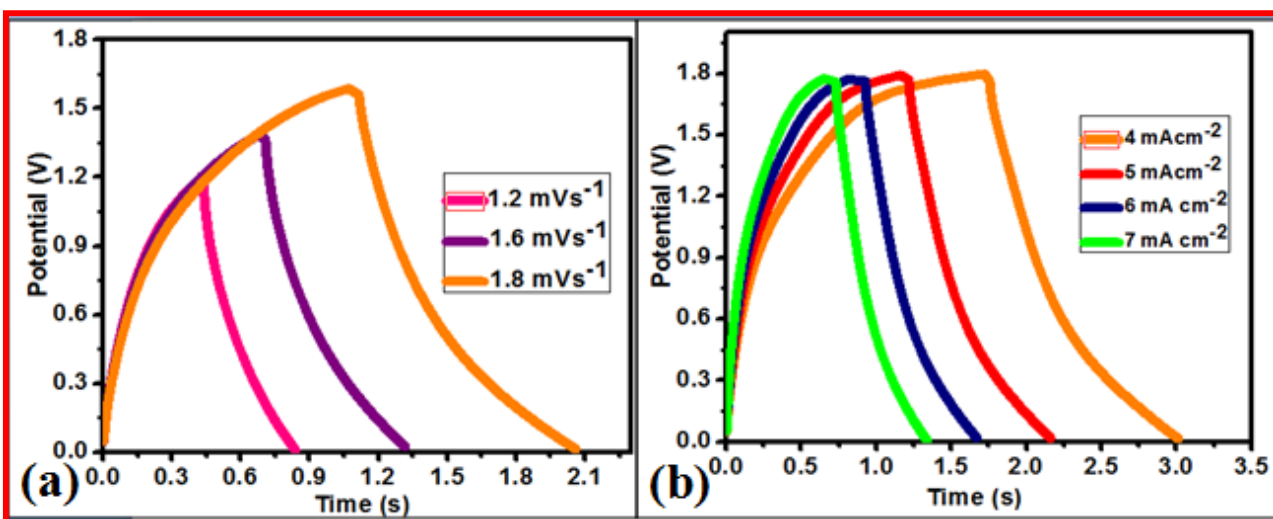


Fig.6.6. (a) The GCD curves at different potential windows and (b) the GCD curves at different charging current densities for GO/Sm₂S₃/PVA-Na₂SO₄/GO/Sm₂S₃ FSSSC device.

(c) Ragone plot-

A high energy density (ED) and powder density (PD) are expected for high performance supercapacitor devices. This phenomenon can be seen on the Ragone plot at various charge-

Device Fabrication of Flexible Symmetric and Asymmetric Supercapacitors: Performance Evaluation

discharge rates (**Fig.6.7**), and ED and PD are calculated using eqs. (2.11) and (2.12), respectively. The GO/Sm₂S₃//PVA-Na₂SO₄//GO/Sm₂S₃ FSSSC device delivers a high ED of 0.65 Whkg⁻¹ and PD of 1800 KWkg⁻¹.

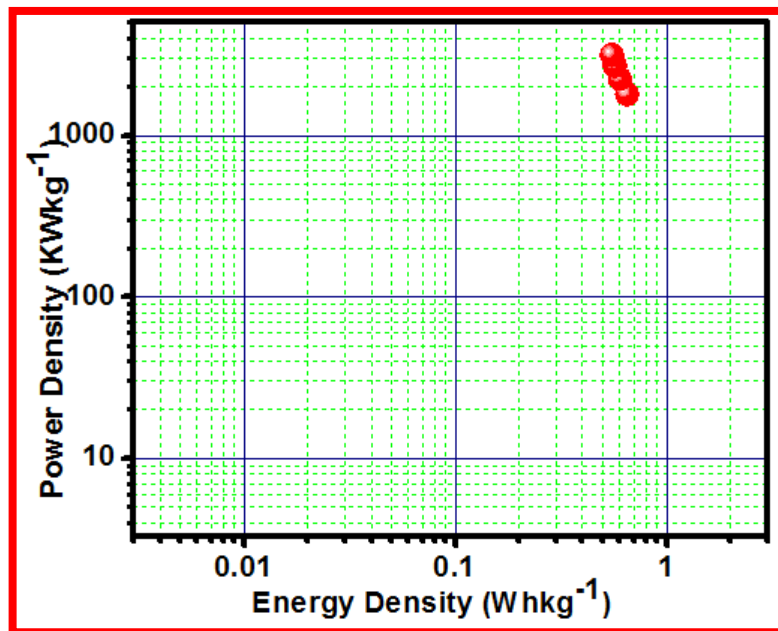


Fig.6.7. Ragone plot of GO/Sm₂S₃//PVA-Na₂SO₄//GO/Sm₂S₃ FSSSC device.

As a practical demonstration of GO/Sm₂S₃//PVA-Na₂SO₄//GO/Sm₂S₃ FSSSC device, lighting of single LED is performed using one flexible Sm₂S₃ devices connected as shown in **Fig. 6.8**. Initially, the device is charged by 3.0 V for 30 s and then discharged through single LED. **Fig. 6.8** demonstrates single red LED lighting up for 20 s.



Fig.6.8 Photograph of device demonstration for glowing red LED for 20 s.

(d) Cyclic Stability Study-

Cycling stability of fabricated GO/Sm₂S₃//PVA-Na₂SO₄//GO/Sm₂S₃ FSSSC device investigated for 1000 CV cycles at scan rate of 100 mVs⁻¹ is shown in **Fig. 6.9**. The specific capacitance of the device decreased slowly and the capacitive retention after 1000 CV cycles is 82.8 % as illustrated in **Fig. 6.9**. The excellent electrochemical stability of GO/Sm₂S₃//PVA-Na₂SO₄//GO/GO/Sm₂S₃ FSSSC device as compared to previous studies could overcome the limitation of dissolution of electrode material in aqueous electrolyte due to employment of solid state electrolyte and porous microstructure of Sm₂S₃ offer more surface area for charge storage [17].

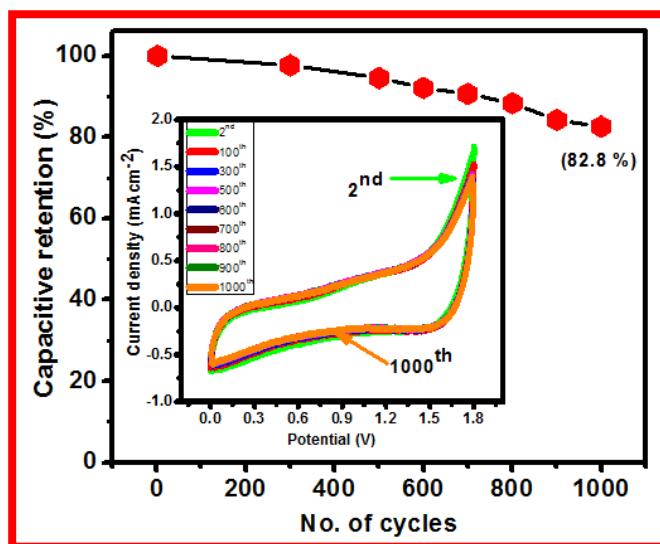


Fig.6.9. Capacity retention of symmetric GO/Sm₂S₃//PVA-Na₂SO₄//GO/Sm₂S₃ FSSSC device (inset shows shape of no. of CV cycles).

(e) EIS Study-

Electrochemical impedance technique (EIS) is a fundamental technique of electrochemistry, which can explore impedance performance of device at the interface of electrode and electrolyte. **Fig. 6.10** shows Nyquist plot of symmetric GO/Sm₂S₃//PVA-Na₂SO₄//GO/Sm₂S₃ device obtained in the frequency range of 100 mHz to 100 kHz for 10 mV ac amplitude. Inset the different impedance parameters obtained from equivalent circuit such as equivalent series resistance (R_s) is $0.54 \, \Omega \, \text{cm}^{-2}$, charge transfer resistance (R_{ct}) is $0.84 \, \Omega \, \text{cm}^{-2}$, Warburg resistance (W) is $1.01 \times 10^{-5} \, \Omega \text{cm}^{-2}$ and double-layer capacitance (Q) is $0.77 \, \Omega \text{cm}^{-2}$ as shown in **Fig 6.10**. The Smaller values of R_s and R_{ct} for PVA-Na₂SO₄ based FSSSC symmetric GO/Sm₂S₃//PVA-Na₂SO₄//GO/Sm₂S₃ device is due to the good ionic conductivity of PVA gel electrolyte and its good compatibility with active electrode material. Hence, the PVA is suitable to fabricate the high performance FSSSC supercapacitor device.

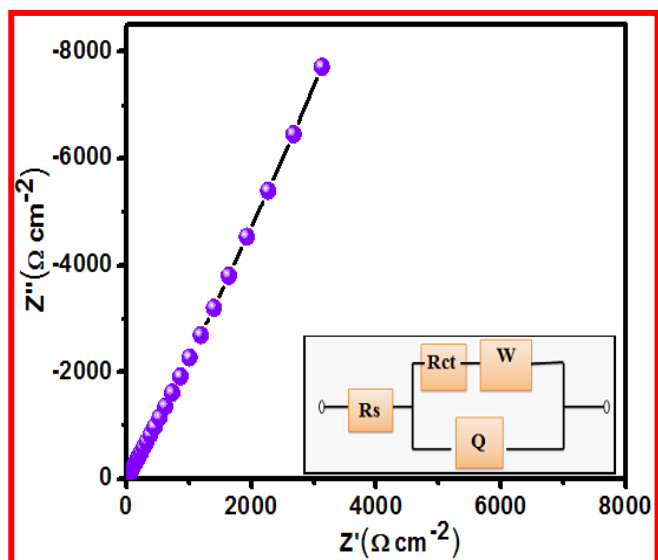


Fig.6.10. Nyquist plot for GO/Sm₂S₃//PVA-Na₂SO₄//GO/Sm₂S₃ FSSSC device and inset shows equivalent circuit diagram.

Table 6.1 Obtained Nyquist plot parameters values fitted with equivalent circuit for GO/Sm₂S₃//PVA-Na₂SO₄//GO/Sm₂S₃ FSSSC device.

GO/Sm ₂ S ₃ //PVA-Na ₂ SO ₄ //GO/Sm ₂ S ₃	
Rs (Ω cm ⁻²)	0.54
Rct (Ω cm ⁻²)	0.84
Q (F)	0.77
W (Ω cm ⁻²)	1.01 × 10 ⁻⁵

6.2.B.2 Electrochemical Performance of GO/La₂S₃//PVA-Na₂SO₄//GO/La₂S₃ Symmetric Supercapacitor Device

(a) CV Study-

Fig.6.11 (a) shows the effect of scan rate on CV plots of GO/La₂S₃//PVA-Na₂SO₄//GO/La₂S₃ FSSSC device in the potential window of 0 to + 1.8 V. The current density under CV curves slowly increases with scan rate. This shows that voltammetric current is directly proportional to scan rate of CV, which is a pseudocapacitive behavior [18]. The variation of specific capacitance with scan rate is shown in **Fig. 6.11 (b)** which reveals that GO/La₂S₃//PVA-Na₂SO₄//GO/La₂S₃ FSSSC device exhibit maximum Cs of 6.34 Fg⁻¹ at scan rate of 5 mVs⁻¹.

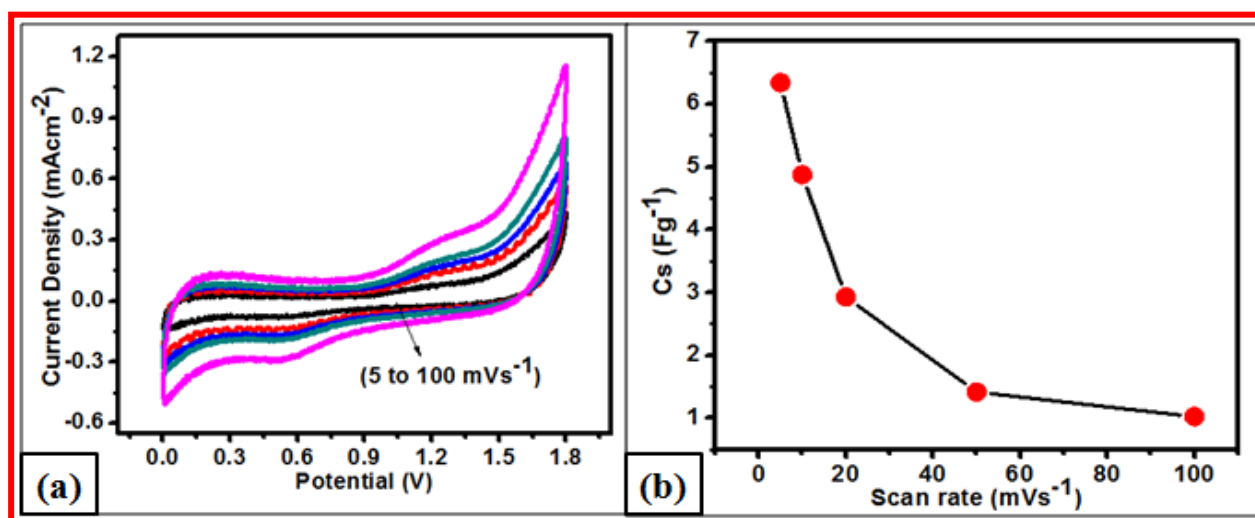


Fig.6.11. (a) The CV curves at different scan rates, and (b) variation of specific capacitance versus scan rate.

(b) GCD Study-

The FSSSC device is further studied for GCD profiles as shown in **Fig. 6.12**. Device is tested for charging and discharging at 4 mAcm⁻² current for various voltages between 1.2 to 1.8 V as seen in **Fig 6.12 (A)**. The highest voltage of 1.8 V is optimized potential window of

Device Fabrication of Flexible Symmetric and Asymmetric Supercapacitors: Performance Evaluation

GO/La₂S₃/PVA-Na₂SO₄/GO/La₂S₃ FSSSC device. All GCD curves comprise initially internal resistance (IR) drop and, it increases with increasing voltage of device. For the highest 1.8 V, longest discharge time obtained which shows capacitive behavior of device. The wide potential window and longest discharge time will enhance capacitance and energy density of device. In order to decide rate capability of device at 1.8 V and at 4, 5, 6 and 7 mAcm⁻² currents density charging and discharging curves of device are recorded as shown in **Fig. 6.12 (B)**. The specific capacitances of device calculated from GCD curves at different current densities are 8.56, 5.22, 3.13 and 4.42 Fg⁻¹, respectively.

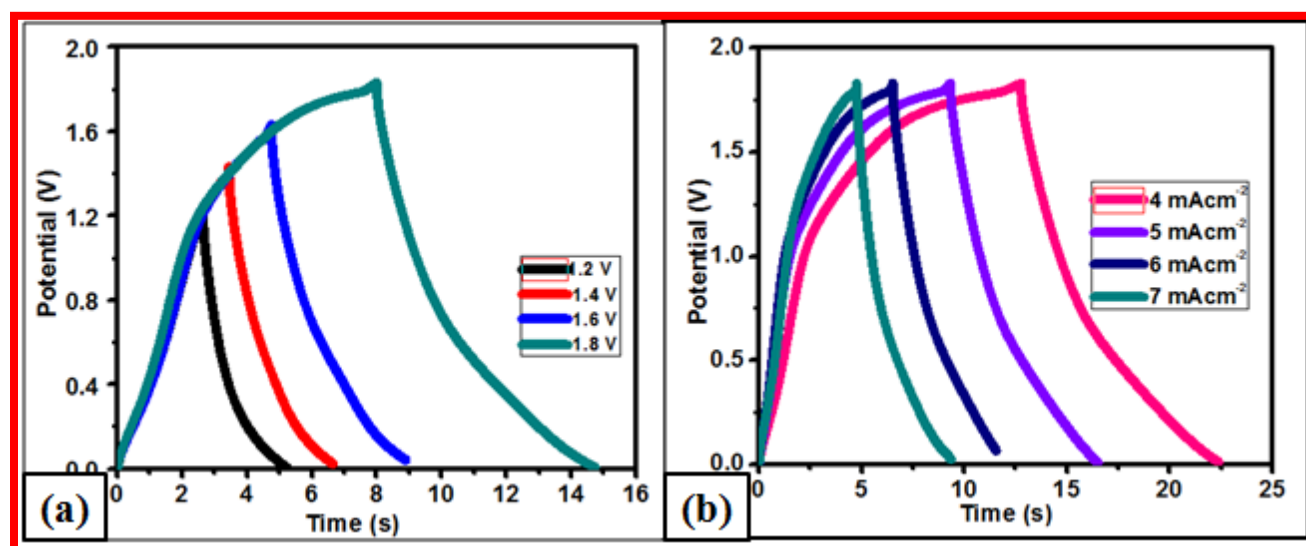


Fig.6.12. (a) The GCD curves of symmetric device at various voltages from 1.2 to 1.8 V, and (b) the GCD curves of device at 1.8 V and at 4, 5, 6 and 7 mAcm⁻² charging current densities.

(d) Ragone Study-

The change in Cs of symmetric device with current density is shown **Fig. 6.13**. The Ragone plot of energy density (ED) and power density (PD) is shown in **Fig. 6.13**. The values of Cs, E.D, and PD are 35.1 Fg⁻¹, 15.8 Wh Kg⁻¹, 3600 KWkg⁻¹, correspondingly. This result shows good rate

Device Fabrication of Flexible Symmetric and Asymmetric Supercapacitors: Performance Evaluation

capability of device. The specific energy in present work is higher than Patil et al [20] for symmetric La_2S_3 device (0.14 Whkg^{-1}).

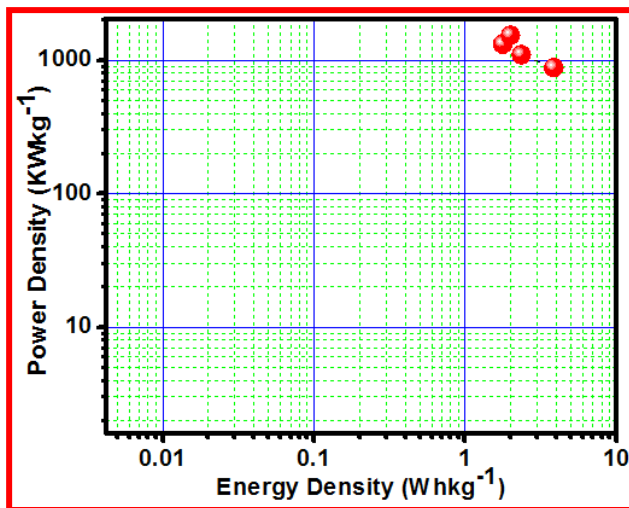


Fig.6.13. Ragone plot of $\text{GO/La}_2\text{S}_3//\text{PVA-Na}_2\text{SO}_4//\text{GO/La}_2\text{S}_3$ FSSSC device.

Fig.6.15 shows the device demonstration of $\text{GO/La}_2\text{S}_3//\text{PVA-Na}_2\text{SO}_4//\text{GO/La}_2\text{S}_3$ devices. The device charged for 30 s at 1.8 V, light up the **Fig.6.15 (a)** shows single red LED charging for 30 s and input voltage of 1.8 V, **(b)** after charging LED glows for 15 s and **(c)** after 15 s LED got glowing intensity down.

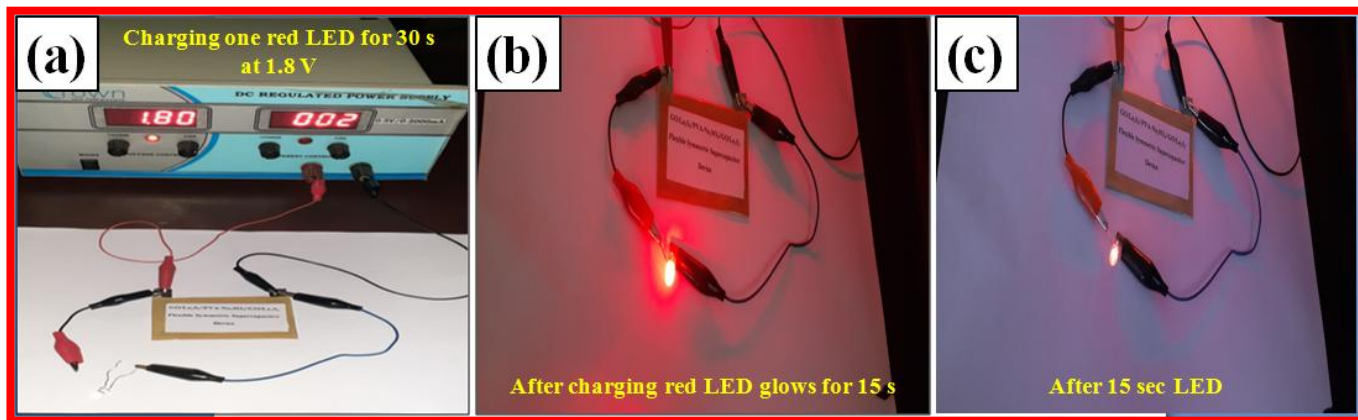


Fig.6.15. Demonstration of $\text{GO/La}_2\text{S}_3//\text{PVA-Na}_2\text{SO}_4//\text{GO/La}_2\text{S}_3$ device.

(e) Cyclic Stability Study-

Electrochemical cycling stability of device is tested for consecutive 1,000 CV cycles at 100 mVs⁻¹ scan rate. Maximum 81.2 % capacity retention of symmetric GO/La₂S₃ device retained after 1,000 CV cycles is shown in **Fig. 6.15**. Inset of **Fig.6.15** shows 2nd, 50th, 100th, 200th, 400th, 600th, 700th, 800th, 900th and 1000th CV curves which indicate that the material behaves reversibly as an excellent capacitor material for a large number of cycles. The decrease in current in the CV curves with surging cycle number shows the change in the surface structure of the electrodes which is the consequence of degradation of electrode material. These results indicate that the FSSSC device possesses not only exceptional electrochemical performance but also excellent stability.

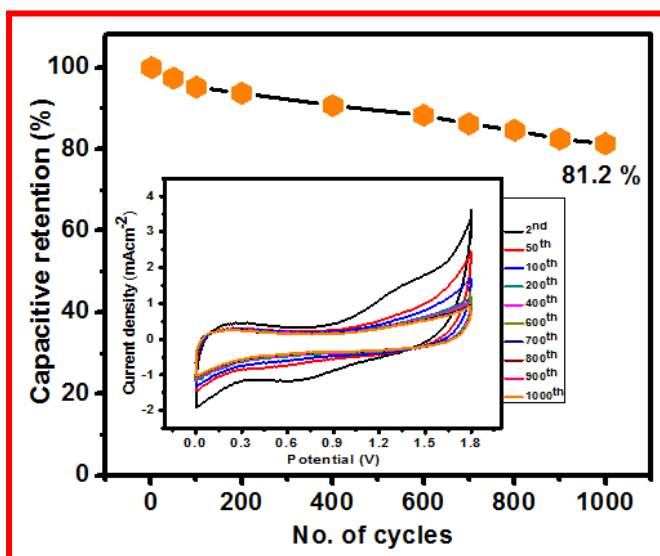


Fig.6.15. Cyclic Stability at 100 mVs⁻¹ scan rate (inset shows shape of CV curves).

(f) EIS Study-

EIS technique is used to study the electrochemical behavior of GO/La₂S₃//PVA-Na₂SO₄//GO/La₂S₃ FSSSC device. **Fig.6.16** shows Nyquist plot consisting of imaginary impedance component (Z'') against the real impedance component (Z') in the frequency range from

Device Fabrication of Flexible Symmetric and Asymmetric Supercapacitors: Performance Evaluation

1 Hz to 1 MHz for GO/La₂S₃//PVA-Na₂SO₄//GO/La₂S₃ FSSSC devices. Nyquist plot is divided into low and high frequency regions. In the high frequency region, it shows indistinct semi-circle indicating good supercapacitive behavior. Inset shows the equivalent circuit diagram, series inductance (L_s) is 2.14 H, resistance (R₁, R₂ and R₃) is 1.15 Ω cm⁻², capacitance (Q₁, Q₂ and Q₃) are 0.48, 0.003 and 0.001 F and Warburg resistance (W) is -18 Ω cm⁻², respectively are determined from Nyquist plot.

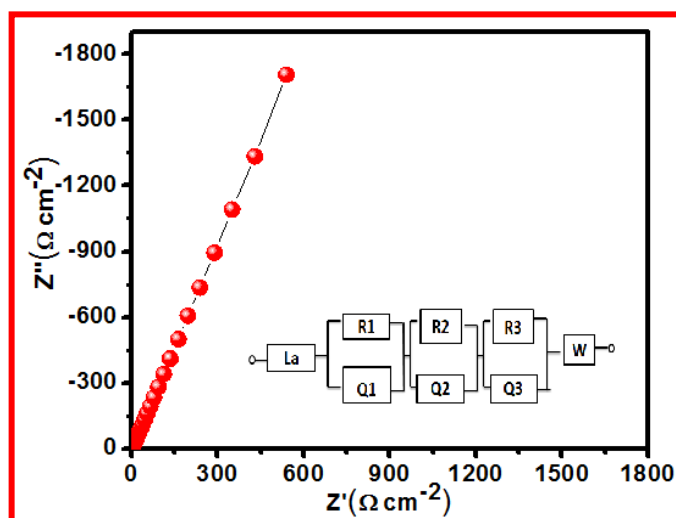


Fig.6.16. (a) Nyquist plot of GO/La₂S₃//PVA-Na₂SO₄//GO/La₂S₃ FSSSC devices and inset shows equivalent circuit diagram.

Table 6.2 Obtained Nyquist plot parameters values fitted with equivalent circuit for GO/La₂S₃//PVA-Na₂SO₄//GO/La₂S₃.

GO/La ₂ S ₃ //PVA-Na ₂ SO ₄ //GO/La ₂ S ₃	
L _s (H)	2.14
Q ₁ (F)	0.48
R ₁ ,R ₂ ,R ₃ (Ω cm ⁻²)	1.15
Q ₂ (F)	0.001
W(Ω cm ⁻²)	-18

6.2. B.3 Performance Evaluation of Flexible Asymmetric GO/Sm₂S₃//PVA-Na₂SO₄//MnO₂ Supercapacitor Device

The asymmetric device was fabricated using GO/Sm₂S₃ as a negative and MnO₂ as a positive and PVA-Na₂SO₄ gel electrolyte. The mass ratio of the positive electrode and negative electrode are adjusted by the equation as,

$$\frac{M^+}{M^-} = \frac{Cs^- \times \Delta E^-}{Cs^+ \times \Delta E^+} \quad (6.a)$$

Here, charge stored by the each electrode depends on potential window (ΔE), mass of the active material (M), and CS of the respective electrode. Using this equation, the optimal mass ratio of the two electrodes M^+/M^- was calculated as 1.49. Thus, out of total mass of loading of 0.257 mg, a mass of 0.197 mg is of GO/Sm₂S₃ and that of 0.06 mg of MnO₂. This demonstrates that the two electrodes provide almost same total charge; thereby the charge balance is realized.

(a) Cyclic Voltammetry (CV) Study-

The flexible asymmetric device of configuration GO/Sm₂S₃/PVA-Na₂SO₄//MnO₂ was fabricated ($5 \times 5 \text{ cm}^{-2}$ area) using GO/Sm₂S₃ as an anode and MnO₂ thin film electrodes as an cathode, respectively. The electrochemical performance of individual electrodes is tested in 1 M Na₂SO₄ electrolyte. The PVA-Na₂SO₄ gel is used as an electrolyte as well as separator to boost operating potential range, ED and cycling stability of device. After fabricating the GO/Sm₂S₃//PVA-Na₂SO₄//MnO₂ flexible asymmetric device the first step is to select the operating potential range by keeping reversibility of both the electrodes. The exact potential window of device is

Device Fabrication of Flexible Symmetric and Asymmetric Supercapacitors: Performance Evaluation

confirmed by taking CV at different potential ranging from +1.2 to +1.8 V, as shown in **Fig.6.18 (a)**.

The CV graphs sustain their curves up to +1.8 V and further rise in the potential disrupts cathodic shape of the CV curve, therefore, GO/Sm₂S₃// MnO₂ device is operated within potential windows of 0 to +1.8 V at different scan rates of 5 to 100 mVs⁻¹ in **(Fig.6.18 (b))**. These CV curves do not distort with changing scan rate, indicating the promising charge/discharge performance for the device. The Cs between 16.5 and 0.75 Fg⁻¹ are observed for scan rates between 5 to 100 mVs⁻¹ for device **(Fig.6.18(c))**. When increasing scan rate, the capacitance decreases due to the effective interaction in between ions in the electrolyte and surface of electrode material.

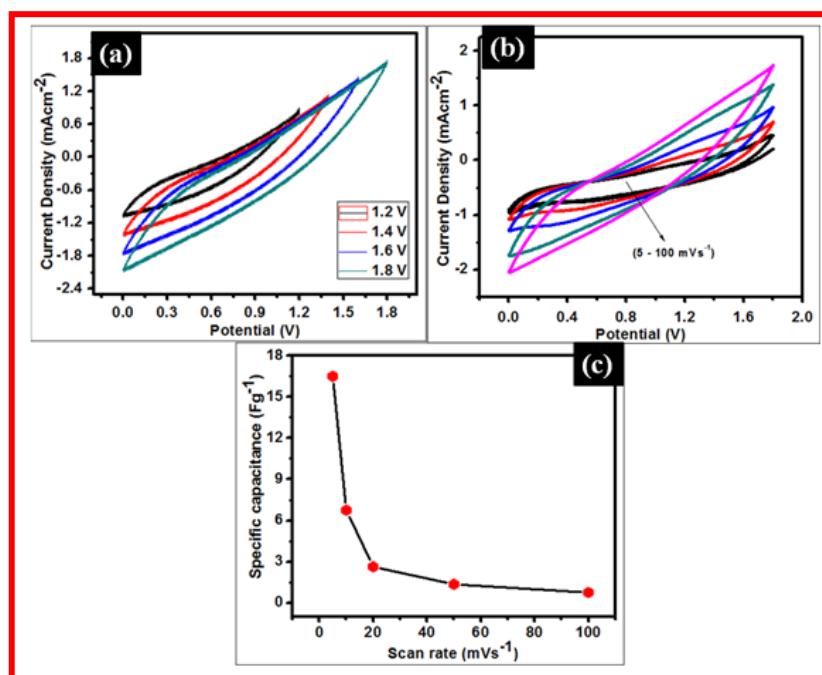


Fig.6.18: (a) The CV curves at different potential windows, (b) the CV curves at different scan rates (5 to 100 mVs⁻¹), and (c) specific capacitance versus scan rate plot for GO/Sm₂S₃/PVA-Na₂SO₄/MnO₂ device.

(c) Galvanostatic Charge/Discharge (GCD) Study-

The GCD curves of device at potentials of 1.2 and 1.8 V, and at 4 mA cm^{-2} current density are shown in **Fig.6.19(a)**. Each curve showing initial IR drop and then resulting non-linear discharge curve, which shows supercapacitive behavior of device. The GCD curves of device at current densities of 4, 5, 6 and 7 mA cm^{-2} at 1.8 V potential window are depicted in **Fig.6.19 (b)**. The Cs of 8.7, 5.4, 4.0 and 3.1 F g^{-1} are observed at 4, 5, 6 and 7 mA cm^{-2} , respectively for the device. The increasing charging current density reduces the value of the capacitance. The capacity reduction with the increasing current density can be attributed to the ineffective utilization of electrolyte ions at the higher current density [22].

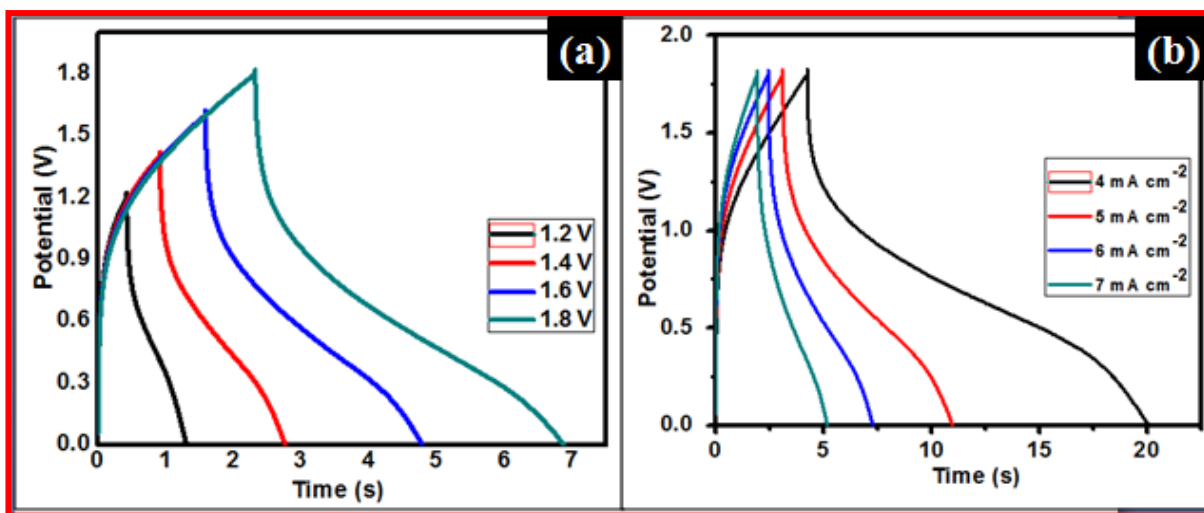


Fig.6.19: (a) The GCD curves at different potential windows at 4 mA cm^{-2} current density and (b) The GCD curves at different current densities of 4, 5, 6 and 7 mA cm^{-2} at 1.8 V potential window of GO/Sm₂S₃/PVA-Na₂SO₄/MnO₂ asymmetric SCs device.

(d) Ragone Plot-

Ragone plot (power density vs. energy density) of GO/Sm₂S₃/PVA-Na₂SO₄/MnO₂ device is shown in **Fig.6.20**. The energy and power densities were derived from charge/discharge

Device Fabrication of Flexible Symmetric and Asymmetric Supercapacitors: Performance Evaluation

curves at various current densities and are calculated from the eq.s 2.4 and 2.5 [23]. The energy density decreases with the increase of power density. The Ragone plot of asymmetric device at four current densities values, which shows that asymmetric device, has obtained highest energy density (ED) of 3.95 Whkg^{-1} of at 900 Wkg^{-1} power density (PD). Fan et al [24] fabricated GO/MnO₂/ACN asymmetric supercapacitor device and tested in the voltage range of 0 to 1.8 V and exhibited maximum ED of 51.1 Whkg^{-1} and PD 102.2 Wkg^{-1} . Gao et al [25] fabricated GH//MnO₂-NF asymmetric supercapacitor device and obtained ED is 14.9 Whkg^{-1} .

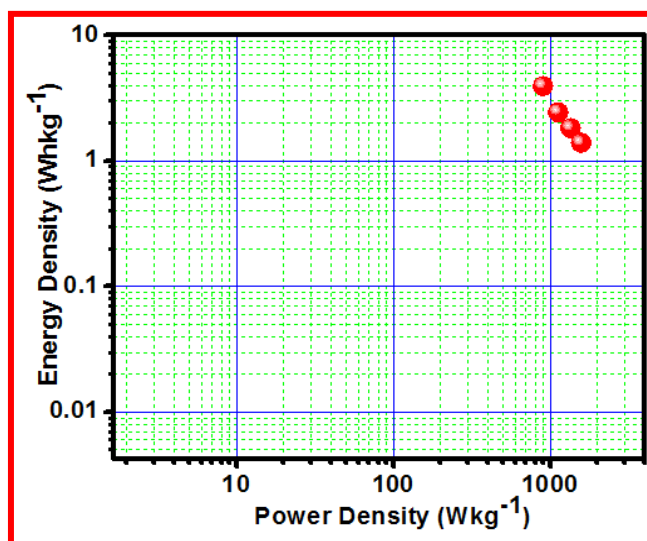


Fig.6.20: The Ragone Plot for GO/Sm₂S₃//PVA-Na₂SO₄//MnO₂ asymmetric device

(e) Electrochemical Cyclic Stability Study-

Long term cycling stability of device is required for the commercialization. Cycling test of GO/Sm₂S₃//PVA-Na₂SO₄//MnO₂ asymmetric FSSSC device was performed over 2000 CV cycles at a constant scan rate of 100 mVs^{-1} in the potential window of 0 to 1.8 V (Fig.6.21). The device preserves 90 % of capacitive retention after 2000 CV cycles, indicating that cycling stability of the device is superior. Inset of Fig.6.19 shows the number of CV cycles such as 2nd, 100th, 400th,

Device Fabrication of Flexible Symmetric and Asymmetric Supercapacitors: Performance Evaluation

600th, 700th, 900th, 1000th, 1200th, 1500th, 1700th and 2000th, respectively. Cao et al [26] fabricated MnO₂//PVA-Na₂SO₄//Graphene asymmetric electrode and reported cyclic stability 96 % for 500 cycles. Zhai et al [27] reported cyclic stability of 1.35 % for 10,000 cycles at 300 mVs⁻¹ scan rate.

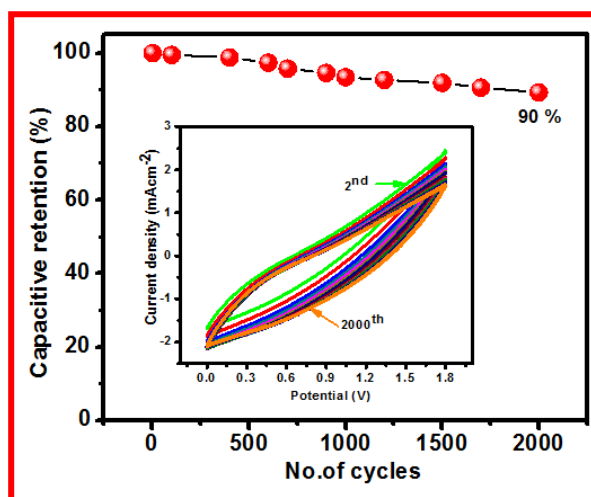


Fig.6.21: The capacity retention and inset shows CV curves for GO/Sm₂S₃//PVA-Na₂SO₄//MnO₂ asymmetric device for 2000 cycles.

(e) EIS Study-

The EIS study of GO/Sm₂S₃//PVA-Na₂SO₄//MnO₂ asymmetric FSSSC device is performed by applying an amplitude of 10 mV in the frequency range of 10 mHz to 100 kHz. The Nyquist plot for device is shown in Fig. 6.22. The plot consists of a small semicircle arc in the higher frequency region and semi-circle with straight line in the lower frequency region [28]. The semicircle arc specifies the double layer capacitance at the interface of electrode and electrolyte. The equivalent series resistance (Rs) of 3.8 Ω cm⁻² and resistance (R1, and R2) is 2.71 and 4.49 Ω cm⁻² and the capacitance (Q1, Q2 and Q3) is 0.81, 0.60 and 0.67 F, respectively are evaluated

Device Fabrication of Flexible Symmetric and Asymmetric Supercapacitors: Performance Evaluation

from the Nyquist plot analysis in **Table 6.3**. The smaller values of R_s and R_{ct} for device suggest the easier electrochemical reactions at the interface between active material and electrolyte and better compatibility with PVA- Na_2SO_4 gel electrolyte.

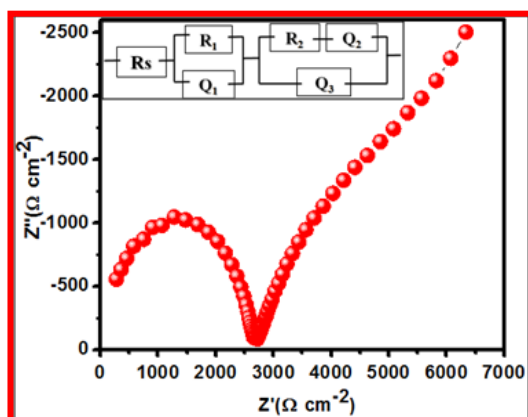


Fig.6.22: Nyquist plot for GO/Sm₂S₃//PVA- Na_2SO_4 //MnO₂ asymmetric FSSSC device

Table 6.3. Nyquist plot parameters fitted with equivalent circuit for GO/Sm₂S₃//PVA- Na_2SO_4 //MnO₂.

GO/Sm ₂ S ₃ //PVA- Na_2SO_4 //MnO ₂	
$R_s(\Omega \text{ cm}^{-2})$	3.8
$Q_1(\text{F})$	0.81
$R_1(\Omega \text{ cm}^{-2})$	2.71
$Q_2(\text{F})$	0.60
$R_2(\Omega \text{ cm}^{-2})$	4.49
$Q_3(\text{F})$	0.67

(f) GO/Sm₂S₃//PVA- Na_2SO_4 //MnO₂ Asymmetric Device Demonstration-

To demonstrate practical applicability one device was connected and charged for 30 s by applying potential of 1.8 V and discharged through the red light emitting diode (LEDs). More

Device Fabrication of Flexible Symmetric and Asymmetric Supercapacitors: Performance Evaluation

outstandingly, GO/Sm₂S₃//PVA-Na₂SO₄//MnO₂ asymmetric device can light up 211 red LEDs for 40 s. The schematic representation of GO/Sm₂S₃//PVA-Na₂SO₄//MnO₂ device with PVA-Na₂SO₄ gel electrolyte is shown in Fig.6.23 (A). The Fig.6.23 (B-D) demonstrates the digital photographs of real time demonstration by glowing red LED for 40 s. This demonstration suggests the potential capability of GO/Sm₂S₃//PVA-Na₂SO₄//MnO₂ asymmetric device in energy storage for various electronic electrical devices.

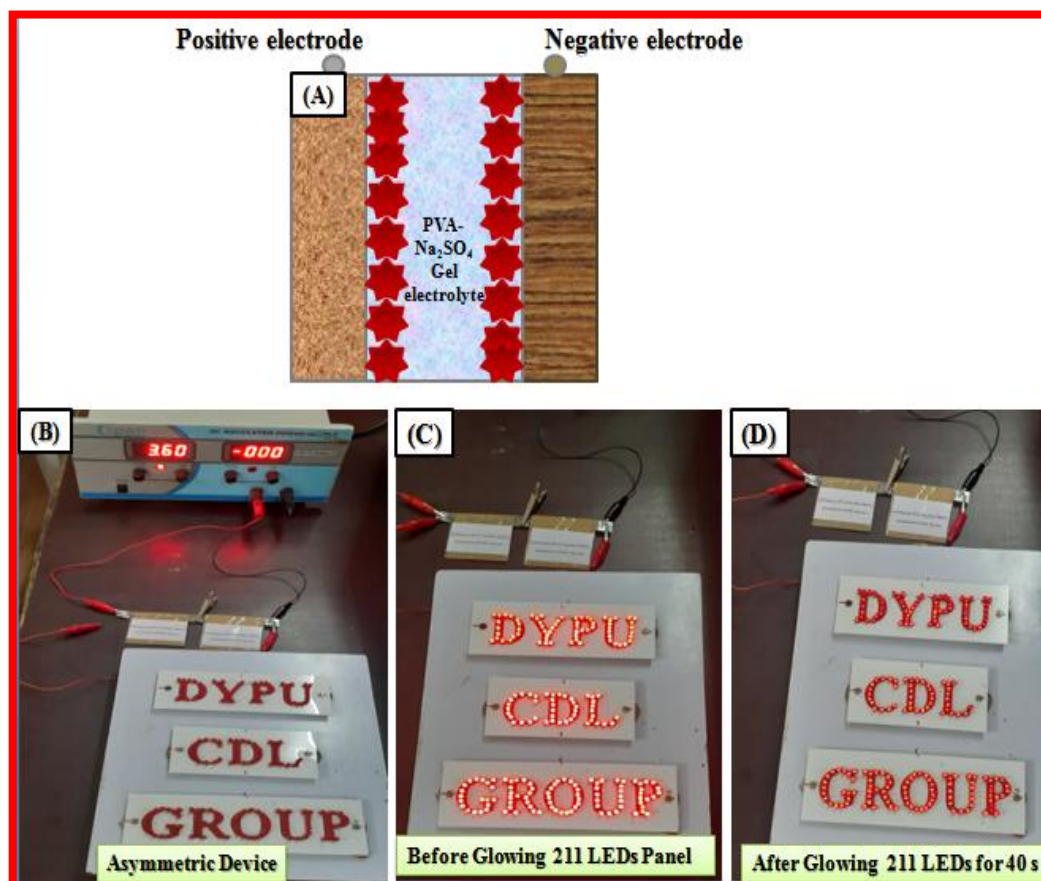


Fig.6.23 (A) The schematic representation of GO/Sm₂S₃//PVA-Na₂SO₄//MnO₂ asymmetric device with PVA-Na₂SO₄ gel electrolyte, (B) digital photograph of demonstration of device, (C) the device is connected to the 211 red LEDs and charged for 30 s and (d) the combination of 211 red LEDs are glowing for 40 s.

6.2. B.4 Performance Evaluation of Flexible Asymmetric GO/La₂S₃// PVA-Na₂SO₄/MnO₂ asymmetric device

(a) Cyclic Voltammetry (CV) Study-

The charge storage by GO/La₂S₃ and MnO₂ thin films is within a potential window of -1 and + 1 V vs.SCE therefore, the GO/La₂S₃// PVA-Na₂SO₄/MnO₂ asymmetric device could achieve a maximum working voltage of + 1.8 V in two electrode system. **Fig.6.24 (a)** demonstrates the CV curves of GO/La₂S₃// PVA-Na₂SO₄/MnO₂ asymmetric device with varying potential windows from 1.2, 1.4, 1.6 and 1.8 V. When increasing the applied voltage from 1.2 to 1.8 V, the CV curves maintained their shape as the applied voltage resulted in a reversible reaction. Therefore, to study the further electrochemical properties, we have selected a potential window of 0 to 1.8 V. **Fig.6.24 (b)** shows the CV curves of GO/La₂S₃// PVA-Na₂SO₄/MnO₂ asymmetric device at different scan rates from 5–100 mVs⁻¹. The CV curves are non-rectangular in shape suggesting pseudo-capacitive behavior of device. The CV curves maintained their shape and reversibility even at high scan rates (100 mVs⁻¹). **Fig.6.24 (c)** shows the variation of specific capacitance with scan rate. The maximum Cs obtained by GO/La₂S₃// PVA-Na₂SO₄/MnO₂ device is 45.2 Fg⁻¹ at 5 mVs⁻¹ scan rate.

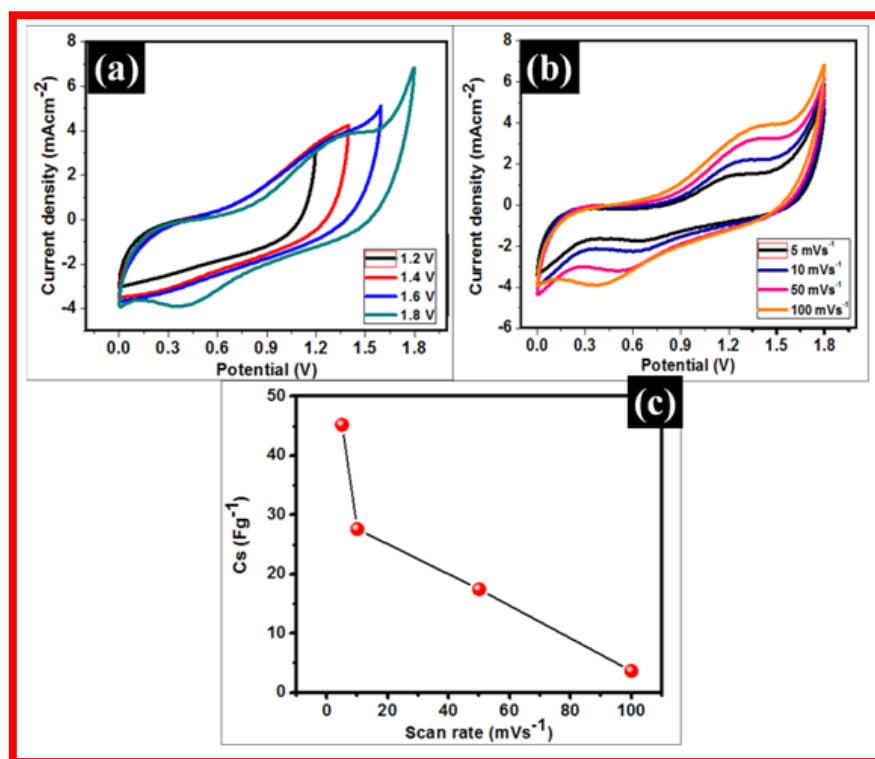


Fig. 6.24 (a) The CV curves of the GO/La₂S₃//PVA-Na₂SO₄//MnO₂ asymmetric device at different potential windows, (b) the CV curves of GO/La₂S₃//PVA-Na₂SO₄//MnO₂ asymmetric device at different scan rates 5 to 100 mVs⁻¹, and (c) variation of specific capacitance vs. scan rate.

(b) Galvanostatic Charge/Discharge (GCD) Study-

To decide the operating potential window of GO/La₂S₃//PVA-Na₂SO₄//MnO₂ asymmetric device, the GCD curves of the device tested at different potential ranging from 1.2 V to 1.8 V at current density of 4 mA cm⁻² are shown in **Fig. 6.24 (a)**. The GCD study is used to examine the applicability of fabricated GO/La₂S₃//MnO₂ asymmetric device, since this technique can easily evaluate the rate capability of device by judging the rate of change of voltage with time during charging and discharging at various current densities within a potential window of 0.0 to 1.8 V.

Device Fabrication of Flexible Symmetric and Asymmetric Supercapacitors: Performance Evaluation

The GCD curves of GO/La₂S₃/PVA-Na₂SO₄/MnO₂ asymmetric device at different current densities are shown in **Fig. 6.24 (b)**. There is a non-linear shape of curves during both charging and discharging processes. The estimated values of specific capacitance (Cs) are 16.6, 7.16, 5.35 and 4.63 Fg⁻¹ different current densities of 4, 5, 6, and 7 mAcm⁻².

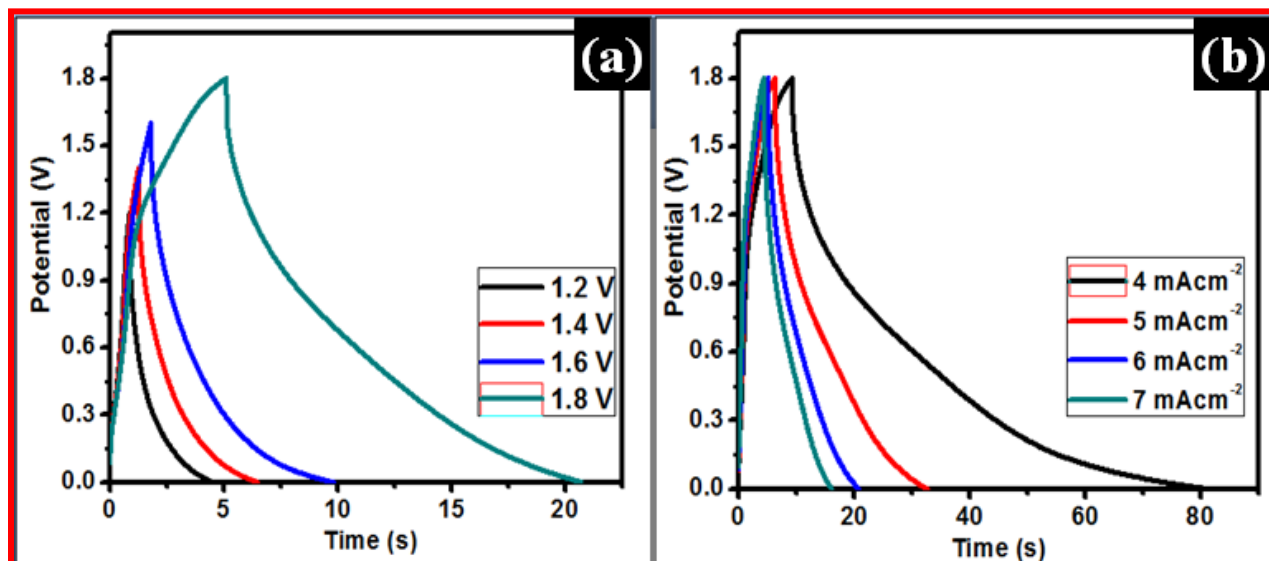


Fig.6.24: (a) The GCD curves at potentials ranging from 1.2 to 1.8 V and (b) the GCD curves at 1.8 V potential window for 0.5, 0.6, 0.7 and 0.8 mA cm⁻² charging current densities.

(c) Ragone Plot-

Using the discharge curve, the energy densities and power densities are calculated and plotted as shown in **Fig.6.25**. The Ragone plot demonstrates the energy density of 7.5 Wh Kg⁻¹ with power density of 360 Wkg⁻¹ at 4 mAcm⁻² current density. More significantly, the energy density of GO/La₂S₃/PVA-Na₂SO₄/MnO₂ asymmetric device is higher than the previous reported **Patil et al [20]** including La₂S₃/La₂S₃ symmetric device (ED=0.14 Whkg⁻¹ and PD=22.7 Wkg⁻¹).

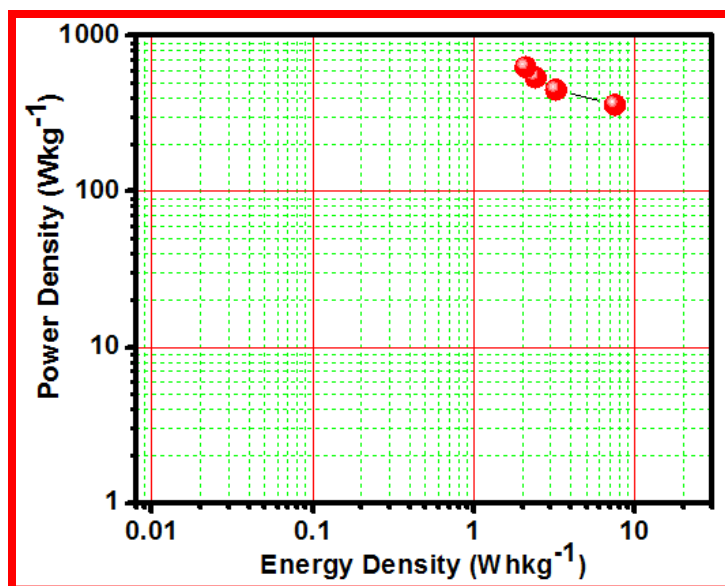


Fig.6.25: Ragone Plot for GO/La₂S₃//PVA-Na₂SO₄/MnO₂ asymmetric device.

(d) Electrochemical Cyclic Stability Study-

The electrochemical cycling stability is a key factor that determines the practical applicability of the device. The cycling stability of GO/La₂S₃//PVA-Na₂SO₄/MnO₂ asymmetric device was tested for 2000 CV cycles at 100 mVs⁻¹ scan rate. **Fig.6.26** shows variation capacity retention with cycle number. The inset of figure reveals the all CV curves overlap over one another indicating good cycling stability. The cycling test of the device shows about 86.8% capacitive retention over 2000 cycles, which is better than previously reported work (73 % for 1000 cycles)[20].

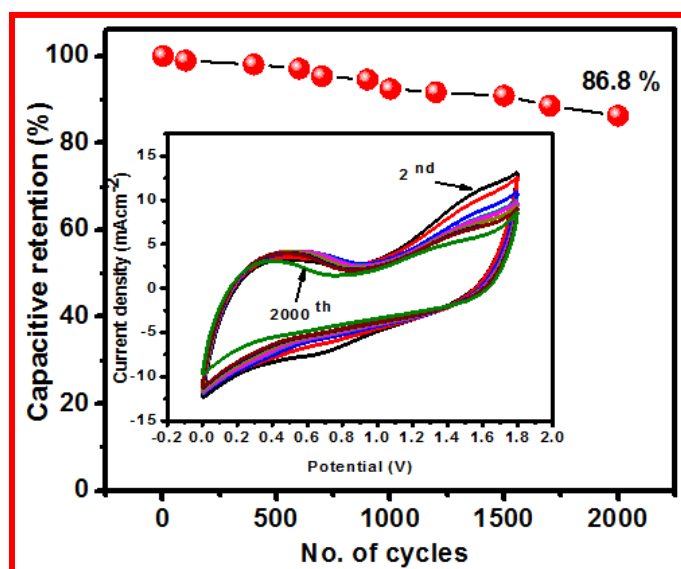


Fig.6.26: Specific capacitance retention (inset shows CV curves for cycles).

(e) EIS Study-

To get the more insight about the rate kinetics the electrochemical impedance analysis is carried out and the corresponding results are presented in the form of Nyquist plot (**Fig.6.27.**) Nyquist plot shows the equivalent series resistance R_s of ($1.01 \Omega\text{cm}^{-2}$) and charge transfer resistance R_{ct} of ($1.47 \Omega\text{cm}^{-2}$). The less value of R_s indicates the facial electrochemical interactions between the active electrode material and electrolyte ions. The inset of **Fig.6.27** shows highly magnified Nyquist plot which shows semicircle is observed in Nyquist plot. The initial barrier in the electrochemical reactions is the charge transfer resistance (R_{ct}) which is represented by the semicircle in the Nyquist plot. Also, shows best fitted equivalent circuit data. The (W) indicates that the Warburg resistance obtained from matched equivalent circuit is $1.36 \Omega\text{cm}^{-2}$. The (Q) indicates the double layer capacitance obtained from circuit is 0.73 F in the **Table 6.4**.

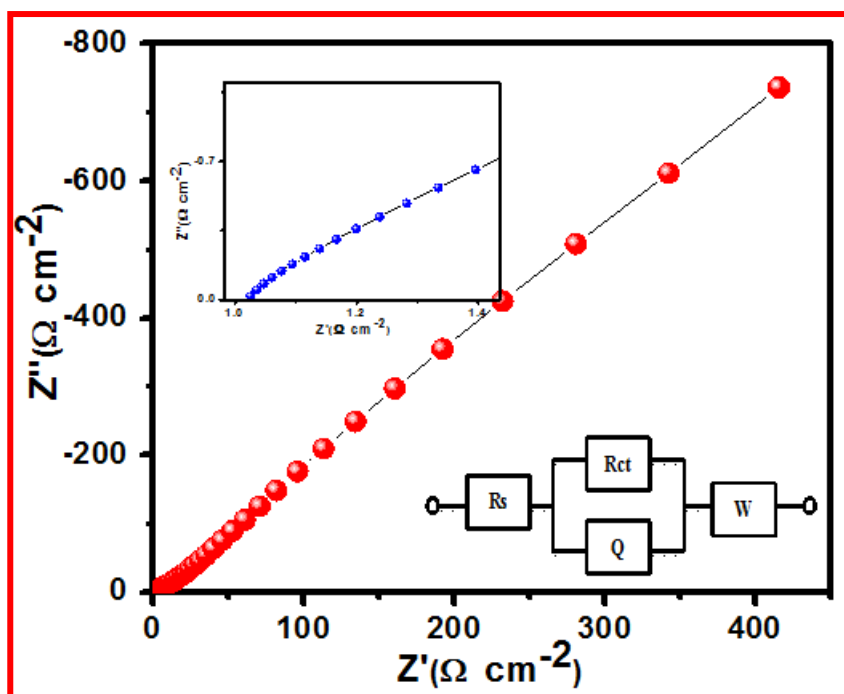


Fig.6.27: The Nyquist plot for GO/La₂S₃//PVA-Na₂SO₄//MnO₂ device and inset shows magnified image of Nyquist plot and equivalent circuit.

Table 6.4. Nyquist plot parameters fitted with equivalent circuit for GO/La₂S₃//PVA-Na₂SO₄//MnO₂.

GO/La ₂ S ₃ //PVA-Na ₂ SO ₄ //MnO ₂	
R _s (Ω cm ⁻²)	1.01
R _{ct} (Ω cm ⁻²)	1.47
Q (F)	0.73
W (Ω cm ⁻²)	1.36

To demonstration of the GO/La₂S₃//PVA-Na₂SO₄//MnO₂ asymmetric supercapacitor device we connected two devices in parallel. The devices were charged for 30 s by applying a voltage of 2.3 V as shown in **Fig.6.28 (A)** and discharged through a panel of 50 red light emitting diodes (LEDs). Impressively, this parallel combination of GO/La₂S₃//PVA-Na₂SO₄//MnO₂ asymmetric

Device Fabrication of Flexible Symmetric and Asymmetric Supercapacitors: Performance Evaluation

devices can easily light up an LED panel for 25 s in **Fig.6.28 (B, C)**. It clearly demonstrates the great potential of $\text{GO}/\text{La}_2\text{S}_3//\text{PVA}-\text{Na}_2\text{SO}_4//\text{MnO}_2$ asymmetric supercapacitor device as a most promising energy storage technology in the area of portable electronic devices.

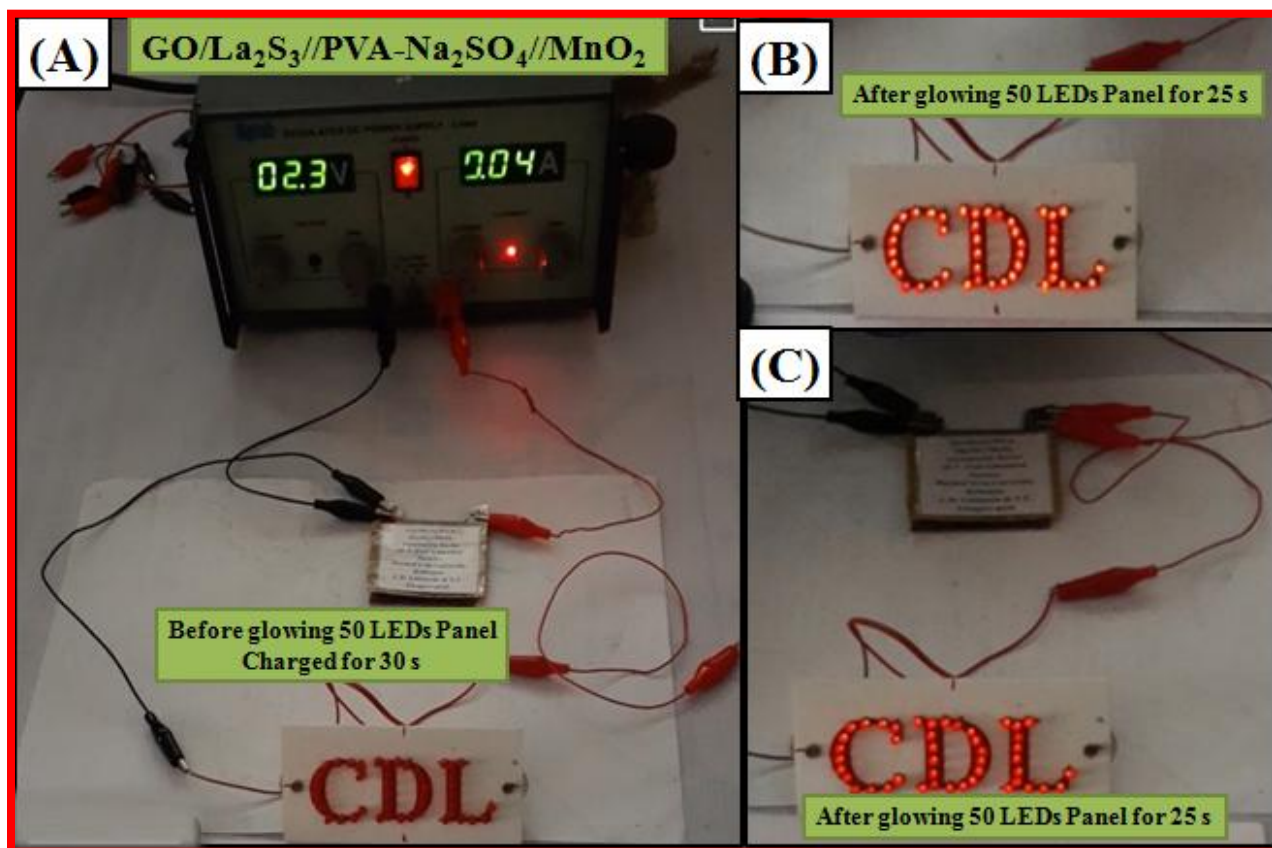


Fig.6.28: (A) Digital photographs of real demonstration of $\text{GO}/\text{La}_2\text{S}_3//\text{PVA}-\text{Na}_2\text{SO}_4//\text{MnO}_2$ asymmetric devices are connected with the 50 red LEDs and charging for 30 s and (B, C) The 50 LEDs are glowing for 25 s.

6.2 Conclusions-

In this chapter, we fabricated symmetric and asymmetric devices configuration of GO/Sm₂S₃//GO/Sm₂S₃, GO/La₂S₃//GO/La₂S₃, GO/Sm₂S₃//MnO₂ and GO/La₂S₃//MnO₂. In asymmetric devices we used MnO₂ as a positive (cathode) and GO/Sm₂S₃, and GO/La₂S₃ as negative (anode) electrodes with PVA-Na₂SO₄ gel electrolyte. The devices exhibit the excellent electrochemical performance with maximum specific capacitance with energy density and power density of (GO/Sm₂S₃//GO/Sm₂S₃ is 68.5 Fg⁻¹, 3.71 Whkg⁻¹ and 1028 KWkg⁻¹) (GO/La₂S₃//GO/La₂S₃ is 60 Fg⁻¹, 15.8 Whkg⁻¹ and 3600 KWkg⁻¹), (GO/Sm₂S₃//MnO₂ is 16.5 Fg⁻¹, 3.95 Whkg⁻¹ and 900 Wkg⁻¹) and (GO/La₂S₃//MnO₂ is 16.5 Fg⁻¹, 7.5 Whkg⁻¹ and 360 Wkg⁻¹), respectively as shown in **Table 6.1 and 6.2**. Moreover, both symmetric and asymmetric devices exhibit good cycling stability with a wide potential window. Thus, the proposed simple and affordable approach of fabricating flexible devices. However, by considering overall performance the GO/Sm₂S₃//PVA-Na₂SO₄//MnO₂) asymmetric devices showed excellent performance and opened up new opportunities for energy storage devices.

Device Fabrication of Flexible Symmetric and Asymmetric Supercapacitors: Performance Evaluation

Table.6.1: Supercapacitive Evaluation of Flexible symmetric (GO/Sm₂S₃//PVA-Na₂SO₄//GO/Sm₂S₃ and GO/La₂S₃//PVA-Na₂SO₄//GO/La₂S₃) FSSSC supercapacitor devices.

GO/Sm ₂ S ₃ // PVA-Na ₂ SO ₄ //GO/Sm ₂ S ₃ Symmetric Device	Values		GO/La ₂ S ₃ //PVA-Na ₂ SO ₄ //GO/La ₂ S ₃ Symmetric Device	Values
Cs (Fg ⁻¹)	12.5		Cs (Fg ⁻¹)	6.34
ED (Whkg ⁻¹)	0.65		ED (Whkg ⁻¹)	15.8
PD (KWkg ⁻¹)	1800		PD (Wkg ⁻¹)	3600
Cyclic stability (%) over 1000 cycles	82.8		Cyclic stability (%) over 1000 cycles	81.2
Rs (Ω cm ⁻²)	0.54		R (Ωcm ⁻²)	1.15
Rct (Ωcm ⁻²)	0.84		W (Ωcm ⁻²)	-18

Table.6.2: Supercapacitive Evaluation of Flexible Asymmetric (GO/Sm₂S₃//PVA-Na₂SO₄//MnO₂ and GO/La₂S₃//PVA-Na₂SO₄//MnO₂) solid-state supercapacitor devices

GO/Sm ₂ S ₃ //PVA-Na ₂ SO ₄ //MnO ₂ Asymmetric Device	Values		GO/La ₂ S ₃ //PVA-Na ₂ SO ₄ //MnO ₂ Asymmetric Device	Values
Cs (Fg ⁻¹)	16.5		Cs (Fg ⁻¹)	45.2
ED (Whkg ⁻¹)	0.98		ED (Whkg ⁻¹)	7.5
PD (Wkg ⁻¹)	225		PD (Wkg ⁻¹)	360
Cyclic stability (%) over 2000 cycles	90		Cyclic stability (%) over 2000 cycles	86.8
Rs (Ωcm ⁻²)	3.8		Rs (Ωcm ⁻²)	1.01
Rct (Ωcm ⁻²)	-		Rct (Ωcm ⁻²)	1.47

References-

1. J. Zhu, W. Zhou, Y. Zhou, X. Cheng, J. Yang, J. Electron. Mater., **48** (2019) 1531-1539.
2. S. Ramesh, K. Karuppasamy, H.S.Kim, H.S.Kim, J.H.Kim, Sci Rep. **8** (2018) 16543-16553.
3. Z.S.Iro, C.Subramani, S.S.Dash, Int. J. Electrochem. Sci., **11** (2016) 10628 – 10643.
4. C.Arbizzani, M.Mastragostino, F.Soavi, J.Power Source **100** (2001) 164–170
5. Y.Z.Zhang, Y.Wang, T.Cheng, W.Y.Lai, H.Pang, W.Huang, Chem.Soc.Rev., **44** (2015) 5181-5199.
6. N.R .Chodankar, A.K. Nanjundan, D. Losic, D.P. Dubal, J.B. Baek, Mater. Today **6** (2020) 100053-100059.
7. B.Liu, Q.Wang, X.Wang, Q.Xiang, D.Chen, G.Shen, ACS Appl. Mater. Interfaces, **5** (2013) 10011–10017.
8. A.Yuan, Q.Zhang, Electrochem. commun., **8** (2006) 1173-1178.
9. Cao, Y.Wang, Y.Zhou, J.H.Ouyang, D.Jia, L.Guo, J. Electroanal. Chem. **689** (2013) 201-206.
10. S. Hu, R.Rajamani, X.Yu, Appl. Phys. Lett. **100** (2012) 104103-104107.
11. C. C.Hu, C.Y.Hung, K.H.Chang, Y.L.Yang, J.Power Source, **196** (2011) 847-850.
12. C.L. Geng, L.Q. Fan, C.Y. Wang Y.L.Wang, S.J. Sun, Z.Y. Song, N. Liu, J.H. Wu, New J.Chem., **43** (2019) 18935-18942
13. V.S. Kumbhar, A.D. Jagadale, C.D. Lokhande, J. Power Source **234** (2013) 107-110.
14. N.R.Chodankar, H. D.Pharm, A.K. Nanjundan, J.F.Fernando, K. Jayaramulu, D.Golberg, Y.K. Han, D. P Dubal, Small **16** (2020), 2002806-2002811.
15. V.S.Kumbhar, A.D.Jagadale, N.S.Gaikwad, C.D.Lokhande, Mater. Res. Bull. **56** (2014) 39-44.

16. V.S. Kumbhar, Y.R. Lee, C.D. Lokhande, D.H. Kim, J.J. Shim New J. Chem **42** (2018) 14805-14816.
17. V.S. Kumbhar, A.C. Lokhande, N.S. Gaikwad, C.D. Lokhande, Ceram. Int. **41** (2015), 5758-5764.
18. S.J. Patil, V.S. Kumbhar, B.H. Patil, R.N. Bulakhe, C.D. Lokhande, J. Alloys Compd. **611**(2014) 191-196
19. S.J.Patil, V.C.Lokhande, N.R. Chodankar, C.D.Lokhande, J. Colloid Interface Sci. **469** (2016) 318-324.
20. S.J.Patil, C.D.Lokhande, Mater. Des. **87** (2015) 939-948.
21. N.R.Chodankar, D.P.Dubal, G.S.Gund, C.D.Lokhande, Energy Technol. **3** (2015), 625-631.
22. G.S.Gund, D.P.Dubal, B.H.Patil, S.SShinde, C.D. Lokhande, Electrochim. Acta **92** (2013) 205-215.
23. D.B.Malavekar, V.C. Lokhande, V.J. Mane, S. B Kale, R.N Bulakhe, U.M. Patil, I.In, C. D. Lokhande, J. Solid State Electr, **24** (2020) 1-12
24. Z.Fan, J.Yan, T.Wei,L. Zhi, G.Ning,T.Li,F.Wei, Adv.Funct.Mater., **21** (2011) 2366-2375.
25. H.Gao, F.Xiao,C.Bun,H.Duan, Appl.,Mater.Interfaces., **4** (2012) 2801-2810.
26. J.Cao,Y.Wang,Y.Zhou, J.H.Ouyang, D.Jia, L. Guo, J. Electroanal. Chem, **689** (2013), 201-206.
27. T.Zhai, F.Wang, M. Yu, S.Xie, C. Lian, Cheng Li, F. Xiao, R. Tang, Q. Wu, X. Lu, Y. Tong, Nanoscale., **5** (2013), 6790-6796.
28. R.T.Binny,K.Chaitra,K.Venkatesh, N.Nagaraju, N.Kathyayini, J. Power Source, **309** (2016), 212-220.

Chapter-7

Summary and Conclusions

The electric charge storage system includes battery, capacitor and supercapacitors. Unlike batteries, supercapacitor charge and discharge very quickly without degrading material. Supercapacitors are designed to bridge the gap between conventional capacitor and battery. The recent trends have attracted to fabrication of the solid-state supercapacitor devices in small scale applications. Supercapacitor was fabricated in such a way that to store and release energy within second. The performance of supercapacitor depends upon the operating voltage, electrolyte stability and nature of electrode surface. Depending upon type of charge storage mechanism, the supercapacitors are classified into three types. The carbonaceous electrode material shows pure electric double layered capacitor (EDLCs) behavior, where non-faradic reaction occurs. The metal oxides, polymers and metal chalcogenides are applied in pseudocapacitor; in which faradic reaction occurs. The rare earth chalcogenides have better reduction potential which can be useful in supercapacitive application to increase the potential window and hence enhanced energy and power densities.

In the present work, synthesis of graphene oxide/samarium sulfide (GO/Sm₂S₃) and graphene oxide/ lanthanum sulfide (GO/La₂S₃) composite thin films using simple, cost effective, successive ionic layer adsorption and reaction (SILAR) method was carried out. The thin films were characterized for structural, surface morphological and surface wettability properties. The supercapacitive properties of (GO/Sm₂S₃) and (GO/La₂S₃) composite thin film electrodes were studied by cyclic voltammetry (CV), galvanostatic charge/discharge and electrochemical impedance spectroscopy (EIS) techniques. After testing of supercapacitive performance of (GO/Sm₂S₃) and (GO/La₂S₃) composite thin film electrodes, best performance of composite film electrode were further utilized for flexible symmetric supercapacitor device fabrication and

subsequently evaluated for supercapacitive performance over all. The work is distributed into six chapters.

Chapter-I begins with introduction of energy storage devices, including batteries, capacitor, supercapacitors and need of supercapacitor. In the chapter-I, a brief account of literature survey on rare earth metal chalcogenides (S, Se and Te) thin film based supercapacitors and their performance is given. Also, the literature survey on samarium/lanthanum chalcogenide (S, Se and Te) thin films and graphene oxide composite rare earth metals thin films with supercapacitor application is included. The orientation of work and purpose of dissertation are discussed at the end of chapter.

Introduction to thin films, classification of thin film deposition techniques, theoretical background of hydrothermal method and successive ionic layer adsorption and reaction (SILAR) methods, their preparative parameters and advantages are explained in the first part of the **Chapter-II**. The thin films are characterized for structural, morphological and surface wettability properties using different characterization techniques are explained in the second part of **Chapter-II**. The X-ray diffraction (XRD) and Fourier transform Raman spectroscopy (FT-Raman) techniques are discussed for structural studies. The emission scanning electron microscopy (FE-SEM). The contact angle (CA), Brunauer-Emmett-Teller (BET) and X-ray photoelectron spectroscopy (XPS) measurement. The third part of **Chapter-II** is focused on supercapacitor. It consists of supercapacitor types, electric double layer capacitors (EDLCs), pseudocapacitor and hybrid capacitors with their working mechanism. The supercapacitive parameters like cyclic voltammetry, galvanostatic charge/discharge and impedance analysis are explained in detail.

The **Chapter-III** describes the synthesis and characterization of Sm_2S_3 thin films by hydrothermal method and $\text{GO}/\text{Sm}_2\text{S}_3$ composite thin film by SILAR method with their supercapacitor evaluation in aqueous electrolyte. The **Chapter-III** is divided into four sections as A1, A2, B1 and B2. **Section ‘A.1’** deals with the synthesis of Sm_2S_3 thin films by simple and cost effective hydrothermal method. The Sm_2S_3 film was carried out at 393 K. After 60 min, Sm_2S_3 thin film was formed on stainless steel substrate. The formation of Sm_2S_3 thin film was revealed from XRD and FT-Raman studies. The FE-SEM study showed the porous spherical micro grains like surface morphology and typical diameter around 1.24 μm . The estimated direct band gap was 2.90 eV for Sm_2S_3 thin film. The surface wettability studies carried out using drop of distilled water on Sm_2S_3 film showed that surfaces is hydrophilic. The calculated surface area by BET is $1.38 \text{ m}^2\text{g}^{-1}$.

Section ‘A.2’ deals with the evaluation of supercapacitive features of different nanostructured Sm_2S_3 thin films in order to study the electrochemical performances. The three-electrode system consisting of platinum as a counter electrode, Sm_2S_3 thin film as a working electrode, saturated calomel electrode (SCE) as a reference electrode and 1 M Na_2SO_4 as an electrolyte was used to evaluate the electrochemical features. The Sm_2S_3 thin film illustrates the specific capacitance of 153 Fg^{-1} at a scan rate of 5 mVs^{-1} . In addition to this, Sm_2S_3 thin film retained 81.6 % of its initial capacitance after 1000 CV cycles. The EIS study disclosed small R_s ($7.8 \Omega \text{ cm}^{-1}$) and R_{ct} ($33.4 \Omega \text{ cm}^{-1}$) for Sm_2S_3 thin film.

Section ‘B.1’ contains synthesis and characterizations of Sm_2S_3 and $\text{GO}/\text{Sm}_2\text{S}_3$ composite thin films using SILAR method. The graphene oxide (GO) prepared by modified hummers method and the thin film of GO was prepared by layer by layer (LBL) method. The experimental details for the synthesis of Sm_2S_3 and $\text{GO}/\text{Sm}_2\text{S}_3$ composite thin films by SILAR

method are described. The formation of nanocrystalline GO, Sm_2S_3 and GO/ Sm_2S_3 composite thin films was confirmed from XRD and FT-Raman analyses. The FE-SEM study revealed the highly porous nano-strips like surface of GO/ Sm_2S_3 composite thin films. The length of nano-strips was 7.75 μm . The surface wettability studies showed that GO/ Sm_2S_3 composite thin films are superhydrophilic in nature. The BET surface area of GO/ Sm_2S_3 composite thin film was calculated to be 31.43 m^2g^{-1} .

The Sm_2S_3 and GO/ Sm_2S_3 composite thin films synthesized by SILAR method are utilized as supercapacitor electrode and discussed **Section ‘B.1’**. **Section ‘B.2’** The supercapacitive performance of Sm_2S_3 and GO/ Sm_2S_3 composite thin films electrode was tested in aqueous (1 M Na_2SO_4) electrolytes. In this study the performance of GO/ Sm_2S_3 composite thin films electrode was studied using cyclic voltammetry (CV), galvanostatic charge/discharge (GCD) and electrochemical impedance analysis (EIS) techniques. From the cyclic voltammetry study, the performance was studied in terms of interfacial and specific capacitances, by varying the scan rate. The galvanostatic charge/discharge study revealed that GO/ Sm_2S_3 composite thin films electrode has good discharge capability. GO/ Sm_2S_3 composite thin film electrode exhibited maximum values of specific capacitance of 360 Fg^{-1} at 5 mVs^{-1} scan rate. The GO/ Sm_2S_3 composite thin film electrode exhibited excellent supercapacitive performance. The 88.14 % cyclic stability of GO/ Sm_2S_3 composite thin film electrode was retained after 2000 cycles at scan rate of 100 mVs^{-1} . The electrochemical impedance analysis of GO/ Sm_2S_3 composite thin film electrodes was carried out in the frequency range from 1 MHz to 0.1 Hz with zero applied biased voltage. The impedance data were further analyzed by plotting the Nyquist plot.

Chapter-IV deals with the chemical synthesis, characterization, and supercapacitive properties of La_2S_3 and GO/ La_2S_3 composite thin films. The chapter is divided into four

sections namely as, A.1, A.2, B.1, and B.2. **Section ‘A.1’**, describes the synthesis and characterizations of La_2S_3 films using the hydrothermal method. The X-ray diffraction analysis showed the formation of an orthorhombic crystal structure. The film has a direct band gap of 3.72 eV useful for optoelectronic devices. Field emission scanning electron microscopy (FE-SEM) images of $\beta\text{-LaS}_2$ films revealed 3D growth of nano-petals-like porous surface morphology. The synthesized films showed hydrophilic nature with a contact angle of 46.9° . **Section ‘A.2’** deals with supercapacitive electrochemical properties in 1 M of Na_2SO_4 electrolyte with a capacitance value of 121.42 Fg^{-1} at a 5 mVs^{-1} scan rate. The cyclic voltammetry and galvanostatic charge/discharge analyses showed that $\beta\text{-LaS}_2$ is a potential candidate for anode material with a potential window of -1.15 to 0 V/SCE . The capacitive retention is obtained after 1000 CV cycles of 84.2 %.

In **Section ‘B.1’**, the La_2S_3 and $\text{GO/La}_2\text{S}_3$ composite films have been synthesized using the SILAR method in an aqueous medium at room temperature to improve the crystallinity film. The XRD and FT-Raman techniques were evident for the structural confirmation of $\text{GO/La}_2\text{S}_3$ composite material. The FE-SEM micrographs of $\text{GO/La}_2\text{S}_3$ composite revealed the formation of a porous well covered grass-like structure with a contact angle of 37.2° indicating the hydrophilic nature. The BET specific surface area calculated for $\text{GO/La}_2\text{S}_3$ composite thin film as $32.36 \text{ m}^2\text{g}^{-1}$. The XPS analyses confirmed the formation of $\text{GO/La}_2\text{S}_3$ composite thin film.

Section ‘B.2’ focuses on the pseudocapacitive behavior of La_2S_3 and $\text{GO/La}_2\text{S}_3$ composite electrodes in 1 M Na_2SO_4 electrolyte. The composite electrode showed higher specific capacitance due to the higher redox activity of composite electrode. The highest specific capacitance obtained for La_2S_3 and composite electrodes are 181.2 and 312 Fg^{-1} , respectively at

a 5 mV s^{-1} scan rate. Also, GO/La₂S₃ composite thin film showed excellent cycling stability with 88.6 % capacity retention after 1000 CV cycles. The EIS measurement showed that composite electrode provides low impedance compared with other two electrodes. The series resistance (R_s : $0.45 \Omega \text{ cm}^{-2}$) and charge transfer resistance (R_{ct} : $3.64 \Omega \text{ cm}^{-2}$) are estimated for composite electrode.

Synthesis of MnO₂ films and their characterization and detailed supercapacitive performance are discussed in **Chapter V**. It describe MnO₂ films deposition on cost effective stainless steel substrate at room temperature by SILAR method. The porous well adherent nano granule like structure with width of 8.2 nm was identified from FE-SEM analyses. The XRD study revealed that MnO₂ film is orthorhombic crystal structure. The electrochemical performance of MnO₂ thin film was carried out in 1 M Na₂SO₄ electrolyte. Nano granular grain composed MnO₂ film showed highest capacitance value of 672 Fg^{-1} at 5 mVs^{-1} CV scan rate. Consecutive 1,000 CV cycling performance of MnO₂ film manifested 90 % capacitive retention and MnO₂ electrode shows lower series resistance (R_s) $1.5 \Omega \text{ cm}^{-2}$ and charge transfer resistance (R_{ct}) $3.6 \Omega \text{ cm}^{-2}$.

Chapter VI included the fabrication and supercapacitive performance evaluation of symmetric (GO/Sm₂S₃//PVA-Na₂SO₄//GO/Sm₂S₃), (GO/La₂S₃//PVA-Na₂SO₄//GO/La₂S₃) and asymmetric (GO/Sm₂S₃//PVA-Na₂SO₄//MnO₂) and (GO/La₂S₃//PVA-Na₂SO₄//MnO₂) FSSSC devices. To achieve best performance, MnO₂ flexible electrode was used as cathode and GO/Sm₂S₃ and GO/La₂S₃ composite flexible electrodes were used as an anode by employing PVA-Na₂SO₄ gel as an electrolyte and separator. This chapter is divided into two sections viz. section 'A' and 'B'. **Section A** gives the detailed information about electrode fabrication, PVA-Na₂SO₄ gel electrolyte preparation and supercapacitor device fabrication process. The films were

Summary and Conclusions

deposited directly on large area ($5 \times 5 \text{ cm}^2$) flexible and conducting stainless steel substrates. **Section B** highlighting the supercapacitive performance evaluation of asymmetric FSS-SCs devices. The (GO/Sm₂S₃//PVA-Na₂SO₄//GO/Sm₂S₃), (GO/La₂S₃//PVA-Na₂SO₄//GO/La₂S₃), (GO/Sm₂S₃//PVA-Na₂SO₄//MnO₂) and (GO/La₂S₃//PVA-Na₂SO₄//MnO₂) FSS-SCs devices exhibit specific capacitance of 12, 6.34, 16.5 and 45.2 Fg⁻¹ at a scan rate of 5 mVs⁻¹, respectively. In addition to this, both supercapacitors show good mechanical flexibility as they illustrate good capacity retentions at different bending angles. The capacitive retentions of symmetric device after 1,000 CV cycles were GO/Sm₂S₃= 82.8 %, GO/La₂S₃= 81.2 % and for asymmetric device GO/Sm₂S₃= 90 %, and GO/La₂S₃= 86.8 %. Two asymmetric (GO/Sm₂S₃//PVA-Na₂SO₄//MnO₂) device was charged and glow the commercial 211 red LEDs glowing for 40 s. The measured output power of 0.73 mWcm⁻².

Table 7.1 Electrochemical parameters of asymmetric FSSSC devices

Sr.no.	Device	Potential window (V)	Cs (Fg ⁻¹)	ED (Wh Kg ⁻¹)	PD (W Kg ⁻¹)	Rs (Ω cm ⁻¹)	Stability (%)
1.	(GO/Sm ₂ S ₃ //PVA-Na ₂ SO ₄ //GO/Sm ₂ S ₃)	1.8	12.5	0.65	1800	0.54	1000= 82.8 %
2.	(GO/La ₂ S ₃ //PVA-Na ₂ SO ₄ //GO/La ₂ S ₃)	1.8	6.34	15.8	3600	1.15	1000= 81.2%
3.	(GO/Sm ₂ S ₃ //PVA-Na ₂ SO ₄ //MnO ₂)	1.8	16.5	3.95	900	1.10	2000 = 90 %
4.	(GO/La ₂ S ₃ //PVA-Na ₂ SO ₄ //MnO ₂)	1.8	45.2	7.5	360	1.01	2000 = 86.8%

The **Chapter-VII** provides the summary and conclusions of all the chapters. The evaluation of electrochemical performance of all the electrode materials is the basic entity to fabricate the supercapacitor device as shown in **Fig.7.1 (a-c)**. **Table 7.1** shows the parameters of symmetric and asymmetric supercapacitive devices such as (GO/Sm₂S₃//PVA-

$\text{Na}_2\text{SO}_4//\text{GO}/\text{Sm}_2\text{S}_3$), $(\text{GO}/\text{La}_2\text{S}_3//\text{PVA}-\text{Na}_2\text{SO}_4//\text{GO}/\text{La}_2\text{S}_3)$, $(\text{GO}/\text{Sm}_2\text{S}_3//\text{PVA}-\text{Na}_2\text{SO}_4//\text{MnO}_2)$ and $(\text{GO}/\text{La}_2\text{S}_3//\text{PVA}-\text{Na}_2\text{SO}_4//\text{MnO}_2)$.

In conclusions, we have synthesized Sm_2S_3 , La_2S_3 , $\text{GO}/\text{Sm}_2\text{S}_3$, $\text{GO}/\text{La}_2\text{S}_3$ and MnO_2 thin film electrodes by hydrothermal and SILAR methods. The supercapacitive properties were successfully tested in aqueous electrolyte using CV, GCD and EIS techniques. Among these thin films and devices, the supercapacitive performance of $(\text{GO}/\text{Sm}_2\text{S}_3//\text{PVA}-\text{Na}_2\text{SO}_4//\text{MnO}_2)$ asymmetric device showed excellent performance. The $(\text{GO}/\text{Sm}_2\text{S}_3//\text{PVA}-\text{Na}_2\text{SO}_4//\text{MnO}_2)$ asymmetric supercapacitor device exhibit maximum specific capacitance of 16.5 Fg^{-1} at a scan rate of 5 mVs^{-1} with cyclic stability of 90 % over 2,000 CV cycles. The ED is 3.95 Whkg^{-1} and PD is 900 Wkg^{-1} . The cost effective $(\text{GO}/\text{Sm}_2\text{S}_3//\text{PVA}-\text{Na}_2\text{SO}_4//\text{MnO}_2)$ asymmetric supercapacitor device can be useful for various commercial applications in portable and foldable devices.

In addition, the practical demonstration of fabricated asymmetric FSSSC device is displayed in **Fig.7.1 (a-c)**. One device has +1.8 V operating potential window, so the series combination of the two devices gives a total potential up to + 3.6 V as shown in **Fig.7.1 (a)**. These devices are charged with a potential of +3.6 V for 30 s and discharged through a panel of 211 red LEDs for 40 seconds **Fig.7.1 (b, c)**. The output power of the device is 0.731 mWcm^{-2} which signifies good charge storing capacity. The larger discharge period compared to the charging period of FSSSC device confirms its suitability for use in practical energy storage devices.

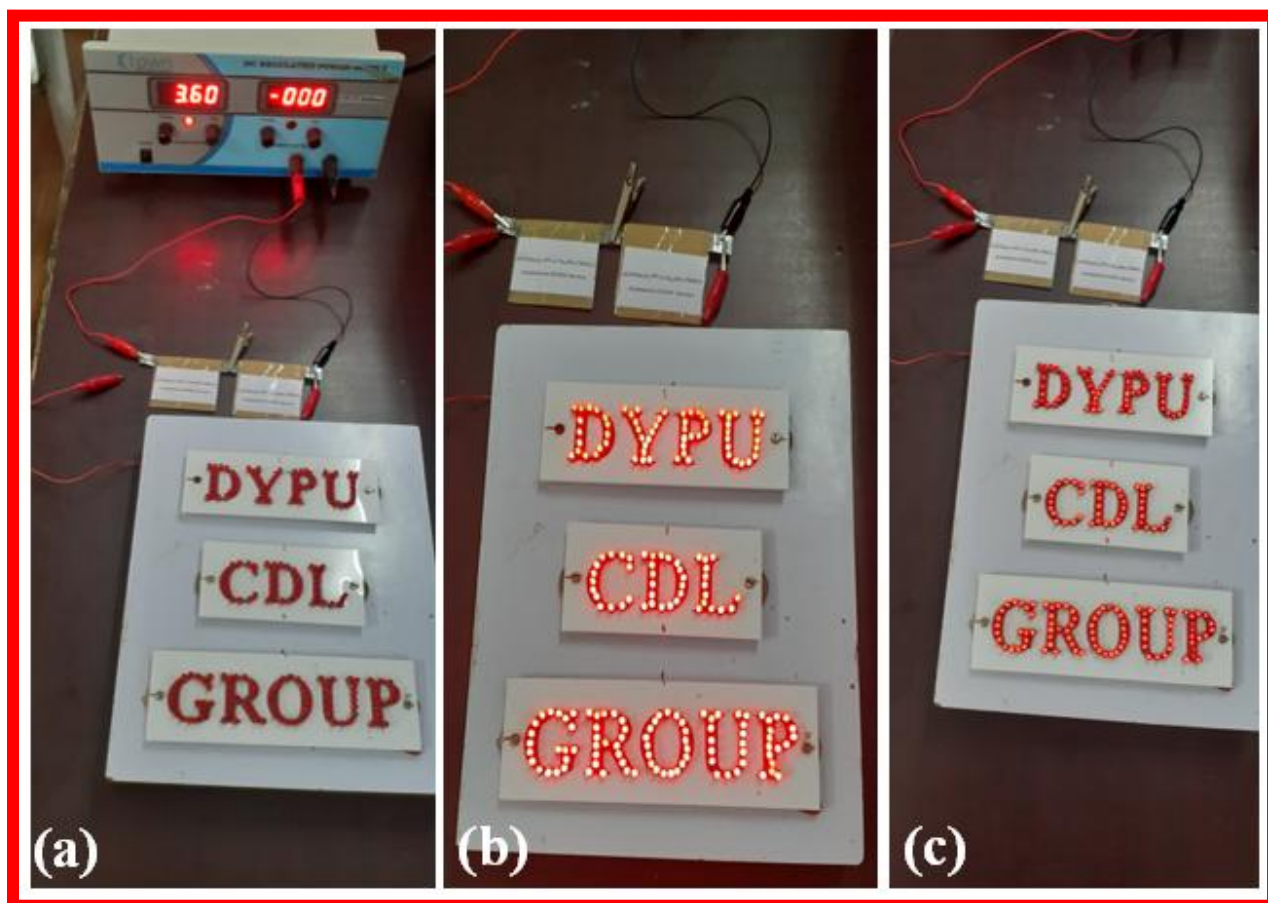


Fig.7.1: Digital photograph of demonstration of (a) two asymmetric (GO/Sm₂S₃//PVA-Na₂SO₄//MnO₂) FSSSC devices charged for +3.6 V, (b) after charging glowing 211 LEDs panel and (c) during discharging of FSSSC device, 211 LEDs panel glows for 40 s.

The I-V characteristic of 211 of red LEDs panel by applying external source is shown in **Fig.7.2 (a)**. At 1.8 V with current 3.9 mA, LEDs panel starts to glow. **Fig.7.2 (b-d)** shows the plot of current, voltage and power with discharge time of device using 211 LEDs panel. It is seen that the discharge current decreases from 192 to 33 mA **(b)** voltage decreases from 3.6 to 1.8 V **(c)** and power also decreases from 0.73 to 0.57 mWcm⁻² **(d)**. This demonstration suggests the

potential capability of GO/Sm₂S₃/PVA-Na₂SO₄/MnO₂ asymmetric device in energy storage for various electronic electrical devices.

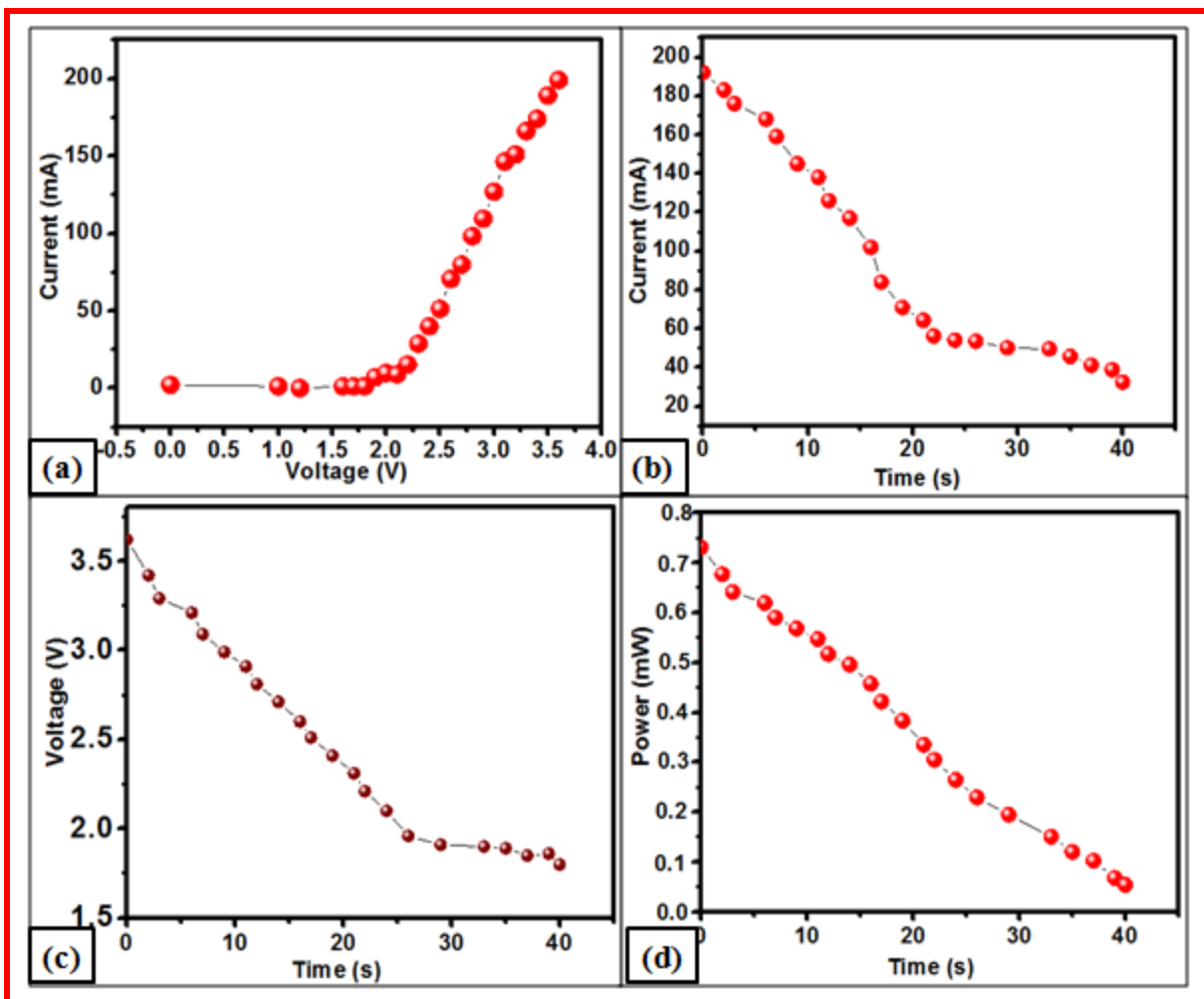


Fig.7.2: (a) The I-V characteristic of 211 red LEDs panel, and (b-d) the I-V characteristics of 211 red LEDs panel operating of FSSSC device during discharging time.